UNIVERSITÉ DE GENÈVE
Département de physique nucléaire et corpusculaire

FACULTÉ DES SCIENCES
Professeur Allan G. Clark

Search for the $\mathrm{B}_d^0 \to \mu\mu K^{*0}$ Decay at CDF and Studies of ATLAS Silicon Tracker Modules

THÈSE

présentée à la Faculté des Sciences de l'Université de Genève
pour obtenir le grade de Docteur ès sciences, mention physique

par

András Zsenei

d'Hongrie

Thèse N^o 3510

GENÈVE
Atelier de reproduction de la Section de Physique
2003

Acknowledgements

This thesis could not have been completed without the advices, efforts, support and encouragement of countless people, a few of which I would like to mention.

First of all I would like to thank Professor Allan Clark for the invaluable guidance he has provided and for giving me the possibility to participate in two great high energy physics experiments – ATLAS and CDF – which are at the forefront of research. I would like to thank Xin Wu who supervised the CDF part of the thesis. He patiently answered all my questions and both his knowledge of the theory and of the ntuples was of great help. I would like also to acknowledge the great discussions we had about statistics with Mario Campanelli, and the clear explanations about the confidence intervals of Bob Cousins.

I would like to thank Prof. Martin Pohl and Prof. Carlo Dionisi for accepting to participate in the jury of my thesis, and for their astute remarks.

I would also like to thank the rest of the University of Geneva group – Daniela, Didier, Lorenzo, Federica, Cristina, Mauro, Monica, Yanwen, Sofia, Manuel, Shulamit, Anna – for everything over the last several years. Special thanks to Mariane who corrected the French part of my thesis.

Many thanks to the technicians of the University of Geneva – Eric, Gérard, Alain, Philippe, Jean, Jean-Pierre – who were a tremenduous help both during the construction of analog modules and the cooling tests. I am also grateful to Catherine and Peggy for the administrative help they gave during all those years, and to Yann whom you could count on to solve any computer problem even late at night.

Kind thanks to all the people with whom I was working at CERN: Peter Weilhammer, Alan Rudge, Wladek, Carlos, Jan, Marcin, Lars and all the others. Julio in particular was a tremenduous help and I had a really great time working with him, whether it was in the beam test over the week-end or in the lab.

I would also like to thank all the people I was working with at Fermilab: Christoph Paus who teached me how to skim the ntuples, Frank Wuerthwein with his thorough knowledge of Bgenerator, Andreas Korn who usually knew the answer to everything and was very helpful to share it.

I would like to thank the Russian community for making life a lot more interesting at Fermilab. The birthday parties, barbecues, lunches, dance lessons and other fun activities with Boris, Alex, Alexei, Andrei, Julia L., Julia P., Konstantin and all the others will be sorely missed. Many thanks to the cubicle co-owners and neighbours

– Anne-Sylvie, Chris, Kirby amongst others –, who not only made it a nice place to be, but brought me to baseball and basketball games as well. There are many other people to whom I am grateful: Houck, James, Jim, Arnold, Jérôme, Stéphane and the list could go on.

I have good memories of working with you all, and wish everyone the best of luck.

Last but not least, I would like to thank my friends and family for all their love and support.

Contents

1 Résumé **xix**
1.1 Introduction théorique xix
1.2 L'expérience CDF au Tevatron xx
1.3 La recherche de la désintégration $B_d^0 \to \mu\mu K^{*0}$ à CDF xxi
1.4 L'expérience ATLAS au LHC xxv
1.5 Construction et évaluation de modules ATLAS équipés de SCTA128 . xxvi

I Theoretical Motivation **1**

2 The Standard Model and beyond **3**
2.1 The Standard Model 3
2.1.1 CP-violation 4
2.1.2 The unitarity triangle 6
2.1.3 Recent results on the CKM Unitarity Triangle 8
2.2 The FCNC Decays of B Mesons 13
2.2.1 Introduction 13
2.2.2 The $b \to sl^+l^-$ decays 15
2.3 Beyond the Standard Model 19

II Search for the $B_d^0 \to \mu\mu K^{*0}$ decay at the CDF experiment **23**

3 The CDF experiment at the Tevatron **25**
3.1 The Tevatron 25
3.1.1 Proton production 26
3.1.2 Antiproton production 27
3.1.3 The Tevatron 27
3.2 The CDF experiment 30
3.2.1 Overview of the CDF experiment 30
3.2.2 The CDF Tracking System 31
3.2.3 The calorimetry 40
3.2.4 Muon detectors 42
3.2.5 The Cherenkov Luminosity Counters 47

3.2.6 Trigger 48

4 Search for the $B_d^0 \to \mu\mu K^{*0}$ decay **59**
4.1 Introduction 59
4.2 The datasets 60
4.3 Preselection 64
4.4 Baseline selection 66
4.5 Optimization of the selection requirements 70
4.5.1 The isolation 70
4.5.2 The transverse decay length 71
4.5.3 The pointing angle 73
4.5.4 The optimization procedure 74
4.6 Acceptance and efficiencies 82
4.6.1 Monte Carlo Calculations 83
4.7 Energy loss, B field corrections and track refitting 86
4.8 Final selection 87
4.9 Future prospects at CDF 92
4.10 Conclusions 93

III Performance of ATLAS modules using the SCTA128 chip **95**

5 The ATLAS experiment at the LHC **97**
5.1 The Large Hadron Collider 97
5.2 ATLAS overview 100
5.3 The Inner Detector 105
5.4 Trigger, Data Acquisition and Controls 111
5.5 The Silicon Tracker (SCT) 112
5.6 The modules 114
5.6.1 Front-end electronics for modules for Si trackers 117
5.6.2 The digital solution (ABCD) 118
5.6.3 The analogue solution (SCTA) 118
5.7 Physics Potential of the ATLAS Detector 119
5.7.1 $B \to \mu\mu(X)$ 120

6 Performance of ATLAS modules using the SCTA128 chip **125**
6.1 Introduction 125
6.2 The digital solution (ABCD) 125
6.2.1 Evolution of the design of the ABCD chip 125
6.2.2 The ABCD chip 127
6.2.3 Electrical module prototypes 128
6.2.4 Effects of radiation on the ABCD 130
6.3 The analogue solution (SCTA128) 131
6.3.1 The SCTA128 chip 132

6.3.2 Laboratory setup 135
6.3.3 Single chip tests 136
6.3.4 Module construction 142
6.3.5 Si strip detector module at the test bench 144
6.3.6 Beam test setup 148
6.3.7 Beam test results 148
6.3.8 Test of a linear optical link 150
6.3.9 Conclusions 156

A Number of signal events for the $B_d^0 \to J/\psi K^{*0}$ decay **159**

B Signal optimization plots for $S^2/(S+B)$ **165**

C Signal optimization plots for $S^2/(a/2+\sqrt{B})^2$ **171**

D Estimated background for the $B_d^0 \to \mu\mu K^{*0}$ decay **177**

E Number of estimated $B_d^0 \to \mu\mu K^{*0}$ events **183**

Bibliography **189**

List of Figures

1.1 Distribution des candidats B pour la désintégration $B^0_d \to J/\psi K^{*0}$ (gauche) et $B^0_d \to \mu\mu K^{*0}$ (droite), $L_{xy} > 0.09\,cm$, $\Delta\Phi < 0.024\,rad$ et $Isolation > 0.65$. Les deux événements $B^0_d \to \mu\mu K^{*0}$ qui sont dans la fenêtre de masse autour de la masse nominale du B^0_d sont affichés en gris. xxiv

1.2 Résolution quand deux bandes de silicium sont touchées (en haut) et quand une seule bande de silicium est touchée (en bas). xxvii

1.3 Spectre de ^{241}Am pour les lignes de transmission en cuivre et pour les lignes de transmission optiques. xxviii

2.1 Unitarity Triangle. 7

2.2 The upper plot shows the Δt distributions for B^0 and $\bar{B}^0$ tags. The middle plot shows the raw asymmetry for low quality tags and the lower plot shows the raw asymmetry for high quality tags. The smooth curves are projections of the unbinned likelihood fit (Belle). 10

2.3 Indirect constraints on the angles of the CKM unitarity triangle compared to the most recent direct measurements of β (blue). The theoretical uncertainties in the indirect constraints are estimated conservatively by the CKM fitter group. 11

2.4 Raw asymmetry for the $B \to \phi K^0_S$ decay for low-quality tags ($0 < r < 0.5$) and for high-quality tags ($0.5 < r < 1.0$). The solid curves show the results of the unbinned maximum-likelihood fit to the Δt distribution, while the dashed line is the expectation from the Standard Model (Belle). 12

2.5 The CKM fit with the constraints from $\sin 2\beta + \gamma$ included (BaBar). . 12

2.6 Diagrams contributing to the $b \to s l^+ l^-$ decays 13

2.7 Beam-energy constrained mass M_{bc} distributions for $K^{(*)}\ell^+\ell^-$ samples from the Belle experiment ($140\,fb^{-1}$). Solid and dotted curves show the results of the fits and the background contributions, respectively. 17

2.8 q^2 distributions for $K\ell^+\ell^-$ and $K^*\ell^+\ell^-$ from the Belle experiment ($140\,fb^{-1}$). Points with error bars show the data while the hatched boxes show the range of SM expectations from various models [18] [20] [22]. 18

2.9 Beam-energy constrained mass (m_{ES}) distribution for the $K\ell^+\ell^-$ modes from the BaBar experiment. The solid curve is the sum of all fit components, including signal; the dashed curve is the sum of all background components. 18
2.10 The dilepton invariant mass squared distribution for $B \to K^*\mu^+\mu^-$. The solid lines represent the SM and the shaded area signals the form-factor related uncertainties. The dotted lines correspond to the SUGRA model with $C_7 = -1.2 \cdot C_7^{SM}$, $C_9 = 1.03 \cdot C_9^{SM}$ and $C_{10} = 1.0 \cdot C_{10}^{SM}$. The long-short dashed lines correspond to an allowed point in the parameter space of the MIA-SUSY model given by $C_7 = -0.83 \cdot C_7^{SM}$, $C_9 = 0.92 \cdot C_9^{SM}$ and $C_{10} = 1.61 \cdot C_{10}^{SM}$. The black lines show the sum of the short-distance and long-distance contributions, while the magenta lines show the corresponding pure short-distance spectra. 20
2.11 The normalized forward-backward asymmetry in $B \to K^*\mu^+\mu^-$ decay as a function of s. The solid line denotes the SM prediction. The dotted lines correspond to the SUGRA model with $C_7 = -1.2 \cdot C_7^{SM}$, $C_9 = 1.03 \cdot C_9^{SM}$ and $C_{10} = 1.0 \cdot C_{10}^{SM}$ with the upper and lower curves representing the $C_7 < 0$ and $C_7 > 0$ case, respectively. The long-short dashed (blue) lines correspond to the MIA-SUSY model, using the parameters $C_7 = \pm 0.83 \cdot C_7^{SM}$, $C_9 = 0.92 \cdot C_9^{SM}$ and $C_{10} = 1.61 \cdot C_{10}^{SM}$ with the upper and lower curves representing the $C_7 < 0$ and $C_7 > 0$ case, respectively. The dashed curves indicating a positive asymmetry for large s correspond to the MIA-SUSY models using the parameters $C_7 = \pm 0.83 \cdot C_7^{SM}$, $C_9 = 0.79 \cdot C_9^{SM}$ and $C_{10} = -0.38 \cdot C_{10}^{SM}$. 21

3.1 The accelerator complex at Fermilab. 26
3.2 Instantenuous luminosities at the start of the stores through the end of 2003 [56]. 29
3.3 The luminosity delivered by the Tevatron since the start of Run II until January 2004 [55]. 29
3.4 The coordinate system of the CDF experiment. 30
3.5 Three dimensional view of the CDF detector showing the position of the detector subsystems. 32
3.6 Elevation view of the CDF detector showing the position of the different subsystems. 33
3.7 Overview of the CDF tracking system. 34
3.8 Overall view of the different silicon subsystems. 35
3.9 Design of the Layer 00. 35
3.10 SVX barrel and bulkhead. 36
3.11 Perspective views of the z and ϕ-sides of a Layer 0 ladder. 37
3.12 Impact parameter resolution in μm as a function of the p_T for tracks passing through passive material without Layer 00 hits (red), and with Layer 00 hits (blue). 37

3.13 Efficiency as a function of η of the calorimeter seeded outside-in silicon tracking for tracks with three (blue), four (green) and five (red) silicon hits. . . . 38
3.14 1/6 section of the COT endplate. . . . 39
3.15 Resolution of the Central Outer Tracker. . . . 40
3.16 Location of the different components of the muon system in azimuth ϕ and pseudorapidity η. . . . 43
3.17 Schematic view of the 16 cells of a CMU module. . . . 44
3.18 Layout of a CMP wall with steel, chambers (CMP) and counters (CSP). Counter readout is located at $z = 0$. Counter layers are offset from the chambers and from each other in x to allow overlapping light guides and PMTs and saving space. . . . 44
3.19 Schematic view of a CMP-CMX tube (left), and the drift tube layout in a CMX module covering 15^0 in azimuth (right). . . . 45
3.20 A detailed section of the IMU Barrel, showing several chamber cells and the corresponding scintillators. . . . 46
3.21 Integrated luminosity delivered by the Tevatron (red) and recorded by CDF (blue) through the end of 2003 [56]. . . . 47
3.22 Functional block diagram of the CDF data flow. . . . 48
3.23 Block diagram of the Run II trigger system. . . . 49
3.24 Level 1 CMU trigger efficiency as a function of muon p_T and muon track ϕ after excluding bad wedge in 240-270 degree. For the efficiency as a function of ϕ the muons are required to have $p_T > 3\,GeV/c$. . . . 51
3.25 Level 1 CMX trigger efficiency as a function of muon $1/p_T$ and muon ϕ. For the right plot the filled square points are for the averaged efficiencies, the dot points are for the East CMX efficiencies, and the open square are for the West CMX efficiencies. . . . 51
3.26 Architecture of the SVT trigger. . . . 53
3.27 Impact parameter distribution of SVT tracks. $\sigma = 50\,\mu m = 35\,\mu m \oplus 33\,\mu m = SVT\,resolution \oplus beam$. . . . 54
3.28 SVT efficiency versus the p_T and ϕ of the muon from $B \to J/\psi X$ decays for tracks with 4 $R-\phi$ silicon hits for data (blue) and Monte Carlo simulation (red) [79]. . . . 55
3.29 Invariant mass distribution of $B \to h^+h^-$ decays. . . . 55
3.30 Level 3 block diagram. . . . 57

4.1 Extrapolating the COT track from the outside into the SVX. . . . 64
4.2 Invariant mass distribution of the dimuons after the preselection. . . . 66
4.3 Different regions of the analysis. . . . 69
4.4 Invariant mass distribution of the B candidates after the baseline selection requirements for the resonant (left) and non-resonant (right) decays. . . . 70

4.5 The points with error bars show background subtracted data for $B_d^0 \to J/\psi K^{*0}$ decays after baseline selection and $L_{xy} > 0.01$, $\Delta\Phi < 0.1$ cuts. The shaded histogram shows the background from the high $500\,MeV$ sideband of the data. 71
4.6 Transverse decay length distribution for the signal region from MC (histogram) and from the high sideband region of $500\,MeV$ from data (shaded histogram). The two histograms are normalized in order to have the same area. 72
4.7 Comparison of background subtracted data (points with error bars) and MC (solid histogram) for $\mathrm{B}_d^0 \to J/\psi K^{*0}$ deacays after baseline selection and $iso > 0.65$, $L_{xy} > 0.01$, $\Delta\Phi < 0.1$ cuts. The shaded histogram shows the background from the $500\,MeV$ high sideband of the data. 72
4.8 Pointing angle distribution for the signal region from $\mathrm{B}_d^0 \to \mu\mu K^{*0}$ MC (histogram) and from the high sideband region of $500\,MeV$ from data (shaded histogram). The two histograms are normalized to have the same area. 73
4.9 Comparison of background subtracted data (points with error bars) and MC (solid histogram) for $\mathrm{B}_d^0 \to J/\psi K^{*0}$ decays after baseline selection and $iso > 0.65$, $L_{xy} > 0.01$, $\Delta\Phi < 0.1$ cuts. The shaded histogram shows the background from the high $500\,MeV$ sideband of the data. 74
4.10 Examples of background fits with cuts that result in high statistics (left, baseline cuts), and with cuts that result in low statistics (right, baseline cuts and $L_{xy} > 0.075$, $isolation > 0.65$). 76
4.11 Correlations between the three discriminating variables for events satisfying the baseline cuts in both the low and high mass sideband (left), and only the high mass sideband (right). 78
4.12 Rejection of the $\Delta\Phi$ and L_{xy} cuts for events passing baseline requirements (but no cut on isolation). 79
4.13 Example of fitting the B peak of $\mathrm{B}_d^0 \to J/\psi K^{*0}$ decay (baseline cuts and $\Delta\Phi < 0.048$, $isolation > 0.7$, $L_{xy} > 0.6$). 80
4.14 Correlations between the three discriminating variables for events satisfying the baseline cuts for the $\mathrm{B}_d^0 \to J/\psi K^{*0}$ decay. On the left side are shown the events in the high sideband region, and on the right the events from the B peak region. 81
4.15 Example plot for number of $\mathrm{B}_d^0 \to J/\psi K^{*0}$ events for $Iso > 0.7$ and different values of L_{xy} and $\Delta\Phi$ cuts (the first column represents events with no L_{xy} cut, while the upper row represents events with no $\Delta\Phi$ cut). 82
4.16 Comparison of background subtracted data (points with error bars) and MC (solid histogram) for $\mathrm{B}_d^0 \to J/\psi K^{*0}$ deacays after baseline selection and $iso > 0.65$, $L_{xy} > 0.01$, $\Delta\Phi < 0.1$ cuts. The shaded histogram shows the background from the $500\,MeV$ high sideband of the data. 84

4.17 Comparison of background subtracted data (points with error bars) and MC (solid histogram) for $B_d^0 \to J/\psi K^{*0}$ deacays after baseline selection and $iso > 0.65$, $L_{xy} > 0.01$, $\Delta\Phi < 0.1$ cuts. The shaded histogram shows the background from the $500\,MeV$ high sideband of the data. 85
4.18 Invariant mass distribution of the B candidates of the $B_d^0 \to J/\psi K^{*0}$ decay without refitting the tracks (left) and applying the refit procedure (right). 86
4.19 Figure of merit $S^2/(1/2+B)^2$ for $iso > 0.7$ without refitting the tracks. 87
4.20 Figure of merit S^2/B for $iso > 0.65$. 88
4.21 B candidate distribution for the $B_d^0 \to \mu\mu K^{*0}$ decay, $L_{xy} > 0.09\,cm$, $\Delta\Phi < 0.024\,rad$ and $Isolation > 0.65$. The two events falling inside the mass window are drawn in grey. 89
4.22 B candidate distribution for the $B_d^0 \to J/\psi K^{*0}$ decay, $L_{xy} > 0.09cm$, $\Delta\Phi < 0.024rad$ and $Isolation > 0.65$. 89
4.23 Scatter plot of $B_d^0 \to \mu\mu K^{*0}$ candidates, $L_{xy} > 0.09cm$, $\Delta\Phi < 0.024rad$ and $Isolation > 0.65$. 90

5.1 Overall view of the LHC accelerator complex. 98
5.2 Overall view of the ALICE, LHCb and CMS detectors. 99
5.3 Overall view of the ATLAS detector 101
5.4 Three-dimensional view of the ATLAS calorimetry 103
5.5 Transverse view of the muon spectrometer 104
5.6 The Inner Detector 105
5.7 Transverse impact parameter resolution (d_0) and longitudinal impact parameter resolution projected transversely to the track direction ($z_0 \times \sin\theta$) as function of $|\eta|$ for muons of $p_T = 1\,GeV$ and $p_T = 200\,GeV$ for both layouts. 108
5.8 Angular resolution in ϕ and $\cot\theta$ of charged tracks as function of p_T for $|\eta| < 0.25$ for both layouts. 109
5.9 Inverse transverse momentum resolution of charged tracks as a function of p_T in $|\eta| < 2.5$ for DC1 layout. The resolution plot for the Initial layout is identical. 110
5.10 Schematic layout of the Trigger and DAQ system of ATLAS. 111
5.11 The four nested barrels of the SCT. 113
5.12 Distribution for number of radiation lengths for pixels, SCT, TRT and external services and patch-panels. 114
5.13 3 SCT barrel modules mounted on a test structure. 115
5.14 SCT forward module. 115
5.15 Four Outer Modules on the Forward Sector with the wiggly cooling pipes. 116
5.16 Reconstructed signal (cross-hatched) and background for $B_d^0 \to K^{*0}\mu\mu$ (left) and $B_s^0 \to \phi^0\mu\mu$ (right) decays with 30 fb^{-1}. 121

5.17 Sensitivity of A_{FB} to the Wilson coefficient C_7. The three points are the simulation results. The solid line shows the Standard Model prediction, the dotted lines show the range predicted by the MSSM for $R_7 = C_7/C_7^{SM} > 0$ and the dashed lines show the range predicted by the MSSM for $R_7 < 0$. 123

6.1 ABCD block diagram. 127
6.2 Noise in mV versus channel number distribution along a module (6 ABCDNT chips). Channels 256-288 are bonded to 6 cm detector strips. Channels 341-383 are not bonded to the detector. All other channels are bonded to 12 cm detector strips. 129
6.3 Noise distribution in mV along one module (6 ABCD2T chips). . . . 130
6.4 Picture of one module prototype with 6 ABCD2T chips for the SCT detector barrel. 131
6.5 Block diagram of the SCTA128VG chips 133
6.6 Simulation results of 2 chips sending data sequentially (only 5 analogue channels simulated instead of 128). 134
6.7 The setup used for the SCTA-DAQ 135
6.8 Single chip tests (the chip is in a protected space underneath the PCB). 137
6.9 Gain linearity for a single channel 138
6.10 Gain across the 128 channels of a single chip 138
6.11 Noise across the 128 channels of a single chip 139
6.12 ADB pedestal map in one SCTA chip 140
6.13 ADB pedestal spread distribution for all channels in a chip 140
6.14 Pulse shapes at the output of the multiplexer obtained from the delay scan for two consecutive trigger delays. 141
6.15 A hybrid equipped with 6 SCTA128HC chips 142
6.16 Module equipped with SCTA128HC chips and AC-coupled ATLAS barrel detectors. 143
6.17 Module equipped with SCTA128HC chips and DC-coupled ATLAS forward detectors. 144
6.18 Characteristics of the two leftmost chips on the hybrid 145
6.19 Characteristics of the leftmost two chips of the module 146
6.20 ENC for SCTA128VG chips connected to various length silicon strip detectors 147
6.21 Linearity of the chip based on radioactive source tests. 147
6.22 Signal over noise for 12.8 cm strips 149
6.23 Resolution of double-hit and single-hit clusters. 149
6.24 Charge sharing among adjacent strips 150
6.25 Noise occupancy versus efficiency for 12.8 cm silicon strip detector module equipped with SCTA128HC chips. 151
6.26 Signal over noise from data taken with 100 GeV pion beam for a chip connected to 12.8 cm detector strips. 151
6.27 VCSEL light output versus current 152

6.28 Residuals of least-squares fit 153
6.29 Header of an SCTA chip with optical readout. 153
6.30 Noise for copper and optical readout. 154
6.31 Calibration linearity for copper and optical readout. 154
6.32 ^{241}Am spectra for both copper and optical readout 155
6.33 Chip response linearity with radioactive sources and optical readout . 156

A.1 Number of $B_d^0 \to J/\psi K^{*0}$ events for $Iso > 0.5$. 160
A.2 Number of $B_d^0 \to J/\psi K^{*0}$ events for $Iso > 0.55$. 160
A.3 Number of $B_d^0 \to J/\psi K^{*0}$ events for $Iso > 0.6$. 161
A.4 Number of $B_d^0 \to J/\psi K^{*0}$ events for $Iso > 0.65$. 161
A.5 Number of $B_d^0 \to J/\psi K^{*0}$ events for $Iso > 0.7$. 162
A.6 Number of $B_d^0 \to J/\psi K^{*0}$ events for $Iso > 0.75$. 162
A.7 Number of $B_d^0 \to J/\psi K^{*0}$ events for $Iso > 0.8$. 163

B.1 Figure of merit $S^2/(S+B)$ for $Iso > 0.5$. 166
B.2 Figure of merit $S^2/(S+B)$ for $Iso > 0.55$. 166
B.3 Figure of merit $S^2/(S+B)$ for $Iso > 0.6$. 167
B.4 Figure of merit $S^2/(S+B)$ for $Iso > 0.65$. 167
B.5 Figure of merit $S^2/(S+B)$ for $Iso > 0.7$. 168
B.6 Figure of merit $S^2/(S+B)$ for $Iso > 0.75$. 168
B.7 Figure of merit $S^2/(S+B)$ for $Iso > 0.8$. 169

C.1 Figure of merit $S^2/(a/2+B)^2$ for $Iso > 0.5$. 172
C.2 Figure of merit $S^2/(a/2+B)^2$ for $Iso > 0.55$. 172
C.3 Figure of merit $S^2/(a/2+B)^2$ for $Iso > 0.6$. 173
C.4 Figure of merit $S^2/(a/2+B)^2$ for $Iso > 0.65$. 173
C.5 Figure of merit $S^2/(a/2+B)^2$ for $Iso > 0.7$. 174
C.6 Figure of merit $S^2/(a/2+B)^2$ for $Iso > 0.75$. 174
C.7 Figure of merit $S^2/(a/2+B)^2$ for $Iso > 0.8$. 175

D.1 Estimated background for the $B_d^0 \to \mu\mu K^{*0}$ decay for $Iso > 0.5$. . . . 178
D.2 Estimated background for the $B_d^0 \to \mu\mu K^{*0}$ decay for $Iso > 0.55$. . . . 178
D.3 Estimated background for the $B_d^0 \to \mu\mu K^{*0}$ decay for $Iso > 0.6$. . . . 179
D.4 Estimated background for the $B_d^0 \to \mu\mu K^{*0}$ decay for $Iso > 0.65$. . . . 179
D.5 Estimated background for the $B_d^0 \to \mu\mu K^{*0}$ decay for $Iso > 0.7$. . . . 180
D.6 Estimated background for the $B_d^0 \to \mu\mu K^{*0}$ decay for $Iso > 0.75$. . . . 180
D.7 Estimated background for the $B_d^0 \to \mu\mu K^{*0}$ decay for $Iso > 0.8$. . . . 181

E.1 Number of estimated $B_d^0 \to \mu\mu K^{*0}$ events for $Iso > 0.5$. 184
E.2 Number of estimated $B_d^0 \to \mu\mu K^{*0}$ events for $Iso > 0.55$. 184
E.3 Number of estimated $B_d^0 \to \mu\mu K^{*0}$ events for $Iso > 0.6$. 185
E.4 Number of estimated $B_d^0 \to \mu\mu K^{*0}$ events for $Iso > 0.65$. 185
E.5 Number of estimated $B_d^0 \to \mu\mu K^{*0}$ events for $Iso > 0.7$. 186
E.6 Number of estimated $B_d^0 \to \mu\mu K^{*0}$ events for $Iso > 0.75$. 186

E.7 Number of estimated $B_d^0 \to \mu\mu K^{*0}$ events for $Iso > 0.8$. 187

List of Tables

2.1 Main properties of the fermions 4
2.2 The CKM matrix elements in the tree and penguin decays of the $\bar{K}$, D and $\bar{B}$ mesons. 13
2.3 Theoretical predictions based on the Standard Model for the exclusive decays B $\rightarrow Kl^+l^-$ 16
2.4 Latest observations and limits of rare B decays by the Belle and BaBar experiments. 16

3.1 Parameters of the Tevatron for Run I and Run II [49] [53]. Recent developments suggest, that Run IIb will use essentially the same parameters as Run IIa [51]. 28
3.2 Characteristics of the Run II silicon detectors. 34
3.3 Characteristics of the Run II calorimeters of the CDF detector. . . . 41
3.4 Design parameters of the CDF II Muon Detectors. 42

4.1 Summary of the Level 1 rare B triggers. 60
4.2 Cuts common to all Level 3 rare B triggers. 61
4.3 Summary of the Level 3 rare B triggers (common cuts are shown in Table 4.2). 61
4.4 Summary of the Level 3 rare B trigger rates, rejections and efficiencies. The rejection is normalized to the corresponding L1 trigger rate. The efficiency is normalized to the number of generated events. 62
4.5 Datasets used in the present study. 63
4.6 Preselection cuts applied to the data sample. Following the CDF convention the various quantities are always expressed in GeV and cm unless otherwise stated. 67
4.7 Baseline selection cuts applied to the data sample. 68
4.8 The linear correlation coefficients for the discriminating variables in the sideband region for the $B^0_d \rightarrow \mu\mu K^{*0}$ decay. 77
4.9 The rejection of isolation cuts from events passing the baseline cuts and $\Delta\Phi < 0.5$. 77
4.10 The linear correlation coefficients for the discriminating variables in the signal region for the $B^0_d \rightarrow J/\psi K^{*0}$ decay. 80
4.11 Selection efficiencies for the $B^0_d \rightarrow \mu\mu K^{*0}$ and $B^0_d \rightarrow J/\psi K^{*0}$ decays. . 85

4.12 Values of the two figures of merit after the baseline cuts, $L_{xy} > 0.09\,cm$ and $\Delta\Phi < 0.024\,rad$ for different values of the isolation cut. 88
4.13 Projected number of $B_d^0 \to \mu\mu K^{*0}$ decays (based on [51]). 92

5.1 Design parameters of the LHC 98

Chapter 1

Résumé

Ce mémoire de thèse est composé de trois parties. La première partie donne une brève introduction théorique au modèle physique des interactions étudiées dans le présent mémoire. La deuxième partie décrit la recherche des désintégrations $B_d^0 \to \mu\mu K^{*0}$ effectuée dans le cadre de l'expérience CDF (Collider Detector at Fermilab). Elle introduit d'abord en détail le détecteur CDF et ses composants, ensuite elle explique la stratégie d'analyse utilisée pour obtenir les rapports de branchement, et le cas échéant, les limites supérieures des rapports de branchement optimales. La troisième partie commence par la description du collisionneur LHC (Large Hadron Collider) et de l'expérience ATLAS (A Toroidal LHC Apparatus). Finalement, la construction et évaluation de modules ATLAS équipés de puces SCTA sera présentée en détail. Ces modules sont essentiels pour la détection des désintégrations des mésons B, comme $B_d^0 \to \mu\mu K^{*0}$, qui peuvent explorer la validité des différentes théories décrivant la physique des particules.

1.1 Introduction théorique

Le Modèle Standard (SM) des interactions électro-faibles et fortes décrit les interactions entre les particules élémentaires en utilisant la théorie quantique des champs. Jusqu'à présent, le Modèle Standard a eu un succès remarquable par ces prédictions qui ont été vérifiées expérimentalement.

A présent, un des objectifs de la physique des particules est de vérifier les valeurs des éléments de la matrice de mélange des quarks, la matrice de Cabibbo-Kobayashi-Maskawa. Le domaine le plus adapté à ces recherches est celui des désintégrations des mésons B. Un type très intéressant de ces désintégrations est celui qui est induit par les courants neutres avec changement de saveur. Dans le Modèle Standard ces courants sont interdits au premier ordre, et ne peuvent procéder qu'à travers des diagrammes d'ordre plus élevé, ce qui implique des rapports de branchement très faibles. De ce fait, la mesure des processus de ce type, comme $B_d^0 \to \mu\mu K^{*0}$, est expérimentalment un défi important. Dans plusieurs extensions du Modèle Standard, notamment dans plusieurs des modèles supersymétriques, ces désintégrations pourraient procéder via des processus additionnels, augmentant le rapport de branche-

ment. La mesure d'un rapport de branchement différent de celui prédit par le Modèle Standard pourrait être l'indication de nouveaux phénomènes physiques au-delà de celui-ci.

1.2 L'expérience CDF au Tevatron

Le Tevatron est un collisionneur de type proton-antiproton situé au Fermi National Laboratory (FERMILAB) à Chicago (Etats-Unis). Son énergie de centre de masse est de $\sqrt{s} = 1.96\,TeV$, ce qui en fait le collisionneur atteignant la plus haute énergie jusqu'à la mise en service du Large Hadron Collider (LHC).

CDF est une des deux expériences multifonctionnelles construites afin de permettre l'étude de collisions $p\bar{p}$ au Tevatron. C'est un détecteur cylindrique avec une symétrie avant-arrière, conçu pour couvrir le plus d'angle solide possible autour du point d'interaction. On utilise un système de coordonnées polaires où r est la distance mesurée à partir du point d'interaction, ϕ est l'angle azimutal se trouvant dans le plan perpendiculaire à la direction du faisceau, et θ est l'angle polaire qui définit la pseudorapidité $\eta = -\ln\tan\frac{\theta}{2}$.

En partant du point d'interaction les particules produites rencontrent trois parties principales du détecteur:

- Les détecteurs de traces de particules chargées: Layer 00 (L00), le Silicon Vertex Detector (SVX II), l'Intermediate Silicon Layer (ISL) et le Central Outer Tracker (COT).
- Les calorimètres électromagnétiques et hadroniques.
- Les chambres à muon: le Central Muon Detector (CMU), le Central Muon Upgrade (CMP) et le Central Muon Extension (CMX).

Le détecteur de vertex au silicium est la première couche cylindrique autour du tube à vide du Tevatron. Il est composé de L00, SVX et ISL. Il s'agit de détecteurs à bandes ou "microstrips" au silicium. L00, étant à $1.35\,cm$, est la couche la plus proche du point d'interaction. Le SVX est composé de trois cylindres de $29\,cm$ de longueur, qui – montés ensemble – mesurent au total $96\,cm$. Chaque cylindre est divisé en douze sections azimutales de 30^o, chacune contenant cinq couches de détecteurs au silicium, qui mesurent la position des traces dans le plan $r-\phi$. Le SVX permet la reconstruction précise des points d'interaction secondaires des particules avec un court temps de vie, comme les mésons B. Il mesure le paramètre d'impact avec une précision allant jusqu'à $50\,\mu m$. Le ISL qui se trouve entre le SVX et le COT prolonge la couverture des détecteurs au silicium à des valeurs de pseudorapidité allant jusqu'à 2.0.

Le COT est une chambre à dérive de $310\,cm$ de long avec un rayon intérieur de $44\,cm$ et un rayon extérieur de $132\,cm$. Elle est composée de 96 couches alternant des fils de mesure axiaux et stéréo. Le COT est capable de reconstruire les traces des particules dans la région de $|\eta| < 1.0$ avec une impulsion transverse supérieure à

$400\,MeV/c$. Les détecteurs de traces se trouvent à l'intérieur du champ magnétique de $1.4\,T$ produit par un aimant solénoïdal placé autour d'eux.

Les calorimètres électromagnétiques et hadroniques basés sur la technologie des scintillateurs mesurent le passage des particules avec $|\eta| < 3.64$. Les chambres à muons sont situées à l'extérieur des calorimètres électromagnétiques et hadroniques. Dans la région centrale ($|\eta| < 0.6$) le CMU est constitué de quatre couches de chambres à dérive. Elles identifient les muons par le biais de leur fort pouvoir de pénétration, en reconstruisant des segments de traces et les associant aux traces reconstruites par le SVX et le COT. Derrière $60\,cm$ d'acier additionnels se trouvent les quatre plans de chambres à dérive du CMP, qui permettent un taux de rejet de bruit de fond encore plus important que le CMU. La couverture des chambres à muons est complétée par le CMX qui couvre la région $0.6 < |\eta| < 1.0$. Les chambres à muons incluent aussi des scintillateurs qui permettent de mesurer avec précision le temps exact de passage de la particule.

Le système de déclenchement est composé de trois niveaux consécutifs, chacun diminuant le nombre d'événements d'un ou deux ordres de grandeur. Une partie spécialement intéressante du deuxième niveau du système de déclenchement est le Silicon Vertex Tracker, qui, pour la première fois pour un collisionneur, permet d'avoir des coupures sur les quantités comme le paramètre d'impact, et cela avec une résolution de $50\,\mu m$. Ceci permet de sélectionner des désintégrations $B^0_d \to \mu\mu K^{*0}$ avec une efficacité accrue tout en rejetant la majeure partie du bruit de fond.

1.3 La recherche de la désintégration $B^0_d \to \mu\mu K^{*0}$ à CDF

Pour la présente recherche, un échantillon de données collectées pendant la période de Mars 2002-Août 2003 correspondant à une luminosité integrée de $215\,pb^{-1}$, est utilisé. Le rapport de branchement de la désintégration $B^0_d \to \mu\mu K^{*0}$ est mesuré par rapport à celui de la désintégration $B^0_d \to J/\psi K^{*0}$. Ainsi, plusieurs facteurs difficiles à déterminer – comme la luminosité, la section efficace de production du méson B^0_d et certaines efficacités de reconstruction et de sélection – et leurs incertitudes peuvent être éliminés. Le K^{*0} est reconstruit à partir d'un kaon et d'un pion, alors que le J/ψ est reconstruit à partir de deux muons pour avoir des états finaux identiques pour les deux désintégrations.

Pour reconstruire les deux désintégrations $B^0_d \to \mu\mu K^{*0}$ et $B^0_d \to J/\psi K^{*0}$, on commence par choisir des événements qui ont été sélectionnés par un des déclenchements à dimuons[1]. Cela signifie que l'impulsion transverse des muons détectés par CMU doit être supérieure à $1.5\,GeV$, ceux détectés par CMX supérieure à $2.0\,GeV$ et ceux détectés par CMP supérieure à $3.0\,GeV$. Pour chacun des muons, la différence entre le point de détection dans une des chambres à muons et l'extrapolation de la trace depuis le système de trajectographie, doit être inférieure à $30\,cm$, $50\,cm$ et $25\,cm$ pour CMU, CMX et CMP, respectivement. Une masse invariante des deux muons entre 0

[1] Ce sont d'ailleurs les déclenchements du niveau 1 qui sont optimisés pour l'acquisition des J/ψ, ce qui est très précieux pour le canal $B^0_d \to J/\psi K^{*0}$.

et $6\,GeV$ est requise.

La prochaine étape, consiste à reconstruire le kaon K^{*0} à partir d'un kaon et d'un pion. Puisque CDF n'est pas très performant pour l'identification des kaons et des pions pour la plage d'impulsions transverses pertinentes, pour chaque trace on envisage les deux hypothèses. L'impulsion transverse de chacune des traces doit être supérieure à $0.5\,GeV$, la masse invariante de la paire kaon-pion doit être dans une fourchette de $\pm 100\,MeV$ autour de la masse de K^{*0} publiée par le Particle Data Group, et l'impulsion transverse du candidat K^{*0} doit être supérieure à $2\,GeV$. Ces coupures diminuent sensiblement le bruit de fond combinatoire dû à l'identification erronée kaon-pion.

La dernière étape est la reconstruction du méson B_d^0. Un fit cinématique de moindres-carrés des quatre traces est effectué où les traces sont contraintes de provenir d'un même vertex, et la variable décrivant la qualité du fit devant être inférieure à 15. Ainsi les candidats dont les traces sont proches dans l'espace mais ne proviennent pas d'un même vertex, seront éliminés. L'impulsion transverse du candidat B_d^0 doit être supérieure à $6\,GeV$.

Pour les candidats $\mathrm{B}_d^0 \to J/\psi K^{*0}$, la masse invariante des deux muons doit être à moins de $200\,MeV$ de la masse du J/ψ, et la masse invariante du candidat doit être à moins de $50\,MeV$ de la masse du B_d^0. Pour les candidats $\mathrm{B}_d^0 \to \mu\mu K^{*0}$, la masse invariante du candidat doit aussi être à moins de $50\,MeV$ de la masse du B_d^0. Par contre, on exclut les régions de $\pm 200\,MeV$ autour de la résonance J/ψ, et $\pm 100\,MeV$ autour de la résonance $\psi(2S)$.

Après les coupures de base, qui viennent d'être décrites, une optimisation est effectuée sur trois variables choisies pour diminuer le bruit de fond dans la mesure du possible, tout en gardant une efficacité maximale pour le signal recherché. Les trois variables choisies pour l'optimisation sont l'isolation, la longueur de désintégration transverse et l'angle d'ouverture.

Au cours de la fragmentation d'un quark b, le méson B résultant a tendance à emporter la majeure partie de l'impulsion du quark initial. Il en résulte qu'une grande fraction de l'impulsion mesurée dans un cône autour de méson B est portée par les particules issues de la désintégration du méson B. Cette fraction, définie comme $I = \frac{p_T^B}{p_T^B + \sum p_T}$, est appelée isolation. La somme est une somme scalaire incluant toutes les traces (sauf celles des particules issues de la désintégration du B) qui se trouvent à l'intérieur du cône défini par $\Delta R = \sqrt{(\Delta\eta)^2 + (\Delta\phi)^2}$ autour du vecteur d'impulsion du candidat.

La deuxième variable d'optimisation est liée au fait que les mésons B ont un temps de vie relativement long comparé au celui de la majeure partie du bruit de fond. Ainsi, la longueur de désintégration propre permet d'éliminer une grande portion de ce bruit de fond. Pour la détermination de cette quantité il est très important de reconstruire la position de la désintégration du méson, appelée vertex secondaire, avec une grande précision. Pour obtenir cette précision on requiert que le passage des particules soit enregistré dans au moins 20 (16) couches axiaux (stéréo) du COT, et 3 couches du SVX. Pour les pions et kaons de basse impulsion transverse cette exigence

est encore plus stricte, car on demande que le passage de la particule soit enregistré dans au moins 4 des couches du détecteur au silicium. La longueur de désintégration transverse est définie comme $L_{xy} = \vec{l}_{xy} \cdot \vec{p}^B_T / p^B_T$, où $\vec{l_{xy}}$ est le vecteur qui pointe du vertex primaire[2] au vertex secondaire, $\vec{p}^B_T$ est le vecteur de l'impulsion transverse du B reconstruit et p^B_T est sa valeur absolue. Pour s'assurer qu'on choisit des traces reconstruites avec une bonne précision, l'incertitude sur la longueur de désintégration transverse doit être inférieure à $150\,\mu m$. Pour éliminer des événements représentant des pathologies, L_{xy} doit être inférieur à $1\,cm$, et la longueur de désintégration propre doit être inférieure à $0.5\,cm$.

Une autre quantité, qui constitue un fort critère de rejet de bruit de fond, est l'angle d'ouverture ($\Delta\Phi$) entre le vecteur d'impulsion du B reconstruit ($\vec{p}^B_T$) et la direction de sa trace ($\vec{l_{xy}}$). Il est clair que les deux muons, le kaon et le pion provenant du même méson B, les deux vecteurs doivent être parallèles.

La procédure d'optimisation est exécutée en évaluant trois différentes "Figure of Merit" (FOM) pour les différentes valeurs de coupure pour ces trois variables. Les FOM déterminent le choix optimal des coupures pour rejeter le plus de bruit de fond possible tout en gardant la plus grande partie du signal. Pour évaluer ces FOM on doit estimer le bruit de fond et le nombre de désintégrations $B^0_d \to \mu\mu K^{*0}$.

Le bruit de fond attendu est estimé en extrapolant le nombre d'événements observés dans les régions latérales, de masse invariante du candidat B entre $4.379\,GeV/c^2$ et $5.179\,GeV/c^2$ et entre $5.379\,GeV/c^2$ et $6.279\,GeV/c^2$. Comme après les coupures de base et les coupures d'optimisation le nombre de candidats commence à devenir relativement bas, pour augmenter la statistique une étude a été faite pour comprendre les dépendences entre les variables d'optimisation. Il en a été déduit, que l'isolation a été indépendante de l'angle d'ouverture et de la longueur de désintégration transverse. Ainsi, le pouvoir de rejet de bruit de fond des coupures sur l'isolation a été étudié indépendamment de celui des deux autres, ce qui a permis d'utiliser des échantillons plus grandes pour les deux études.

Pour estimer le nombre de désintégrations $B^0_d \to \mu\mu K^{*0}$ attendues, on utilise le fait que ce nombre est lié au nombre de désintégrations $B^0_d \to J/\psi K^{*0}$. Il suffit de multiplier ce dernier par le rapport de leurs efficacités de coupures de base respectifs – qu'on extrait en utilisant des simulations Monte Carlo –, par des corrections théoriques et par le rapport des deux rapports de branchement pour obtenir le nombre attendu de désintégrations $B^0_d \to \mu\mu K^{*0}$. Pour calculer le nombre de candidats $B^0_d \to J/\psi K^{*0}$ on effectue un fit de la distribution de la masse invariante des candidats B^0_d avec une fonction Gaussienne combinée avec une fonction linéaire (Figure 1.1). La fonction linéaire tient compte du bruit de fond, alors que la fonction Gaussienne décrit le signal qu'on obtient en l'intégrant entre $5.229\,GeV/c^2$ et $5.329\,GeV/c^2$.

Une fois que toutes les quantités nécessaires pour l'optimisation sont définies, on calcule les FOM pour la combinaison de 10 différentes coupures sur la longueur de désintégration transverse, de 10 différentes coupures sur l'angle d'ouverture et de 10 différentes coupures sur l'isolation. L'optimisation a déterminé que les coupures les

[2] Le vertex d'interaction $p\bar{p}$.

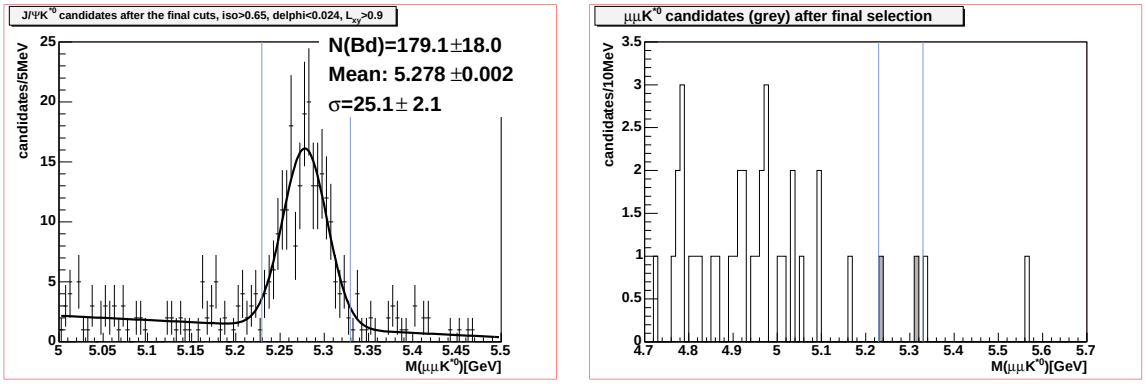

Figure 1.1: Distribution des candidats B pour la désintégration $\mathrm{B}^0_d \to J/\psi K^{*0}$ (gauche) et $\mathrm{B}^0_d \to \mu\mu K^{*0}$ (droite), $L_{xy} > 0.09\,cm$, $\Delta\Phi < 0.024\,rad$ et $Isolation > 0.65$. Les deux événements $\mathrm{B}^0_d \to \mu\mu K^{*0}$ qui sont dans la fenêtre de masse autour de la masse nominale du B^0_d sont affichés en gris.

plus efficaces sont $900\,\mu m$ pour la valeur minimale de la longueur de désintégration transverse, $0.024\,rad$ pour la valeur maximale de l'angle d'ouverture et 0.65 pour la valeur minimale de l'isolation. Les distributions des masses invariantes des candidats $\mathrm{B}^0_d \to J/\psi K^{*0}$ et $\mathrm{B}^0_d \to \mu\mu K^{*0}$ satisfaisant à toutes ces coupures sont montrées sur la Figure 1.1. 179 ± 18 candidats $\mathrm{B}^0_d \to J/\psi K^{*0}$ sont observés dans la région du signal. Il y a deux candidats observés dans la région du signal pour la désintégration $\mathrm{B}^0_d \to \mu\mu K^{*0}$, alors que 1.001 événement de bruit de fond est attendu. La méthode de Feldman et Cousins, basée sur des distributions de Poisson et sur l'approche de la statistique fréquentiste, donne les intervalles de confiance suivantes sur le rapport de branchement de la désintégration $\mathrm{B}^0_d \to \mu\mu K^{*0}$:

$$[0.84, 19.57] \times 10^{-7} \quad CI = 68.75\% \tag{1.1}$$

$$[0.0, 29.56] \times 10^{-7} \quad CI = 90\% \tag{1.2}$$

$$[0.0, 34.44] \times 10^{-7} \quad CI = 95\% \tag{1.3}$$

Cela implique une observation pour un intervalle de confiance à 68.75%, et des limites supérieures pour des intervalles de confiance à 90% et 95%. L'incertitude sur les limites des intervalles a été estimée en changeant l'estimation du bruit de fond par une déviation standard, ce qui donne les erreurs suivantes pour les limites des intervalles: $0.84^{+0.79}_{-0.73}$, 19.57 ± 2.52, 29.56 ± 3.67 et 34.44 ± 4.24. L'expérience CDF continuera à acquérir des données jusqu'en 2009, et devrait avoir au total 40-80 événements $\mathrm{B}^0_d \to \mu\mu K^{*0}$ pour cette date, ce qui permettrait l'observation de cette désintégration pour les intervalles de confiance à 90% et 95%.

1.4 L'expérience ATLAS au LHC

Le projet LHC est un collisionneur pp qui est en cours de construction au Centre Européen de Recherche Nucléaire (CERN). Il représente la prochaine étape dans l'évolution des accélérateurs à hautes énergies, ayant une énergie du centre de masse de $\sqrt{s} = 14\,TeV$.

Quatre expériences seront installées autour des quatre points d'interaction du LHC, l'une d'entre elles étant ATLAS (A Toroidal LHC Apparatus). ATLAS, qui est un détecteur plurifonctionnel, a beaucoup de similitudes dans sa construction avec CDF. En partant de l'intérieur vers l'extérieur on trouve les composants suivants:

- Les détecteurs de traces de particules chargées (Inner Tracker): les détecteurs au silicium à pixels (Pixels), le Semiconductor Tracker (SCT) et le Transition Radiation Tracker (TRT).
- Les calorimètres électromagnétiques et hadroniques.
- Les chambres à muons.

Le choix des technologies pour les trois parties du traceur des particules chargées est motivé par le compromis entre la précision de la mesure et le nombre de canaux de lecture. Près du point d'interaction on trouve des détecteurs qui fournissent relativement peu de points, mais avec une grande précision (Pixels et SCT). Plus loin, on trouve un détecteur qui fournit beaucoup de points de mesure, mais avec moins de précision (TRT). La partie intérieure du Inner Tracker est constituée de détecteurs au silicium à pixels, arrangés en trois cylindres à des rayons de $5.05\,cm$, $8.85\,cm$ et $12.25\,cm$, et de trois disques de chaque côté du détecteur central. Ces détecteurs fournissent une précision de $50\,\mu m$ dans le plan $r-\phi$ et de $400\,\mu m$ le long de la direction du faisceau. De $30\,cm$ à $52\,cm$ du tube à vide contenant le faisceau se trouvent les quatre couches du SCT, ainsi que neuf disques de chaque côté du détecteur central. La partie cylindrique ("avant-arrière") du SCT est constitué de 2112 (1976) modules au silicium qui contiennent aussi l'électronique nécessaire pour la lecture de bandes de silicium. Les modules de la partie cylindrique mesurent le passage d'une particule avec une précision de $17\,\mu m$ dans le plan $r-\phi$ et $500\,\mu m$ le long de la direction du faisceau. L'élément extérieur du système de traceurs d'ATLAS est le TRT, une chambre à fils. La partie centrale contient 50000 fils, et les 36 disques des régions "avant-arrière" en contiennent 320000. Par rapport aux détecteurs au silicium la résolution est moindre ($170\,\mu m$), mais cela est équilibré par le nombre important de points de mesure, typiquement 36 par trace. Le TRT permet la reconnaissance des électrons grâce à leur radiation de transition caractéristique (d'où le nom du détecteur). Entre les traceurs de particules et les calorimètres se trouve le solenoïde supraconducteur qui crée un champ magnétique de $2\,T$ dans le volume des traceurs.

Les calorimètres, qui couvrent la région de $|\eta| < 3.2$, sont basés sur la technologie d'argon liquide et des tuiles de scintillateurs plastiques. Les calorimètres sont entourés par les chambres à muons qui occupent l'espace jusqu'à un rayon de $11\,m$ et jusqu'à $\pm 23\,m$ dans la direction du faisceau. Différentes technologies sont utilisées pour les

chambres à muons remplissant différentes tâches. Des "Monitored Drift Tubes" et des "Cathode Strip Chambers" sont utilisés pour les mesures de précision, alors que pour les déclenchements des "Resistive Plate Chambers" et des "Thin Gap Chambers" sont prévus. ATLAS prévoit un système de déclenchement à trois niveaux, similaire à celui de CDF.

1.5 Construction et évaluation de modules ATLAS équipés de puces SCTA128

Un des composants cruciaux pour la physique du méson B est le SCT, car il contribue de manière très significative à la reconstruction précise des points d'interaction secondaires. Il est essentiel d'effectuer des analyses étendues des modules du SCT afin de s'assurer que leurs performances soient conformes aux attentes.

Dans la présente thèse deux types de modules sont étudiés:

- Des modules équipés de puces ABCD pour une lecture digitale du détecteur. La conception digitale permet une solution plus compacte et réduit la quantité de données à transmettre. Par contre, elle est sensible aux interférences électromagnétiques.
- Des modules équipés de puces SCTA pour une lecture analogique du détecteur. C'est la solution qui a été utilisée jusqu'à maintenant dans la plupart des détecteurs au silicium. Elle permet le traitement individuel des canaux et permet de contrôler et d'éliminer facilement le bruit causé par des interférences électromagnétiques provenant des sources extérieures. Le prix à payer, c'est le large volume de données à transmettre vers le système d'acquisition de données.

Différents modules équipés avec des puces de lecture ABCD ont été évalués tant au niveau des performances électriques, qu'au niveau de la résistance face aux radiations. Les mêmes tests pour des modules équipés avec des puces de lecture SCTA seront aussi présentés. De plus, les résultats de tests effectués en faisceau et avec des lignes de transmission optiques seront aussi décrits.

Plusieurs modules avec des puces ABCD satisfaisant les critères de ATLAS SCT ont été construits. Leurs performances électriques ont été mesurées en utilisant des équipements dédiés, installés au laboratoire. Le gain des puces a été conforme aux valeurs prévues avec une dispersion de 5%, le bruit a été de $430\,e^-$ pour les canaux qui n'étaient pas connectés à des bandes de silicium, $770\,e^-$ pour les canaux qui étaient connectés à des bandes de silicium de $6\,cm$ et $1400\,e^-$ pour les canaux qui étaient connectés à des bandes de silicium de $12\,cm$. Ce chiffre est inférieur à la valeur de $1500\,e^-$, nécessaire pour avoir un rapport signal/bruit supérieur à 15, qui assure une bonne efficacité de reconstruction de traces tout en gardant un taux d'occupation en bruit suffisamment bas.

La puce SCTA a été dévéloppée comme solution supplémentaire pour la lecture des détecteurs au silicium du Inner Tracker. La puce contient 128 canaux avec des amplificateurs, suivis d'une mémoire analogique pour 128 événements et d'un multiplexeur

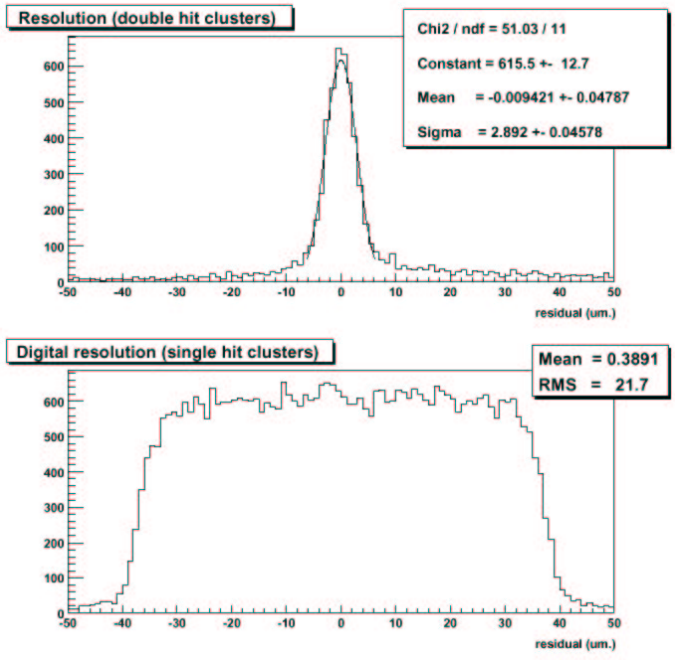

Figure 1.2: Résolution quand deux bandes de silicium sont touchées (en haut) et quand une seule bande de silicium est touchée (en bas).

analogique pour transmettre les données vers le système d'acquisition de données. La caractérisation des propriétés analogiques de la puce SCTA est non seulement importante pour le projet SCTA, mais aussi pour la version digitale, ABCD. En effet, le traitement initial des signaux est identique pour SCTA et ABCD, mais dans la seconde tous les effets présents avant le discriminateur sont masqués par le fait que le signal est binaire.

La première étape de la caractérisation des puces s'est effectuée immédiatement après leur fabrication. Ensuite, les caractéristiques – comme le gain et les différents composants du bruit – ont été recontrôlées au laboratoire immédiatement après le découpage. Les puces ont aussi été irradiées pour contrôler leur conformité avec les exigences posées par l'environnement du LHC. Les puces jugées adéquates ont été ensuite montées sur des modules correspondants aux normes d'ATLAS.

Après leur construction les modules analogiques ont été évalués en utilisant une installation dédiée au laboratoire. Le gain des puces était conforme aux spécifications, et le bruit a été de $1700\,e^-$ pour les bandes de détecteur de $12\,cm$, et $1100\,e^-$ pour les bandes de détecteur de $6\,cm$, ce qui montre l'influence de la capacité représentée par les bandes de silicium. La linéarité des puces SCTA a été vérifiée en utilisant des sources radioactives de Terbium, Americium et Cobalt.

Une étape très importante pour l'évaluation des modules analogiques est de vérifier leur comportement dans des conditions les plus proches possibles de celles rencontrées dans LHC, i.e dans un faisceau test. Les résultats de ces expériences montrent que

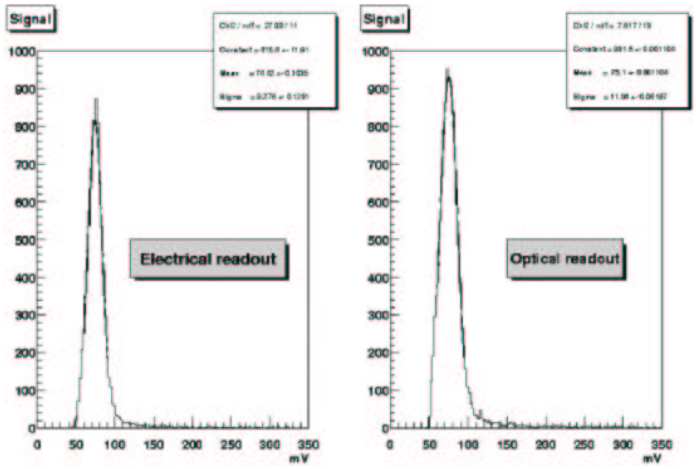

Figure 1.3: Spectre de ^{241}Am pour les lignes de transmission en cuivre et pour les lignes de transmission optiques.

la résolution des modules en cas de trajectoires perpendiculaires aux modules pour les cas quand une seule bande de silicium enregistre le passage de la particule est de $21\,\mu m$, alors qu'elle est de $3\,\mu m$ quand deux bandes adjacentes enregistrent le passage de la particule (Figure 1.2). Le comportement des modules analogiques pour des trajectoires inclinées a été satisfaisant. Cela a été aussi le cas pour le taux d'occupation en bruit qui est de l'ordre de 10^{-4} pour des efficacités proches de 99%.

Les modules analogiques ont aussi été utilisés pour caractériser la ligne de transmission optique développé pour la transmission des signaux analogiques. Les expériences ont montré que la ligne contribue de manière négligeable aux bruits déjà existants de la lecture électronique des modules. Des mesures effectuées avec des sources radioactives ont aussi montré que les spectres des rayons γ de ces sources sont transmis sans modification apparente (Figure 1.3), ce qui prouve le bon fonctionnement de la ligne de transmission optique.

Part I

Theoretical Motivation

Chapter 2

The Standard Model and beyond

2.1 The Standard Model

The experimental and theoretical developments of the last 50 years have led to the development of the Standard Model (SM) of strong and electroweak interactions. Since it is described in great detail in many textbooks (for example [1] and [2]), the discussion given here will be brief.

The most important concept of the modern fundamental physics is that of symmetry. Noether's theorem states that to every symmetry corresponds a conserved quantity. For example, invariance under translations, time displacements, rotations and Lorentz transformations lead to the conservation of momentum, angular momentum, and energy. Other symmetries include the parity, that is, the mirror image of any physical process also represents a perfectly possible physical process; charge conjugation which changes a particle to its antiparticle[1]. Apart from the discrete symmetries, like the ones just mentioned, there are also local gauge symmetries: the phase variation permitted by a local symmetry conserves the invariance of the lagrangian if there is a compensating field which is considered to be the mediator of interactions between particles. The Standard Model describes the fundamental particles and their interactions via the electroweak and the strong force. The force of gravity is negligibly small at the particle level and is not yet described by the SM.

The SM has three types of particles:

- fermions which are the elementary particles and have spin $\frac{1}{2}$
- bosons which are the interaction fields between fermions and have spin 1
- the Higgs-boson which is a consequence of the spontaneous symmetry breaking of the electroweak sector, and has spin 0. The Higgs boson is yet to be discovered experimentally

The main properties of the fermions are summarized in Table 2.1.

[1] It changes all the 'internal' quantum numbers – charge, baryon number, lepton number, strangness, beauty – while leaving mass, energy, momentum and spin untouched.

Quarks	d	u	s	c	b	t
Mass (GeV/c^2)	0.008	0.004	0.15	1.4	4.5	174
Charge	-1/3	+2/3	-1/3	+2/3	-1/3	+2/3
Leptons	e	ν_e	μ	ν_μ	τ	ν_τ
Mass (GeV/c^2)	0.0005	0	0.105	0	1.8	0
Charge	-1	0	-1	0	-1	0

Table 2.1: Main properties of the fermions

2.1.1 CP-violation

Not all symmetries are conserved by all interactions. The weak interactions are not invariant under the parity transformation P; the cleanest evidence for this is the fact that the antimuon emitted in the pion decay

$$\pi^+ \rightarrow \mu^+ + \nu_\mu \tag{2.1}$$

is always produced left-handed. Nor are the weak interactions invariant under C, the charge-conjugated version of reaction 2.1 would be

$$\pi^- \rightarrow \mu^- + \overline{\nu}_\mu \tag{2.2}$$

with a left-handed muon, whereas in fact the muon is always produced with a right-handed helicity. However, combining the two operations gives a true picture: CP turns the left-handed anti-muon into a right-handed muon, which is exactly what is observed in nature. Contrary to parity transformations the CP transformations were believed to be conserved. However, in some cases, CP is not strictly conserved. The contradiction came from the neutral K mesons. CP violation can be parametrized (though not explained) by means of a phase in the Cabbibo-Kobayashi-Maskawa (CKM) matrix [3] [4].

The matrix that connects the weak eigenstates (d', s', b') and the corresponding mass eigenstates d, s, b is

$$\begin{pmatrix} d' \\ s' \\ b' \end{pmatrix} = \begin{pmatrix} V_{ud} & V_{us} & V_{ub} \\ V_{cd} & V_{cs} & V_{cb} \\ V_{td} & V_{ts} & V_{tb} \end{pmatrix} \begin{pmatrix} d \\ s \\ b \end{pmatrix} \tag{2.3}$$

After introducing the notation $c_{ij} = \cos\theta_{ij}$ and $s_{ij} = \sin\theta_{ij}$ with i and j being generation labels $(i, j = 1, 2, 3)$, the standard parametrization is then given as follows [3]:

$$V = \begin{pmatrix} c_{12}c_{13} & s_{12}c_{13} & s_{13}e^{-i\delta} \\ -s_{12}c_{23} - c_{12}s_{23}s_{13}e^{i\delta} & c_{12}c_{23} - s_{12}s_{23}s_{13}e^{i\delta} & s_{23}c_{13} \\ s_{12}s_{23} - c_{12}c_{23}s_{13}e^{i\delta} & -s_{23}c_{12} - s_{12}c_{23}s_{13}e^{i\delta} & c_{23}c_{13} \end{pmatrix}, \tag{2.4}$$

where δ is the phase necessary for CP violation. c_{ij} and s_{ij} can all be chosen to be positive and δ may vary in the range $0 \leq \delta \leq 2\pi$. However, the measurements of CP violation in K decays force δ to be in the range $0 < \delta < \pi$.

Extensive phenomenology of the last years has shown that s_{13} and s_{23} are small numbers: $\mathcal{O}(10^{-3})$ and $\mathcal{O}(10^{-2})$, respectively. Consequently to an excellent accuracy $c_{13} = c_{23} = 1$ and the four independent parameters are given as

$$s_{12} = |V_{us}|, \quad s_{13} = |V_{ub}|, \quad s_{23} = |V_{cb}|, \quad \delta \tag{2.5}$$

with the phase δ extracted from CP violating transitions or loop processes sensitive to $|V_{td}|$. The latter fact is based on the observation that for $0 \leq \delta \leq \pi$, as required by the analysis of CP violation in the K system, there is a one–to–one correspondence between δ and $|V_{td}|$.

For numerical evaluations the use of the standard parametrization is strongly recommended. However, once the four parameters in (2.5) have been determined it is often useful to make a change of basic parameters in order to see the structure of the result more transparently. This brings us to the Wolfenstein parametrization.

The original Wolfenstein parametrization is an approximate parametrization of the CKM matrix in which each element is expanded as a power series in the small parameter $\lambda = |V_{us}| = 0.22$,

$$V = \begin{pmatrix} 1 - \frac{\lambda^2}{2} & \lambda & A\lambda^3(\varrho - i\eta) \\ -\lambda & 1 - \frac{\lambda^2}{2} & A\lambda^2 \\ A\lambda^3(1 - \varrho - i\eta) & -A\lambda^2 & 1 \end{pmatrix} + \mathcal{O}(\lambda^4)\,, \tag{2.6}$$

and the set (2.5) is replaced by

$$\lambda, \qquad A, \qquad \varrho, \qquad \eta\,. \tag{2.7}$$

Looking back at (2.4) and imposing the following relations

$$s_{12} = \lambda\,, \qquad s_{23} = A\lambda^2\,, \qquad s_{13}e^{-i\delta} = A\lambda^3(\varrho - i\eta) \tag{2.8}$$

to all orders in λ. It follows then that

$$\varrho = \frac{s_{13}}{s_{12}s_{23}}\cos\delta, \qquad \eta = \frac{s_{13}}{s_{12}s_{23}}\sin\delta. \tag{2.9}$$

(2.8) and (2.9) represent simply the change of variables from (2.5) to (2.7). Making this change of variables in the standard parametrization (2.4) it follows that the CKM matrix as a function of $(\lambda, A, \varrho, \eta)$ satisfies unitarity exactly. Another property is that in view of $c_{13} = 1 - \mathcal{O}(\lambda^6)$ the relations between s_{ij} and $|V_{ij}|$ in (2.5) are satisfied to high accuracy.

In order to improve the accuracy of the unitarity triangle discussed below the $\mathcal{O}(\lambda^5)$ correction to V_{td} is also included. In summary then V_{us}, V_{cb}, V_{ub}, V_{td} and V_{ts} are given to an excellent approximation as follows:

$$V_{us} = \lambda, \qquad V_{cb} = A\lambda^2 \tag{2.10}$$

$$V_{ub} = A\lambda^3(\varrho - i\eta), \qquad V_{td} = A\lambda^3(1 - \bar{\varrho} - i\bar{\eta}) \tag{2.11}$$

$$V_{ts} = -A\lambda^2 + \frac{1}{2}A(1 - 2\varrho)\lambda^4 - i\eta A\lambda^4 \tag{2.12}$$

with

$$\bar{\varrho} = \varrho(1 - \frac{\lambda^2}{2}), \qquad \bar{\eta} = \eta(1 - \frac{\lambda^2}{2}). \tag{2.13}$$

The advantage of this generalization of the Wolfenstein parametrization over other generalizations found in the literature is the absence of relevant corrections to V_{us}, V_{cb} and V_{ub} and an elegant change in V_{td} which allows a simple generalization of the unitarity triangle.

The Wolfenstein parameterization has several nice features. In particular, it offers in conjunction with the unitarity triangle a very transparent geometrical representation of the structure of the CKM matrix and allows the derivation of several analytic results. This turns out to be very useful in the phenomenology of rare decays and of CP violation.

2.1.2 The unitarity triangle

The unitarity $VV^+ = 1$ of the CKM-matrix implies orthogonality of the different rows and columns. The orthogonality relations can be represented as six "unitarity" triangles in the complex plane. Analyzing the shape of the six unitarity triangles by using the original Wolfenstein parametrization, it turns out that most of these triangles are very squashed ones.

Only in two of the unitarity triangles are all three sides of comparable magnitude ($\mathcal{O}(\lambda^3)$), while in the others one side is suppressed relative to the remaining ones by $\mathcal{O}(\lambda^4)$ and $\mathcal{O}(\lambda^2)$. For the two triangles with comparable sides the sides agree at the $\mathcal{O}(\lambda^3)$ level and differ only through $\mathcal{O}(\lambda^5)$ corrections. Neglecting the latter subleading contributions they describe *the* unitarity triangle that appears usually in the literature:

$$V_{ud}V_{ub}^* + V_{cd}V_{cb}^* + V_{td}V_{tb}^* = 0. \tag{2.14}$$

Phenomenologically this triangle is very interesting as it involves simultaneously the elements V_{ub}, V_{cb} and V_{td}.

In most analyses of the unitarity triangle present in the literature only terms $\mathcal{O}(\lambda^3)$ are kept in (2.14). It is, however, straightforward to include the next-to-leading $\mathcal{O}(\lambda^5)$ terms.

$$V_{cd}V_{cb}^* = -A\lambda^3 + \mathcal{O}(\lambda^7). \tag{2.15}$$

Thus to an excellent accuracy $V_{cd}V_{cb}^*$ is real with $|V_{cd}V_{cb}^*| = A\lambda^3$. Keeping $\mathcal{O}(\lambda^5)$ corrections and rescaling all terms in (2.14) by $A\lambda^3$

$$\frac{1}{A\lambda^3}V_{ud}V_{ub}^* = \bar{\varrho} + i\bar{\eta}, \qquad \frac{1}{A\lambda^3}V_{td}V_{tb}^* = 1 - (\bar{\varrho} + i\bar{\eta}) \tag{2.16}$$

with $\bar{\varrho}$ and $\bar{\eta}$ defined in (2.13). Thus (2.14) can be represented as the unitarity triangle in the complex $(\bar{\varrho}, \bar{\eta})$ plane. This is shown in Figure 2.1. The length of the side CB which lies on the real axis equals unity when eq. (2.14) is rescaled by $V_{cd}V_{cb}^*$. Beyond the leading order in λ the point A does not correspond to (ϱ, η) but to $(\bar{\varrho}, \bar{\eta})$. Clearly within 3% accuracy $\bar{\varrho} = \varrho$ and $\bar{\eta} = \eta$. Yet in the distant future the accuracy of experimental results and theoretical calculations may improve considerably so that the more accurate formulation will be appropriate.

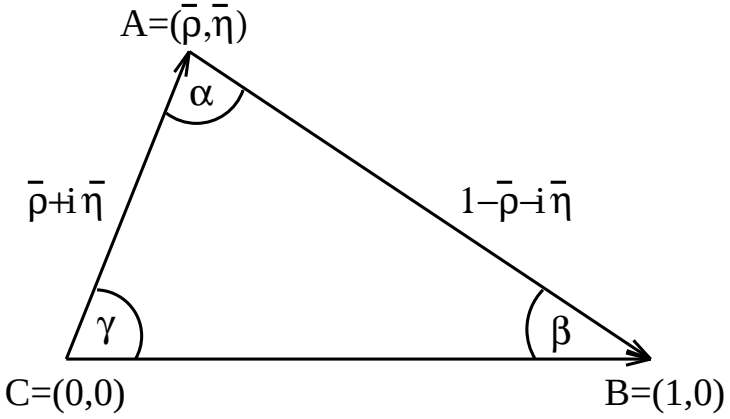

Figure 2.1: Unitarity Triangle.

For numerical calculations the following procedure for the construction of the unitarity triangle is recommended:

- Use the standard parametrization in phenomenological applications to find s_{12}, s_{13}, s_{23} and δ.
- Translate to the set $(\lambda,\ A,\ \varrho,\ \eta)$ using (2.8) and (2.9).
- Calculate $\bar{\varrho}$ and $\bar{\eta}$ using (2.13).

Using simple trigonometry $\sin(2\phi_i)$, $\phi_i = \alpha, \beta, \gamma$, can be expressed in terms of $(\bar{\varrho}, \bar{\eta})$ as follows:

$$\sin(2\alpha) = \frac{2\bar{\eta}(\bar{\eta}^2 + \bar{\varrho}^2 - \bar{\varrho})}{(\bar{\varrho}^2 + \bar{\eta}^2)((1-\bar{\varrho})^2 + \bar{\eta}^2)} \tag{2.17}$$

$$\sin(2\beta) = \frac{2\bar{\eta}(1-\bar{\varrho})}{(1-\bar{\varrho})^2 + \bar{\eta}^2} \tag{2.18}$$

$$\sin(2\gamma) = \frac{2\bar{\varrho}\bar{\eta}}{\bar{\varrho}^2 + \bar{\eta}^2} = \frac{2\varrho\eta}{\varrho^2 + \eta^2}. \tag{2.19}$$

The lengths CA and BA in the rescaled triangle of Figure 2.1, denoted by R_b and R_t, respectively, are given by

$$R_b \equiv \frac{|V_{ud}V_{ub}^*|}{|V_{cd}V_{cb}^*|} = \sqrt{\bar{\varrho}^2 + \bar{\eta}^2} = (1 - \frac{\lambda^2}{2})\frac{1}{\lambda}\left|\frac{V_{ub}}{V_{cb}}\right| \tag{2.20}$$

$$R_t \equiv \frac{|V_{td}V_{tb}^*|}{|V_{cd}V_{cb}^*|} = \sqrt{(1-\bar{\varrho})^2+\bar{\eta}^2} = \frac{1}{\lambda}\left|\frac{V_{td}}{V_{cb}}\right|. \tag{2.21}$$

The expressions for R_b and R_t given here in terms of $(\bar{\varrho},\bar{\eta})$ are excellent approximations. Clearly R_b and R_t can also be determined by measuring two of the angles ϕ_i:

$$R_b = \frac{\sin(\beta)}{\sin(\alpha)} = \frac{\sin(\alpha+\gamma)}{\sin(\alpha)} = \frac{\sin(\beta)}{\sin(\gamma+\beta)} \tag{2.22}$$

$$R_t = \frac{\sin(\gamma)}{\sin(\alpha)} = \frac{\sin(\alpha+\beta)}{\sin(\alpha)} = \frac{\sin(\gamma)}{\sin(\gamma+\beta)}. \tag{2.23}$$

The angles β and γ of the unitarity triangle are related directly to the complex phases of the CKM-elements V_{td} and V_{ub}, respectively, through

$$V_{td} = |V_{td}|e^{-i\beta}, \quad V_{ub} = |V_{ub}|e^{-i\gamma}. \tag{2.24}$$

The angle α can be obtained through the relation

$$\alpha+\beta+\gamma = 180^\circ \tag{2.25}$$

expressing the unitarity of the CKM-matrix.

The triangle depicted on Figure 2.1 together with $|V_{us}|$ and $|V_{cb}|$ gives a full description of the CKM matrix. Looking at the expressions for R_b and R_t, it is clear that within the Standard Model the measurements of four CP conserving decays sensitive to $|V_{us}|$, $|V_{ub}|$, $|V_{cb}|$ and $|V_{td}|$ can tell whether CP violation ($\eta \neq 0$) is predicted in the Standard Model. This is a very remarkable property of the Kobayashi-Maskawa picture of CP violation: quark mixing and CP violation are closely related to each other. In the context of the SM, the potential interest in rare B-decays is that they would provide a quantitative determination of the quark-flavor rotation matrix, in particular the matrix elements V_{td}, V_{tb} and V_{ts}, the first one being extremely important, as together with V_{ub} it carries the CP-violating phase [5] [6].

There is, of course, the very important question whether the CKM picture of CP violation is correct and more generally whether the Standard Model offers a correct description of weak decays of hadrons. In order to answer these important questions it is essential to calculate as many branching ratios as possible, measure them experimentally and check whether they all can be described by the same set of the parameters $(\lambda, A, \varrho, \eta)$. In the language of the unitarity triangle this means that the various curves in the $(\bar{\varrho},\bar{\eta})$ plane extracted from different decays should cross each other at a single point. Moreover the angles (α,β,γ) in the resulting triangle should agree with those extracted in the future from CP-asymmetries in B-decays.

2.1.3 Recent results on the CKM Unitarity Triangle

With the successful turn-on of the BaBar and Belle experiments in the last few years, many experimental measurements in the b sector have achieved impressive precision. The Fermilab Tevatron, with the upgraded CDF and D0 detectors has also started to

produce measurements which are complimentary to those of BaBar and Belle, as they offer the opportunity to measure the heavier B hadrons which are not accessible at the $\Upsilon(4S)$ resonance. The primary mission of the B-factory experiments is to search for the breaking of the CP-symmetry in B meson decays and examine the consistency of the measurements with the expected values within the CKM mechanism.

The measurement of $\sin 2\beta$, the CP-violating asymmetry in B^0 decays to charmonium final states ($b \to c\bar{c}s$), by the CDF, BaBar and Belle collaborations established the breaking of CP-symmetry in B decays [7] [8] [9]. The way to measure the large CP-asymmetries in the decays of neutral B mesons to CP eigenstates is to study the $\Upsilon(4S) \to B^0\bar{B}^0 \to f_{CP}f_{tag}$ decay chain, where one of the B mesons decays at time t_{CP} to a final state f_{CP} and the other decays at time t_{tag} to a final state f_{tag} that distinguishes between B^0 and $\bar{B}^0$. The decay rate has a time dependence given by [10] [11]

$$\frac{e^{-\frac{|\Delta t|}{\tau_{B^0}}}}{4\tau_{B^0}} \{1 + q \cdot [\mathcal{S}\sin(\Delta m_d \Delta t) + \mathcal{A}\cos(\Delta m_d \Delta t)]\} \tag{2.26}$$

where τ_{B^0} is the B^0 lifetime, Δm_d is the mass difference between the two B^0 mass eigenstates, $\Delta t = t_{CP} - t_{tag}$, $q = +1(-1)$ is the b flavor charge when the tagging B meson is a B^0 ($\bar{B}^0$), and $\mathcal{S}$ and $\mathcal{A}$ are the CP-violation parameters. To a good approximation the SM predicts

$$\mathcal{S} = -\xi_f \sin 2\beta \tag{2.27}$$

where $\xi_f = +1(-1)$ corresponds to CP-even (CP-odd) final states. Direct CP-violation, $\mathcal{A}$= 0 is expected for both $b \to c\bar{c}s$ and $b \to s\bar{s}s$ transitions. BaBar and Belle reconstruct B^0 decays to the following $b \to c\bar{c}s$ eigenstates: $J/\psi K_S$, $\psi(2S)K_S$, $\chi_{c1}K_S$ for $\xi_f = -1$ and $J/\psi K_L$ for $\xi_f = +1$. The two classes should have CP-asymmetries of opposite sign. Both experiments also use $B^0 \to J/\psi K^{*0}$ decays with $K^{*0} \to K_S\pi^0$, where the final state is a mixture of even and odd CP with the CP-odd fraction relatively small ($(19 \pm 4)\%$ for Belle and $(16 \pm 3.5)\%$ for BaBar). The samples of CP-eigenstates are large and clean [10]. Figure 2.2 shows the new Belle data. The Δt distributions show a clear shift between B^0 and $\bar{B}^0$ tags. For low-quality tags ($0 < r < 0.5$) only a modest asymmetry is visible, while for high-quality tags ($0.5 < r < 1.0$) a very clear asymmetry with a sinusoidal time modulation is present. The final results are extracted from an unbinned maximum likelihood fit to the Δt distributions that takes into account resolution, mistagging and background dilution. The new Belle result with $140\, fb^{-1}$ is

$$\sin 2\beta = 0.733 \pm 0.057 \pm 0.028 \tag{2.28}$$

while the same analysis from BaBar ($78\, fb^{-1}$) yields

$$\sin 2\beta = 0.741 \pm 0.067 \pm 0.03 \tag{2.29}$$

From these results a new world average can be calculated

$$\sin 2\beta = 0.736 \pm 0.049 \tag{2.30}$$

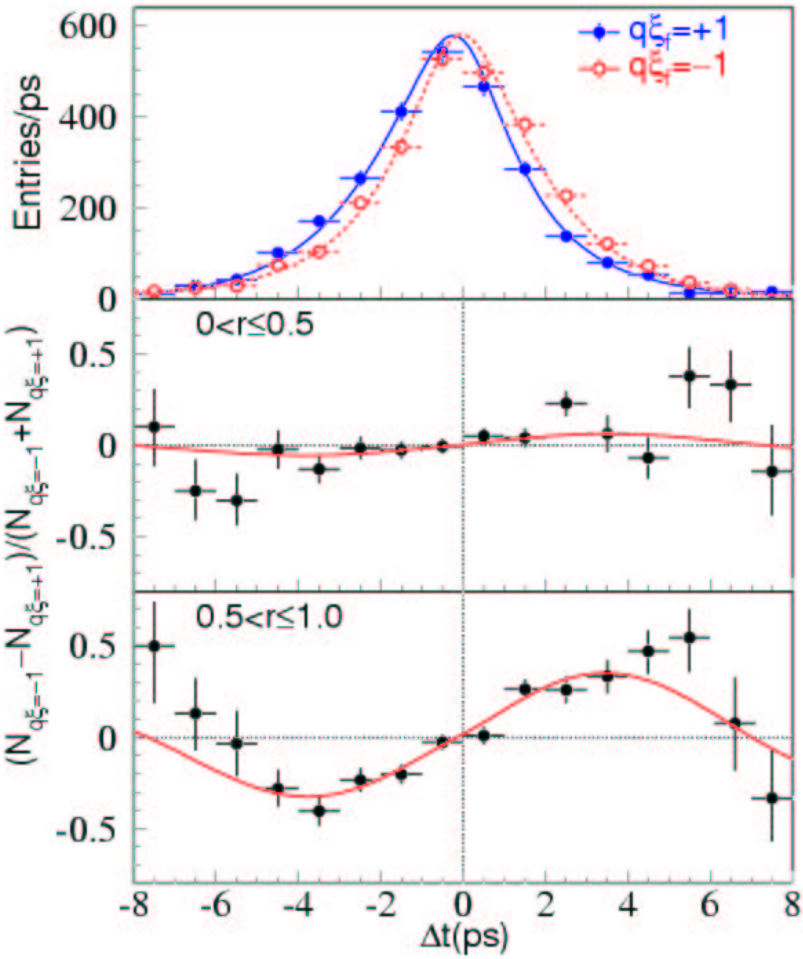

Figure 2.2: The upper plot shows the Δt distributions for B^0 and $\bar{B}^0$ tags. The middle plot shows the raw asymmetry for low quality tags and the lower plot shows the raw asymmetry for high quality tags. The smooth curves are projections of the unbinned likelihood fit (Belle).

which can be compared to the indirect determinations on the unitarity triangle [12] [13] [14]. This comparison is shown in Figure 2.3 and is consistent with the hypothesis that the CKM phase is the source of CP-violation. The values obtained from $b \to c\bar{c}d$ and $b \to sq\bar{q}$ processes are also consistent with the Standard Model expectation, with the exception of the value for the $B \to \phi K^0_S$ from Belle [15]. Figure 2.4 shows the raw asymmetries from Belle for low-quality tags ($0 < r < 0.5$) and for high-quality tags ($0.5 < r < 1.0$). The solid curves show the results of the unbinned maximum-likelihood fit to the Δt distribution. An evaluation of the significance of the result using the Feldman-Cousins method and allowing for systematic uncertainties shows that this result deviates by $3.5\,\sigma$ from the Standard Model.

The knowledge of $\sin\beta$ leads to four possible solutions in the (ρ, η) plane (Figure 2.3), one of which coincides with the allowed region by the indirect measure-

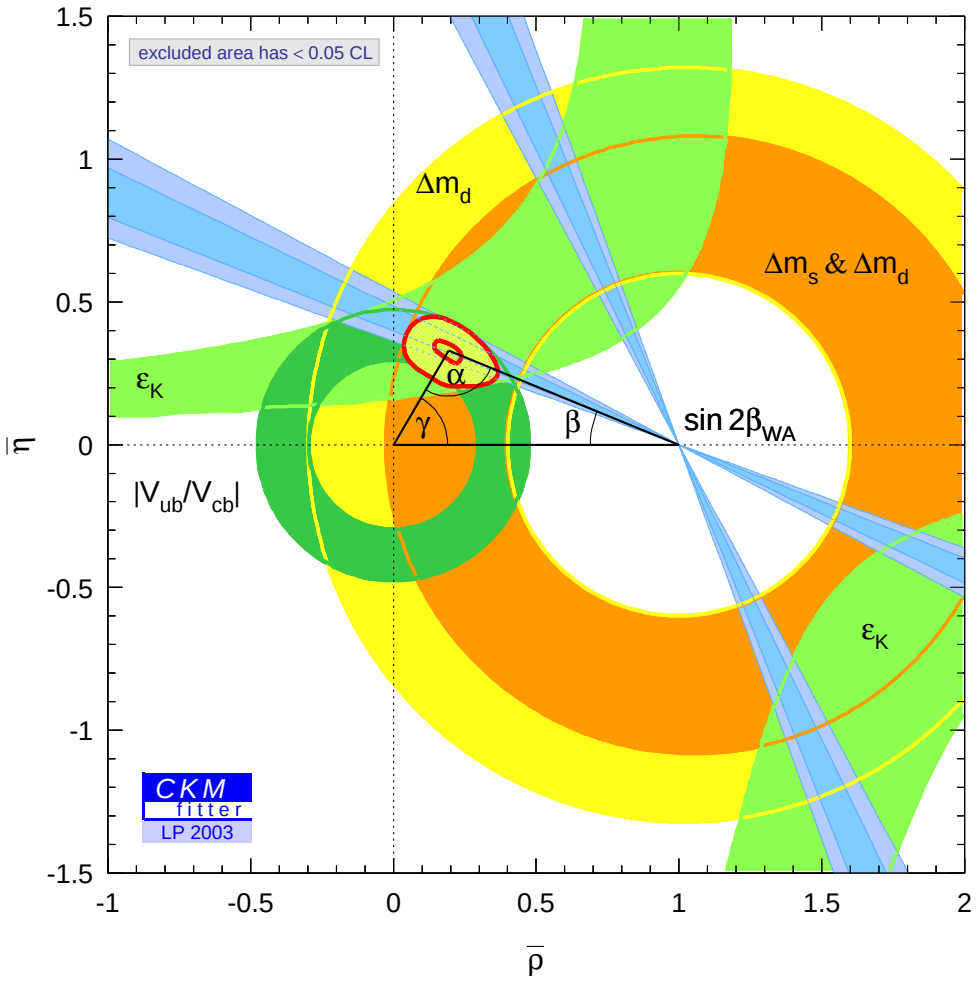

Figure 2.3: Indirect constraints on the angles of the CKM unitarity triangle compared to the most recent direct measurements of β (blue). The theoretical uncertainties in the indirect constraints are estimated conservatively by the CKM fitter group.

ments. The fit also yields the allowed ranges $77^o < \alpha < 122^o$, $37^o < \gamma < 80^o$ at 95% CL, which gives a starting point for comparison with direct measurements [16]. Both BaBar and Belle have performed measurements of the time dependent CP observables in the channel $B \to \pi^+\pi^-$. They have not yet established CP-violation in this channel, but are consistent with the expected values from the Standard Model. Significant progress has been made in identifying and measuring the components of the 2-body charmless B decays, such as $B \to \pi^0\pi^0$, $B \to \rho\pi$ and $B \to \rho\rho$, which together with theoretical models and symmetry relations will eventually lead to the determination of the angles α and γ. The BaBar collaboration has presented limits on $\sin 2\beta + \gamma$ using time-dependent CP-violation analysis of the $B \to D^{*+}\pi^-$ decay. A limit of $|\sin 2\beta + \gamma| > 0.76$ at 90% CL has been set. Figure 2.5 shows the result of this limit in the $(\bar{\rho}, \bar{\eta})$ plane, indicating that it is consistent with the SM. At the

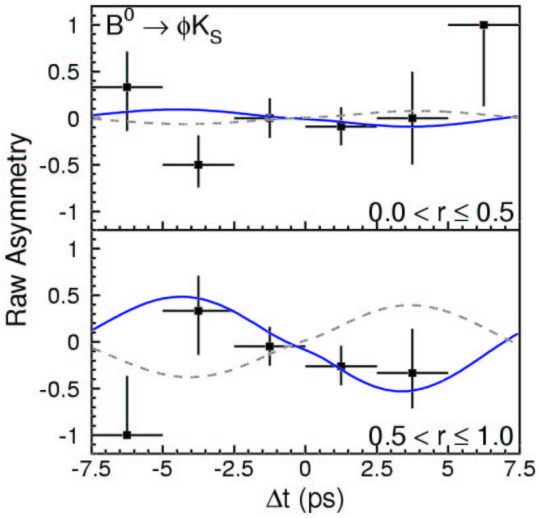

Figure 2.4: Raw asymmetry for the $B \to \phi K^0_S$ decay for low-quality tags ($0 < r < 0.5$) and for high-quality tags ($0.5 < r < 1.0$). The solid curves show the results of the unbinned maximum-likelihood fit to the Δt distribution, while the dashed line is the expectation from the Standard Model (Belle).

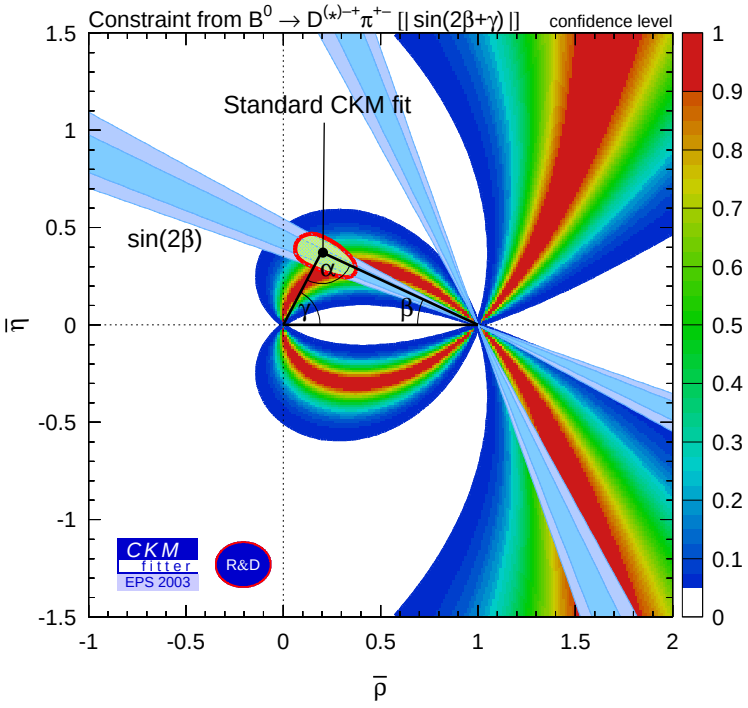

Figure 2.5: The CKM fit with the constraints from $\sin 2\beta + \gamma$ included (BaBar).

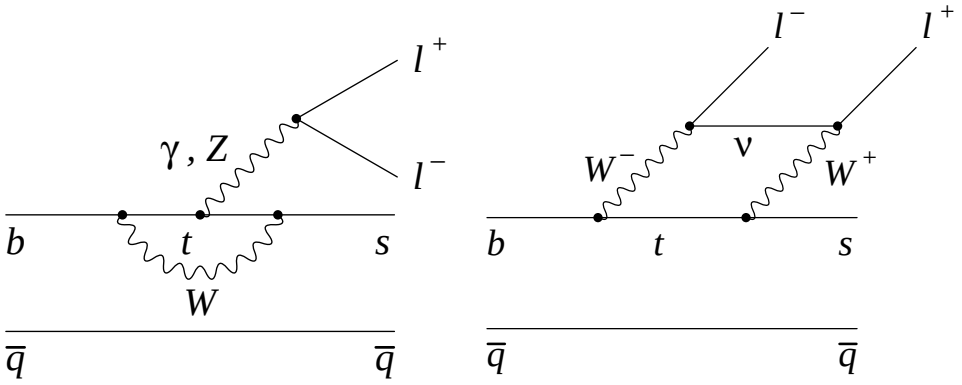

Figure 2.6: Diagrams contributing to the b $\rightarrow sl^+l^-$ decays

current level of experimental and theoretical accuracies, all of the measurements of α and γ can be accomodated within the SM and the CKM picture.

2.2 The FCNC Decays of B Mesons

2.2.1 Introduction

In the Standard Model the Flavor Changing Neutral Current processes are forbidden at tree level, and can only proceed through higher order diagrams, such as the penguin diagrams and box diagrams shown in Figure 2.6. Such loop diagrams are expected to be sensitive to new physics. Heavy particles beyond the Standard Model, such as Higgs or SUSY particles (neutralino, chargino, etc) could contribute to additional loop diagrams, and modify the branching ratios, CP-violation parameters and kinematic variables expected by the Standard Model. B meson decays is an excellent place to study flavor changing neutral currents as long distance effects which hide the weak effects are small due to its heavy quark mass. Also the relevant CKM matrix elements are comparable to those of a tree decay, while in the K or D meson systems they are $O(\lambda^4)$ or $O(\lambda^5)$ smaller than those of the comparable tree decays (Table 2.2).

Meson	tree decay	penguin decay
$\bar{K}$	$V_{us}V_{ud}^* = O(\lambda)$	$V_{ts}V_{td}^* = O(\lambda^5)$
D	$V_{cs}V_{ud}^* = O(1)$	$V_{cb}V_{ub}^* = O(\lambda^5)$
$\bar{B}$	$V_{cb}V_{ud}^* = O(\lambda^2)$	$V_{tb}V_{ts}^* = O(\lambda^2)$

Table 2.2: The CKM matrix elements in the tree and penguin decays of the $\bar{K}$, D and $\bar{B}$ mesons.

The effective Hamiltonian generating the b $\rightarrow s\gamma$ and b $\rightarrow sl^+l^-$ transitions can

be written as follows[2]:

$$H_{eff} = -\frac{4G_F}{\sqrt{2}} V_{ts}^* V_{tb} \sum_{i=1}^{10} C_i(\mu) O_i(\mu) \tag{2.31}$$

where $O_i(\mu)$ are dimension-six operators at the scale μ, $C_i(\mu)$ are the corresponding Wilson coefficients which represent the effective strength of short distance interactions, G_F is the Fermi coupling constant, and the Cabibbo-Kobayashi-Maskawa dependence has been made explicit. The operators can be chosen as follows [17] [18]:

$$O_1 = (\bar{s_L}\gamma_\mu T^a c_L)(\bar{c_L}\gamma^\mu T^a b_L) \tag{2.32}$$

$$O_2 = (\bar{s_L}\gamma_\mu c_L)(\bar{c_L}\gamma^\mu b_L) \tag{2.33}$$

$$O_3 = (\bar{s_L}\gamma_\mu b_L)\sum_q (\bar{q}\gamma^\mu q) \tag{2.34}$$

$$O_4 = (\bar{s_L}\gamma_\mu T^a b_L)\sum_q (\bar{q}\gamma^\mu T^a q) \tag{2.35}$$

$$O_5 = (\bar{s_L}\gamma_{\mu_1}\gamma_{\mu_2}\gamma_{\mu_3} b_L)\sum_q (\bar{q}\gamma^{\mu_1}\gamma^{\mu_2}\gamma^{\mu_3} q) \tag{2.36}$$

$$O_6 = (\bar{s_L}\gamma_{\mu_1}\gamma_{\mu_2}\gamma_{\mu_3} T^a b_L)\sum_q (\bar{q}\gamma^{\mu_1}\gamma^{\mu_2}\gamma^{\mu_3} T^a q) \tag{2.37}$$

$$O_7 = \frac{e}{g_s^2} m_b (\bar{s_L}\sigma^{\mu\nu} b_R) F_{\mu\nu} \tag{2.38}$$

$$O_8 = \frac{1}{g_s} m_b (\bar{s_L}\sigma^{\mu\nu} T^a b_R) G^a_{\mu\nu} \tag{2.39}$$

$$O_9 = \frac{e^2}{g_s^2}(\bar{s_L}\gamma_\mu b_L)\sum_l (\bar{l}\gamma^\mu l) \tag{2.40}$$

$$O_{10} = \frac{e^2}{g_s^2}(\bar{s_L}\gamma_\mu b_L)\sum_l (\bar{l}\gamma^\mu \gamma_5 l) \tag{2.41}$$

where the subscripts L and R refer to left- and right-handed components of the fermion fields, $F_{\mu\nu}$ and $G^a_{\mu\nu}$ denote the QED and QCD field strength tensors respectively. The $C_i(\mu)$ are evaluated perturbatively at the high energy scale $O(m_W)$. In order to obtain the low energy theory, the $C_i(\mu)$ are evolved down to the scale $O(m_b)$ using renormalization group equations which guarantee that the μ dependence of $C_i(\mu)$ is cancelled by the μ dependence of $O_i(\mu)$, thus the observables should not depend on the renormalization scale μ. The advantage of this approach is that if

[2]The assumption here is that the combination $(V_{us}^* V_{ub})$ of the CKM matrix elements can be neglected.

non-SM physics contributes to the additional diagrams, it will only modify the relevant Wilson coefficients. The amplitude of the B meson decaying into the final state F can be written as:

$$A(B \to F) = \langle F|H_{eff}|B\rangle = \frac{G_F}{\sqrt{2}} V_{ts}^* V_{tb} \sum_{i=1}^{10} C_i(\mu)\langle F|O_i(\mu)|B\rangle \tag{2.42}$$

As the Wilson coefficients represent the short distance interactions, the matrix elements $\langle F|O_i(\mu)|B\rangle$ will take into account the long distance strong interactions. Hence, the operator elements can not be obtained preturbatively because of the confining nature of strong interactions at large distances. If $\langle F|$ is an inclusive final state, the leading order term can be represented using the matrix element for free quark transition which can be easily calculated. However, when $\langle F|$ is an exclusive final state the operator element is more difficult to obtain. Fortunately, if part of $\langle F|$ is a non-hadronic state, like $\langle K^* l^+ l^-|$ it is possible to compute the operator element. Since leptons and photons are not involved in long distance interactions, the operator element can be factorized into hadronic and non-hadronic currents:

$$\langle F|O_i(\mu)|B\rangle = \langle hL|O_i(\mu)|B\rangle = \langle h|J_1|B\rangle\langle L|J_2|0\rangle \tag{2.43}$$

where the second term can be written explicitely, and the former can be calculated by non-perturbative methods, even though these methods have limitations.

2.2.2 The $b \to s l^+ l^-$ decays

While the measurement of the $B \to X_s\gamma$ is being consolidated, searches are being made for several other radiative and semileptonic rare B decays. In the SM the $b \to s l^+ l^-$ decay rate is expected to be nearly two orders of magnitude lower than that of $b \to s\gamma$. However, it depends on the magnitude and sign of three Wilson coefficients C_7, C_9 and C_{10} in the effective Hamiltonian, while $b \to s\gamma$ depends only on the magnitude of C_7. These three Wilson coefficients are likely places for new physics to appear, as they come from loop and box diagrams. Upper limits on the branching fraction for $b \to s l^+ l^-$ thus place constraints on new physics; an observation at a rate in excess of that predicted by the Standard Model would provide evidence for new physics. New heavy particles can affect the rate and decay distributions.

C_7, C_9 and C_{10} can be completely determined by measuring the dilepton invariant mass distributions and the forward-backward charge asymmetry of the dilepton together with the $b \to s\gamma$ decay rate.

While for the moment $B \to X_s\gamma$ remains more restrictive over most of the supersymmetric space, this is expected to change with improved precision on the semileptonic rare B decays.

The $b \to s l^+ l^-$ decays receive short-distance contributions from the electromagnetic penguin, the Z penguin, and the W box diagrams. They also receive long distance contributions from the $b \to s(c\bar{c}) \to s l^+ l^-$ with both resonant (J/ψ and ψ') and continuum intermediate states. For the dimuon invariant masses around the

Authors	B $\to Kl^+l^-$ $\times 10^{-6}$	B $\to K^*\mu^+\mu^-$ $\times 10^{-6}$	B $\to K^*e^+e^-$ $\times 10^{-6}$
Ali et al. (2002) NNLO [18]	0.35±0.12	1.19±0.39	1.58±0.49
Ali et al. (2000) [19]	0.57	1.9	2.3
Melikhov et al. (1998) [20]	0.44	1.15	1.5
Geng and Kao (1996) [21]	0.5	1.4	
Colangelo et al. (1996) [22]	0.3	1.0	

Table 2.3: Theoretical predictions based on the Standard Model for the exclusive decays B $\to Kl^+l^-$.

resonant regions the decay is dominated by the long-distance contributions, while away from these resonances short-distance processes dominate. Table 2.3 shows some predicted branching ratios for b $\to sl^+l^-$ decays. It is important to note that the theoretical uncertainties in the decay rates are estimated to be typically ±35% [19].

Mode	Belle [31] [32] $\mathcal{B} \pm stat \pm syst \pm model\ [\times 10^{-7}]$	BaBar [33] $\mathcal{B} \pm stat \pm syst [\times 10^{-7}]$
$B \to K^+e^+e^-$	$6.3^{+1.9}_{-1.7} \pm 0.3 \pm 0.1$	$10.5^{+2.5}_{-2.2} \pm 0.7$
$B \to K^+\mu^+\mu^-$	$4.5^{+1.4}_{-1.2} \pm 0.3 \pm 0.1$	$0.7^{+1.9}_{-1.1} \pm 0.2$
$B \to K^0e^+e^-$	$0.0^{+2.0\ +0.3}_{-1.2\ -0.4} \pm 0.0$	$-2.1^{+2.3}_{-1.6} \pm 0.8$
$B \to K^0\mu^+\mu^-$	$5.6^{+2.9}_{-2.3} \pm 0.4 \pm 0.3$	$16.3^{+8.2}_{-6.3} \pm 1.4$
$B \to K^{*0}e^+e^-$	$12.9^{+5.7}_{-4.9} \pm 1.1 \pm 0.1$	$11.1^{+5.6}_{-4.7} \pm 1.1$
$B \to K^{*0}\mu^+\mu^-$	$13.3^{+4.2}_{-3.7} \pm 1.0 \pm 0.5$	$8.6^{+7.9}_{-5.8} \pm 1.1$
$B \to K^{*+}e^+e^-$	$20.2^{+12.7\ +2.3}_{-10.1\ -2.4} \pm 0.7$	$2.0^{+13.4}_{-8.7} \pm 2.8$
$B \to K^{*+}\mu^+\mu^-$	$6.5^{+6.9\ +1.4}_{-5.3\ -1.5} \pm 0.4$	$30.7^{+25.8}_{-17.8} \pm 4.2$
$B \to Ke^+e^-$	$4.8^{+1.5}_{-1.3} \pm 0.3 \pm 0.1$	$7.4^{+1.8}_{-1.6} \pm 0.5$
$B \to K\mu^+\mu^-$	$4.5^{+1.4}_{-1.2} \pm 0.3 \pm 0.1$	$4.5^{+2.3}_{-1.9} \pm 0.4$
$B \to K\ell^+\ell^-$	$4.8^{+1.0}_{-0.9} \pm 0.3 \pm 0.1$	$6.5^{+1.4}_{-1.3} \pm 0.4$
$B \to K^*e^+e^-$	$14.9^{+5.2\ +1.2}_{-4.6\ -1.3} \pm 0.2$	$9.8^{+5.0}_{-4.2} \pm 1.1$
$B \to K^*\mu^+\mu^-$	$11.7^{+3.6}_{-3.1} \pm 0.9 \pm 0.5$	$12.7^{+7.6}_{-6.1} \pm 1.6$
$B \to K^*\ell^+\ell^-$	$11.5^{+2.6}_{-2.4} \pm 0.8 \pm 0.2$	$8.8^{+3.3}_{-2.9} \pm 1.0$

Table 2.4: Latest observations and limits of rare B decays by the Belle and BaBar experiments.

Until the advent of B factories the most stringent limits on the B $\to K^{(*)}l^+l^-$ decays have been placed by the CLEO [24] and CDF [23] collaborations. Now the B factories are starting to observe these decays instead of measuring upper limits [25] [26] [27] [28] [29] [30]. As of January 2004, using a data sample of $152 \times 10^6\, B\bar{B}$ pairs, corresponding to $140\, fb^{-1}$ taken at the $\Upsilon(4S)$ resonance, the Belle experiment has reported observation (i.e. more than $3\,\sigma$ significance) for half of the modes ($B \to K^+e^+e^-$, $B \to K^{*0}\mu^+\mu^-$, $B \to K^0\mu^+\mu^-$ and $B \to K^+\mu^+\mu^-$) and all the

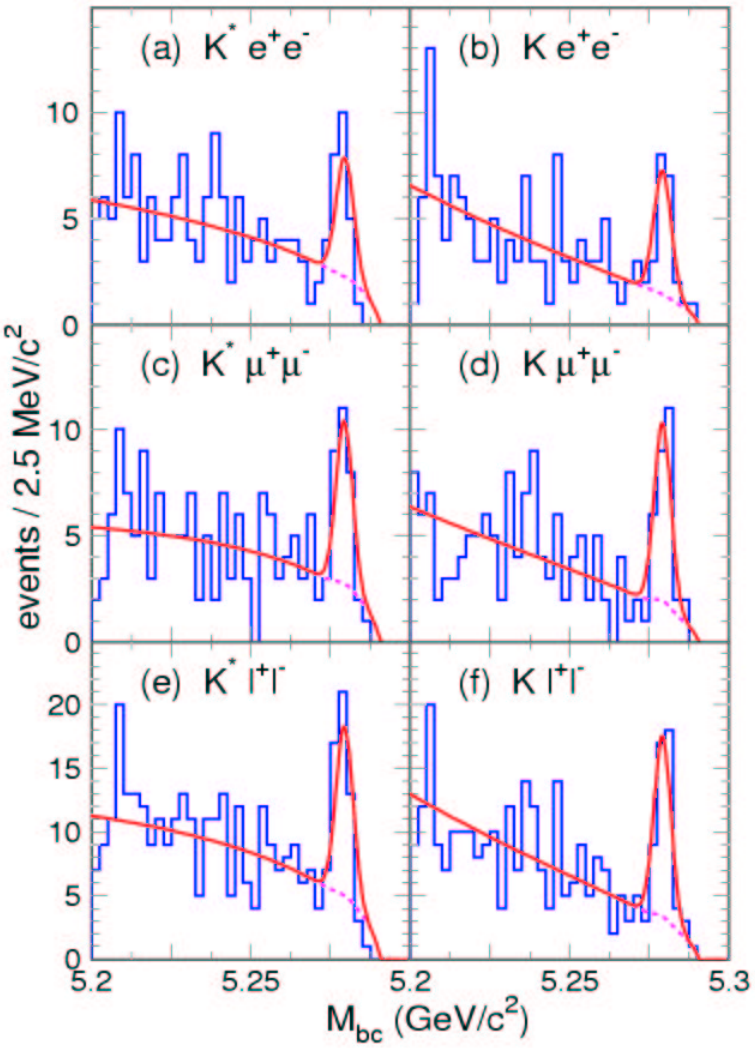

Figure 2.7: Beam-energy constrained mass M_{bc} distributions for $K^{(*)}\ell^+\ell^-$ samples from the Belle experiment ($140\,fb^{-1}$). Solid and dotted curves show the results of the fits and the background contributions, respectively.

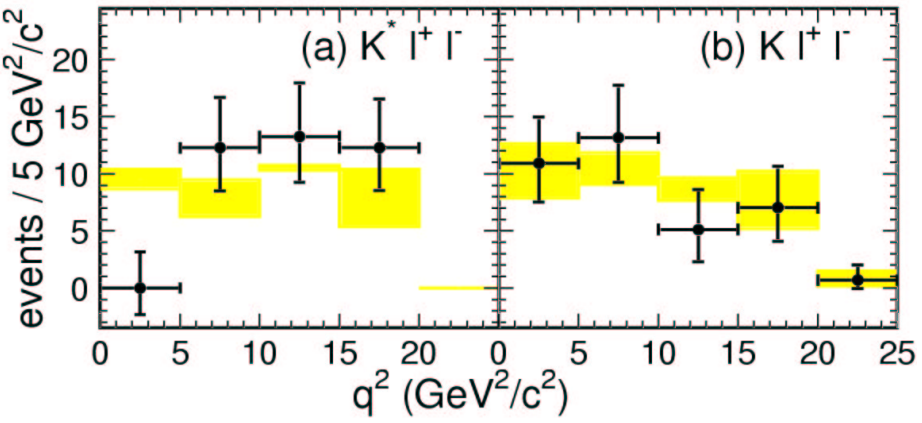

Figure 2.8: q^2 distributions for $K\ell^+\ell^-$ and $K^*\ell^+\ell^-$ from the Belle experiment ($140\,fb^{-1}$). Points with error bars show the data while the hatched boxes show the range of SM expectations from various models [18] [20] [22].

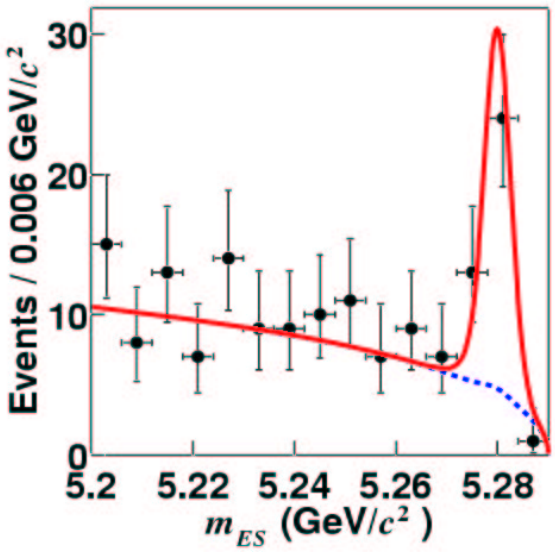

Figure 2.9: Beam-energy constrained mass (m_{ES}) distribution for the $K\ell^+\ell^-$ modes from the BaBar experiment. The solid curve is the sum of all fit components, including signal; the dashed curve is the sum of all background components.

combined modes [31] [32]. Some of the remaining modes are also likely to be discovered: $B \to K^{*0}e^+e^-$'s significance is $2.8\,\sigma$, and that of $B \to K^{*+}e^+e^-$ is $1.9\,\sigma$. The BaBar experiment, using a data sample of $123 \times 10^6\,\Upsilon(4S) \to B\bar{B}$ decays, has also observed several of the modes [33]. The latest results of the two experiments are summarized in Table 2.4[3]. Figure 2.7 shows the beam-energy constrained mass $M_{bc} = \sqrt{(E^*_{beam}/c^2)^2 - |p^*_B/c|^2}$ distributions for $K^{(*)}\ell^+\ell^-$ samples from the Belle experiment, where p^*_B is the measured momentum of the B candidate, and E^*_{beam} is the beam energy in the $\Upsilon(4S)$ rest frame. Figure 2.8 shows that the Belle experiment is not only observing the different decay modes, but has also started to measure the invariant mass square $q^2 = M^2_{\ell\ell}c^2$ distributions as well. Figure 2.9 shows the beam-energy constrained mass distribution for the four $K\ell^+\ell^-$ modes for the BaBar experiment. The significance of the $B \to K\ell^+\ell^-$ signal from the simultaneous fit is $8\,\sigma$.

2.3 Beyond the Standard Model

The assumption is that the dominant effects of an underlying supersymmetric theory can be implemented by using the SM operator basis for the effective Hamiltonian. Thus, supersymmetric effects enter in the theoretical analysis through the modifications of the Wilson coefficients. Restricting the operator basis to the one in the SM obviously does not cover the most general supersymmetric case, but it covers an important part of the underlying parameter space, and hence can be employed to undertake searches for supersymmetric effects in rare B decays.

Several papers have discussed the possible effects of different non-SM theories on FCNC decays [18] [19] [34] [35] [36] [37] [38] [39] [40] [41]. It is important to note, that due to the large theoretical uncertainties, any effect beyond the Standard Model will only be noticed if it is a drastic effect. For example in the $\mathrm{B} \to Kl^+l^-$ and $\mathrm{B} \to K^*l^+l^-$ sector the most important quantities where to look for non-SM effects are the dilepton invariant mass distribution and the normalized forward-backward asymmetry. Figure 2.10 shows the dilepton invariant mass squared distribution of the $\mathrm{B} \to K^*\mu^+\mu^-$ decay for several different models. One can clearly notice the poles corresponding to the resonant modes J/ψ and $\psi(2S)$. The solid line represents the Standard Model prediction and the shaded area represents the form-factor related uncertainties. The dotted line corresponds to a SUGRA model with $C_7 = -1.2 \cdot C_7^{SM}$, $C_9 = 1.03 \cdot C_9^{SM}$ and $C_{10} = 1.0 \cdot C_{10}^{SM}$. It corresponds to $\tan\beta = 30$[4] in which case C_7 becomes positive, resulting in a constructive interference of the terms depending on C_7 and C_9 in the dilepton invariant mass spectra. In the low-q^2 region it results in a 100% enhancement of the branching ratio for $\mathrm{B} \to K^*\mu^+\mu^-$ which is clearly distinguishable from the SM-related theoretical uncertainties. The effect of the positive C_7 is even

[3] These experimental numbers refer to the so-called non-resonant branching ratios integrated over the entire dilepton invariant mass spectrum, where judicious cuts were used to remove dominant resonant contributions arising from the B decays where the dilepton is coming from a J/ψ or ψ'.

[4] For small $\tan\beta$ the sign of C_7 is the same as in the SM and no spectacular deviations from the SM can be expected.

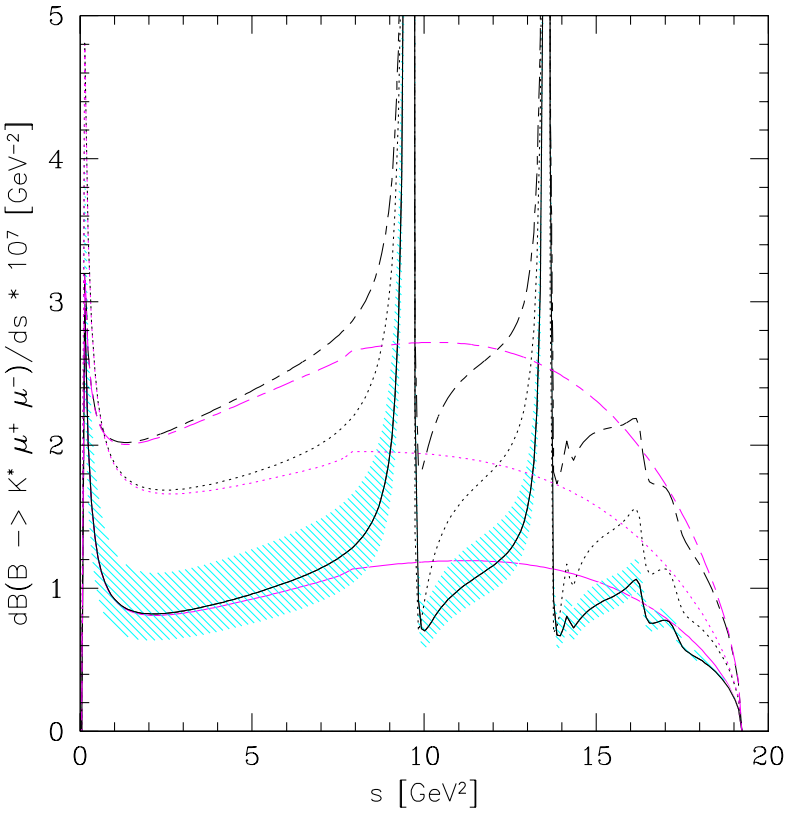

Figure 2.10: The dilepton invariant mass squared distribution for B $\to K^*\mu^+\mu^-$. The solid lines represent the SM and the shaded area signals the form-factor related uncertainties. The dotted lines correspond to the SUGRA model with $C_7 = -1.2 \cdot C_7^{SM}$, $C_9 = 1.03 \cdot C_9^{SM}$ and $C_{10} = 1.0 \cdot C_{10}^{SM}$. The long-short dashed lines correspond to an allowed point in the parameter space of the MIA-SUSY model given by $C_7 = -0.83 \cdot C_7^{SM}$, $C_9 = 0.92 \cdot C_9^{SM}$ and $C_{10} = 1.61 \cdot C_{10}^{SM}$. The black lines show the sum of the short-distance and long-distance contributions, while the magenta lines show the corresponding pure short-distance spectra.

more striking in the FB asymmetry shown in Figure 2.11. The dotted lines represent two SUGRA models which are identical except for the sign of C_7. The solution which does not have a zero crossing below the J/ψ-resonant region is the one with the positive C_7 coefficient.

Another possible approach is the minimal insertion approach (MIA) which aims at including all possible squark mixing effects in a model independent way. The flavor changes are incorporated by a non-diagonal mass insertion in the squark propagator. The long-short dashed line of the dilepton invariant mass plot shows the result for a MIA-SUSY calculation with $C_7 = -0.83 \cdot C_7^{SM}$, $C_9 = 0.92 \cdot C_9^{SM}$ and $C_{10} = 1.61 \cdot C_{10}^{SM}$. As in the case of the SUGRA model there is an important enhancement of the branching ratio. Concerning the forward-backward asymmetry the long-short dashed lines correspond to the MIA-SUSY model using parameters $C_7 = \pm 0.83 \cdot C_7^{SM}$,

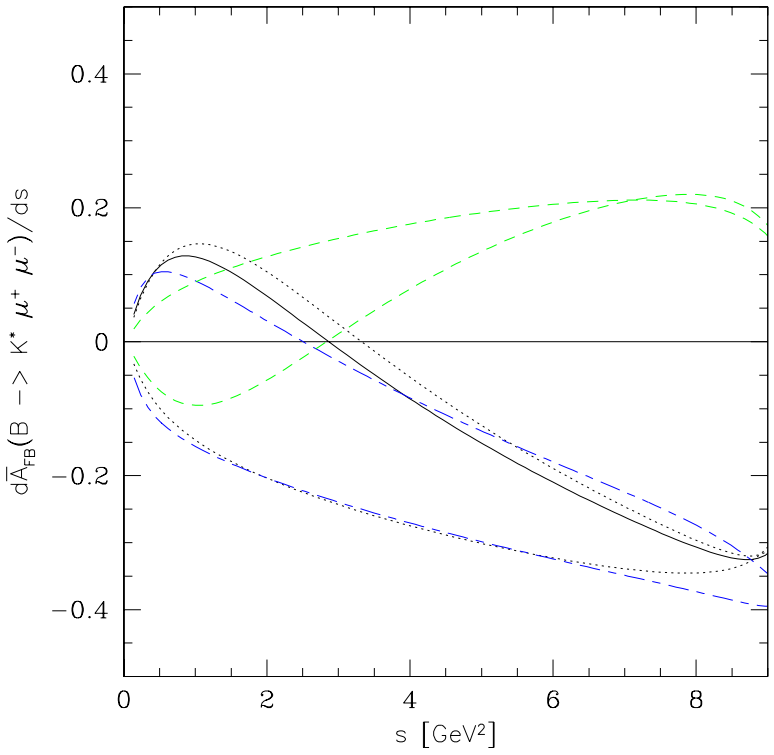

Figure 2.11: The normalized forward-backward asymmetry in B $\to K^*\mu^+\mu^-$ decay as a function of s. The solid line denotes the SM prediction. The dotted lines correspond to the SUGRA model with $C_7 = -1.2 \cdot C_7^{SM}$, $C_9 = 1.03 \cdot C_9^{SM}$ and $C_{10} = 1.0 \cdot C_{10}^{SM}$ with the upper and lower curves representing the $C_7 < 0$ and $C_7 > 0$ case, respectively. The long-short dashed (blue) lines correspond to the MIA-SUSY model, using the parameters $C_7 = \pm 0.83 \cdot C_7^{SM}$, $C_9 = 0.92 \cdot C_9^{SM}$ and $C_{10} = 1.61 \cdot C_{10}^{SM}$ with the upper and lower curves representing the $C_7 < 0$ and $C_7 > 0$ case, respectively. The dashed curves indicating a positive asymmetry for large s correspond to the MIA-SUSY models using the parameters $C_7 = \pm 0.83 \cdot C_7^{SM}$, $C_9 = 0.79 \cdot C_9^{SM}$ and $C_{10} = -0.38 \cdot C_{10}^{SM}$.

$C_9 = 0.92 \cdot C_9^{SM}$ and $C_{10} = 1.61 \cdot C_{10}^{SM}$ with the upper and lower curves representing the $C_7 < 0$ and $C_7 > 0$ case respectively. An important possibility in the MIA approach is that the C_{10} coefficient could change sign. This has no effect in the dilepton invariant mass distributions, as they depend quadratically on C_{10}, but it would change the sign of the forward-backward asymmetry. This scenario is shown by the dashed curves indicating a positive asymmetry for large s correspond to the MIA-SUSY models $C_7 = 0.83 \cdot C_7^{SM}$, $C_9 = 0.79 \cdot C_9^{SM}$ and $C_{10} = -0.38 \cdot C_{10}^{SM}$.

Even though all current data are consistent with the Standard Model, present experimental measurements allow considerable room for beyond-the-SM effects.

Part II

Search for the $\mathrm{B}_d^0 \to \mu\mu K^{*0}$ decay at the CDF experiment

Chapter 3

Detectors for studying rare B decays I: The CDF experiment at the Tevatron

The Collider Detector at Fermilab (CDF) is one of the two general purpose detectors built to study high-energy $p\bar{p}$ collisions at the Tevatron, located at the Fermi National Accelerator Laboratory. After introducing the accelerator chain, the different components of the detector and the trigger system will be described in detail.

3.1 The Tevatron

The Tevatron is a proton-antiproton collider located at the Fermi National Accelerator Laboratory (FNAL) in Chicago. It produced the first $p\bar{p}$ collisions in 1983, and since then has had several phases of running. Between 1992 and 1996 the center of mass collision energy achieved by the accelerator was $1.8\,TeV$. This phase is called Run I and $120\,pb^{-1}$ of data[1] have been collected which enabled, amongst other measurements, the discovery of the top quark [47]. In 1996 the accelerator was temporarily shut down in order to implement a series of improvements to increase substantially the luminosity [48]. This second phase, called Run II, was initially aimed at achieving $15\,fb^{-1}$ integrated luminosity. Due to some experimental difficulties described later in this section the integrated luminosity goals have been adjusted first to $6.5-11\,fb^{-1}$ [49], then to $4.4-8.6\,fb^{-1}$ [51]. Run II itself was planned to consist of two parts, Run IIa and Run IIb. Between the two runs a shutdown of several months was foreseen in order to replace the silicon detectors of the experiments designed to survive $2\,fb^{-1}$ of integrated luminosity. Because of lack of funding and the lower than expected luminosity CDF will not replace the silicon detectors as planned, and continue to take data without major upgrades of the detector. For Run II the center of mass collision energy has also been raised to $\sqrt{s} = 1.96$ TeV, so until the Large Hadron Collider is completed at CERN, it will remain the highest energy collider in

[1] Integrated luminosities are usually given in units of barn^{-1}, corresponding to $10^{24}\,cm^{-2}$, i.e. $1\,pb^{-1} = 10^{36}\,cm^{-2}$.

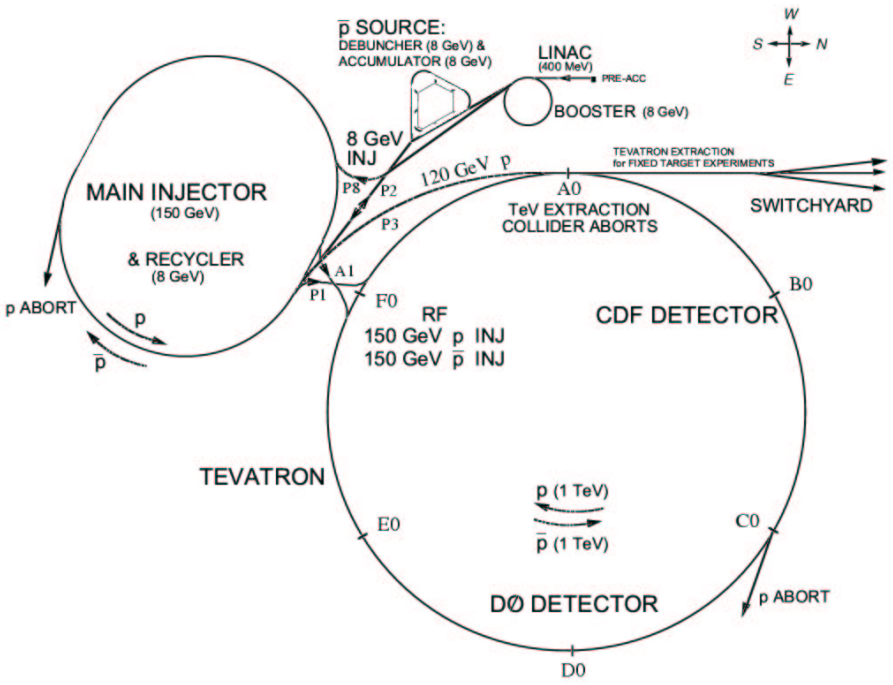

Figure 3.1: The accelerator complex at Fermilab.

the world ($\sqrt{s}$ is one of the most important parameters in collider experiments, as the cross-sections of the different processes and the masses of the particles which can be created, depend on its value). Another very important parameter is the luminosity which determines the size of the data sample that can be collected during a given period of time. The number of events collected (N) can be written as:

$$N = \sigma \int_{\Delta t} L dt = \sigma \mathcal{L} \tag{3.1}$$

where σ is the cross-section of the process, Δt is the length of the data taking period, L is the instantenuous luminosity and $\mathcal{L}$ is the integrated luminosity. In order to achieve the luminosity goals set for Run II the accelerator chain was deeply modified with the construction of two additional rings, the Main Injector and the Recycler [53].

3.1.1 Proton production

The first element of the accelerator chain (Figure 3.1) is the Cockroft-Walton pre-accelerator in which hydrogen gas is ionized to create negative ions H^-, which are subsequently accelerated and reach an energy of $0.75\,MeV$ [54]. Next, the negative hydrogen ions are accelerated in the Linac, a $130\,m$ long linear accelerator, where they reach an energy of $400\,MeV$. At the end of this phase of acceleration, the ions pass through a carbon foil, which removes the electrons, leaving only the positively

charged protons. The third stage of the accelerator chain is the Booster, a synchrotron with a diameter of $475\,m$, where electric fields accelerate protons until they reach an energy of $8\,GeV$. The fourth stage is the Main Injector. It is a new synchrotron with a diameter of $1\,km$ which was completed in 1999. The Main Injector accelerates the protons from $8\,GeV$ to $150\,GeV$ and groups them in bunches of 2.7×10^{11} particles.

3.1.2 Antiproton production

The antiproton production rate is one of the main limiting factors in achieving higher luminosity, so for Run II particular emphasis was put onto the improvement of the antiproton beam. Besides producing proton bunches for the collisions in the Tevatron, as mentioned earlier, the Main Injector is also producing $120\,GeV$ protons in bunches of 2×10^{12} particles which then enter in collision with a nickel target. The resulting particles are collected with magnetic lenses, then the antiprotons are filtered with a dipole magnet. On the average, 50000 protons are needed for the production of every single antiproton. The antiprotons are then sent to the Debuncher which is a triangular ring of $505\,m$ in length. The Debuncher reduces the dispersion of the energy of the antiprotons using stochastic cooling. Finally, the antiprotons are transferred to the Accumulator where they are further cooled and stacked in bunches before being transferred to the Main Injector. The complex described above needs 8 hours in order to accumulate 1.3×10^{12} antiprotons. The antiprotons are then accelerated in the Main Injector to $150\,GeV$ and form bunches of 3×10^{10} particles.

One of the main improvements of Run II is the construction of the Recycler, which is installed in the same tunnel as the Main Injector. Originally its aim was to recycle the antiprotons remaining after the end of a store (which corresponds to 75% of the initial number). This would have enabled to double the number of antiprotons for the next store. As of early 2004, work on recycling antiprotons has been stopped and the Recycler is expected to serve as a second antiproton storage ring, fulfilling the original aim in a different fashion [50]. After the installation of the electron cooling the Recycler is expected to be integrated in the rest of the complex in early 2005 [51] [52].

3.1.3 The Tevatron

The last element in the chain of the accelerators is the Tevatron, a superconducting synchrotron. The Tevatron accelerates protons and antiprotons, which it receives from the Main Injector, from $150\,GeV$ to $980\,GeV$. Between Run I and Run II the energy of the beam has been increased from 900 to $980\,GeV$ and a new cryogenic system has been installed. There are 36 bunches of protons and 36 bunches of antiprotons circulating in the opposite direction. The two beams are focused using quadrupole magnets in two regions around the ring where they collide every 396 ns. The two general purpose collider experiments installed in these two regions are CDF and D0. In the region of CDF the beam has a longitudinal dispersion of $\sigma_z \simeq 30\,cm$, and a transverse dispersion of $\sigma_t \simeq 30\,\mu m$.

	Run Ib	Run II present	Run IIa nominal	Run IIb nominal
p bunches $\times$ $\bar{p}$ bunches	6×6	36×36	36×36	140×121
p/bunch	$2.3 \cdot 10^{11}$	$2.1 \cdot 10^{11}$	$2.7 \cdot 10^{11}$	$2.7 \cdot 10^{11}$
$\bar{p}$/bunch	$5.5 \cdot 10^{10}$	$2.5 \cdot 10^{10}$	$3.0 \cdot 10^{10}$	$3.0 \cdot 10^{10}$
$L\,[cm^{-2}s^{-1}]$	$0.16 \cdot 10^{31}$	$4.1 \cdot 10^{31}$	$8.6 \cdot 10^{31}$	$16 \cdot 10^{31}$
$\mathcal{L}\,[pb^{-1}/week]$	3.2	6-8	17	32
Bunch spacing $[ns]$	$\approx$3500	396	396	132
Crossing angle $[\mu rad]$	0	0	0	136
Energy $(p+\bar{p})$ $[GeV]$	$900+900$	$980+980$	$980+980$	$980+980$

Table 3.1: Parameters of the Tevatron for Run I and Run II [49] [53]. Recent developments suggest, that Run IIb will use essentially the same parameters as Run IIa [51].

The accelerator has been running since March 2001. Many improvements have been implemented to correct the problems that were identified during the start-up period:

- Modification of the injection helix
- Proton beam loading compensation in Main Injector
- Accumulator stochastic cooling upgrade
- C-0 Lambertson magnets removal

However, there are still several problems to which satisfactory solutions have not been found yet:

- Emittance preservation throughout the complex
- Beam-beam interaction in the Tevatron
- Proton and antiproton acceleration efficiencies (Tevatron)
- Beam lifetimes
- Transfer losses

At present[2] the instantenuous initial luminosity is topping out at $5 \times 10^{31}\,cm^{-2}s^{-1}$ (see Figure 3.2), which is significantly lower than expected (Table 3.1). The same can be said about the weekly integrated luminosity which is 2-3 times lower than planned (Figure 3.3). The modified aim is to reach $3 \times 10^{32}\,cm^{-2}s^{-1}$ instantenuous luminosity and $4.4 - 8.6\,fb^{-1}$ integrated luminosity by 2009[3] [49]. For the Run IIb a structure of 140 proton bunches and 121 antiproton bunches was foreseen. However, this would have implied the reduction of time between collisions to $132\,ns$, significantly increasing

[2] i.e. end of 2004.

[3] However, this number could be decreased by 15% if the 7 month shutdown goes ahead as planned in 2006.

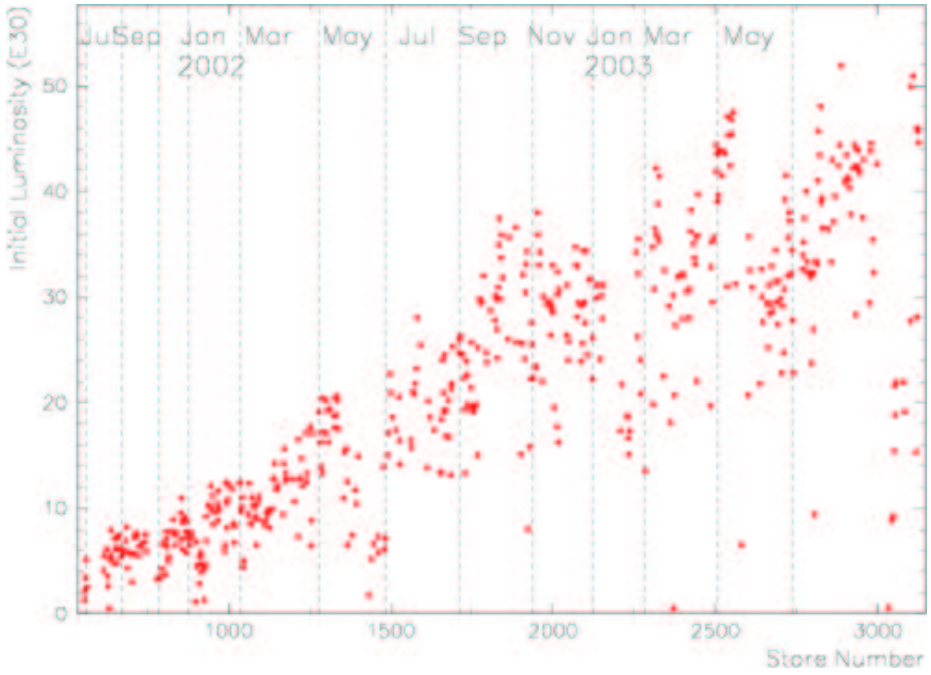

Figure 3.2: Instantenuous luminosities at the start of the stores through the end of 2003 [56].

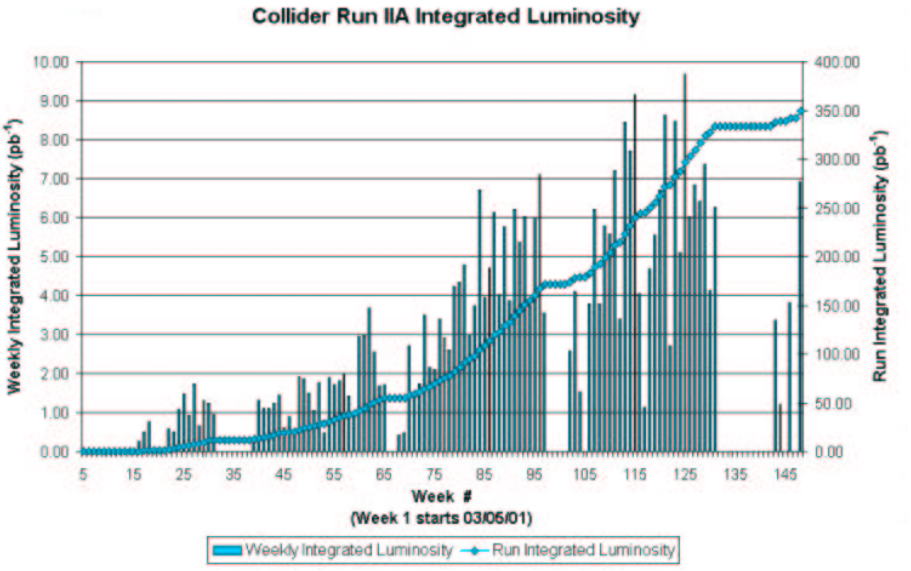

Figure 3.3: The luminosity delivered by the Tevatron since the start of Run II until January 2004 [55].

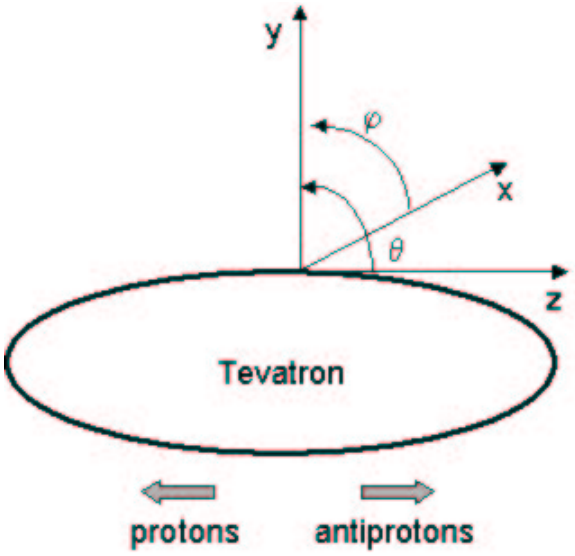

Figure 3.4: The coordinate system of the CDF experiment.

beam-beam effects, and the introduction of an angle between the two beams. As the primary motivation for increasing the number of bunches, the expected high luminosity, was not achieved, plans for operating the Tevatron with $132\,ns$ bunch spacing have been abandoned, so the same 36×36 configuration will be used for Run IIb as for Run IIa.

3.2 The CDF experiment

3.2.1 Overview of the CDF experiment

CDF is a general purpose detector designed to detect secondary particles produced in $p\bar{p}$ collisions at the Tevatron. It is a cylindrical detector with forward-backward symmetry designed to cover as much solid angle as possible.

For the description that follows to be clear, it is useful to define the quantities that will be used. CDF uses a cartesian coordinate system (Figure 3.4), where the z axis is oriented along the nominal direction of the beam pointing along the direction of the incoming protons, the protons circling clockwise. The center of the coordinate system is the nominal interaction point, which coincides with the center of the detector. The y axis points upwards, while the x axis is directed radially outwards in the horizontal plane of the Tevatron. There is also a spherical coordinate system defined, where r is the radial distance measured from the center of the detector, ϕ is the azimuthal angle measured anti-clockwise from the positive x axis in the transverse plane, and θ is the polar angle measured with respect to the proton direction. So

$$z = r \cdot \cos\theta \tag{3.2}$$

and the transverse momentum (the projection of the momentum onto the $x-y$ plane) is defined as

$$p_T = p \cdot \sin\theta = \sqrt{p_x^2 + p_y^2} \tag{3.3}$$

The natural unit of measurement in collider physics is the rapidity, defined as

$$y = \frac{1}{2} \ln \frac{E + p_z}{E - p_z} \tag{3.4}$$

because the shape of the particle density distribution in rapidity is invariant under Lorentz transformations along the beam direction. The rapidity is approximately equal to the pseudorapidity

$$\eta = -\ln \tan \frac{\theta}{2} \tag{3.5}$$

for highly relativistic particles ($p \gg mc$). Pseudorapidity is much more convenient to use, because it is independent of the particle type and depends only on the polar angle.

The CDF II which is a general purpose solenoidal detector is shown on Figure 3.5 and 3.6. The innermost tracking layer of the CDF II detector system consists of silicon detectors (Layer00, SVX II and ISL) surrounded by a drift chamber (COT), and the whole contained in a superconducting solenoid, $1.5\,m$ in radius and $4.8\,m$ in length, which generates a $1.4\,T$ magnetic field parallel to the beam axis. Progressing towards the outside are placed the electromagnetic and hadronic calorimeters, followed by the muon chambers. The luminosity is measured by Cherenkov counters which are located in the forward regions very close to the beam pipe. All these subsystems will be described in greater detail in the following sections.

3.2.2 The CDF Tracking System

The elements of the CDF tracking system and their electronics must be capable of handling the high luminosity and high repetition rate provided by the Tevatron. The anchor of the Run II tracking system is a large open cell drift chamber for charged particle reconstruction in the central region ($|\eta| < 1.0$). At small radii a new silicon detector consisting of three subsystems provides precision tracking and secondary vertexing, enabling stand-alone silicon tracking over the full region of $|\eta| < 2.0$ (Figure 3.7).

The Silicon Detectors

Silicon tracking provides precise track coordinate measurements in the $r-\phi$ plane and precise secondary vertex reconstruction for the long-lived b and c hadrons. In Run II the silicon inner tracker consists of three concentric subsystems (Figure 3.8). The one closest to the interaction point is Layer 00 (L00), which is located at the radius of $1.35\,cm$, and consists of single-sided radiation resistant silicon modules which are actively cooled (Figure 3.9). Its main advantage lies in improved impact parameter

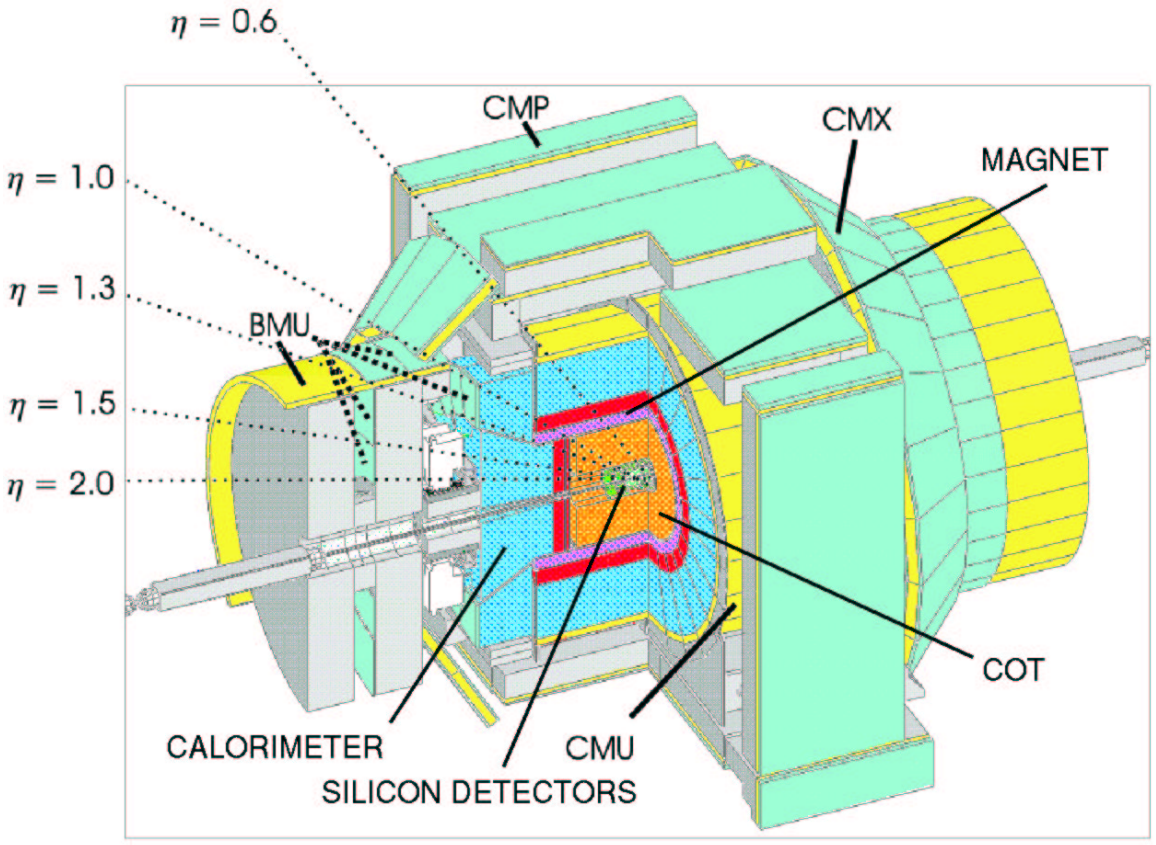

Figure 3.5: Three dimensional view of the CDF detector showing the position of the detector subsystems.

resolution and b-tagging. L00 is followed by a five-layer detector, the Silicon Vertex Detector, which covers the region between $2.5\,cm$ and $10.6\,cm$. It provides CDF with three dimensional vertex reconstruction and tracking. Finally, the Intermediate Silicon Layer (ISL) extends the coverage of the silicon up to $|\eta| < 2.0$. The information provided by the SVX and ISL is sufficient to reconstruct three dimensional tracks independently of the COT[4]. It also helps to link COT tracks to SVX tracks more efficiently. The total sensor area adds up to approximately $6\,m^2$. As L00, ISL and the corresponding reconstruction software were still maturing during the data-taking period of the present analysis, the data from these subsystems were not used. The properties of the Run II silicon detectors are summarized in Table 3.2.

The Silicon Vertex Detector (SVX) consists of three barrels (Figure 3.10), each $29\,cm$ long, which mounted together add up to a $96\,cm$ total length. There are 12 wedges in ϕ, each containing five layers of silicon. Of the five layers, three (Layers 0, 1 and 3) combine an $r-\phi$ measurement on one side with a 90^o stereo measurement on the other. The remaining two (Layers 2 and 4) combine $r-\phi$ with small angle stereo

[4]This is called the stand-alone mode, and amongst others it allows to measure the efficiency of the COT tracking.

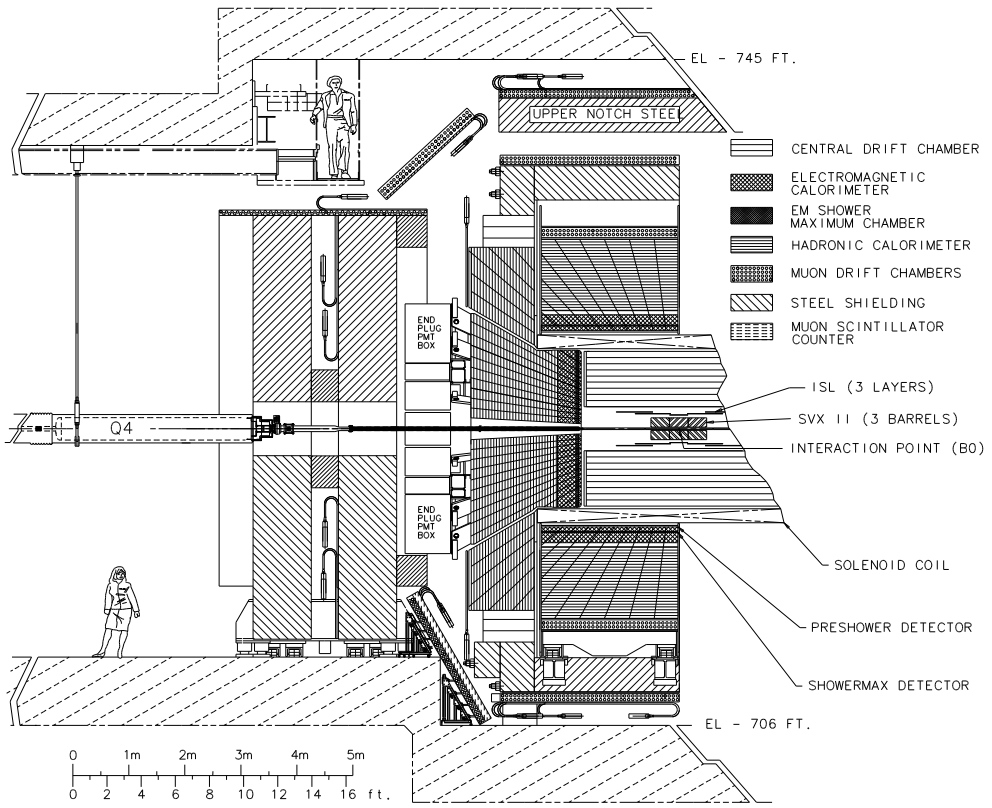

Figure 3.6: Elevation view of the CDF detector showing the position of the different subsystems.

at 1.2^o. This is designed to permit good resolution in locating the z-position of the secondary vertices and improve pattern recognition and 3-D vertex reconstruction.

The sensors used in the detector modules have a bulk silicon thickness of $300 \pm 15\,\mu m$ for the 90^o stereo layers and $275 \pm 15\,\mu m$ for the small angle layers. The HV biasing uses polysilicon resistors and the readout is AC-coupled. The 90^o stereo sensors have strips running lengthwise on the sensor's $p-n$ junction side to measure the $r-\phi$ position of the particle, and strips running laterally on the ohmic contact side (n-side) to measure the $r-z$ position. Both sets of strips are read out at the end of the sensors. A substantial R&D program, similar to that of the ATLAS SCT has been carried out in order to achieve the full potential of the tracker[5]. The detector modules are assembled in "ladders", 12 ladders corresponding to the 12 wedges in ϕ and making a layer. In each barrel, the silicon ladders are mounted between two precision-machined beryllium bulkheads which also carry the water cooling channels for the readout electronics. The bulkheads define the precision of the barrel assembly and, therefore, had to be machined to very low tolerances. Beryllium was used beacause of its long radiation length and stiffness. The coolant is circulated through the integrated cooling channels of the bulkheads at approximately $-5\,C^0$. In order to allow a possible

[5]See [59] Chapter 5 for more details and references.

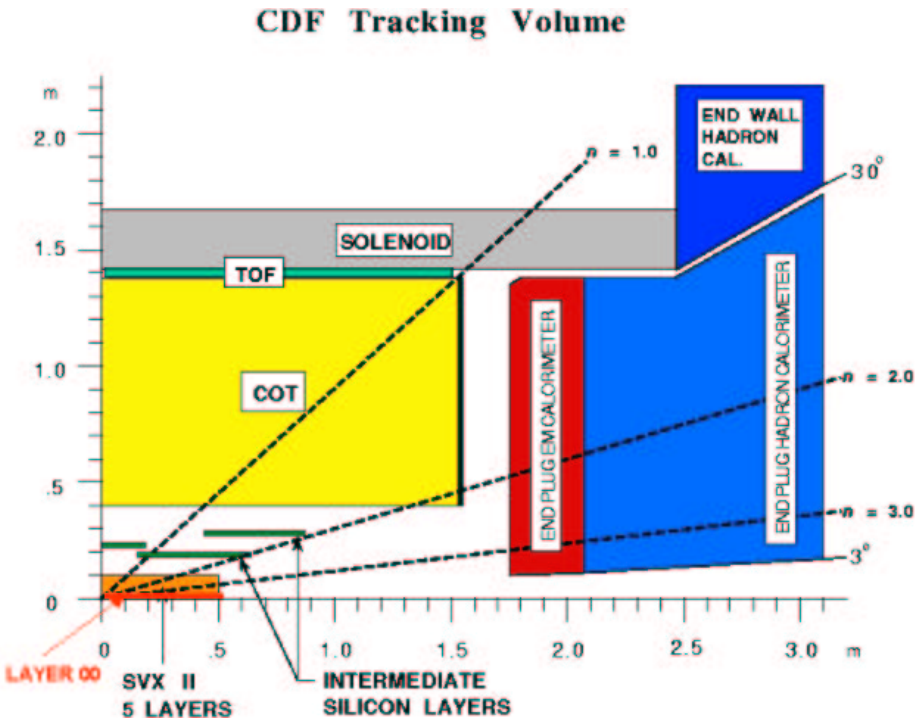

Figure 3.7: Overview of the CDF tracking system.

	Layer 00	SVX II	ISL	Total
Layers	1	5	2	8
Length	0.9 m	0.9 m	1.9 m	
Channels	13824	405504	303104	722432
Modules	48 SS	360 DS	296 DS	704
Readout Length	14.8 cm	14.5 cm	21.5 cm	
Inner Radius	1.35 cm	2.5 cm	20 cm	1.35 cm
Outer Radius	1.65 cm	10.6 cm	28 cm	28 cm
Power	100 W	1.4 kW	1. kW	2.5 kW

Table 3.2: Characteristics of the Run II silicon detectors.

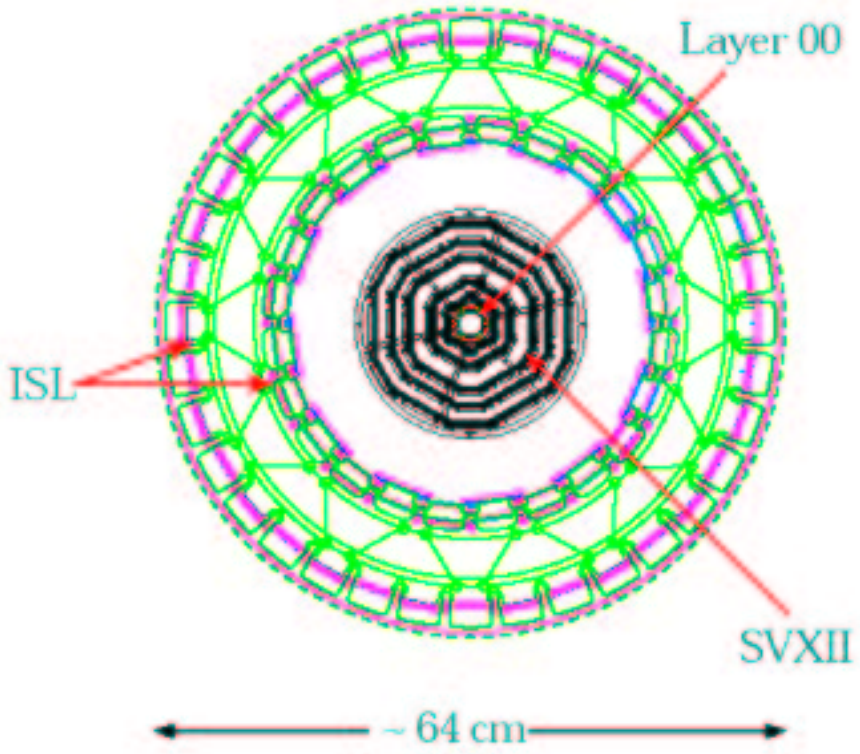

Figure 3.8: Overall view of the different silicon subsystems.

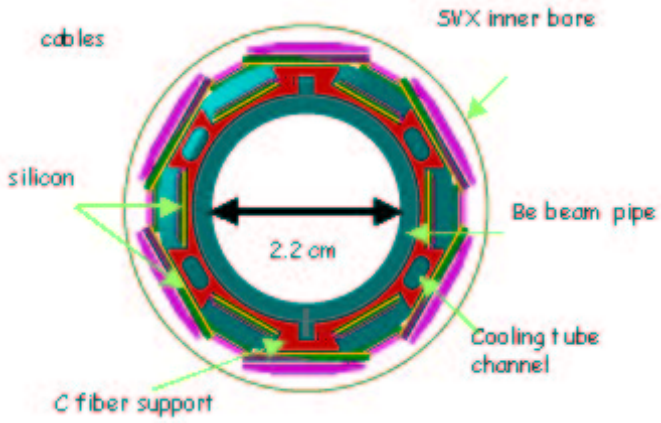

Figure 3.9: Design of the Layer 00.

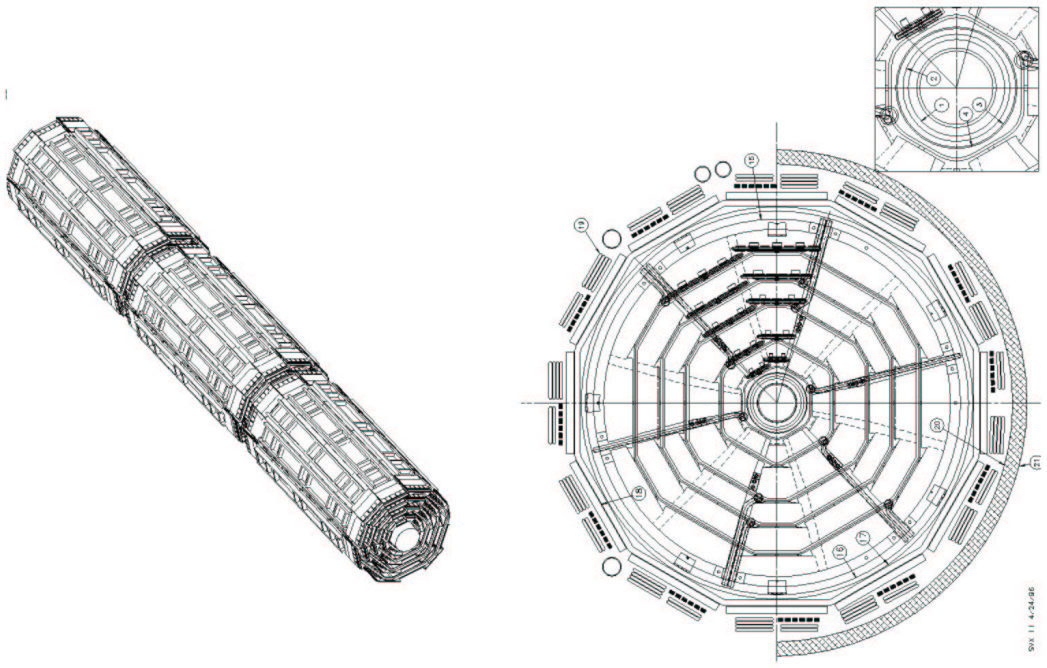

Figure 3.10: SVX barrel and bulkhead.

replacement of the inner two layers, the bulkhead assembly was divided into two parts, with the inner two layers separate from the outer three layers.

A perspective view of both sides of a Layer 0 ladder is shown on Figure 3.11. A notch on the ladder end is used to precisely locate ladders relative to their support structure. The ϕ-side, where the detector strips are parallel to the beam line, is on the top of the ladder with the readout chips being opposite the cooling channel. The z-side readout chips are on the underside of the ladder located inboard of the cooling channel. The ladders consist of two halves, each containing two crystals. As soon as the ϕ-side hybrid had adhered to the surface, the second detector was precisely located relative to the first and the two detectors were wirebonded. In the next step the support rail was connected to the surface in order to make a single structure before the completion of the z-side.

The readout chips (SVX3D) are mounted on an electrical BeO hybrid on the surface of the silicon detectors. A 46-cell analog pipeline with 4 buffer cells stores the data while the Level-1 trigger decision is made. This pipeline supports simultaneous digitization and readout of data, which takes only $10\,\mu s$ resulting in a L1 trigger accept rate of $50\,kHz$ with minimal deadtime. The high speed is required in order to use the SVX data in the Level 2 vertex trigger processor (SVT, see section 3.2.6 for more details). The dynamic pedestal subtraction enables to suppress on-chip common mode noise, so that the threshold which correponds to 99% of efficiency is usually 4-5 rms noise values away from the pedestals [60]. As there are 128 channels in each

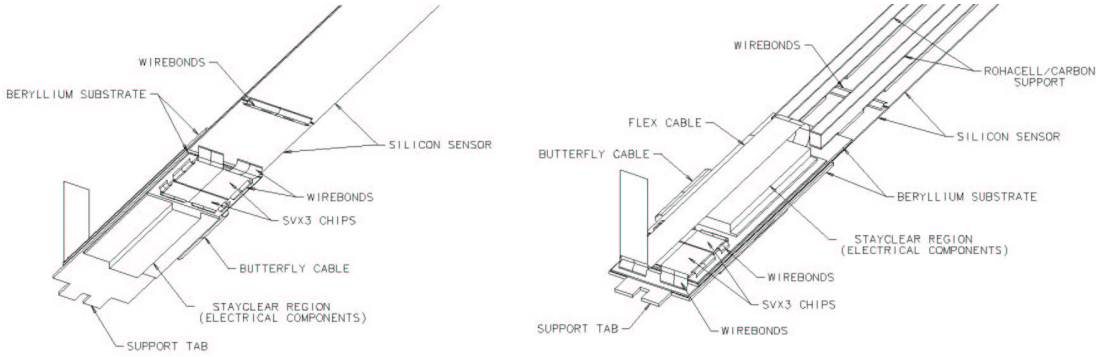

Figure 3.11: Perspective views of the z and ϕ-sides of a Layer 0 ladder.

chip, 88 chips in each wedge, 12 wedges in each barrel and 3 barrels, it adds up to 405504 channels for the whole system. In order to be able to read out such a large system within the required time a highly parallel fiber-based data acquisition system has been implemented.

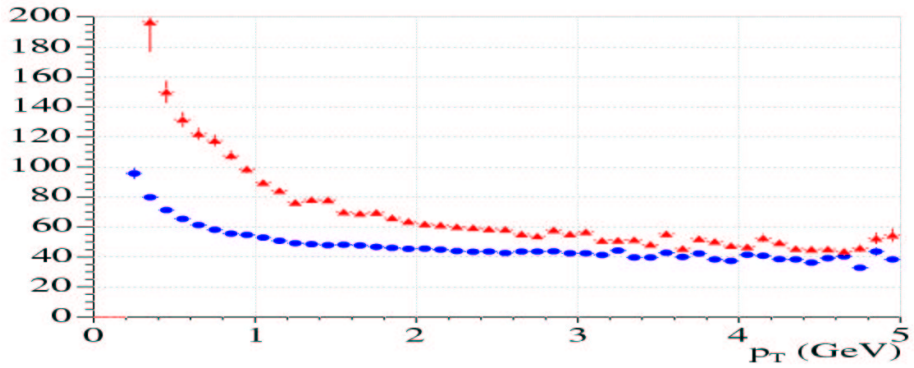

Figure 3.12: Impact parameter resolution in μm as a function of the p_T for tracks passing through passive material without Layer 00 hits (red), and with Layer 00 hits (blue).

The commissionning of the SVX II detector was completed in June 2002. 92.5% of the modules are operating, of which 87% are good ladders with an error rate below 1% [61]. The analog performance of the detector is excellent, the charge collection efficiency being higher than 99% [62]. The signal-to-noise ratio ranges from 14:1 for the $r-\phi$ side of SVX II to 10:1 for Layer 00. The best position resolution achieved is $9\,\mu m$ for two-strip and $18\,\mu m$ for single-strip clusters in the SVX II, and the average offline tracking efficiency is 94% [63]. As it will be described in Section 5.6 for ATLAS the resolution for single-strip clusters will be $\sim 23\,\mu m$. The average fake rate is 1.7% (that of the ATLAS Silicon Tracker is required to be $< 1\%$ (Section 5.5)). The single track impact parameter resolution was measured to be $50\,\mu m$ [64]. However,

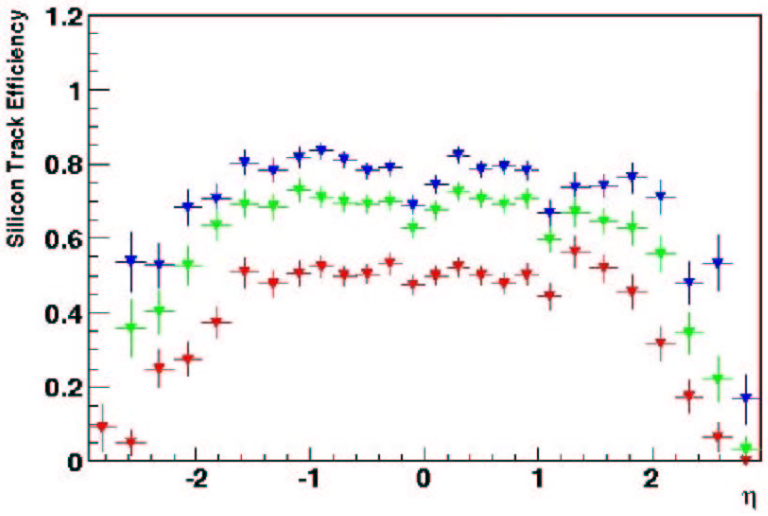

Figure 3.13: Efficiency as a function of η of the calorimeter seeded outside-in silicon tracking for tracks with three (blue), four (green) and five (red) silicon hits.

this resolution can be improved, particularly for low-p_T tracks, as soon as Layer 00 data will be included in the physics analysis framework. Figure 3.12 shows the improvement of the impact parameter resolution with recently improved alignment and with the use of Layer 00. The improvement is the most spectacular at low p_T, where multiple scattering is the dominant component. The current Layer 00 hit efficiency is only 65% as a result of aggressive clustering cuts. This number does not include the effects of the substantial fraction of overlapping strips in L00 design. Moreover, it should get better with final alignment and optimized clustering. In ATLAS the impact parameter resolution is expected to be $\sim 110 - 150\,\mu m$, the difference coming primarily from the fact that CDF has Layer 00 at $1.5\,cm$ and the first two layers of SVX II at 2.7 and $4.3\,cm$, while the first layer of pixels in ATLAS is situated at $5.05\,cm$ (see Section 5.3). The resolution of the impact parameter and similar quantities, like the transverse decay length, is extremely important for rare B decays. Not only some of the triggers are based on them, but these quantities are also used as very strong background rejection cuts, so measuring them with high precision is essential. The forward silicon layers of ISL allow tracking where there is no COT coverage. Efficiencies in excess of 70% have been achieved out to $|\eta| < 2$ with minimal fake rates (Figure 3.13). This extended coverage is especially important for analyses with multi-lepton final states and statistically limited measurements. An example is the top dilepton cross-section measurement which gave the result $\sigma_{t\bar{t}} = (7.6 \pm 3.4(stat) \pm 1.5(syst))\,pb$ which is $\sim 30\%$ better than the Run I measurement despite having about the same luminosity. It is important to note, that no degradation in performance has yet been observed in the two years of operation. On the contrary, the performance continues to increase as alignment, clustering and tracking algorithms improve.

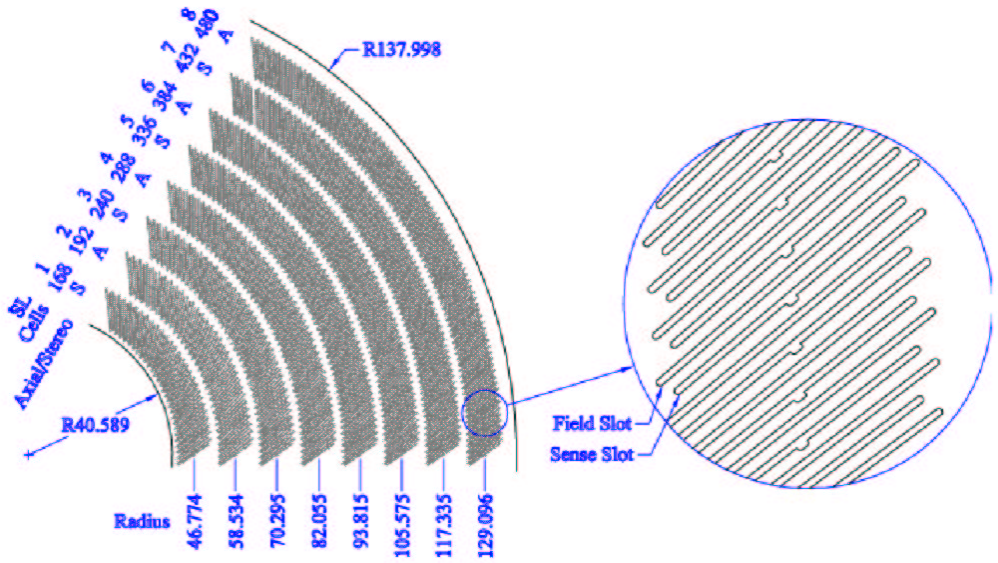

Figure 3.14: 1/6 section of the COT endplate.

COT

The Central Outer Tracker (COT) is a cylindrical open-cell drift chamber spanning from 44 to 132 cm in radii and 310 cm along the beamline[6]. It operates inside a 1.4 T solenoidal magnetic field and is designed to find charged tracks in the region of $|\eta| < 1.0$ with transverse momentum as low as 400 MeV/c. A reconstructed track provides accurate information in the $r-\phi$ view for the measurement of transverse momentum, and substantially less accurate information in the $r-z$ view for the measurement of η. In addition, the COT is designed to link tracks to segments in the inner silicon detectors, to provide an overall momentum resolution of $\delta p_T/p_T^2 < 0.1\%/(GeV/c)$.

The COT is segmented into 8 super-layers (Figure 3.14) alternating stereo and axial, with a stereo angle of $\pm 2^o$. Each super-layer contains 12 sense wires alternated with 13 potential wires which provide the field shaping within the cell, yielding a total of 96 measurement layers. The wire planes and field sheets are strung in precision slots between two precision machined aluminum endplates. The endplates are separated by a 0.251 cm thick carbon-fiber composite inner cylinder and an 0.635 cm thick aluminum outer cylinder. The tension on each wire is 150 g resulting in a total endplate load of 40 tons. High voltage distribution and readout electronics are both mounted on the chamber face. At present the COT uses Argon-Ethane (50:50), resulting in a drift field of 1.9 keV/cm and a maximum drift time of 180 ns. Motherboards feed through the sense and potential wire connections to daughter boards that contain the ASDQ readout chips on one end and distribute high voltage on the other. Following the ASDQ, the signals are transmitted to the TDC boards housed in VME

[6]For more details on the Central Outer Tracker see [59] [65] [66]

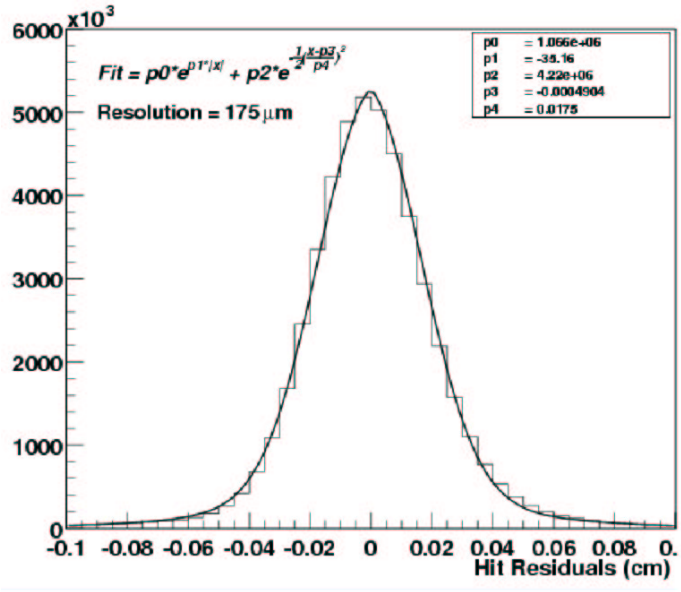

Figure 3.15: Resolution of the Central Outer Tracker.

crates at the corners of the End Wall. From the TDC, fast signals are sent to the XFT to produce a track trigger at Level 1, and digitized signals are sent through the remainder of the readout chain. The COT's high single-hit efficiency provides $\sim 99\%$ tracking efficiency, which is uniform for tracks with $p_T > 2\,GeV$ [67]. For muons with $p_T > 1.5\,GeV$ the efficiency was found to be $99.61 \pm 0.02(stat)^{+0.34}_{-0.91}(stat)$ [68], which is very important for efficiently reconstructing rare B decays, like $B^0_d \to \mu\mu K^{*0}$. The measured COT resolution was found to be $175\,\mu m$ meeting the design goal of $180\,\mu m$ (Figure 3.15).

3.2.3 The calorimetry

Located immediately outside the solenoid, scintillator-based calorimetry covers the region $|\eta| < 3.64$. Its primary goal is to measure the energy of electrons, photons, jets, and the net transverse energy flow. All the calorimeters are segmented in pseudorapidity and azimuth. The uniform segmentation in pseudorapidity, as opposed to that in polar angle, has been chosen, because in high energy collisions the number of charged particles per unit of rapidity is constant in the central region. The calorimetry is divided into two geometrical regions: the central region ($|\eta| < 1.1$) and the plug region ($1.1 < |\eta| < 3.64$). The properties of each calorimeter are summarized in Table 3.3 (the thickness is given in radiation length (X_0) for the electromagnetic calorimeters and interaction lengths (λ) for the hadronic calorimeters).

The central region is further subdivided into an electromagnetic (CEM) and a hadronic portion (CHA). In the central region, the CEM [59] [69] is a sampling calorimeter composed of $3.2\,mm$ thick lead sheets interspersed with $5\,mm$ thick

	Coverage	Energy resolution $\sigma(E)/E$	Segmentation $\Delta\eta \times \Delta\phi$	Thickness
CEM	$\|\eta\| < 1.1$	$14\%/\sqrt{E_T}$	0.1×15^o	$19X_0, 1\lambda$
CHA, WHA	$\|\eta\| < 1.3$	$75\%/\sqrt{E_T}$	0.1×15^o	4.5λ
PEM	$1.1 < \|\eta\| < 3.6$	$16\%/\sqrt{E}$	0.1×7.5^o,0.16×7.5^o	$21X_0, 1\lambda$
PHA	$1.2 < \|\eta\| < 3.6$	$80\%/\sqrt{E}$	0.16×7.5^o,$0.2 - 0.6 \times 15^o$	7λ

Table 3.3: Characteristics of the Run II calorimeters of the CDF detector.

polystyrene scintillator layers. Due to the geometry of the solenoid the central region is covered by two hadronic calorimeters: the central (CHA) and the wall (WHA) hadronic calorimeters. These use acrylic scintillators sandwiched between sheets of iron using a similar scheme to that of the CEM. The central calorimeter is divided into two halves at $\eta = 0$, each half consisting of 24 wedges in ϕ. A wedge is segmented into ten towers subtending 15^o in ϕ and 0.1 in η. Particles which pass through the calorimeter interact with the material producing showers of photons and electrons. Incoming photons and electrons will start showering earlier and their showers will be almost completely contained in the electromagnetic portion of the calorimeter. Hadrons (such as pions) will release a significant fraction of their energy later in the hadronic section of the calorimeter. Proportional chambers (CES) are embedded near the shower maximum about six radiation lengths deep into the EM calorimeters. They determine the location of the incident particle within a tower and allow shower-track matching. Another set of proportional chambers, the Central Preradiator (CPR) is placed in front of the wedges and perform the task of a shower presampler. They use the magnet coil and the tracking material as a radiator.

As in the case of the central region, the plug calorimeter is divided into an electromagnetic (PEM) and hadronic (PHA) portion as well. Unlike the central part, the gas calorimeters of Run I were incompatible with the crossing rates of Run II, so a new scintillating tile plug calorimeter has been constructed. In both sections the active elements are scintillator tiles read out by wavelength shifting (WLS) fibers embedded in the scintillator. The WLS fibers are sliced to clear fibers, which carry the light out to the PMTs located on the back plane of each endplug. The EM calorimeter (PEM) is a lead/scintillator sampling device where $4\,mm$ thick scintillator layers are sandwiched between $4.5\,mm$ thick lead layers. There is a preshower (PPR) and shower-max (PES) detector in the plug portion of the calorimeter as well. The hadron calorimeter (PHA) is a 23 layer iron and scintillator sampling device with a unit layer composed of $2\,inch$ iron and $6\,mm$ scintillator.

With the completion of the CDF II upgrade, both the electromagnetic and hadronic calorimeters have the same geometry and disposition of towers, so that a comparison of energy deposition in each element can be made for any individual tower.

	CMU	CMP/CSP	CMX/CSX	IMU
Pseudo-rapidity coverage	$\|\eta\| \leq 0.6$	$\|\eta\| \leq 0.6$	$0.6 \leq \|\eta\| \leq 1.0$	$1.0 \leq \|\eta\| \leq 1.5$
Drift tube cross section	$2.68\times6.35\,cm$	$2.5\times15\,cm$	$2.5\times15\,cm$	$2.5\times8.4\,cm$
Drift tube length	$226\,cm$	$640\,cm$	$180\,cm$	$363\,cm$
Max drift time	$800\,ns$	$1.4\,\mu s$	$1.4\,\mu s$	$800\,ns$
Total drift tubes	2304	1076	2208	1728
Scintillation counter thickness	-	$2.5\,cm$	$1.5\,cm$	$2.5\,cm$
Scintillation counter width	-	$30\,cm$	$30-40\,cm$	$17\,cm$
Scintillation counter length	-	$320\,cm$	$180\,cm$	$180\,cm$
Total counters	-	269	324	864
Pion interaction lengths	5.5	7.8	6.2	6.2-20
Minimum detectable muon p_T	$1.4\,GeV/c$	$2.2\,GeV/c$	$1.4\,GeV/c$	$1.4-2.0\,GeV/c$
Multiple scattering resolution	$12\,cm/p$	$15\,cm/p$	$13\,cm/p$	$13-25\,cm/p$

Table 3.4: Design parameters of the CDF II Muon Detectors.

3.2.4 Muon detectors

Unlike electrons and hadrons which lose most of their energy in the calorimeters, muons traverse the tracking system and calorimeters with ease. Triggering and reconstructing muons is at the core of several broad physics programs and is the basis of the present analysis. In order to detect these particles muon chambers are placed outside the calorimetry. CDF II uses four systems of scintillators and proportional chambers in the detection of muons over the region $|\eta| < 2.0$ (Figure 3.16). The design parameters of these detectors are summarized in Table 3.4.

The performance of the central muon systems was satisfactory during Run I, so the structure remains largely unchanged, and changes for Run II represent incremental improvements. In the forward region, however, the muon system's lower granularity would have transformed into higher occupancy, so it was replaced by a new forward muon system (IMU). In all of the systems the long drift times relative to the beam crossing time necessitate a pipelined TDC.

The Central Muon Detector

The Central Muon System (CMU) [71], the original set of muon chambers consists of 144 modules with 16 rectangular cells per module (Figure 3.17), located behind the $\sim 5.5\,\lambda$ absorption material of the CHA. Each cell is $6.35 \times 2.68 \times 226\,cm$ in size and has a $50\,\mu m$ stainless steel wire in the center. The 16 cells in the module are stacked four deep in the radial direction, with a small offset between the first and third and between the second and fourth layers. The first and third (and the second and fourth) ϕ cells have their wires ganged together in the readout, and each wire pair is instrumented with a TDC to measure the muon's location in ϕ, and an ADC

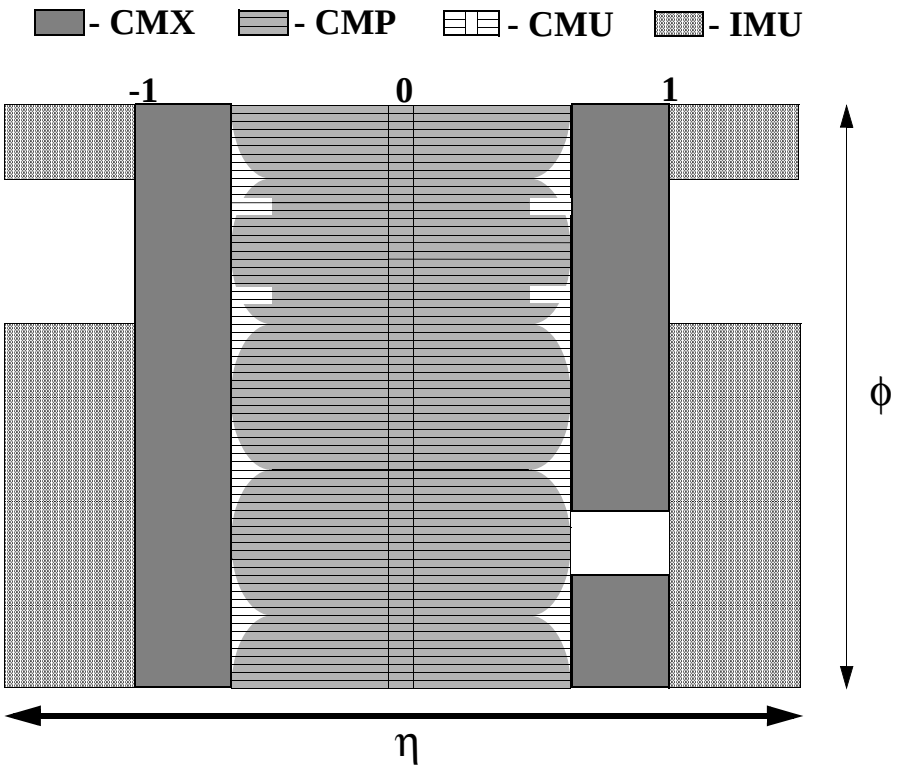

Figure 3.16: Location of the different components of the muon system in azimuth ϕ and pseudorapidity η.

on each end to measure the muon's location in z via charge division. The only major change compared to the Run I is that the CMU chambers are run in proportional, rather than limited streamer mode of Run I, which implied the installation of new pre-amplifiers on the chambers. Also the cell ganging scheme has been changed from alternate cells to adjacent cells, improving the granularity at the trigger level from a 5^o azimuthal arc to 2.5^o.

Central Muon Upgrade

In spite of all the material represented by the calorimeters in front of the CMU $\sim 0.5\%$ of the hadrons[7] will reach the CMU and fake a muon signal. These hadrons create a significant background, especially for muons near jets. In order to improve the rejection of this hadronic background another set of muon chambers is placed behind the CMU. The Central Muon Upgrade (CMP)[72] [73] consists of a second set of muon chambers behind an additional $60\,cm$ of steel in the region $55^o \leq \theta \leq 90^o$ ($|\eta| \leq\sim 0.6$). The return yoke of CDF solenoid provides the necessary steel above and below the central detector, while on the two sides two non-magnetized retractable

[7] Called punch-through in the case of interacting hadrons and sail-through in the case of non-interacting hadrons.

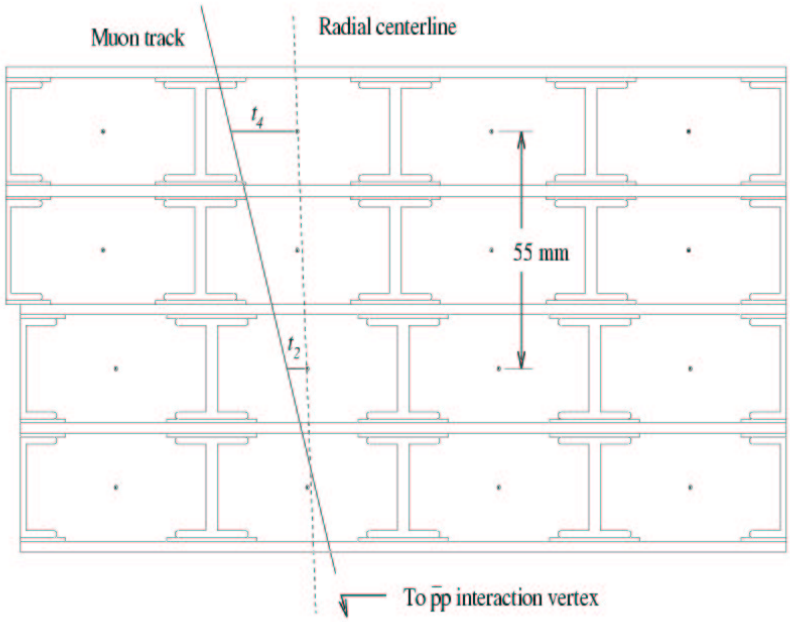

Figure 3.17: Schematic view of the 16 cells of a CMU module.

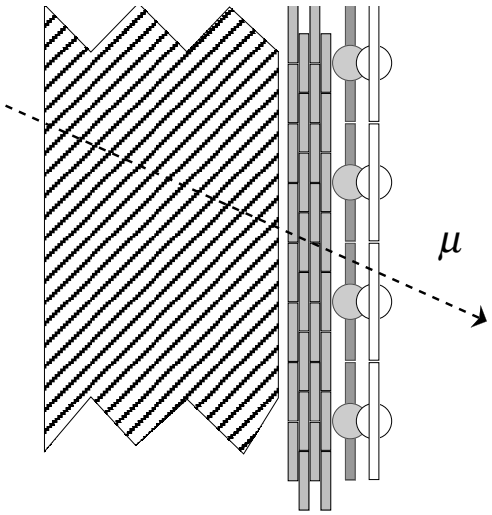

Figure 3.18: Layout of a CMP wall with steel, chambers (CMP) and counters (CSP). Counter readout is located at $z = 0$. Counter layers are offset from the chambers and from each other in x to allow overlapping light guides and PMTs and saving space.

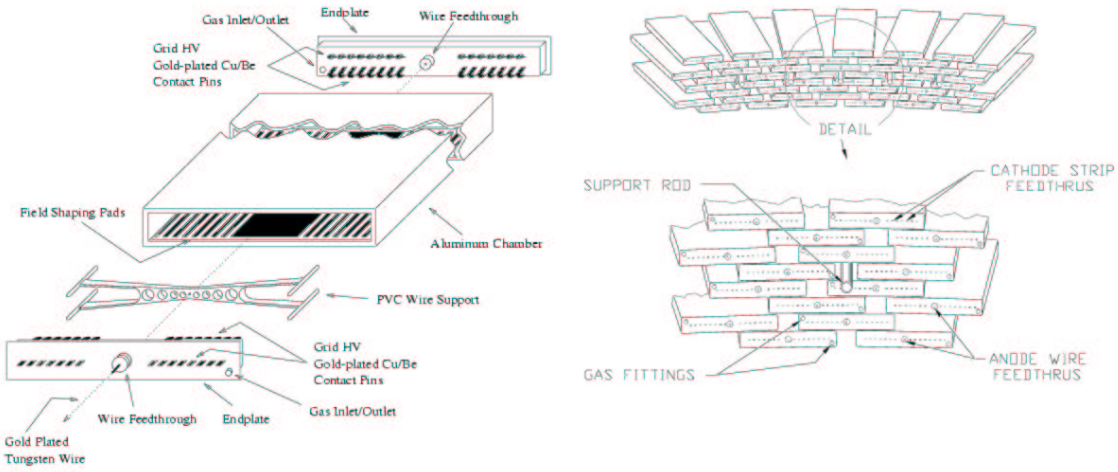

Figure 3.19: Schematic view of a CMP-CMX tube (left), and the drift tube layout in a CMX module covering 15^0 in azimuth (right).

walls have been added, resulting in the reduction of the punch-through hadron rate by a factor of 20. The CMP chambers are rectangular, single wire drift tubes configured in four layers with alternate half-cell staggering (Figure 3.18 and 3.19). They are of fixed length in z and form a box around the central detector. The tubes are made of aluminum extrusions with $0.26\,cm$ walls. They have a single wire in the center and field shaping cathode strips on the top and bottom. The extrusions are glued into four-tube stacks with a half-cell staggering of the second and fourth layers relative to the first and third. Compared to the Run I the CMP coverage was extended in several places to fill existing gaps, such as that on top of the north wall, at the south of the south yoke etc. These additions increased the CMP coverage by approximately 17 %. Steel has been added where it was necessary.

A layer of scintillation counters (CSP) is installed on the outside surface of the wall drift chambers in order to identify the beam crossing of the muon track.

The Central Muon Extension

The Central Muon Extension consists of drift tubes (CMX) and scintillation counters (CSX) located at each end of the central detector. They extend the coverage of the CMU to $42^o \leq \theta \leq 55^o$ ($\sim 0.6 \leq |\eta| \leq \sim 1.0$). The CMX drift tubes are arranged as a logical extension of the CMU. There are four logical layers of twelve tubes for each 15^o sector in ϕ, and successive layers are half-cell offset in order to eliminate ambiguities. Each logical layer consists of two physical layers which partially overlap with each other, resulting in a stereo angle of $3.6\,mrad$ and thus permitting the measurement of the polar angle of the track. On the average a muon intersects six cells. The drift tubes of the CMX differ from those of the CMP only in length ($180\,cm$ as opposed

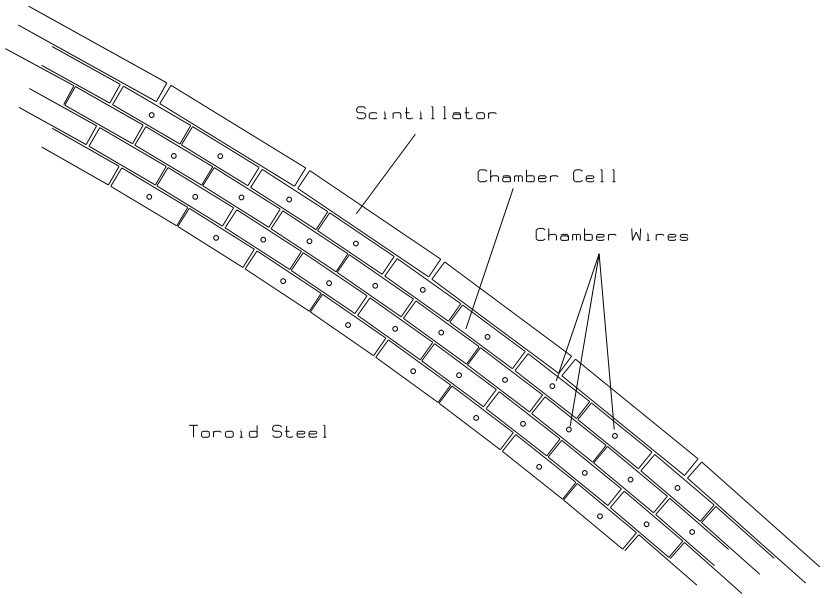

Figure 3.20: A detailed section of the IMU Barrel, showing several chamber cells and the corresponding scintillators.

to 640 cm of the CMP).

A layer of four CSX scintillation counters is installed on both the inside and outside surfaces of each CMX sector. The counters on the inside are half-cell staggered compared to those on the outside doubling the effective granularity of the system. The excellent timing resolution of the counters rejects large CMX backgrounds from out-of-time interactions in the beam pipe and the face of the forward calorimeter.

Compared to Run I the coverage has been increased by instrumenting the top 30 degrees in ϕ on the west side of the detector and the bottom 90 degrees of ϕ as well. The latter is commonly called the "miniskirt" and due to the presence of the floor of the collision hall requires a different geometrical configuration. These upgrades result in a 45% increase in coverage.

The Intermediate Muon System

The CDF II tracking system, in particular the ISL, provides the ability to reconstruct trajectories with $1.0 < |\eta|$ in the solenoid, where the resolution is not dominated by multiple scattering. In order to improve acceptance a new Intermediate Muon System (IMU) was constructed. It provides coverage for $1.0 < |\eta| < 1.5$ with fine granularity, and providing coverage sufficient to identify isolated high p_T tracks as muons or hadrons between $\eta = 1.5$ and $\eta = 2.0$. The IMU consists of a barrel of drift chambers (BMU) and scintillation counters around the FMU toroid steel (TSU), with additional counters between the toroids and on the endwall (BSU). The IMU chambers and counters are virtually identical to the central muon detectors and use the same readout electronics (Figure 3.20). The toroids will not be energized and the

p_T measurement will be provided by the tracking system. This muon subsystem is not used in the present analysis.

3.2.5 The Cherenkov Luminosity Counters

In CDF the beam luminosity is measured using the process of inelastic $p\bar{p}$ scattering. The inelastic $p\bar{p}$ events are efficiently detected using Cherenkov Luminosity Counters (CLC) [74] [75] [76]. There are two CLC modules, installed at small angles in the proton and anti-proton directions with rapidity coverage between 3.75 and 4.75. Each module consists of 48 thin, long, isobutane-filled, Cherenkov counters. The counters are arranged around the beam-pipe in three concentric layers, with 16 counters each, and pointing to the center of the interaction region. The cones are about 180 cm and 110 cm long in the two outer and inner layers respectively. Isobutane is used as radiator, because of its large index of refraction and good transparency for photons in the ultra-violet part of the spectrum where most of the Cherenkov light is emitted.

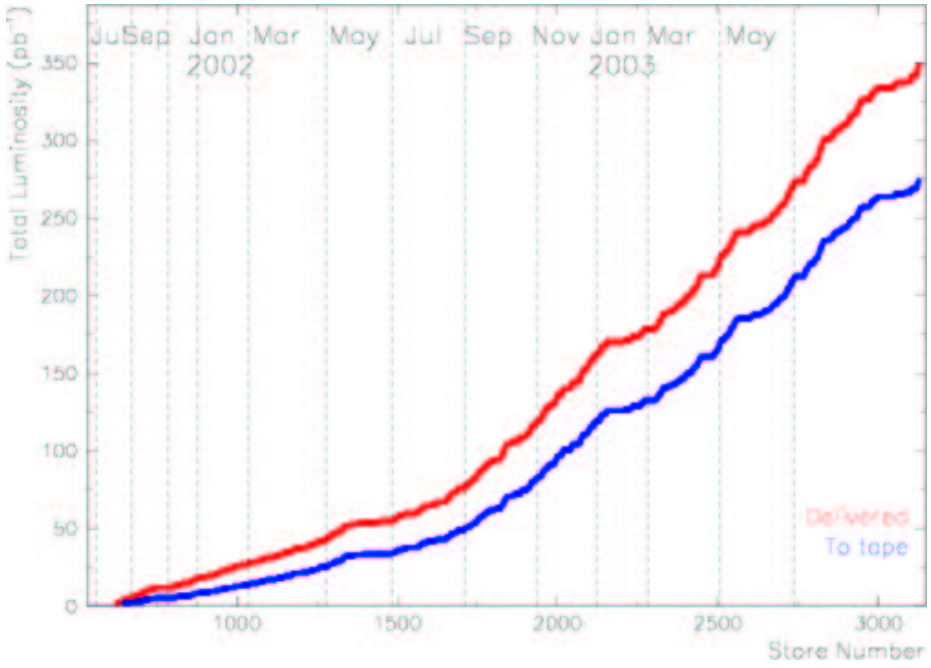

Figure 3.21: Integrated luminosity delivered by the Tevatron (red) and recorded by CDF (blue) through the end of 2003 [56].

The detector has performed very well during the first part of Run II and is an essential part in measuring both the Tevatron and the CDF luminosity (Figure 3.21). The systematic error of the luminosity measurement is dominated by the uncertainities of the inelastic $p\bar{p}$ cross-section ($\sim 3\%$), the CLC acceptance ($\sim 2\%$), and the non-linearity of the CLC acceptance ($< 2\%$), so that the total systematic error is below 5%.

3.2.6 Trigger

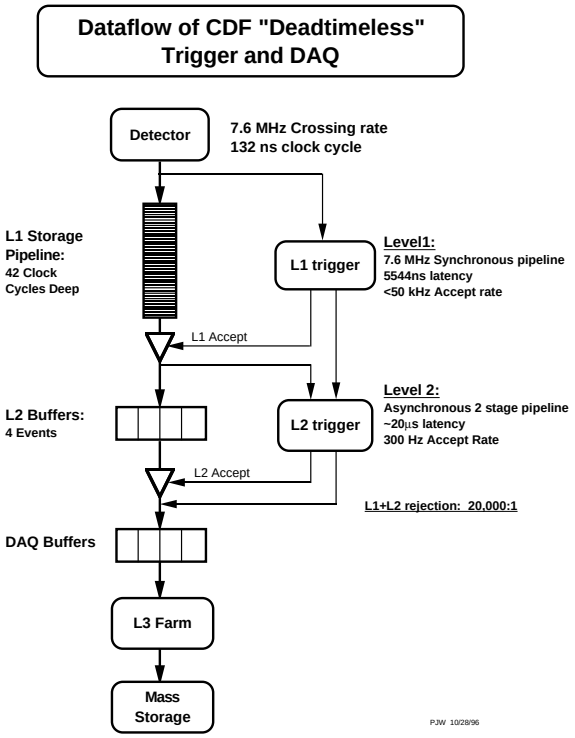

Figure 3.22: Functional block diagram of the CDF data flow.

In hadron collider experiments the collision rate is much higher than the rate at which data can be stored on tape. In Run II the maximal collision rate is expected to be $7.6\,MHz$ while the tape writing speed will not exceed $50\,Hz$. The role of the trigger is to efficiently reject uninteresting events while keeping events of potential interest with high efficiency. The trigger system of CDF uses a three level architecture with each level providing a rate reduction sufficient to allow for processing in the next level with minimal deadtime (Figure 3.22).

Level-1 (L1) uses custom designed hardware to find physics objects (i.e. muons, electrons, etc) based on a subset of detector information. In order to make the L1 trigger decision, each detector element has local data buffering for the 42 beam crossings correponding to the $132\,ns$ separation and $5.5\,\mu sec$ L1 trigger latency[8]. If an event is accepted by the Level-1 trigger, the front-end electronics move the data to one of four on-board Level-2 buffers. The Level-2 (L2) trigger is asynchronous with an average latency of $20\,\mu sec$. It uses custom hardware to make a limited event reconstruction which is performed in programmable processors. The L2 trigger can accept as many as 300 events per second which are then transferred to the Level-3 processor farm. Level-3 (L3) takes advantage of the full detector resolutions in order

[8] i.e the time needed to process an event.

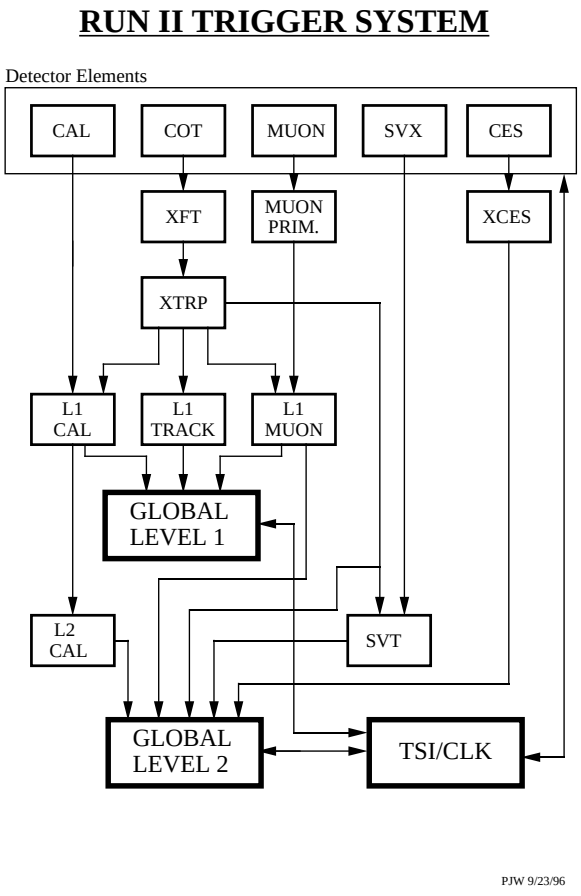

Figure 3.23: Block diagram of the Run II trigger system.

to fully reconstruct events and these events can also be viewed by online monitoring programs. Figure 3.23 shows the functional block diagram of the trigger system.

To keep the count of the passed triggers every event has a set of trigger bits. Each of the trigger bits is reserved for one particular trigger. If an event passes the requirements of the trigger, the corresponding trigger bit is set. A set of consequent L1, L2 and L3 triggers is called a Trigger Path. Only those events which have the required L1, L2 and L3 bits can pass the Trigger Path. A given Trigger Path is intended to determine potentially interesting events for one particular type of physics. To accommodate the different physics interests, several Trigger Paths are used in parallel and all compete for DAQ bandwidth. Such a collection of Trigger Paths is called a Trigger Table. Trigger Table structure and preferences are usually a complicated compromise between several physics and technical requirements.

Front-end and trigger electronics are housed in VME crates, and the trigger decision information is distributed by the Trigger System Interface (TSI). The data is read out from the trigger modules by commercial processors and is delivered to the VME readout boards (VRB) and the Event Building subsytem, which, in turn,

concentrates and delivers the data to the L3 trigger subsystem. L3 is a "farm" of commercial parallel processors, where each event is processed by a single processor. Finally, the Data Logging system writes the events to mass storage and a subset of events to the DAQ monitoring system.

Level 1

The L1 hardware consists of three parallel synchronous processing streams which output their data to the Global L1 processing unit. One of the streams finds muons (MUON PRIM and L1 MUON of Figure 3.23), another one finds calorimeter based objects (L1 CAL), and the third one finds tracks in the COT (XFT - XTRP - L1 TRACK). This latter is the most significant change from Run I, as previously track finding was available only at L2. As the muon and electron triggers require a track pointing at the corresponding detector element, the tracks are also fed to the muon and calorimeter streams. Up to 64 different triggers can be formed using simple ANDs and ORs of objects from these streams. The decision is made every $132\,ns$ by the Global L1 unit.

The addition of the eXtremely Fast Tracker (XFT) is a significant improvement over Run I where tracks were available only at L2. The XFT is highly parallel and processes data from each bunch crossing. The tracking results from the XFT are available fast enough so that they can be used in L1 trigger decisions. Its track-finding efficiency is 96 % for tracks with $p_T > 1.5\,GeV$, the momentum resolution is $\sigma(1/p_T) = 1.7\%/GeV$, and the resolution in ϕ_0 is $5\,mrad$ [77]. The latter is very important for the present analysis as XFT tracks will be used as the seed for the SVT at L2. Track identification is accomplished in two subsystems, the Finder and the Linker. The Finder searches for high-p_T track segments in each of the outer-four axial superlayers of the COT. Each found segment is characterized by a mean ϕ position in the axial SL. The Linker then searches for a four-out-of-four match among segments in the four layers, consistent with a prompt high-p_T track. The XFT divides the COT into 288 segments, each covering 1.25 degrees, with one track allowed per segment. Each XFT board sends its list of tracks to the extrapolation unit (XTRP), which distributes the tracks or information derived from the tracks to the L1 and L2 trigger subsystems.

The calorimeter triggers are divided into object triggers (electrons, photons and jets) and global triggers ($\sum E_T$ and $\not\!\!E_T$). In the case of the object triggers the thresholds are applied to individual calorimeter trigger towers, while in the case of the global triggers those thresholds are applied after summing energies over all towers. Some of the calorimeter triggers use track information in order to reduce the trigger rate. For example, in the case of the low-E_T electron trigger tracks from the L1 track processor (XFT) are available for matching to the tower, and towers with significant hadronic energy can be rejected.

A muon trigger is defined as a muon stub match with an associated XFT track. A muon stub is defined as a pattern of hits in the muon chambers consistent with the passage of a charged particle. CMU and CMX stubs represent a pair of hits on

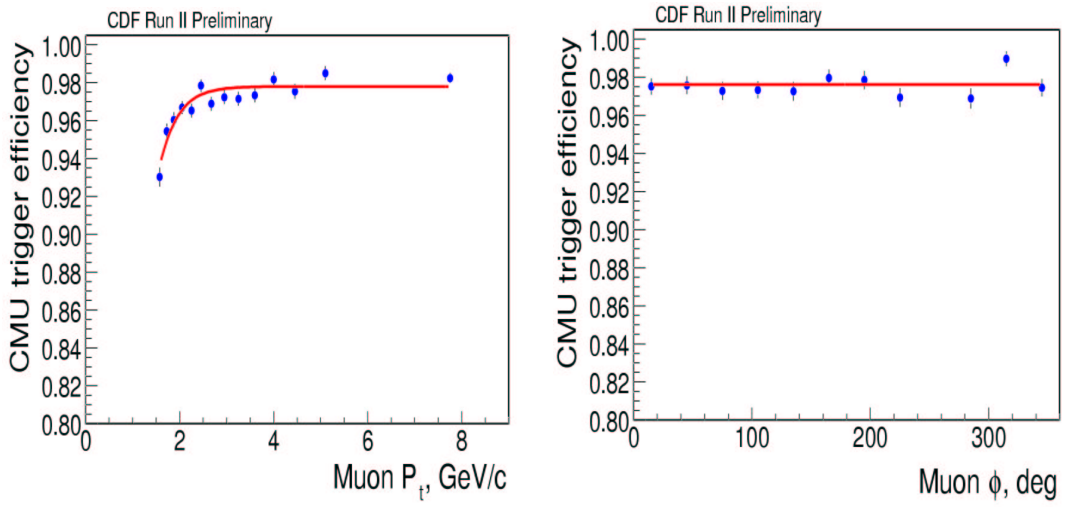

Figure 3.24: Level 1 CMU trigger efficiency as a function of muon p_T and muon track ϕ after excluding bad wedge in 240-270 degree. For the efficiency as a function of ϕ the muons are required to have $p_T > 3\,GeV/c$.

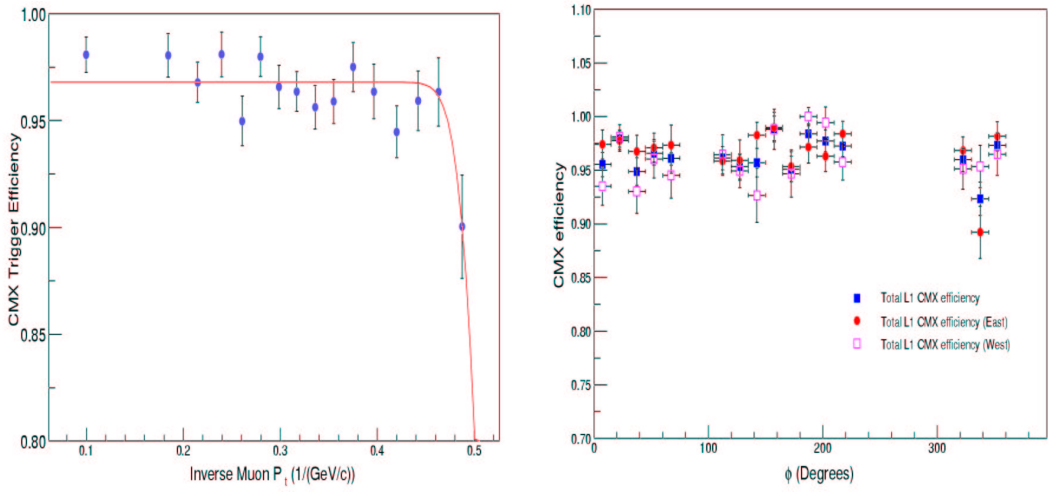

Figure 3.25: Level 1 CMX trigger efficiency as a function of muon $1/p_T$ and muon ϕ. For the right plot the filled square points are for the averaged efficiencies, the dot points are for the East CMX efficiencies, and the open square are for the West CMX efficiencies.

projective wires with a time difference less than some downloaded value, which is set to select tracks above a p_T threshold. For the CMP a stub corresponds to a pattern of hits in a tube stack consistent with a muon. Matching is done by extrapolating XFT tracks to the muon chambers and looking for the presence of a muon stub within 2.5^o. Figure 3.24 shows the CMU trigger efficiency as a function of muon p_T and muon track ϕ [78]. The efficiency was obtained from the $4\,GeV$ inclusive CMUP Level 1 single muon trigger, where the second leg of a J/ψ was used as the probe muon. The CMU efficiency was found to be 0.9774 ± 0.0020. Figure 3.25 shows the CMX trigger efficiency as a function of muon $1/p_T$ and muon track ϕ, which give an efficiency of 0.9672 ± 0.0029 for CMX. These high efficiencies are essential as they enter in the overall efficiency of collecting $\mathrm{B}^0_d \to \mu\mu K^{*0}$ decays.

Level 2

The L2 trigger selection is composed of several asynchronous systems which input their data into the Global L2 crate taking the decision whether any of the trigger conditions has been satisfied. L2 decision starts after the event is written into one of the four L2 buffers. In order to keep the buffers from filling up and causing deadtime the time between L2 decisions should be $< 16\,\mu sec$. As the latency is $20\,\mu sec$, the L2 decision is pipelined in two stages each taking approximately $10\,\mu sec$ resulting in a minimal deadtime even with a L1 accept rate of $50\,KHz$[9].

The data for the decision is collected from the L2 buffers of the L1 trigger systems (XFT and L1 MUON) and from the calorimeter shower maximum detector (XCES). At the same time a track processor finds tracks in the silicon vertex detector (SVT) and a hardware cluster finder (L2 CAL) processes the calorimeter data. Based on the data collected a decision is made by the Global L2 subsystem.

Since jets are not fully contained in trigger towers used by the L1 trigger, the L1 thresholds must be set much lower than the jet energy in order to provide efficient triggers. At Level-2 L2 CAL combines a contiguous region of calorimeter towers with non-trivial energy to form clusters. For each cluster found the total electromagnetic and hadronic energies are calculated and recorded along with the number of towers, and the η and ϕ coordinates of the seed tower.

The ability to use impact parameter information in the trigger to detect secondary vertices can substantially increase the physics reach and the Silicon Vertex Tracker (SVT) is providing this capability, which is the first time in a hadron-collider experiment. Studies of B decays are greatly enhanced by the SVT. Decay channels important for the study of CP violation like $\mathrm{B}^0 \to \pi^+\pi^-$ would be virtually undetectable at the Tevatron without an impact parameter trigger. Other interesting decay modes like the one described in the present thesis will also benefit from an impact parameter trigger in terms of better rejection against background and higher statistics on tape. In order to obtain impact parameter information at L2, the SVX II is read out after each L1 trigger. In the next step the SVT combines this data with L1

[9]For technical reasons at present the maximum L1 trigger rate is $\approx 20\,kHz$.

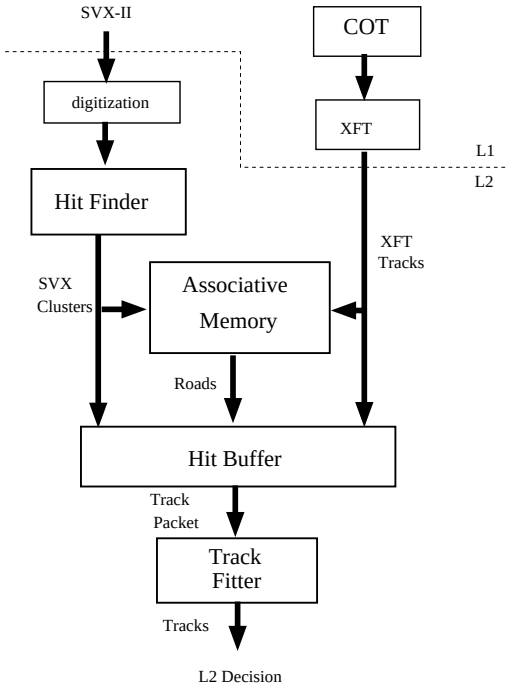

Figure 3.26: Architecture of the SVT trigger.

tracking information from the XFT and computes track parameters with resolution and efficiency comparable to full offline analysis[10].

The SVT has been implemented on custom design VME 9U boards, organized in 12 identical subsystems, corresponding to the 12 wedges of the SVX along the azimuthal angle. After tracking information is received from SVX II it is fed to the Hit Finder boards (Figure 3.26). The Hit Finder performs pedestal subtraction and bad channel suppression. It then scans the data for clusters of hit strips. As soon as clusters satisfying the requirements are found, the centroid of the cluster and the most probable track intersection point at that SVX layer is computed. In the meantime, the list of tracks found by the XTRP is transmitted to the Associative Memory Sequencer (AMS). As soon as the clusters from the Hit Finder are available from the output of the Merger, they are also transmitted to the Associative Memory Sequencer. The AMS uses a lookup table to convert the 14-bit cluster centroid into a coarser Superstrip in preparation for the pattern recognition stage[11] and transmits the information to the Associative Memory (AM) boards. On the AM boards each chip stores 128 combinations of outer tracks and coarse SVX hits. Each combination represents a legitimate particle trajectory and is called a road. The roads are programmable, so

[10]Unfortunately, during the initial period of running there several parts of the SVT system were brought into functioning gradually. That means during the initial period of running the acceptance of the SVT was significantly lower than expected.

[11]The size of the Superstrip is programmable.

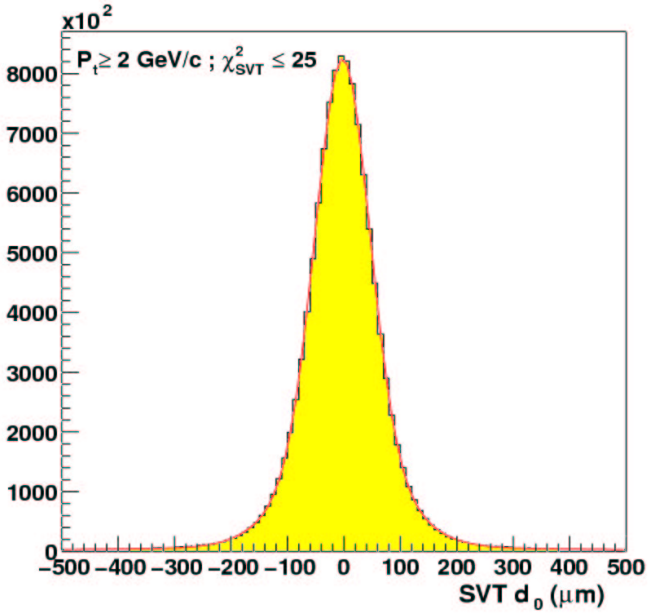

Figure 3.27: Impact parameter distribution of SVT tracks. $\sigma = 50\,\mu m = 35\,\mu m \oplus 33\,\mu m = SVT\,resolution \oplus beam$.

that they can be changed in case of geometric misalignment[12] and other potential problems. Each chip tries to match its input data to a road, and, if a match is found, outputs the track candidate's road number. All the data from the Hit Finder, the AM and the XFT are collected in the Hit Buffer and transmitted to the Track Fitter, where a linear 2-D fit[13] consisting of a set of scalar products is performed.

The resolution after correcting for SVX alignment and beam line position has been found to be $\sim 50\,\mu m$, which is the result of the convolution of $35\,\mu m$ SVT resolution and the beam spot $33\,\mu m$ wide (Figure 3.27) [80] [81]. Figure 3.28 shows the efficiency as a function of p_T and ϕ of the muons for both the data and Monte Carlo simulation for $B \rightarrow J/\psi X$ decays [79]. It not only shows that the SVT is performing at a good efficiency, but that this efficiency is well understood and correctly reproduced by the Monte Carlo simulation. The efficiency for fiducial offline muon tracks from J/Ψ decay having $p_T > 1.5\,GeV$ and hits in the four silicon planes used by the SVT is measured to be 85% [82]. The exact definition of the efficiency depends on the given physics analysis. Requiring the tracks to have $p_T > 2.0\,GeV$ increases the latter eficiency to 90%, while requiring 3 silicon hits instead of 4 diminishes the efficiency by $10 - 15\%$. In mid-2003 the SVT patterns have been upgraded, which resulted in an improvement of up to 15% of the efficiency [83]. Having a good impact parameter resolution and a high efficiency is important in order to collect those $B_d^0 \rightarrow \mu\mu K^{*0}$ and other decays, which are not covered by the non-SVT rare B triggers. With the help of the SVT

[12] Since the SVT does not have z information for tracks, an angular misalignment between the SVX and the beam would result in incorrect impact parameter results.

[13] The fit is performed in the plane perpendicular to the beam axis.

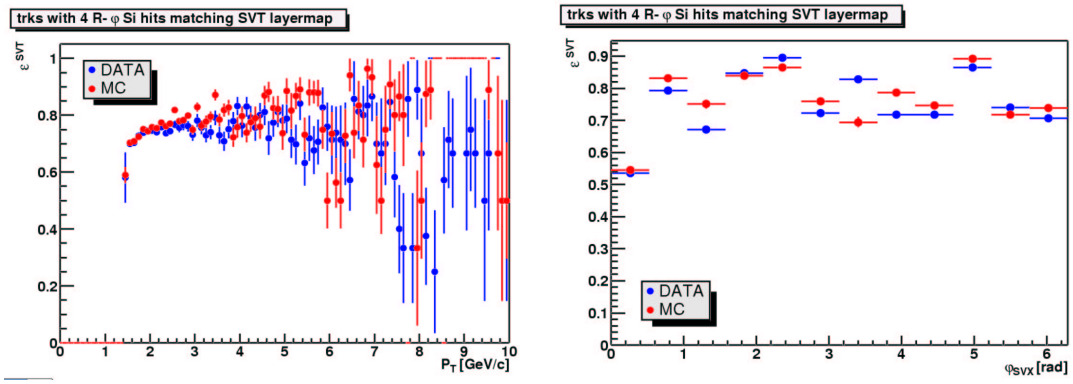

Figure 3.28: SVT efficiency versus the p_T and ϕ of the muon from $B \to J/\psi X$ decays for tracks with 4 $R-\phi$ silicon hits for data (blue) and Monte Carlo simulation (red) [79].

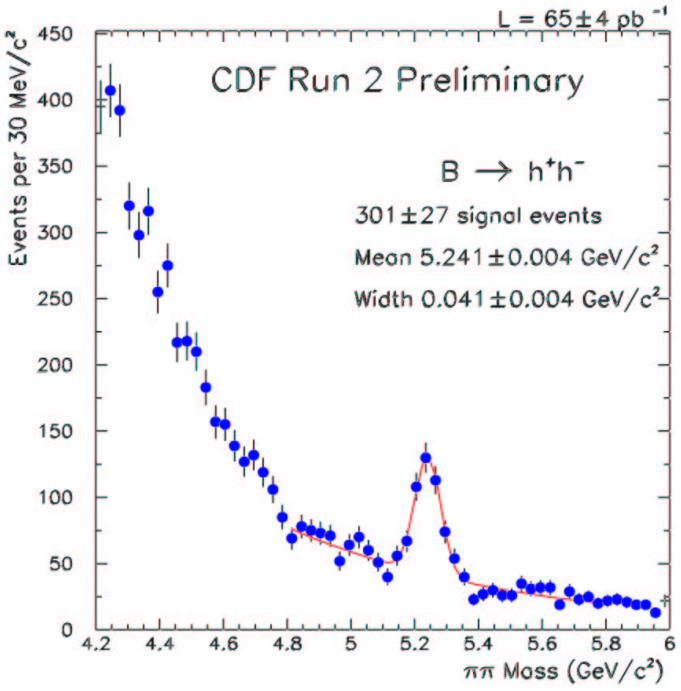

Figure 3.29: Invariant mass distribution of $B \to h^+h^-$ decays.

for the first time it is possible to trigger on tracks with a large impact parameter at the hardware level, which paves the way for triggering on fully hadronic decays and enhances the semileptonic triggers. As an example of the former, the invariant mass distribution of two tracks of opposite charge, assuming the pion hypothesis for each track, is shown on Figure 3.29. The peak[14] is the first evidence of charmless B_s decays, and is a step towards direct CP asymmetry measurements in $B^0 \to K^+\pi^-$ and CP asymmetry measurements in $B^0 \to \pi\pi$.

Finally, the data from the five major sources (L2 CAL, L1 MUON, SVT, XTRP, XCES) is collected and the L2 decision is made in a set of four L2 processors sitting in the Global L2 crate. As the SVT is the system which has the longest processing time, if all triggers which require SVT impact parameters are rejected by other cuts (i.e. kinematics), then the impact parameter cut won't be tested.

Level 3

The Level-3 (L3) trigger system consists of two major subsystems, the Event Builder (EVB) and the Level 3 Farm [84][85]. The L1 and L2 physics cuts and prescales are tuned so that the output rate is about $300\,Hz$, which is the designed input rate of EVB. L1 and L2 systems need to make their decisions at a very high rate which makes it impossible to fully reconstruct each event. L1 and L2 algorithms use only small predefined pieces of event data to make their decision. After a L2 decision is made, the Event Builder assembles all event fragments from the Front End crates into one data block (Figure 3.30). The Level 3 Farm receives a single and complete but disordered block of event data from the Event Builder. The L3 Filter extracts L1 and L2 trigger bits from the trigger banks of the event, looks through the Trigger Paths of the Trigger Table, fully reconstructs the event and makes a final trigger decision. For example even though the impact parameter resolution of the SVT is similar to the offline resolution, the SVT resolution has significant non-Gaussian tails, which is caused by the handling of large clusters of overlapping hits in the silicon detector. More time and information for more complex pattern recognition enable the software of Level 3 to handle the non-Gaussian resolution tails, thus reducing the background while keeping the events of interest with high efficiency [86]. Events passing L3 are sent to Consumer Server Logger (CSL). The CSL writes event data to disk and distributes a small fraction of events to Consumers to allow the shift crew to monitor the quality of incoming data from the Control Room.

While L1 and L2 systems are making their decision the disjointed pieces of event data are waiting in the L1 and L2 data buffers in FE crates. When the L2 trigger decision is made the data fragments of the accepted event are transmitted to 15 EVB VRB crates. Each VRB crate reads event data from a group of FE crates, corresponding to some logical part of the detector (COT, SVX etc). Data flow from the detector is equally distributed between the 15 groups of FE crates to provide the same load for all the VRB crates. Each VRB crate is controlled by a single board

[14]The peak is a mixture of $B^0, B_s \to \pi\pi, K\pi, KK$ decays, which can be separated based on track dE/dx and kinematics.

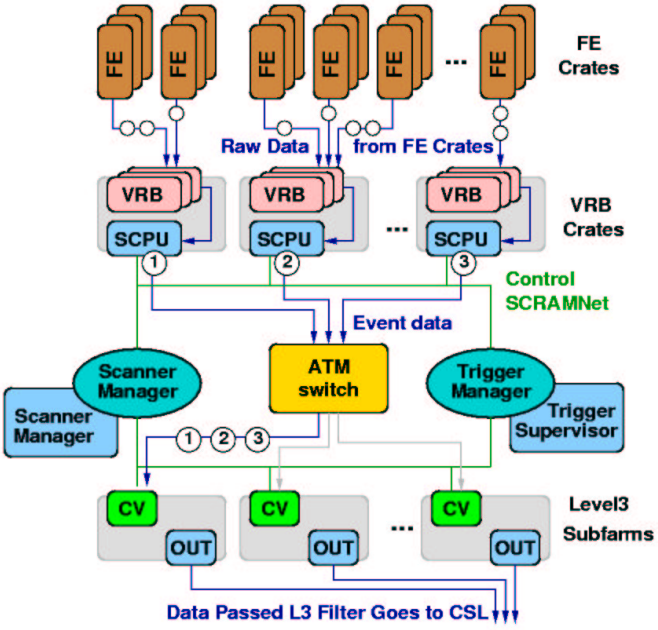

Figure 3.30: Level 3 block diagram.

computer called a Scanner CPU (SCPU) and can serve as a separate unit in data taking.

Event fragments from EVB crates are next sent to the L3 Farm. It takes about a second for one Linux PC to make a trigger decision on one event. It requires a large farm of 250 Dual PentiumIII PCs to deal with the required input rate. Each of the 250 Processor nodes runs an instance of L3 Filter code on each of two CPUs and reconstructs two events in parallel. The 250 processors are divided into 16 subfarms, each subfarm being controlled by a Linux computer called a Converter node. The Scanner Manager (SM), a single board computer, controls all the components of the EVB via SCRAMNet network. It receives L2 trigger from the Trigger Supervisor (TS) and synchronizes data flow from SCPUs to Converters. The data received from the Converter must go through the Reformatter in order to be used by the reconstruction code on the processors. The L3 algorithms can take advantage of the full detector information instead of relying only on subsystems. The L3 Filter also runs a reconstruction based on the offline analysis packages, hence the resolution is greatly improved compared to the lower trigger levels. It determines the event type and makes the L3 trigger decision, accepting events at a rate of approximately 75 Hz. Eight Output nodes, each shared by two subfarms, are dedicated to the output from the Level3 Farm to the CSL.

Chapter 4

Search for the $\mathrm{B}^0_d \to \mu\mu K^{*0}$ decay

4.1 Introduction

Chapter 2 showed that B physics in general, and especially in the last few years, is one of the most interesting areas of high energy physics for testing the Standard Model. The importance of the $\mathrm{b} \to s l^+ l^-$ decays for discerning supersymmetric effects in observed physics quantities has been described. One of the most promising decays was found to be $\mathrm{B}^0_d \to \mu\mu K^{*0}$, which can show supersymmetric contributions either by an enhanced branching ratio, or by a change in the forward-backward asymmetry.

In the previous chapter it was shown why the CDF detector is especially well adapted for carrying out measurements in the field of B physics. It has a powerful tracking system with silicon layers as close as $1.35\,cm$ to the interaction region providing the precision tracking and a drift chamber providing the continuous tracking. Together with the SVT the silicon detector provides $50\,\mu m$ resolution for the impact parameter, which enables CDF to select events of interest with higher efficiency already at the trigger level. Extensive muon systems provide an excellent basis for collecting events of semi-muonic or muonic decays, like $\mathrm{B}^0_d \to \mu\mu K^{*0}$.

Although the present data is not sufficient to measure the forward-backward asymmetry in $\mathrm{B}^0_d \to \mu\mu K^{*0}$ decays, its branching ratio is starting to be within the reach of the CDF experiment. The present chapter will describe the principle of the measurement performed in order to obtain that branching ratio, or – if the case arises – set an upper limit on it. The chapter first introduces the data sample on which the analysis was performed and the trigger cuts inherent to them. Various selection cuts, aimed at eliminating the background, will be described next. Three of the most efficient discriminating variables were chosen in order to perform an optimization procedure on them. The procedure, based on figures of merit will be described in Section 4.5. Section 4.6 will show how the efficiencies of various cuts have been obtained from Monte Carlo calculations. Finally, the branching ratios and upper limits for various confidence intervals will be presented together with a short outlook to the future of the $\mathrm{B}^0_d \to \mu\mu K^{*0}$ decay at CDF.

4.2 The datasets

The study of rare B decays with dimuon final states is one of the strong points of hadron colliders compared to the B factories. The clean final states allow to trigger and select the relevant events out of the overwhelming background, making it possible to take full advantage of the much larger b quark production cross section at hadron colliders. The present analysis uses the data of dimuon rare B triggers from Run II acquired during the period starting from March 2002 until September 2003. In that time frame CDF collected data for a total integrated luminosity of $\int \mathcal{L}dt = 215\,pb^{-1}$. Unlike the Run I, where several different triggers had to be combined in order to cover the relevant mass range [87] in Run II a set of rare B triggers designed explicitely for decays such as $B^0_d \to \mu\mu K^{*0}$ were introduced [88].

Both the L1 and L2 muon triggers and the XFT have thresholds at $1.5\,GeV$. The resulting high rate implies that additional cuts must be implemented at L2 and L3 in order to reduce the rate to manageable levels. The most important new cut used is the requirement that one of the muon tracks has large impact parameter. It is not only simple to implement with the help of the SVT, but is also more inclusive than requiring an extra track for example, as it will be sensitive to decays like $B_{d,s} \to \mu\mu$ as well.

Trigger	Cuts
`L1_TWO_CMU1.5_PT1.5`	$p_T > 1.5\,GeV$ for both CMU muons
`L1_CMU1.5_PT1.5_&_CMX1.5_PT2_PS1`	$p_T > 1.5\,GeV$ for the CMU muon
	$p_T > 2.0\,GeV$ for the CMX muon
	run$\geq$152953, added CSX scintillator veto

Table 4.1: Summary of the Level 1 rare B triggers.

The L1 cuts are the same as for the J/ψ triggers, i.e. two central muons are required to trigger an event. More precisely, the rare B triggers use the `L1_TWO_CMU1.5_PT1.5` and `L1_CMU1.5_PT1.5_&_CMX1.5_PT2_PS1` triggers in their trigger path. The first one requires two muons in the CMU with $p_T > 1.5\,GeV$ each, while the second one asks for one muon with $p_T > 1.5\,GeV$ in the CMU and another one with $p_T > 2.0\,GeV$ in the CMX. In each case the subdetector requires a muon exceeding the threshold of $1.5\,GeV$ and the p_T cut is applied on the information provided by the XTRP. During the data taking period several minor changes have been implemented. From run 145532 the CMX extrapolation has been tightened. The XFT maps have been changed to allow only 1 miss instead of 2 beginning with Run 152636. Starting from run 152953 a CSX scintillator veto has been added to the CMX selection requirement at Level 1 in order to reduce the rate of the fakes generated by the noise in the CMX. The rejection[1] of the CMU-CMU and CMU-CMX trigger is $\sim 4 \cdot 10^4$ and $\sim 10^5$, respectively. It is also worth noting that there is an implicit angle cut,

[1]The rejection is calculated with respect to the `L1_MB_CLC_PS10K` minimum bias trigger.

characteristic of the dimuon triggers, of $\Delta\Phi > 2.5^o$, which is the minimal separation between two muons.

At this moment, there is no cut at L2, i.e. all events are automatically accepted (triggers `L2_AUTO_L1_TWO_CMU1.5_PT1.5` and `L2_AUTO_L1_CMU1.5_PT1.5_&_CMX1.5_PT2`). At the moment, the luminosity is lower than expected, and rate is not an issue at L2. However, when the luminosity increases to its nominal level, muon boards should allow a selection on the muon parameters and the SVT should allow a cut on the impact parameter at Level 2.

two muons with opposite charge
$p_T > 1.5\,GeV$ for CMU, $p_T > 2.0\,GeV$ for CMX and $p_T > 3.0\,GeV$ for CMP muons
$dx < 30\,cm$ for CMU, $dx < 50\,cm$ for CMX and $dx < 25\,cm$ for CMP muons
$\Delta z_0 < 5.0\,cm$ for the two muons
$\Delta\phi < 2.25\,rad$ for the two muons
$0 <$ invariant mass of the two muons $< 6\,GeV$

Table 4.2: Cuts common to all Level 3 rare B triggers.

Trigger	Cuts
`RAREB_CMUPCMU`	
`RAREB_CMUPCMX`	
`RAREB_CMUCMU_SUMPT`	$\sum p_T > 5\,GeV$
	run$\geq$153067, prescale of 10
	run$\geq$155433, invariant mass$> 2.7\,GeV$, no more prescale
`RAREB_CMUCMU_SVT`	one of the muons has $d_0 > 0.01\,cm$
`RAREB_CMUCMU_LXY`	$\lvert L_{xy}\rvert > 0.01\,cm$
`RAREB_CMUCMX_SUMPT`	$\sum p_T > 5\,GeV$
	run$\geq$155433, invariant mass$> 2.7\,GeV$
`RAREB_CMUCMX_CMUSVT`	the CMU muon has $d_0 > 0.01\,cm$
`RAREB_CMUCMX_CMXSVT`	the CMX muon has $d_0 > 0.01\,cm$
`RAREB_CMUCMX_LXY`	$\lvert L_{xy}\rvert > 0.01\,cm$

Table 4.3: Summary of the Level 3 rare B triggers (common cuts are shown in Table 4.2).

The basic L3 strategy is to confirm the L1 cuts. Confirming L1 muons with L3 reconstructed muons cleans up fake muons and fake tracks. At the moment, the impact parameter cut is implemented at L3. In the future, it will be done at L2, and L3 will only confirm it using silicon tracking. There are cuts in L3 which are common to all rare B triggers (Table 4.2). Two `CdfMuons` of opposite charge are required to be in the event with the difference of their longitudinal impact parameters $\Delta z_0 < 5.0\,cm$ and $\Delta\phi < 2.25\,rad$. The invariant mass of the two muons is required to be between 0

and $6\,GeV$, hence these triggers are very interesting for other analyses as well, because there are very few triggers that do not have a lower limit on the dimuon invariant mass. The L1 transverse momentum cuts are also confirmed (i.e. $p_T > 1.5\,GeV$ for CMU, $p_T > 3.0\,GeV$ for CMP and $p_T > 2.0\,GeV$ for CMX). There are also cuts on the muon stub matching, i.e. the $r\Delta\phi$ between the position of the stub and the track extrapolation to the stub[2]. For CMU it is required to be less than $30\,cm$, while for CMP $dx < 25\,cm$ and for CMX $dx < 50\,cm$ are required.

Trigger	Rates $[Hz]$	Rejection	Efficiency
RAREB_CMUPCMU	0.25	42	0.082
RAREB_CMUPCMX	0.02	$7 \cdot 10^2$	0.016
RAREB_CMUCMU_SUMPT	1.1	10	0.105
RAREB_CMUCMU_SVT	0.3	39	0.075
RAREB_CMUCMX_SUMPT	0.18	75	0.044
RAREB_CMUCMX_SVT	0.06	$4 \cdot 10^2$	0.028

Table 4.4: Summary of the Level 3 rare B trigger rates, rejections and efficiencies. The rejection is normalized to the corresponding L1 trigger rate. The efficiency is normalized to the number of generated events.

The SUMPT triggers have the additional requirement that the scalar sum of the transverse momentum of the two trigger muons has to exceed $5\,GeV$. The SVT triggers have an added requirement on the the transverse impact parameter, i.e. $d_0 > 0.01\,cm$ (Table 4.3). Several studies [88] [89] [90] were performed in order to optimize the different rare B triggers, so that they reject efficiently the background while keeping the signal with high efficiency. Table 4.4 summarizes the rejection and efficiency[3] of the triggers[4], where the rejection is normalized to the corresponding L1 trigger rates. As happened with the L1 triggers, the L3 triggers have gone through modifications as well. Because of the increase in luminosity the rate had to be reduced. First, the RAREB_CMUCMU_SUMPT trigger responsible for most of the rate was prescaled starting from run 153067. Starting from run 155433 this prescale was removed, but a lower limit of $2.7\,GeV$ on the invariant mass of the two muons was introduced on both SUMPT triggers. The p_T cuts were moved from the level of the XTRP to the level of the XFT with their values changing slightly beginning with run 155368 ($1.52\,GeV$ instead of $1.5\,GeV$ for CMU tracks, and $2.04\,GeV$ instead of $2.0\,GeV$ for CMX). There was a major modification for triggers that used an impact parameter cut. They have been replaced by triggers cutting on the L_{xy} obtained from the L3 reconstruction beginning with run 163117. L_{xy} is defined as a projection of the vector pointing to the two track crossing point in 2D on the direction of the momentum of the two track system. It can be positive (displacement of the two track vertex is in the same direction as the pair momentum) or negative. This cut implies that both muons have to have silicon

[2] In common CDF jargon $r\Delta\phi$ is the same as *drphi* and *dx*.
[3] The efficiency is normalized to the number of the generated MC events.
[4] RAREB_CMUCMX_SVT is the sum of the RAREB_CMUCMX_CMUSVT and RAREB_CMUCMX_CMXSVT triggers.

Dataset	Runs	Date	Total size	Luminosity
jbmu08	140886-152952	13.03-16.10.2002	$501\,GB$	$45\,pb^{-1}$
jrar08	152953-158732	16.10.2002-13.02.2003	$239\,GB$	$48\,pb^{-1}$
jrar09	158733-168889	13.02-06.09.2003	$775\,GB$	$122\,pb^{-1}$
All	140886-168889	13.03.2002-06.09.2003	$1515\,GB$	$215\,pb^{-1}$

Table 4.5: Datasets used in the present study.

tracks with $|\eta| < 1.2$ associated with them.

Level 3 writes out the data to appropriate streams. All the data relevant to the present thesis were written out to stream J, which is the stream containing the events triggered by muons. The data is reconstructed offline and is further divided into different datasets. The advantage of the offline is that it has much more time and information at its disposal than Level 3. It has access to the run dependent conditions, such as alignment and calibration constants of the various subdetector systems. These datasets are closely related to the Level 3 triggers.

The present analysis spans a time frame where three types of datasets were used[5]:

- Runs 140886-152952: the rare B triggers were written out to the jbmu08 dataset together with other dimuon triggers
- Runs 152953-158732: as the number of datasets increased from 20 to 34 the rare B triggers were assigned a separate dataset, jrar08.
- Runs 158733-168889: the version of the production was changed, so the rare B triggers were written out to the dataset jrar09[6].

The data corresponding to these datasets were written out to tapes. The advantage of the tapes is that space is freely available, however, running analysis on data which is stored on tapes, can be slow. The alternative solution is to store the data on hard disks on file servers. It reduces considerably the time needed for analyses, however, the space tends to be limited. In order to be able to store the data necessary for the present analysis on hard disks, it has been "stripped", i.e. its size has been greatly reduced. In order to reduce data size, raw data banks which were not necessary for the present study were dropped and in the case of the jbmu08 dataset, events corresponding to other triggers than the rare B triggers, were dropped as well. The resulting data were stored on the `fcdfdata041` file server.

[5]Theoretically, the number at the end of the dataset describes the version. Hence, jbmu06 was processed with version 4.8.0 of the offline software, jbmu08 and jrar08 with version 4.8.4a etc. However, the processing pass 09 is a special one. Of the 2429 files 681 were processed with version 4.8.4a, 1047 with version 4.8.4g1, 701 with version 4.8.5, and 81 with version 4.8.4a but with no silicon alignment, so they were omitted.

[6]Actually, there are a couple of runs from the 153xxx and 155xxx range that were processed already for the jrar09 dataset, but there is no duplication between jrar08 and jrar09.

4.3 Preselection

The first step of the analysis is to convert the data into ntuples, a format which is appropriate for fast and efficient analysis. In order to perform the optimization on a reasonably sized data file, a first set of selection requirements was applied during the ntuple-making. Only events accepted by one of the rare B triggers are kept. Quality requirements are imposed on tracks in order to reduce uncertainties on derived parameters. The default tracking algorithm used for tracking is called "outside-in" tracking. It is seeded by tracks found in the COT and progressively searches for the silicon hits inward, hence its name "outside-in". The use of silicon improves the tracking in a dramatic fashion, the resolution of the J/ψ width is reduced from $22\,MeV$ to $16\,MeV$, while the resolution of the longitudinal impact parameter goes down from $0.797\,cm$ to $0.0144\,cm$ [60].

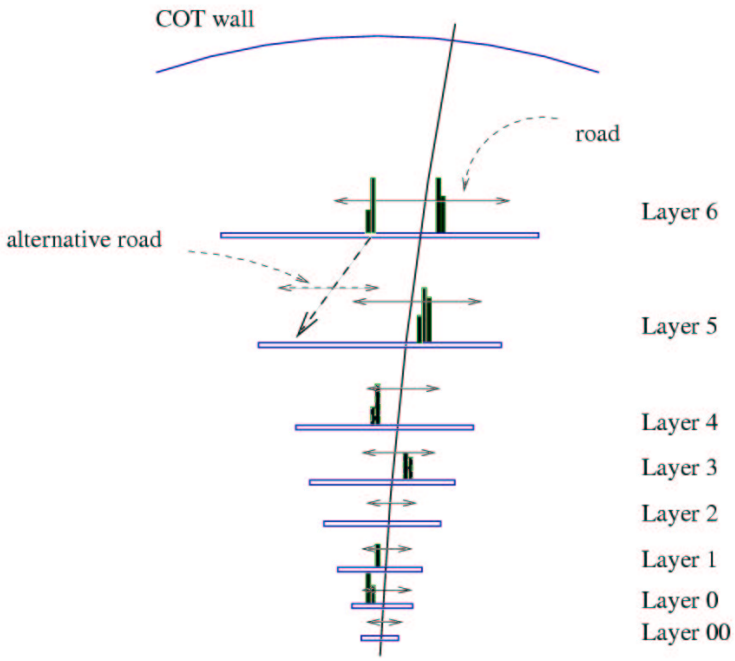

Figure 4.1: Extrapolating the COT track from the outside into the SVX.

The drift chamber is at larger radius than the silicon tracker, thus the relative track density is lower there than in the vertex detector. The isolation of the tracks is also higher which results in lower combinatorial background and faster track reconstruction. After being reconstructed in the COT the tracks are extrapolated into the silicon vertex detector. As the extrapolation proceeds, the track error matrix is adjusted to reflect the amount of scattering material encountered. At each layer of silicon a road size in $r\phi$ is established based on the error matrix of the track[7].

[7] At present it is set to 4σ.

$r\phi$ hits that are within the road are added to the track, and the track parameters and the error matrix are refit[8] with this new information (Figure 4.1). A new track candidate is generated for each hit on the road. In order to take account of potential hit inefficiencies a candidate without a hit in the given layer is included as well. Each of these new candidates are then ranked based on the number of hits found so far, and only the best two candidates are kept and extrapolated into the next layer where the process is repeated. At the end of this process the candidate that has hits in the largest number of silicon layers is chosen. If there are several such candidates, the best and second best candidate are chosen based on the χ^2 of the fit in the silicon and the number of hits in the wedge overlap region. Optionally, the whole algorithm is repeated by adding z hits via a progressive fit. However, as the z resolution of the COT is one order of magnitude worse than in $r\phi$, the stereo linking of COT to silicon is much more challenging and special care is required. For the algorithm to function properly an excellent alignment is required between the COT and the silicon detectors, and the COT covariance matrix must be scaled properly. For a more precise description on this and other tracking algorithms see [91], [92] and [93].

In the present analysis we require the tracks to be reconstructed in the COT with at least 20 axial hits and 10 stereo hits. There also must be at least 2 axial and 2 stereo superlayers with at least 4 hits each. The tracks are required to have their transverse momentum in excess of $0.4\,GeV$.

Only events accepted by one of the chosen dimuon triggers are kept. In the CDF offline software muons are a combination of a track and one or several stubs of the different muon systems. For the present study, the CMU muons selected are required to have the matching $\chi^2 < 9$, which is the value representing the quality of the track-stub match[9]. The minimum momentum requirement is $1.5\,GeV$, while $|\eta|$ must not exceed 1.0 (which is equivalent to ask for CMU, CMP, CMX muons). The difference in z between the position of the stub and the track extrapolation to the stub is required to be less than $10\,cm$ for CMU and CMX. The $r\Delta\phi$ cuts of the Level 3 are confirmed as well.

The B meson candidate is reconstructed during the preselection step, the fit parameters being saved, so that they can also be used in later stages. At this stage the cuts are aimed at cleaning up the sample, by requiring the transverse momentum of the K^{*0} to be greater than $2\,GeV$ and the reconstructed K^{*0} mass to be within $100\,MeV$ of the nominal mass.

In the process of refitting first two muons are found by the `RareBDimuonModule` and fitted to a common vertex. Then, in the `RareBKstarModule` two further tracks of opposite charge are associated with the muon pair. All measured charged tracks have to be considered as kaon tracks, as in the relevant momentum range, apart from muons, CDF lacks the ability to identify charged particles. The Time Of Flight system of CDF is not able to efficiently separate kaons from pions in the momentum range relevant to the present analysis. This results in a significant combinatorial

[8] Currently, there are two main progressive fitting methods in use at CDF, the Kalman fitter and the G3X fitter.

[9] More precisely, it is the χ^2 formed from the $r\Delta\phi$ on which the cut is preformed. There are several other χ^2 variables implemented. Unfortunately, at present only two of them are filled in by default, and only for CMU stubs.

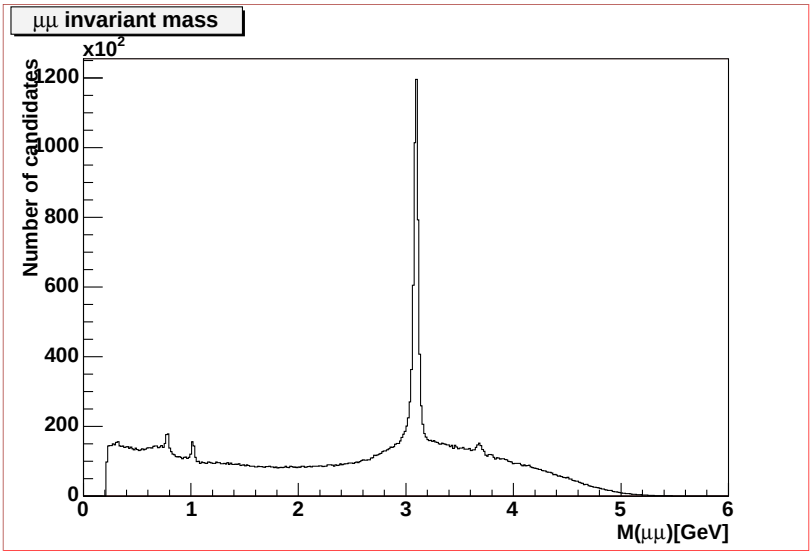

Figure 4.2: Invariant mass distribution of the dimuons after the preselection.

background.

As refitting tracks is a very time-consuming operation, it is only done on the four tracks that form a B candidate. A least-square kinematic fit of the candidate tracks is performed, the tracks being constrained to come from a common secondary vertex[10].

There is no mass constraint applied to the muon pair as in FCNC decays the dimuon mass is not fixed and at this stage no attempt is made to separate $B^0_d \to \mu^+\mu^- K^{*0}$ and $\mathrm{B^0_d} \to \mathrm{J/\psi K^{*0}}$ candidates, as the former ones will be used for normalization and different other studies. The summary of the applied cuts is listed in Table 4.6.

The dimuon invariant mass distribution after the preselection cuts is shown in Figure 4.2. There is a very pronounced J/ψ peak, and one can also clearly distinguish the $\psi(2S) \to \mu^+\mu^-$, $\phi \to K^+K^- \to \mu^+\mu^-$ and $\rho \to \pi^+\pi^- \to \mu^+\mu^-$ peaks.

4.4 Baseline selection

Runs, in order to be selected in the analysis, must satisfy certain conditions. The relevant detectors must be declared operational by both the online and offline monitoring. Online monitoring starts from basic checks, such as whether the given detector subsystem and all its components are turned on, and continues with the monitoring of the performance of each detector subsystem by looking at the monitoring programs attached to the DAQ system, which provide in real time plots of different physics quantities corresponding to data from various triggers. These real time checks are followed by more in-depth checks once the data is written to tapes, where additional information and the full analysis framework are used to show through various

[10] This is called a vertex-constrained fit.

	`RareBDimuonModule`	`RareBKstarModule`
Cuts on muons	opposite charge $p_T(\mu) > 1.5$ $\|\eta\| < 1.0$ $dz(CMU) < 10.0$ $\chi^2_{xposition} < 9.0$ $dz(CMX) < 10.0$ axial hits ≥ 20 stereo hits ≥ 10 axial SL ≥ 2 with hits ≥ 4 stereo SL ≥ 2 with hits ≥ 4 $dphi < 3.14$ $dx(CMU, CMP) < 30.0$ $dx(CMX) < 50.0$	
Cuts on tracks		$p_T(track) > 0.4$ axial hits ≥ 20 stereo hits ≥ 10 axial SL ≥ 2 with hits ≥ 4 stereo SL ≥ 2 with hits ≥ 4
Cuts on K^{*0}		$p_T(K^{*0}) > 2.0$ $0.796 < M(K^{*0}) < 0.996$ $0 < dphi(K\pi) < 180$ $dz(K\pi) < 10.0$

Table 4.6: Preselection cuts applied to the data sample. Following the CDF convention the various quantities are always expressed in GeV and cm unless otherwise stated.

Cuts on muons	$p_T(\mu) > 1.5$
Cuts on tracks	$p_T(track) > 0.5$ axial hits ≥ 20 stereo hits ≥ 16 Si hits ≥ 3 Si hits ≥ 4 for tracks with $p_T(track) < 1.5$
Cuts on K^{*0}	$0.792 < M(K^{*0}) < 0.992$ $p_T(K^{*0}) > 2.0$
Cuts on B^0	$p_T(B^0) > 6$ $l_{xy} < 1.0$ $c\tau < 0.5$ $\sigma_{l_{xy}} < 0.015$ $\chi^2_{fit} < 15.0$

Table 4.7: Baseline selection cuts applied to the data sample.

physics quantities, such as the yield of J/ψ-s etc, that the performance of the detector is satisfactory. For the present analysis the following bits are required to be set in the database: SVX_ONLINE, COT_ONLINE, CMU_ONLINE, CMP_ONLINE, L1T_ONLINE, L2T_ONLINE, L3T_ONLINE, CLC_ONLINE, OFFLINE_STATUS, COT_OFFLINE, CMU_OFFLINE, CMP_OFFLINE. Additionally, for CMX muons the CMX_ONLINE and CMX_OFFLINE bits are required to be set as well. As the location of the primary interaction vertex is essential in this study for measuring lifetimes, pointing angles and L_{xy}, runs for which the beam position measured by SVX is not available are discarded.

The preselection cuts are refined. We require 16 stereo hits in the COT instead of 10. Each track is required to have at least 3 hits in the SVX (for the moment ISL and L00 are not used), and 4 hits for kaon and pion tracks with $p_T < 1.5\,GeV$. For the tracking algorithm to produce a high track-finding efficiency together with a good resolution of track parameters, the cut on the transverse momentum of the tracks is raised to $0.5\,GeV$.

We require that the muons have $p_T > 1.5$ which is a clean-up cut as the trigger muons should satisfy this criteria. However, compared to the Run I, where the lower limit on the p_T was $2\,GeV$, it is a major change as it enables to increase the acceptance.

There are several additional cuts that are applied to the B meson. Some are clean-up cuts, the aim of which is to get rid of odd events, such as requiring the proper decay length to be shorter than $0.5\,cm$, the transverse decay length to be shorter than

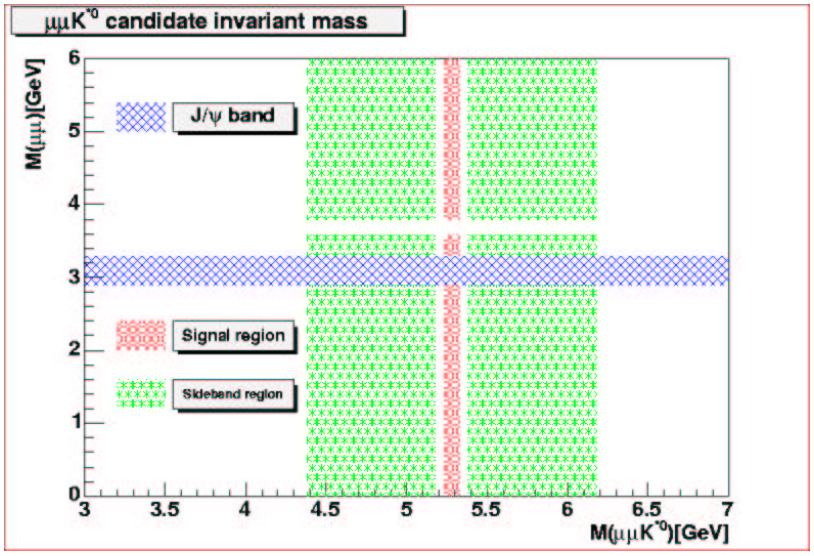

Figure 4.3: Different regions of the analysis.

$1.0\,cm$ and the uncertainty on it be inferior to a certain value ($\sigma_{l_{xy}} < 0.015\,cm$). There is an important cut on the confidence level of the fit, which eliminates candidates with tracks that are close spatially, but are not consistent with a common vertex ($\chi^2_{fit} < 15.0$). The transverse momentum of the B meson candidate is required to be larger than $6\,GeV$ as well.

Depending on the invariant mass of the dimuon pair we define two distinct regions:

- For the non-resonant $B^0_d \to \mu\mu K^{*0}$ candidates the invariant mass of the two muons is required to be in the interval of $0 - 6\,GeV/c^2$ excluding the regions corresponding to the resonant J/ψ ($\pm 200\,MeV/c^2$ around the PDG value of the J/ψ mass) and $\psi(2S)$ ($\pm 100\,MeV/c^2$ around the PDG value of the $\psi(2S)$ mass) decays.
- For the resonant $B^0_d \to J/\psi K^{*0}$ candidates, the invariant mass of the muon pair is required to be within $200\,MeV/c^2$ around the PDG value of the J/ψ mass (Figure 4.3).

After the refit of the four tracks that make up the B^0_d candidate a vertex-fit with no mass or pointing constraint is performed. The invariant mass distribution of the B candidates for the resonant and non-resonant regions after the baseline cuts are shown in Figure 4.4. The signal region is defined as a window of $50\,MeV$, i.e. approximately $2\,\sigma$ around the nominal B meson mass. As expected, no evidence of a peak in the signal region is seen for the non-resonant dimuon masses. By fitting the B peak for the $B^0_d \to J/\psi K^{*0}$ decay to the sum of a gaussian and a first order polynomial 475 ± 73 resonant decays are found in the signal region. The fitted width of the gaussian is $22\,MeV$, while the mean is $5.285\,GeV$. The non-resonant dimuon mass region of Figure 4.4 has 9500 entries in the signal region. Section 4.5 will describe

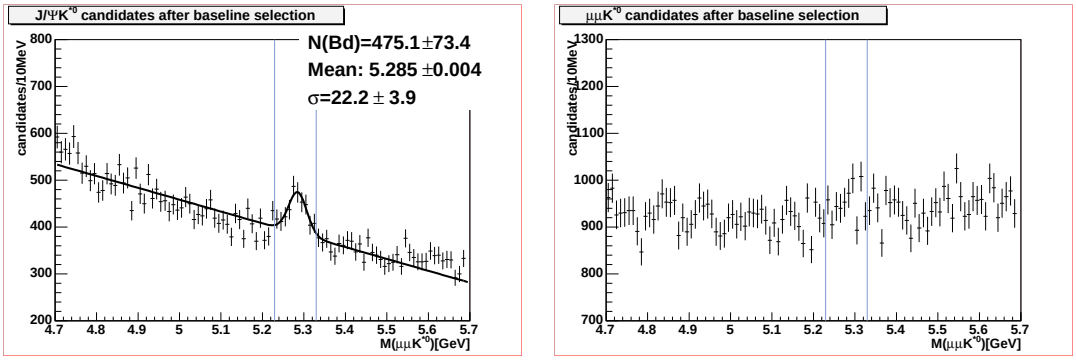

Figure 4.4: Invariant mass distribution of the B candidates after the baseline selection requirements for the resonant (left) and non-resonant (right) decays.

how a tighter selection is chosen after a careful optimization in order to measure the branching fraction or set an upper limit on it.

4.5 Optimization of the selection requirements

Three variables were chosen on which to perform the optimization of the cuts after the baseline selection: the isolation, the transverse decay length and the pointing angle. The aim is to reduce background, while retain a high efficiency for the sought signal. This is achieved by maximizing the figure of merit. The three quantities mentioned above will be described in greater detail in the first three parts of the present section. The optimization procedure based on the figure of merit will be described in Section 4.5.4, while the choice of the final cut values will be presented in Section 4.8.

4.5.1 The isolation

The basic idea of B meson isolation is that due to their hard fragmentation B mesons tend to carry a large fraction of the momentum of the particles in a local region around the B. As noted in [94], since the fragmentation process and the underlying event are independent of the decay mode of the B meson, the isolation of B mesons is general enough to be useful for many analyses. The definition of isolation used in the present analysis is that of [95]:

$$I = \frac{p_T^B}{p_T^B + \sum p_T} \tag{4.1}$$

where the sum is a scalar sum over all the tracks (except the descendents of the B) inside the cone defined by $\Delta R = 1$ (which was shown to be the most efficient cone size in [95]) around the momentum vector of the B candidate, where

$$\Delta R = \sqrt{(\Delta\eta)^2 + (\Delta\phi)^2} \tag{4.2}$$

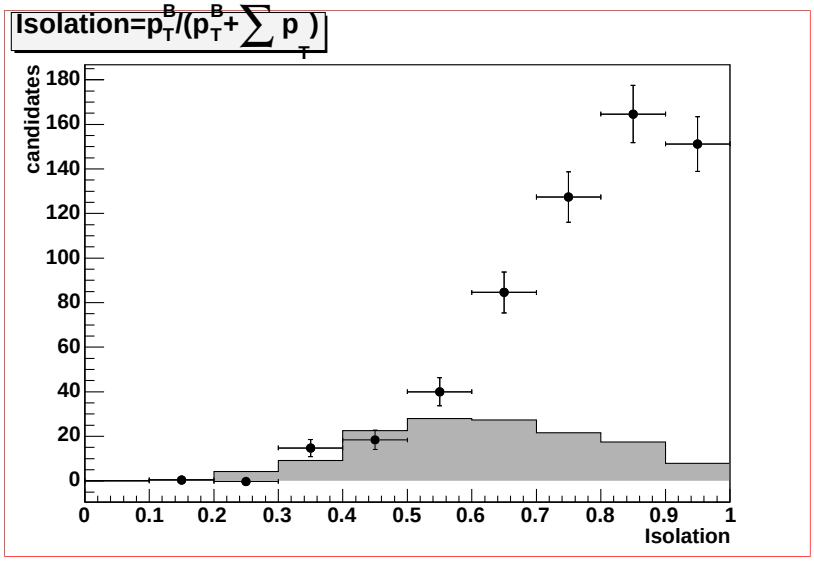

Figure 4.5: The points with error bars show background subtracted data for $B_d^0 \to J/\psi K^{*0}$ decays after baseline selection and $L_{xy} > 0.01$, $\Delta\Phi < 0.1$ cuts. The shaded histogram shows the background from the high $500\,MeV$ sideband of the data.

Figure 4.5 shows that isolation is a good discriminating variable. As it is very complicated to model the underlying event, the isolation for signal and background is shown for the $\mathrm{B}_d^0 \to J/\psi K^{*0}$ decay, where one can clearly separate signal and background. As noted above, the fragmentation process and the underlying event are independent of the decay mode, i.e. the above plot should qualitatively apply to $\mathrm{B}_d^0 \to \mu\mu K^{*0}$ decays as well.

4.5.2 The transverse decay length

As the lifetime of the B mesons is relatively long, it provides a strong rejection criteria against the mostly short-lived background. The transverse decay length L_{xy} is defined as

$$L_{xy} = \frac{\overrightarrow{l_{xy}} \cdot \overrightarrow{p_T^B}}{p_T^B} \tag{4.3}$$

where $\overrightarrow{l_{xy}}$ is the vector pointing from the primary interaction vertex to the secondary decay vertex, $\overrightarrow{p_T^B}$ is the transverse momentum vector of the B candidate, and p_T^B is the absolute value of the transverse momentum vector of the B candidate. Both these quantities are derived from the vertex fit performed in the `RareBKstarModule`. Figure 4.6 shows the transverse decay length distribution for $\mathrm{B}_d^0 \to \mu\mu K^{*0}$ Monte Carlo together with that for its sideband from data. Figure 4.7 shows the same comparison together with the sideband subtracted distribution from the $\mathrm{B}_d^0 \to J/\psi K^{*0}$ signal region.

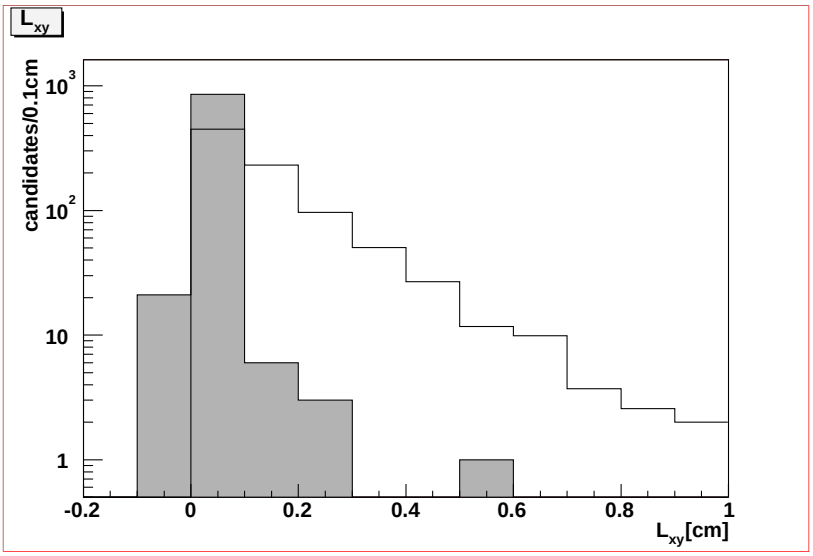

Figure 4.6: Transverse decay length distribution for the signal region from MC (histogram) and from the high sideband region of $500\,MeV$ from data (shaded histogram). The two histograms are normalized in order to have the same area.

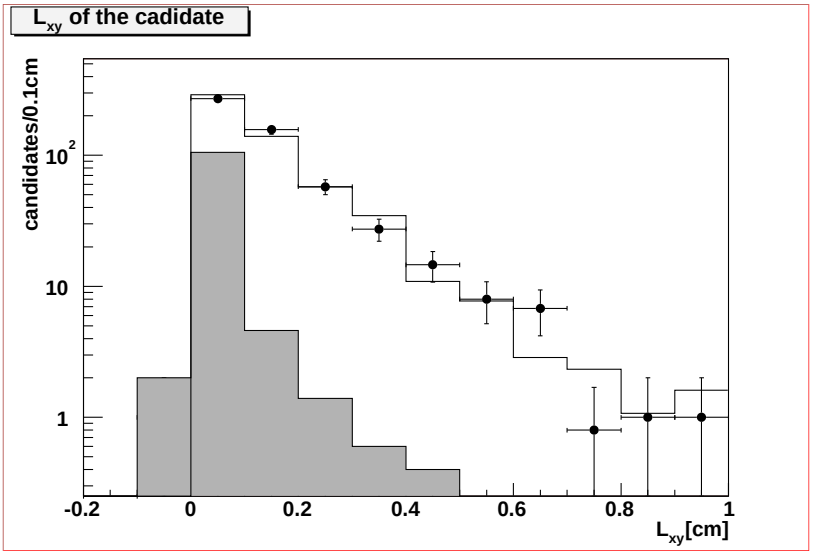

Figure 4.7: Comparison of background subtracted data (points with error bars) and MC (solid histogram) for $B^0_d \to J/\psi K^{*0}$ deacays after baseline selection and $iso > 0.65$, $L_{xy} > 0.01$, $\Delta\Phi < 0.1$ cuts. The shaded histogram shows the background from the $500\,MeV$ high sideband of the data.

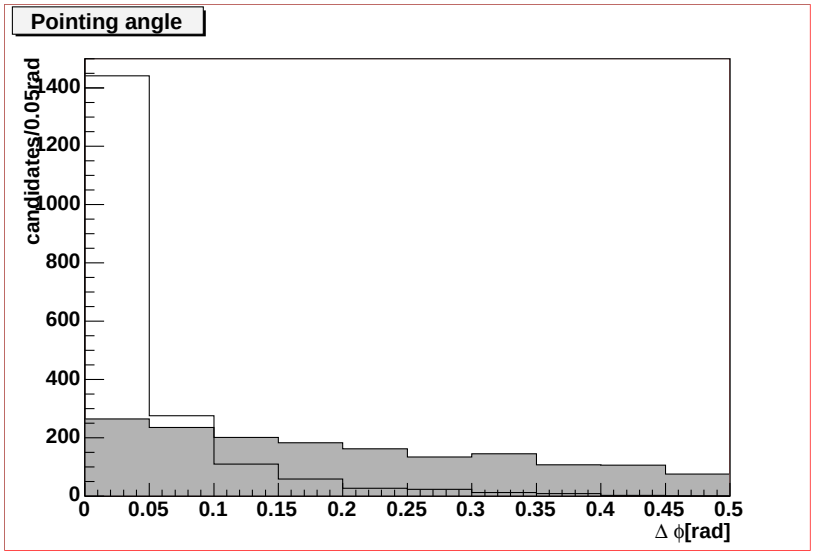

Figure 4.8: Pointing angle distribution for the signal region from $B_d^0 \to \mu\mu K^{*0}$ MC (histogram) and from the high sideband region of $500\,MeV$ from data (shaded histogram). The two histograms are normalized to have the same area.

Another quantity related to the transverse decay length is the proper decay length:

$$c\tau = L_{xy} \cdot \frac{m_{B^0}}{p_T^B} \tag{4.4}$$

Even though the variable used for optimization is the minimum transverse decay length, cuts on its maximal value and on the maximal value of the proper decay length are used as clean-up cuts as discussed earlier. The requirements on the transverse decay length, proper decay length, as well as that on the pointing angle, which will be discussed next, require precise measurement of the primary and secondary vertices. A beamline calculated by the SVX is required for each run used in this study so that the primary vertex is measured with sufficient precision, and all tracks are required to have at least three silicon hits in order to have a precise secondary vertex reconstruction.

4.5.3 The pointing angle

The final variable used as a strong rejection criteria in the optimization is the pointing angle, which is the angle between the momentum vector of the B meson ($\overrightarrow{p_T^B}$) and its flight path in the transverse ($r-\phi$) plane ($\overrightarrow{l_{xy}}$). It is clear that because the two muons, the kaon and the pion are coming from the B, the two vectors should point in the same direction, i.e. $\Delta\Phi$ should be close to 0 (Figure 4.8 for $B_d^0 \to \mu\mu K^{*0}$). Figure 4.9 shows both the comparison between MC signal and the signal obtained from the data, and the distribution from the sidebands of the data for the $B_d^0 \to J/\psi K^{*0}$ decay.

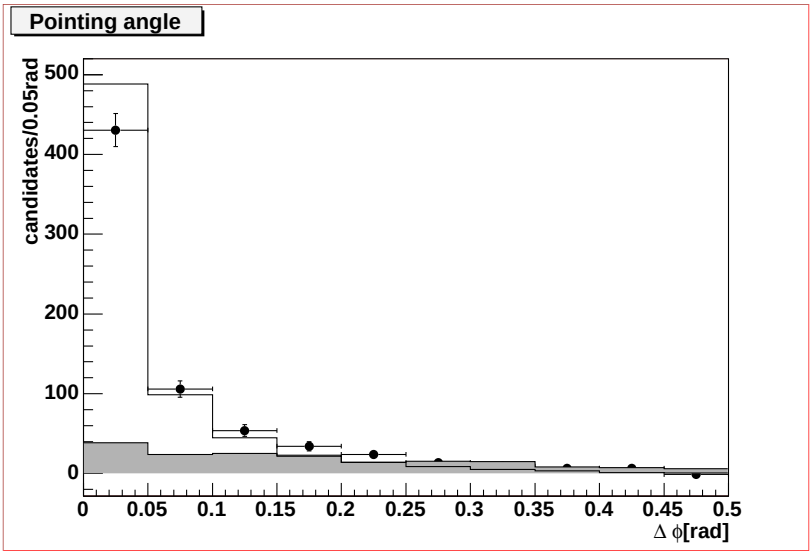

Figure 4.9: Comparison of background subtracted data (points with error bars) and MC (solid histogram) for $B^0_d \to J/\psi K^{*0}$ decays after baseline selection and $iso > 0.65$, $L_{xy} > 0.01$, $\Delta\Phi < 0.1$ cuts. The shaded histogram shows the background from the high $500\,MeV$ sideband of the data.

4.5.4 The optimization procedure

Our procedure for the cut optimization is to evaluate the figures of merit

$$fom1 = \frac{S^2}{B} = \frac{S^2(B^0_d \to \mu\mu K^{*0})}{B(B^0_d \to \mu\mu K^{*0})} \tag{4.5}$$

$$fom2 = \frac{S^2}{S+B} = \frac{S^2(B^0_d \to \mu\mu K^{*0})}{S(B^0_d \to \mu\mu K^{*0}) + B(B^0_d \to \mu\mu K^{*0})} \tag{4.6}$$

$$fom3 = \frac{S^2}{(\frac{a}{2} + \sqrt{B})^2} = \frac{S^2(B^0_d \to \mu\mu K^{*0})}{(\frac{a}{2} + \sqrt{B(B^0_d \to \mu\mu K^{*0})})^2} \tag{4.7}$$

where Eq. 4.5 and Eq. 4.6 are expressions that are commonly used for optimization purposes and Eq. 4.7 is a new formula proposed in [96], where a is the number of standard deviations corresponding to one-sided Gaussian tests for the sought significance. With the present integrated luminosity only a couple $B^0_d \to \mu\mu K^{*0}$ events are expected, so for the remainder of the analysis a is set to 1. As we are not expecting a large enough signal for $B^0_d \to \mu\mu K^{*0}$ to be able to optimize on, we will extract the signal strength for the optimization from the signal of the reference decay $B^0_d \to J/\psi K^{*0}$. As

$$S(B^0_d \to \mu\mu K^{*0}) = \sigma \cdot \mathcal{L} \cdot \mathcal{B}(B^0_d \to \mu\mu K^{*0}) \cdot \epsilon_{baseline}(B^0_d \to \mu\mu K^{*0}) \cdot \epsilon_{iso,L_{xy},\Delta\Phi} \tag{4.8}$$

and

$$S(B_d^0 \to J/\psi K^{*0}) = \sigma \cdot \mathcal{L} \cdot \mathcal{B}(B_d^0 \to J/\psi K^{*0}) \cdot \epsilon_{baseline}(B_d^0 \to J/\psi K^{*0}) \cdot \epsilon_{iso,L_{xy},\Delta\Phi} \quad (4.9)$$

where the efficiencies of the isolation, L_{xy} and pointing cuts can be considered the same for the two decays. Dividing Eq. 4.8 by Eq.4.9 gives

$$S(B_d^0 \to \mu\mu K^{*0}) = S(B_d^0 \to J/\psi K^{*0}) \cdot \frac{\mathcal{B}(B_d^0 \to \mu\mu K^{*0})}{\mathcal{B}(B_d^0 \to J/\psi K^{*0})} \cdot \frac{\epsilon_{baseline}(B_d^0 \to \mu\mu K^{*0})}{\epsilon_{baseline}(B_d^0 \to J/\psi K^{*0})} \cdot \epsilon_{rel} \quad (4.10)$$

Let us define

$$\epsilon = \frac{\mathcal{B}(B_d^0 \to \mu\mu K^{*0})}{\mathcal{B}(B_d^0 \to J/\psi K^{*0})} \cdot \frac{\epsilon_{baseline}(B_d^0 \to \mu\mu K^{*0})}{\epsilon_{baseline}(B_d^0 \to J/\psi K^{*0})} \cdot \epsilon_{rel} \quad (4.11)$$

where ϵ_{rel} denotes all the other relative efficiencies discussed in Section 4.6.1 and the branching ratios are:

- $\mathcal{B}(B_d^0 \to \mu\mu K^{*0}) = 11.7^{+3.6}_{-3.1} \pm 0.8 \pm 0.6 \times 10^{-7}$ from the results presented at the Lepton-Photon 2003 conference by the Belle experiment [30], which is in excellent agreement with the $1.19 \pm 0.39 \times 10^{-6}$ recently published by Ali. et al. [18].
- $\mathcal{B}(B_d^0 \to J/\psi K^{*0}) = 1.31 \pm 0.07 \times 10^{-3}$ from [3][11]
- $\mathcal{B}(J/\psi \to \mu^+\mu^-) = 5.88 \pm 0.10\,\%$ from [3]

hence

$$\frac{\mathcal{B}(B_d^0 \to \mu\mu K^{*0})}{\mathcal{B}(B_d^0 \to J/\psi K^{*0})} = 1.52 \pm 0.49 \times 10^{-2} \quad (4.12)$$

so equations 4.5, 4.6 and 4.7 can be rewritten

$$fom1 = \frac{S^2(B_d^0 \to J/\psi K^{*0}) \cdot \epsilon^2}{B(B_d^0 \to \mu\mu K^{*0})} \quad (4.13)$$

$$fom2 = \frac{S^2(B_d^0 \to J/\psi K^{*0}) \cdot \epsilon^2}{S(B_d^0 \to J/\psi K^{*0}) \cdot \epsilon + B(B_d^0 \to \mu\mu K^{*0})} \quad (4.14)$$

$$fom3 = \frac{S^2(B_d^0 \to J/\psi K^{*0}) \cdot \epsilon^2}{(\frac{1}{2} + \sqrt{B(B_d^0 \to \mu\mu K^{*0})})^2} \quad (4.15)$$

So, in order to calculate the two types of figure of merit, two quantities are needed to be measured from the data for each set of cuts:

- $B(B_d^0 \to \mu\mu K^{*0})$: the background expected in the signal region.
- $S(B_d^0 \to J/\psi K^{*0})$: the number of $B_d^0 \to J/\psi K^{*0}$ decays observed.

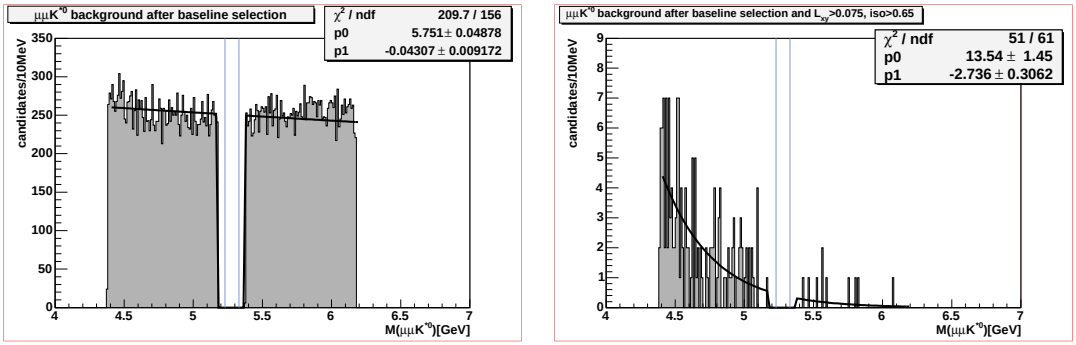

Figure 4.10: Examples of background fits with cuts that result in high statistics (left, baseline cuts), and with cuts that result in low statistics (right, baseline cuts and $L_{xy} > 0.075$, $isolation > 0.65$).

In order to estimate the background in the signal window, the sidebands are used (see Figure 4.3). The background in the $[M_{B^0_d} - 900\,MeV, M_{B^0_d} - 100\,MeV]$ low sideband region and the $[M_{B^0_d} + 100\,MeV, M_{B^0_d} + 900\,MeV]$ high sideband region is approximated by an exponential. This approximation gives good results whether it is performed after the baseline selection, where the background is almost linear, or after additional selection cuts, where the background becomes more exponential (Figure 4.10). Linear fits over various regions were also tested and they gave similar results to that of the exponential fit, except for the region where the statistics is very low. The fit procedure takes into account only the bins of the region defined above. The expected background in the signal region is calculated as the integral of the fitted exponential in the signal region $[M_{B^0_d} - 50\,MeV, M_{B^0_d} + 50\,MeV]$. This type of background estimation, where all cuts are applied in the sideband regions and the surviving number of events is scaled to get a prediction in the signal region suffer from a serious problem. The problem is that very few events survive all the cuts, which makes the optimization difficult. One way to improve the background estimate is to factorize the expected rejection for each cut separately[12]. For this method to be accurate the correlations among the optimization variables must be small. The linear correlation coefficient between each of the two variables is:

$$\rho_{xy} = \frac{\frac{1}{n}\sum_{i=1}^{n} x_i y_i - \left(\frac{1}{n}\sum_{i=1}^{n} x_i\right)\cdot\left(\frac{1}{n}\sum_{i=1}^{n} y_i\right)}{\sigma_x \cdot \sigma_y} \tag{4.16}$$

where n is the total number of events, σ_x is the standard deviation of the variable x:

$$\sigma_x = \sqrt{\frac{1}{n}\left\{\sum_{i=1}^{n} x_i^2 - \frac{1}{n}\left(\sum_{i=1}^{n} x_i\right)^2\right\}} \tag{4.17}$$

[11] In the equations presented throughout the present thesis $\mathcal{B}(B^0_d \to J/\psi K^{*0})$ implicitly means $\mathcal{B}(B^0_d \to J/\psi K^{*0}) \cdot \mathcal{B}(J/\psi \to \mu^+\mu^-)$, so that the final state is identical to $\mathcal{B}(B^0_d \to \mu\mu K^{*0})$. Here, exceptionally, the decay of the J/ψ into two muons is not included implicitly.

[12] This is the method used in [97] [98].

	Isolation	L_{xy}	Pointing angle
Isolation	1	0.025	-0.017
L_{xy}		1	-0.367
Pointing angle			1

Table 4.8: The linear correlation coefficients for the discriminating variables in the sideband region for the $B_d^0 \to \mu\mu K^{*0}$ decay.

and similarly for y.

The resulting values for the sideband region are given in Table 4.8. Only the transverse decay length and the pointing angle are significantly correlated, whether one takes both the low and high mass sideband, or only the high mass sideband (Figure 4.11). The y error bars on Figure 4.11 represent the RMS of the mean value, $< y >$, in each bin of x. The fact that between the other variables there is very little correlation, or in the case of the high mass sideband no correlation at all, implies that the rejection factors can be estimated using

$$R_{optvar} = R(L_{xy}, \Delta\Phi) \cdot R_{Isolation} \tag{4.18}$$

Cut value	$R_{isolation}$
$Iso > 0.45$	1.5 ± 0.0134
$Iso > 0.50$	1.7631 ± 0.03003
$Iso > 0.55$	2.1125 ± 0.05775
$Iso > 0.60$	2.6794 ± 0.08769
$Iso > 0.65$	3.5678 ± 0.1158
$Iso > 0.70$	4.8837 ± 0.2134
$Iso > 0.75$	7.1077 ± 0.3951
$Iso > 0.80$	10.8497 ± 0.6707
$Iso > 0.85$	17.6895 ± 1.6496

Table 4.9: The rejection of isolation cuts from events passing the baseline cuts and $\Delta\Phi < 0.5$.

It implies that the optimization of the isolation cut can be performed on a sample with very loose L_{xy} and $\Delta\Phi$ cuts, thus reducing the associated uncertainity. Table 4.9 summarizes the results for the rejection of the different cuts on isolation for events passing the baseline cuts and having $\Delta\Phi < 0.5$. The error is the systematic error obtained by looking at rejections for different L_{xy} cuts (no L_{xy} cut, $L_{xy} > 150\,\mu m$ and $L_{xy} > 300\,\mu m$). The statistical errors obtained from the background fit through error propagation are an order of magnitude smaller than the systematic ones. Using equation 4.18 once more leads to Figure 4.12 which shows the rejection factors $R(L_{xy}, \Delta\Phi)$ of the different $(L_{xy}, \Delta\Phi)$ cut combinations in the case of events passing the baseline cuts. The advantage of this approach is that, although it should give the

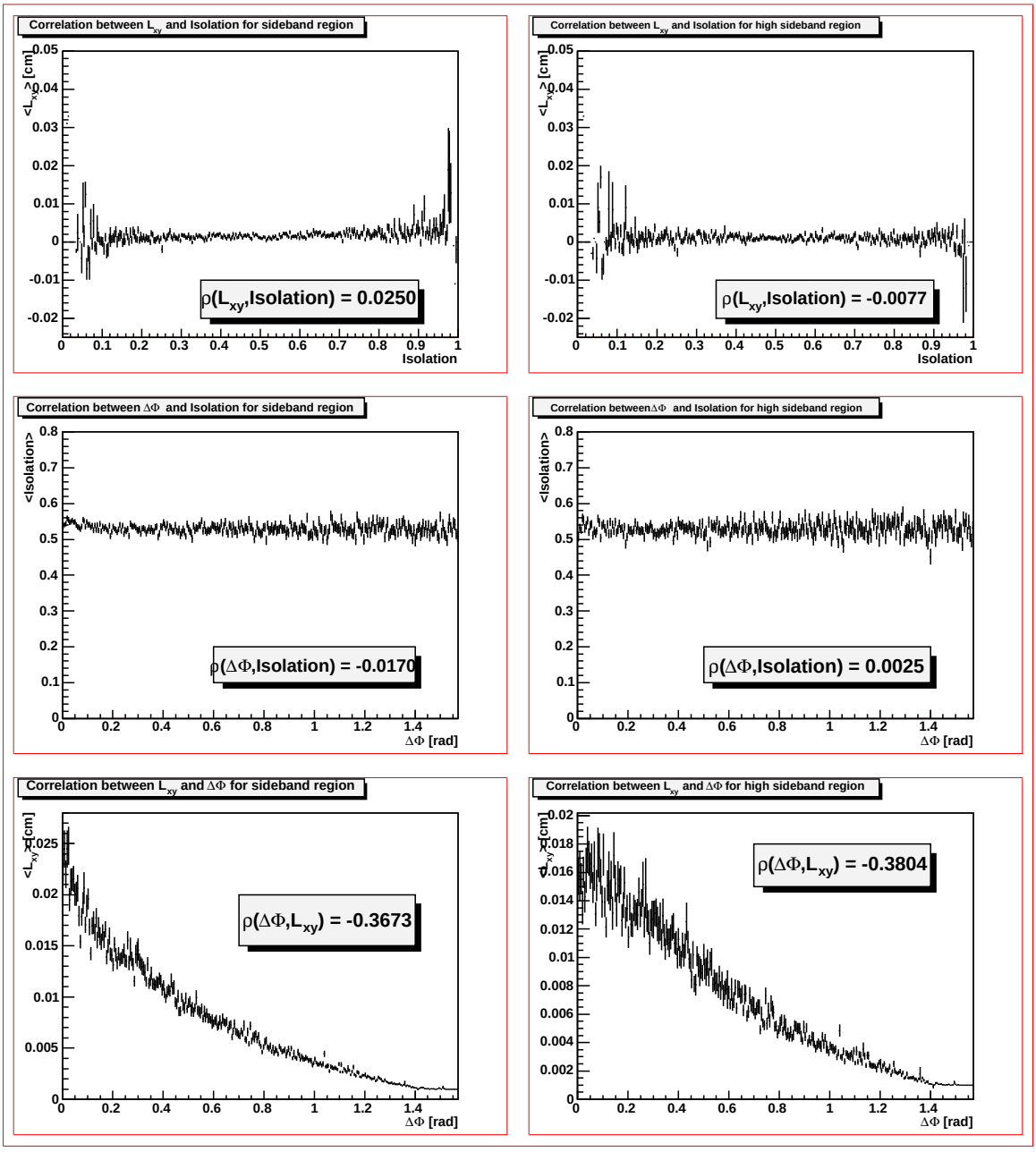

Figure 4.11: Correlations between the three discriminating variables for events satisfying the baseline cuts in both the low and high mass sideband (left), and only the high mass sideband (right).

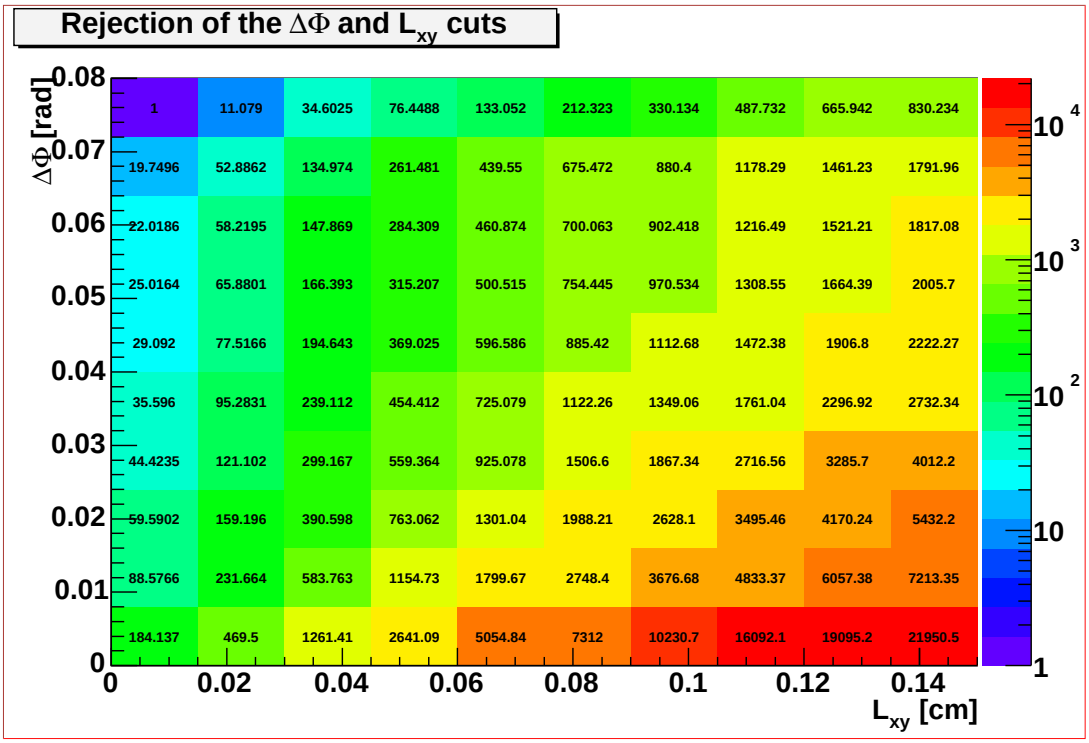

Figure 4.12: Rejection of the $\Delta\Phi$ and L_{xy} cuts for events passing baseline requirements (but no cut on isolation).

same rejection as with a supplementary isolation cut, it reduces the error (as omitting the isolation cut increases statistics).

On Figure 4.12 the first column represents the rejection factors when there is no L_{xy} cut applied, while the other nine columns represent cuts from $0.015\,cm$ up to $0.135\,cm$ in steps of $0.015\,cm$; the uppermost row represents rejection factors when there is no $\Delta\Phi$ cut applied, while the other nine rows represent upper cuts on $\Delta\Phi$ from $0.072\,rad$ down to $0.008\,rad$ in steps of $0.008\,rad$. The systematic error was obtained from the comparison with the linear fit and was found to be $\pm(5-15)\%$, so that we can assign a $\pm 15\%$ error to the estimated background obtained from:

$$B(B_d^0 \to \mu\mu K^{*0}) = B_0(B_d^0 \to \mu\mu K^{*0}) * R_{optvar}^{-1} \tag{4.19}$$

where $B_0(B_d^0 \to \mu\mu K^{*0})$ is the background without any of the optimization cuts.

In order to calculate the number of the $B_d^0 \to J/\psi K^{*0}$ decays exactly the same baseline cuts as for $\mathrm{B_d^0} \to \mu^+\mu^-\mathrm{K^{*0}}$ were applied and the dimuon invariant mass was required to be within $200\,MeV$ of the J/ψ mass given by the PDG. In order to obtain the number of B mesons, the invariant mass distribution of the B meson candidates was fitted using a Gaussian combined with a first order polynomial in the range of $[5.0\,GeV, 5.5\,GeV]$ (Figure 4.13). The number of signal events was simply the integral of the Gaussian in a $\pm 50\,MeV$ window around the B meson mass.

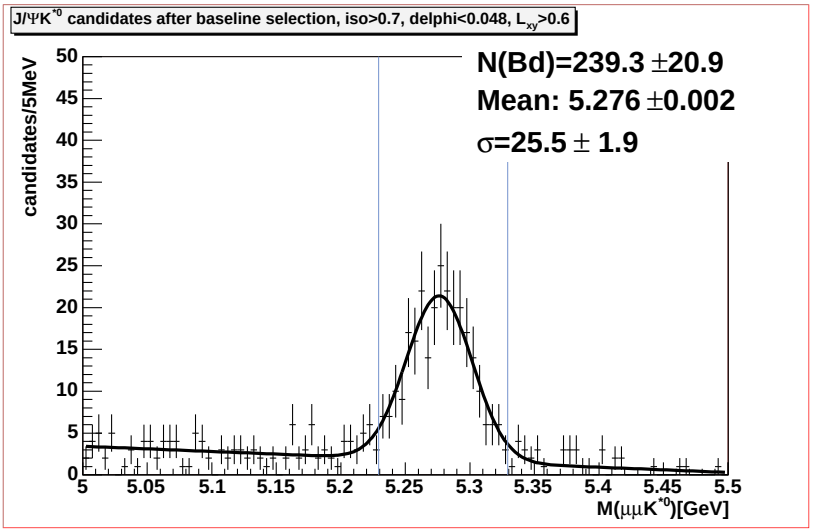

Figure 4.13: Example of fitting the B peak of $B^0_d \to J/\psi K^{*0}$ decay (baseline cuts and $\Delta\Phi < 0.048$, $isolation > 0.7$, $L_{xy} > 0.6$).

	Isolation	L_{xy}	Pointing angle
Isolation	1	0.266	-0.204
L_{xy}		1	-0.434
Pointing angle			1

Table 4.10: The linear correlation coefficients for the discriminating variables in the signal region for the $B^0_d \to J/\psi K^{*0}$ decay.

As Figure 4.14 and Table 4.10 show, the optimization variables in the signal region for the $B^0_d \to J/\psi K^{*0}$ decays are correlated, as one would expect from variables meant to cut on background but preserve the signal. This implies that the number of $B^0_d \to J/\psi K^{*0}$ decays must be calculated by varying the three optimization variables simultaneously. A typical plot for the number of $B^0_d \to J/\psi K^{*0}$ events found is shown on Figure 4.15 (see Appendix A for the plots displaying the number of $B^0_d \to J/\psi K^{*0}$ signal events for the other isolation cuts). The error on the number of the $B^0_d \to J/\psi K^{*0}$ events is typically 10%.

The final step consists of combining the results of Table 4.9, Figure 4.12 with Figures A.1 through A.7 of Appendix A and insert them into Equations 4.13, 4.14 and 4.15. However, before doing that one needs to extract from Monte Carlo simulations the ratio:

$$\frac{\epsilon_{baseline}(B^0_d \to \mu\mu K^{*0})}{\epsilon_{baseline}(B^0_d \to J/\psi K^{*0})} \tag{4.20}$$

and ϵ_{rel} which will be described in the next section.

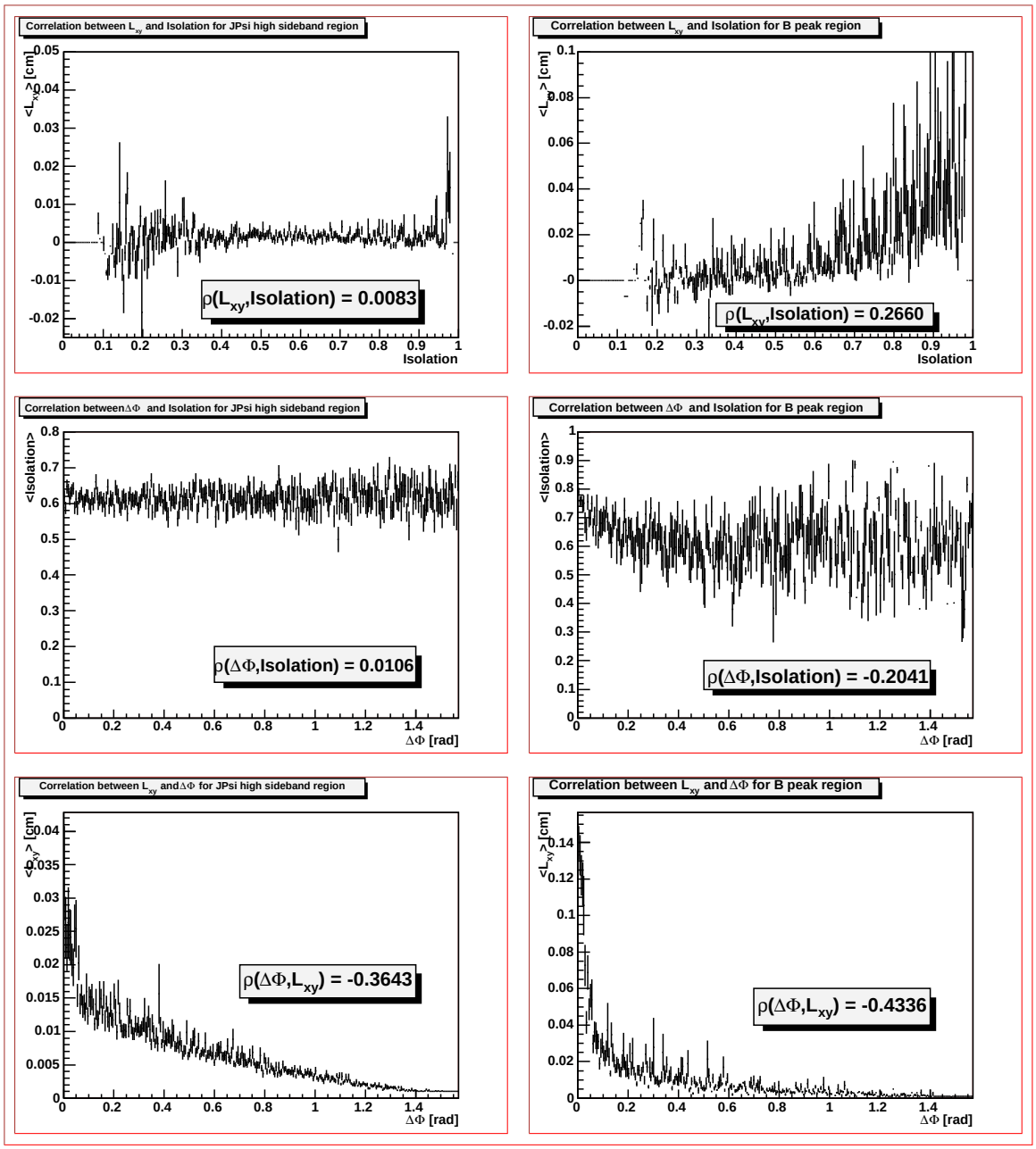

Figure 4.14: Correlations between the three discriminating variables for events satisfying the baseline cuts for the $B_d^0 \to J/\psi K^{*0}$ decay. On the left side are shown the events in the high sideband region, and on the right the events from the B peak region.

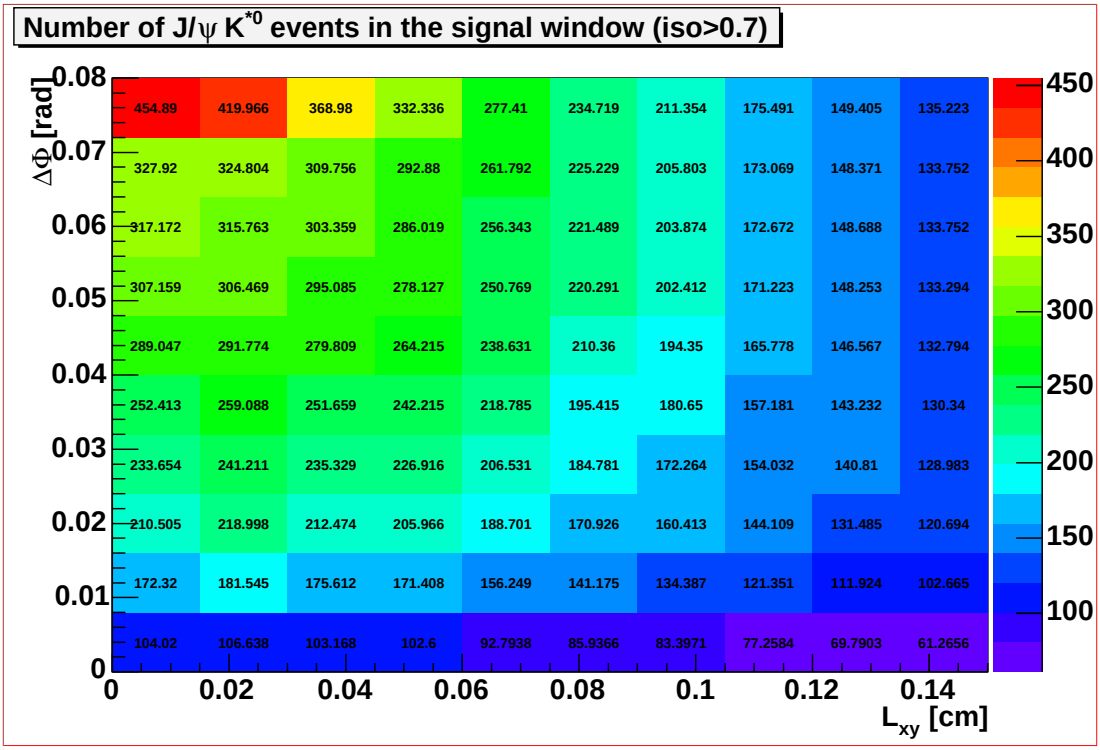

Figure 4.15: Example plot for number of $B^0_d \to J/\psi K^{*0}$ events for $Iso > 0.7$ and different values of L_{xy} and $\Delta\Phi$ cuts (the first column represents events with no L_{xy} cut, while the upper row represents events with no $\Delta\Phi$ cut).

4.6 Acceptance and efficiencies

It is very convenient to analyze the $B^0_d \to \mu\mu K^{*0}$ decay together with the $B^0_d \to J/\psi K^{*0}$ decay. As the two final states contain the same particles (where we take the events where the J/ψ is decaying into two muons) the topologies are very similar, so the B production cross section and several common reconstruction and selection efficiencies will cancel. The same can be said of the integrated luminosity (on the condition, of course, of using the same sample for both).

There will be a difference due to theoretical factors. We are looking for a rare decay which does not proceed through resonant states (i.e. J/ψ or ψ'). In order to do that the mass range is divided into resonant and non-resonant regions. Unfortunately, decays from resonant states will contribute to the signal observed in the non-resonant mass regions, i.e. experimentally we can only determine the decay rate into final states with non-resonant dimuon masses. Even though this effect is small, it must be accounted for. If we use the terms resonant and non-resonant to refer to different dimuon mass regions while the rare and resonance induced amplitudes will be called short-distance (SD) and long-distance (LD) respectively, we can write for the $B^0_d \to \mu\mu K^{*0}$ decay:

$$\mathcal{B}(SD+LD,nonres) = \underbrace{\frac{\mathcal{B}(SD+LD,nonres)}{\mathcal{B}(SD,nonres)}}_{\epsilon_{SD}} \cdot \underbrace{\frac{\mathcal{B}(SD,nonres)}{\mathcal{B}(SD,total)}}_{\epsilon_{nonres}} \cdot \mathcal{B}(SD,total)) \tag{4.21}$$

So the quantity $\mathcal{B}(B_d^0 \to \mu\mu K^{*0})$ of Equation 4.10 is in reality $\mathcal{B}(SD,total)$, and in order to estimate the number of observed events it must be multiplied by

$$\epsilon_{rel} = \epsilon_{SD} \cdot \epsilon_{nonres} \tag{4.22}$$

to obtain $\mathcal{B}(SD+LD,nonres)$, where $\epsilon_{SD} = 1.055 \pm 0.023$ and $\epsilon_{nonres} = 0.792 \pm 0.019$ [87]. The luminosity and reconstruction efficiency cancel out for the two decays. The acceptance and the relative selection efficiencies are obtained from Monte Carlo simulations described in the next subsection.

4.6.1 Monte Carlo Calculations

In order to generate $\mathrm{B}_d^0 \to \mu\mu K^{*0}$ events, the following chain of modules was used:

- `Bgenerator` was used to generate the B mesons. They were generated with $p_T > 5\,GeV$ and with $|\eta| < 2.0$. Going to lower p_T would have increased the generation time and data size considerably while adding negligible amount of events, while the cut on η is motivated by the CMU, CMP, CMX geometry.
- The generated B mesons were then decayed using `EvtGen`, which forced all of them to decay via the $\mathrm{B}_d^0 \to \mu\mu K^{*0}$ channel.
- The resulting events were passed through full detector simulation and standard reconstruction.
- In order to save disk space, the resulting data were filtered and only events which had two `CdfMuon`s with some very loose cuts[13] were kept.

The same procedure was applied in order to generate the $\mathrm{B}_d^0 \to J/\psi K^{*0}$ decay, where the J/ψ further decays into two muons, giving exactly the same final state as $\mathrm{B}_d^0 \to \mu\mu K^{*0}$. The resulting Monte Carlo files are analyzed the same way as the data, applying the same selection requirements[14]. The MC description of the resonant decays agrees reasonably well with the data (Figures 4.16 and 4.17). The data is represented by the points with error bars and is shown background subtracted, where the background is taken from the $[M(B) + 100\,MeV, M(B) + 600\,MeV]$ sideband of the data and scaled by the relative size of the mass window. The background itself is represented by the shaded histogram. The Monte Carlo sample has approximately

[13] Two muons were required with $p_T > 1.35\,GeV$, with $dx < 40\,cm$ for CMU and $dx < 60\,cm$ for CMX.

[14] In reality, there are some minor differences. For example, the Monte Carlo events are generated using ideal beam line, which is not the case of real data, where the beam position must be corrected on a run-by-run basis. The Monte Carlo also assumes that the detector subsystems are functioning correctly. However, the reconstruction procedure, the algorithms used are exactly the same for Monte Carlo as for the data

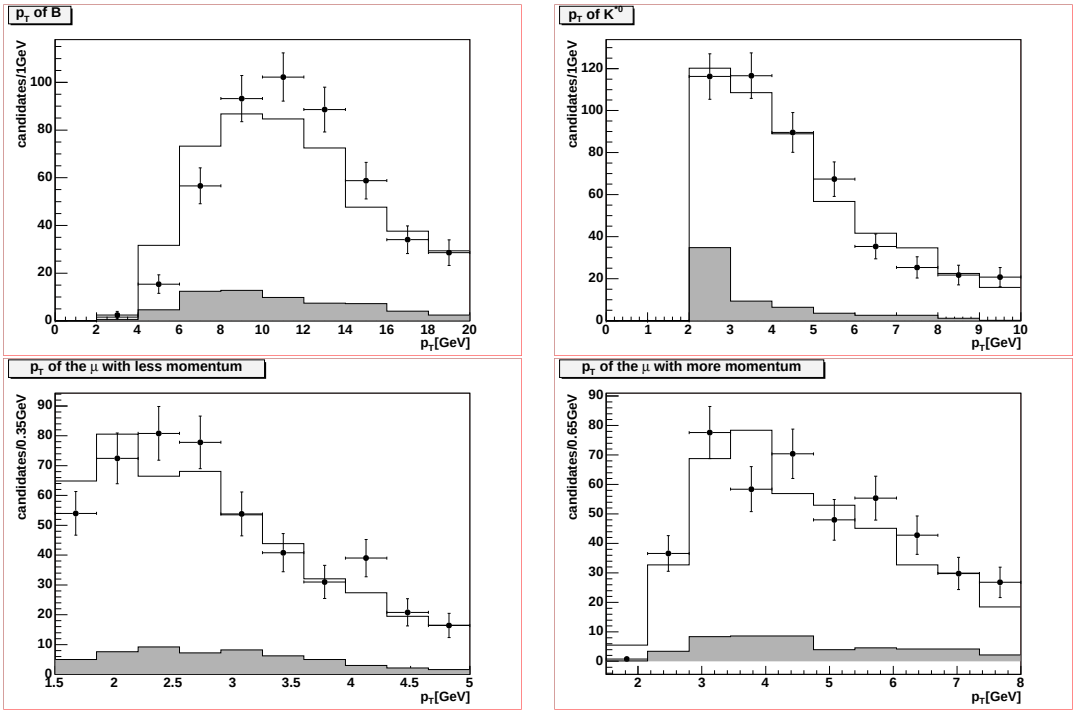

Figure 4.16: Comparison of background subtracted data (points with error bars) and MC (solid histogram) for $B^0_d \to J/\psi K^{*0}$ deacays after baseline selection and $iso > 0.65$, $L_{xy} > 0.01$, $\Delta\Phi < 0.1$ cuts. The shaded histogram shows the background from the $500\,MeV$ high sideband of the data.

4 times the statistics of the data. It is scaled in order to yield the same amount of events as in the background subtracted data separately for each plot. For each plot, the cut on the given quantity has been removed while all other baseline cuts have been applied[15]. In addition to the baseline cuts, $Isolation > 0.65$, $L_{xy} > 0.01$, $\Delta\Phi < 0.1$ cuts have been applied as well.

After checking the quality of the Monte Carlo simulation on the $B^0_d \to J/\psi K^{*0}$ decay, the relative efficiencies of the selection requirements were calculated. The relative efficiency of the selection requirements was obtained by comparing the $B^0_d \to \mu\mu K^{*0}$ MC sample with the $B^0_d \to J/\psi K^{*0}$ MC sample. There are various cuts, for which the accuracy of the Monte Carlo cannot be trusted, like the error on the L_{xy}, the χ^2 of the fit, or the cuts concerning the number of the silicon or COT hits. Fortunately, these cuts should be very similar for both decays and their relative efficiency is close to 1. The acceptance was also incorporated into the baseline selection efficiencies. The efficiencies of the various cuts are summarized in Table 4.11 and yield

$$\frac{\epsilon_{baseline}(B^0_d \to \mu\mu K^{*0})}{\epsilon_{baseline}(B^0_d \to J/\psi K^{*0})} = 0.85543 \pm 0.0113398 \tag{4.23}$$

[15]Obviously some preselection cuts have a clear effect, like $p_T(K^{*0}) > 2\,GeV$.

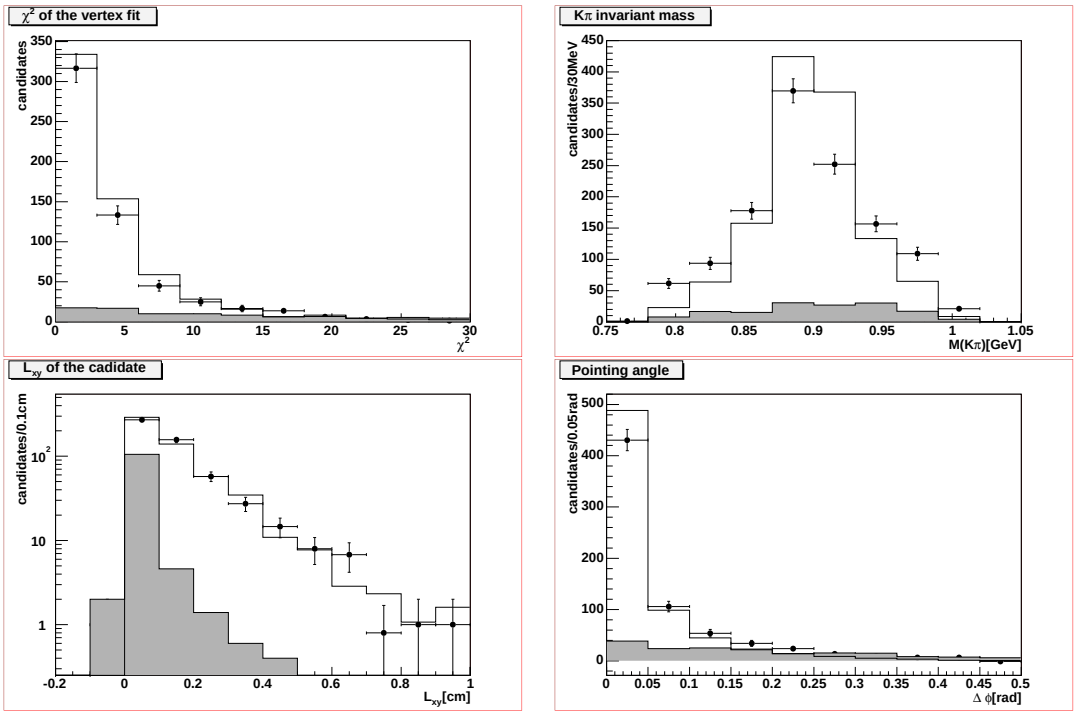

Figure 4.17: Comparison of background subtracted data (points with error bars) and MC (solid histogram) for $B_d^0 \to J/\psi K^{*0}$ deacays after baseline selection and $iso > 0.65$, $L_{xy} > 0.01$, $\Delta\Phi < 0.1$ cuts. The shaded histogram shows the background from the $500\,MeV$ high sideband of the data.

	$B_d^0 \to \mu\mu K^{*0}$ MC 2100000 events	$B_d^0 \to J/\psi K^{*0}$ MC 675000 events	Relative efficiency $B_d^0 \to \mu\mu K^{*0}$ / $B_d^0 \to J/\psi K^{*0}$
Acceptance and preselection	0.01207±7.53e-05	0.01427±0.00014	0.8453±0.01005
p_T of the muons $> 1.5\,GeV$	0.9998±8.82e-05	0.9997±0.00018	1.00011±0.0002
z_0 of the muons $< 50\,cm$	0.9282±0.00162	0.9296±0.0026	0.9985±0.0033
p_T of the tracks $> 0.5\,GeV$	0.9641±0.00121	0.9648±0.00195	0.9993±0.00238
p_T of the $K^{*0} > 2.0\,GeV$	0.9972±0.00035	0.9985±0.00042	0.9987±0.00055
K^{*0} mass within $\pm 100\,MeV$	0.9742±0.00105	0.9728±0.00175	1.00145±0.0021
p_T of the $B_d^0 > 6\,GeV$	0.9373±0.00163	0.9244±0.00288	1.0139±0.0036
All cuts	0.00983±6.74e-05	0.01149±0.00013	0.8554±0.0113

Table 4.11: Selection efficiencies for the $B_d^0 \to \mu\mu K^{*0}$ and $B_d^0 \to J/\psi K^{*0}$ decays.

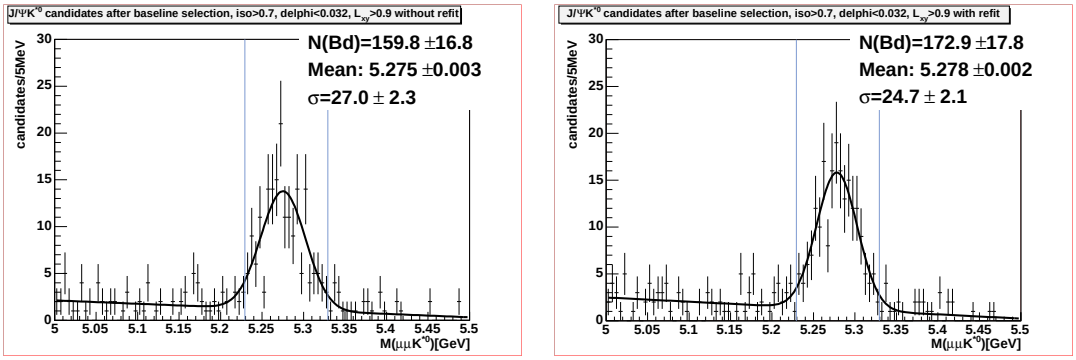

Figure 4.18: Invariant mass distribution of the B candidates of the $B^0_d \to J/\psi K^{*0}$ decay without refitting the tracks (left) and applying the refit procedure (right).

The errors are obtained by propagating the initial statistical errors ($\sqrt{n}$) through the calculations[16]. Inserting this result, the result of Eq. 4.12 and Eq. 4.22 into Eq. 4.11 gives

$$\epsilon = 0.01086 \pm 0.00354 \tag{4.24}$$

4.7 Energy loss, B field corrections and track refitting

The track parameters of particles must be corrected for the energy loss when passing through the detector material, as mass fits would result in lower values than the true value otherwise. As the relative effect becomes smaller as the momentum of the particle increases, the variation of the measured J/ψ mass for different J/ψ p_T-s turns out to be a very precise indicator of whether all material has been included properly. The relevant detector material is dominated by the silicon system and, at present, the description is accurate to about 20% [99]. In order to address this deficiency the missing material is incorporated into GEANT by effectively putting a uniform layer of material around the inner COT wall. In addition, the overall scale of the CDF B-field is corrected by adjusting the extracted J/ψ mass to its PDG value. Without the B-field correction the B mass values would be shifted down by $\approx 6 - 10\, MeV$. Figure 4.18 shows that refitting and correcting for the missing detector material shifts the B candidate mass up by approximately $2 - 4\, MeV$ more so that the value is now consistent with the PDG value. At the same time refitting also reduces the width by $\approx 10\%$.

The final judge for the refit procedure is whether it improves our figure of merit. Figure 4.19 shows the figure of merit obtained without refitting the tracks, while Figure C.5 shows the same with the refit. There is a 15-20% improvement after the refit. The refit procedure is thus adopted for this analysis.

[16] In the procedure everything was expressed as a function of events that passed the cut and failed the cut, which are independent of each other. If one uses the number of events passed and the total number of events, these two variables are not independent, as the total number of events does depend on the number of events passed!

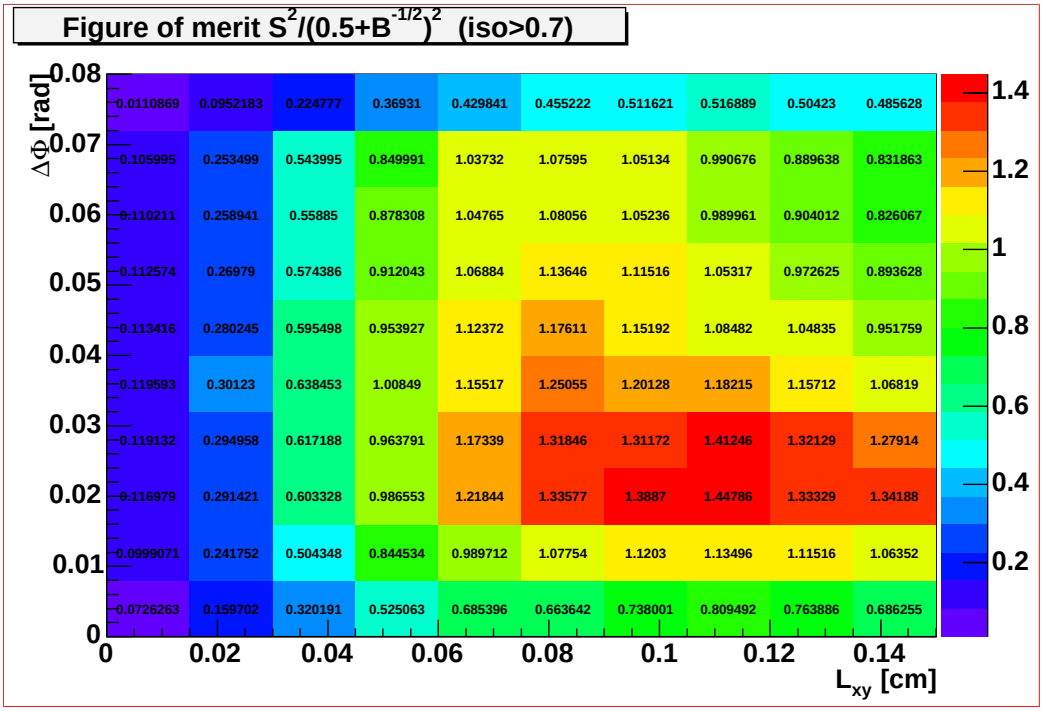

Figure 4.19: Figure of merit $S^2/(1/2+B)^2$ for $iso > 0.7$ without refitting the tracks.

4.8 Final selection

The results of Table 4.9 and Figure 4.12 can now be combined with those of Figures A.1 through A.7 of Appendix A and inserted into Equations 4.14 and 4.15, which will give Figures B.1 through B.7 of Appendix B, and Figures C.1 through C.7 of Appendix C. These plots represent the figures of merit for each different set of optimization cuts, where what remains is to choose the set with the highest figure of merit. As one can see the figures of merit of Eq. 4.13 were not used in finding the optimal cut values. It turned out that this figure of merit tends to choose very hard cuts (Figure 4.20). Indeed, if the expected signal rate is in the low statistics Poisson range, the cuts which maximize $S/\sqrt{B}$ will push the efficiency of the experiment to very small values. Another pathology is that the number of $B_d^0 \to J/\psi K^{*0}$ signal events calculated when there are no L_{xy} and $\Delta\Phi$ cuts applied seems to be smaller than the number of events when there is an $L_{xy} > 0.015\,cm$ cut applied. The reason is that when there are no cuts applied, the peak is harder to fit with all the background present (see for example Figure 4.4), while even mild L_{xy} and/or $\Delta\Phi$ cuts will eliminate most of the background which will result in a peak, which is a lot easier to fit (Figure 4.13). So the pathology is present only for the bin without L_{xy} and $\Delta\Phi$ cuts, and is propagated for all the quantities that involve the number of $B_d^0 \to J/\psi K^{*0}$ signal events (i.e. figures of merit and number of expected $B_d^0 \to \mu\mu K^{*0}$ events).

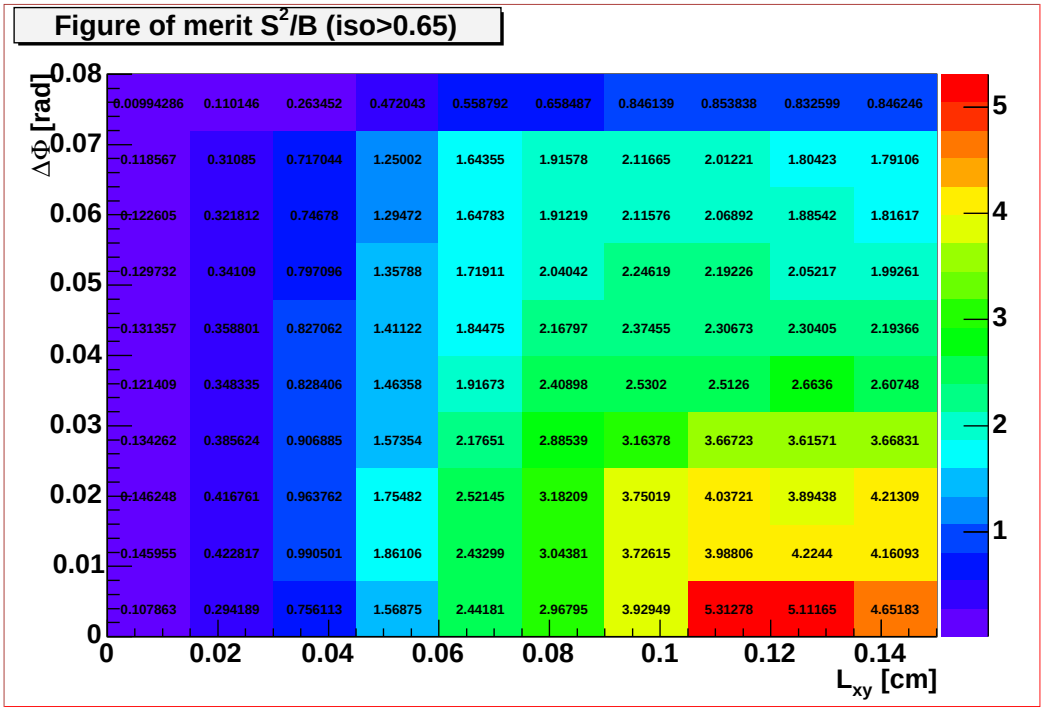

Figure 4.20: Figure of merit S^2/B for $iso > 0.65$.

The optimization plots show that both the $S^2/(S+B)$ and $S^2/(1/2+\sqrt{B})^2$ figures of merit give identical L_{xy} and $\Delta\Phi$ cuts over a wide range of different $Isolation$ cuts, namely $L_{xy} > 0.09\,cm$ and $\Delta\Phi < 0.024\,rad$. Table 4.12 shows the figures of merit for several different $Isolation$ cuts with the above L_{xy} and $\Delta\Phi$ cuts. The typical error on the figures of merit obtained by error propagation is ~ 0.3.

$Isolation$	$S^2/(S+B)$	$S^2/(1/2+B)^2$
> 0.55	1.13	1.31
> 0.6	1.20	1.46
> 0.65	1.28	1.67
> 0.7	1.23	1.65
> 0.75	1.13	1.55

Table 4.12: Values of the two figures of merit after the baseline cuts, $L_{xy} > 0.09\,cm$ and $\Delta\Phi < 0.024\,rad$ for different values of the isolation cut.

For both $S^2/(S+B)$ and $S^2/(1/2+\sqrt{B})^2$ the value corresponding to $Isolation > 0.65$ turned out to be optimal. From these results the optimal values for the three optimization cuts are: $\mathbf{L_{xy} > 0.09\,cm}$, $\mathbf{Isolation > 0.65}$ and $\mathbf{\Delta\Phi < 0.024\,rad}$.

The B candidate mass distribution for $B^0_d \to \mu\mu K^{*0}$ is shown in Figure 4.21. There are two events in the signal region. Figure 4.22 shows the B candidate mass distri-

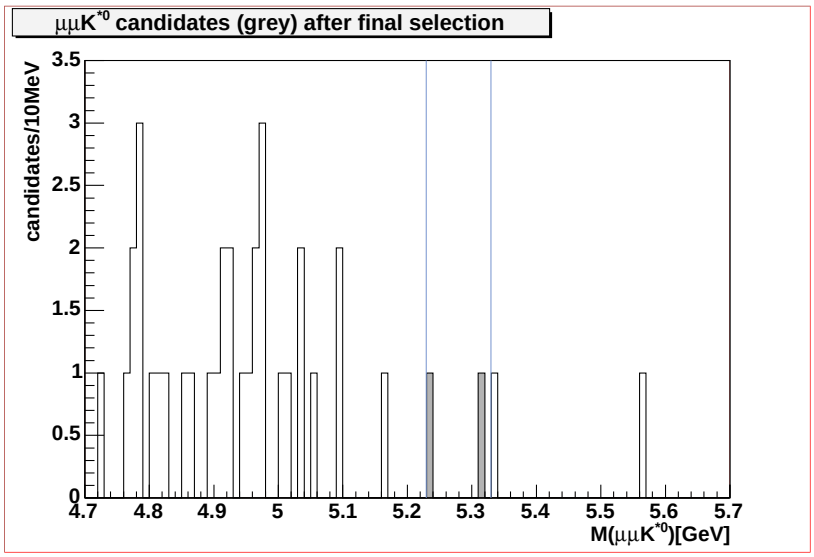

Figure 4.21: B candidate distribution for the $B_d^0 \to \mu\mu K^{*0}$ decay, $L_{xy} > 0.09\,cm$, $\Delta\Phi < 0.024\,rad$ and $Isolation > 0.65$. The two events falling inside the mass window are drawn in grey.

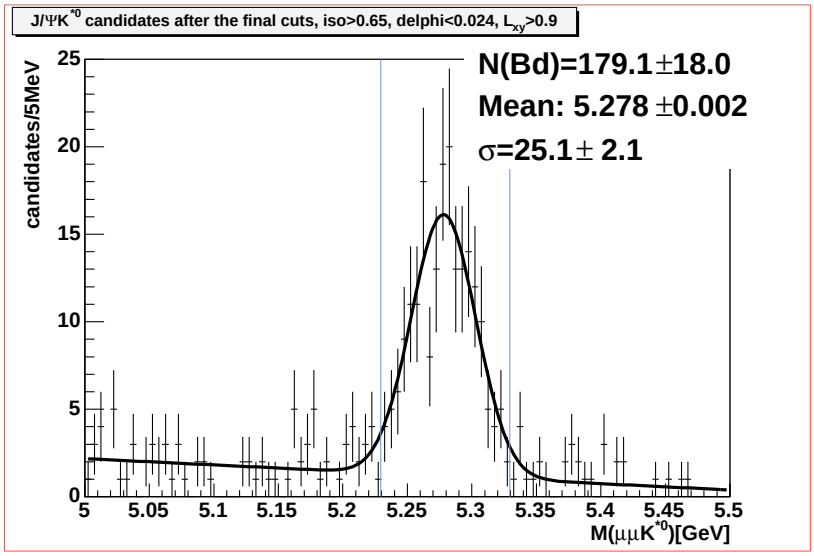

Figure 4.22: B candidate distribution for the $B_d^0 \to J/\psi K^{*0}$ decay, $L_{xy} > 0.09cm$, $\Delta\Phi < 0.024rad$ and $Isolation > 0.65$.

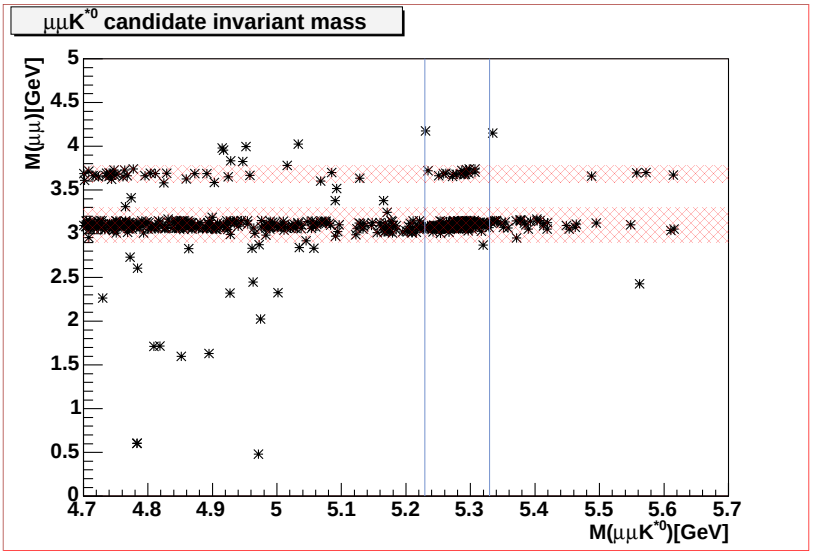

Figure 4.23: Scatter plot of $B^0_d \to \mu\mu K^{*0}$ candidates, $L_{xy} > 0.09\,cm$, $\Delta\Phi < 0.024\,rad$ and $Isolation > 0.65$.

bution for the $B^0_d \to J/\psi K^{*0}$ decays. Figure 4.23 shows the scatter plot of both the $B^0_d \to \mu\mu K^{*0}$ and $B^0_d \to J/\psi K^{*0}$ candidates. The horizontal bands are the regions around the J/ψ and $\psi(2S)$ resonances. The signal region is delimited by the two blue lines at $\pm 50\,MeV$ around the B mass. The background is considerably higher in the low mass sideband than in the high mass sideband in the resonant case, where partially reconstructed $B \to J/\psi X$ decays account for the excess in the low mass sideband region. However, there is no such explanation for the non-resonant case.

The resonant signal has 179 events in the signal region. In the non-resonant case there are 2 candidates in the signal region. The expected number of background events is 1.001 (see Appendix D), while the expected number of signal events is 1.94 (see Appendix E), which adds up to 2.94 events in the signal region. The next step is to deduce a confidence interval of 68.27% C.L. for the number of signal events. In order to do that the method described in [100] will be used. It is also part of the methods recommended by the PDG [3]. The advantage of this method is that it unifies the treatment of upper confidence limits for null results and two-sided confidence intervals for non-null results. The interval resulting from the calculation is overcovering and is conservative. Rather than using the Bayesian approach with an "objective prior", it uses classical confidence intervals. The present measurement is described by a Poisson distribution with a background, i.e. the observable x is the total number of observed events n, consisting of signal events with mean μ and background events with known mean b:

$$P(n|\mu) = (\mu + b)^n exp(-(\mu + b))/n! \tag{4.25}$$

Next, confidence intervals $[x_1, x_2]$ for each value of μ are constructed such that

$P(x \in [x_1, x_2]|\mu) = \alpha$. The confidence interval $[\mu_1, \mu_2]$ we are looking for is the union of all values of μ for which the corresponding acceptance interval contains the measured value (i.e. $n_0 = 2$). From Table II of [100] for $b = 1.0$ and $n_0 = 2$ the corresponding interval is:

$$[\mu_1, \mu_2] = [0.14, 3.25] \quad CI = 68.75\% \tag{4.26}$$

In particular, the interval contains the fixed unknown μ_t (number of signal events) in a fraction $\alpha = 68.27\%$ of experiments. This is different from the Bayesian statement that the degree of belief that μ_t is in $[\mu_1, \mu_2]$ is α. Using the same procedure confidence intervals for $\alpha = 90\%$ and $\alpha = 95\%$ can be constructed:

$$[\mu_1, \mu_2] = [0.0, 4.91] \quad CI = 90\% \tag{4.27}$$

$$[\mu_1, \mu_2] = [0.0, 5.72] \quad CI = 95\% \tag{4.28}$$

In these latter cases the confidence intervals transform automatically into upper limits. Unfortunately, at present, there is no accepted method to incorporate the uncertainty in the background estimate into the result [101]. Work is still in progress to find an adequate solution to the problem [102] [103] [104] [105] [106]. Taking the $\pm 15\%$ systematic error of Section 4.5.4 on the background estimate of 1.001 the background is varied by one standard deviation, and using the tables of [107] $0.14^{+0.13}_{-0.12}$ and 3.25 ± 0.15 are obtained for the lower and upper limits of the confidence interval for 68.75%. The same numbers for the lower and upper limits of the 90% (95%) confidence intervals are 0.0 and 4.91 ± 0.15 (0.0 and 5.72 ± 0.15), respectively[17]. The corresponding confidence intervals for the branching ratios can be obtained using Eq. 4.10:

$$\mathcal{B}(B_d^0 \to \mu\mu K^{*0}) = \mathcal{B}(B_d^0 \to J/\psi K^{*0}) \cdot \frac{S(B_d^0 \to \mu\mu K^{*0})}{S(B_d^0 \to J/\psi K^{*0})} \cdot \frac{\epsilon_{baseline}(B_d^0 \to J/\psi K^{*0})}{\epsilon_{baseline}(B_d^0 \to \mu\mu K^{*0})} \cdot \frac{1}{\epsilon_{rel}} \tag{4.29}$$

$$[0.84, 19.57] \times 10^{-7} \quad CI = 68.75\% \tag{4.30}$$

$$[0.0, 29.56] \times 10^{-7} \quad CI = 90\% \tag{4.31}$$

$$[0.0, 34.44] \times 10^{-7} \quad CI = 95\% \tag{4.32}$$

These are consistent both with the theoretical predictions presented in Chapter 2 and with the results presented at the Lepton-Photon 2003 conference by the Belle experiment [31] [32]. By propagating the error on the interval limits stemming from the uncertainty on the background and combining it with the errors on the other quantities of Eq. 4.29 the following values are obtained for the lower and upper limits

[17] There is no error on the 0.0, as it represents the transition to an upper limit.

of the intervals for the branching ratio: $0.84^{+0.79}_{-0.73}$, 19.57 ± 2.52, 29.56 ± 3.67 and 34.44 ± 4.24.

4.9 Future prospects at CDF

Fiscal Year	Goal $[fb^{-1}]$	Stretch Goal $[fb^{-1}]$	Number of $B^0_d \to J/\psi K^{*0}$ decays	Number of $B^0_d \to J/\psi K^{*0}$ decays (stretch)	Number of $B^0_d \to \mu\mu K^{*0}$ decays	Number of $B^0_d \to \mu\mu K^{*0}$ decays (stretch)
Sept03	0.215	0.215	179	179	1.94	1.94
FY02	0.08	0.08	67	67	0.72	0.72
FY03	0.2	0.22	167	183	1.8	2.0
FY04	0.31	0.38	258	316	2.8	3.4
FY05	0.39	0.67	325	558	3.5	6.0
FY06	0.50	0.89	416	741	4.5	8.0
FY07	0.63	1.53	525	1274	5.7	13.8
FY08	1.14	2.37	949	1973	10.3	21.4
FY09	1.16	2.42	966	2015	105	21.8
Total	4.41	8.56	3672	7127	39.8	77.2

Table 4.13: Projected number of $B^0_d \to \mu\mu K^{*0}$ decays (based on [51]).

Based on the projections from [51] it is possible to estimate the number of expected $B^0_d \to \mu\mu K^{*0}$ decays. Using the cuts found to be optimal there are 179 $B^0_d \to J/\psi K^{*0}$ decays in the data corresponding to $215\,pb^{-1}$ delivered luminosity, which enables to make a projection for the following years (Table 4.13). Obviously these numbers are describing the delivered luminosity, the recorded luminosity with all the necessary detector elements functioning properly being 16% smaller for CMUP muons, and 22% smaller for CMX muons. Part of this inefficiency can be explained by the early problems of the Tevatron and CDF detector[18]. As more and more is learned about both and the running of the system settles down, these efficiencies are expected to go up. Unfortunately, some of the effect will be balanced by the inefficiencies appearing due to the ageing of the detector, like small parts of the silicon detector destroyed by random Tevatron quenches or components, which cannot be replaced due to access problems, failing after years' of operation in the high radiation environment.

More luminosity means more signal and also more background. However, with more signal events softer cuts can be used. Also, with the increased statistics it may be possible to identify some of the backgrounds, and cut them out, increasing the S/B.

[18] Even though these do not include the early start-up problems, as the RAREB triggers were introduced only starting from Run 140886.

4.10 Conclusions

A search for the flavor changing neutral current process $B_d^0 \to \mu\mu K^{*0}$ has been performed in $p\bar{p}$ collisions at $\sqrt{s} = 1.96\,TeV$ produced at the Collider Detector at Fermilab (CDFII). These decays are forbidden at tree-level in the Standard Model, but proceed at low rate through penguin and box diagrams. The search for the $B_d^0 \to \mu\mu K^{*0}$ decay has been conducted using data accumulated until September 2003 corresponding to $215\,pb^{-1}$ integrated luminosity. Judicious cuts have been applied in order to reduce the background to an acceptable level. Three strongly discriminating variables have been chosen and the cuts on them were optimized using diverse figures of merit. Due to its similarity to the $B_d^0 \to \mu\mu K^{*0}$ decay the $B_d^0 \to J/\psi K^{*0}$ decay was used as a reference. Monte Carlo simulations were used to calculate those efficiencies which could not be obtained from the data. Analysis performed on the data yields the following confidence intervals for the branching ratio of $B_d^0 \to \mu\mu K^{*0}$:

$$[0.84, 19.57] \times 10^{-7} \quad CI = 68.75\% \tag{4.33}$$

$$[0.0, 29.56] \times 10^{-7} \quad CI = 90\% \tag{4.34}$$

$$[0.0, 34.44] \times 10^{-7} \quad CI = 95\% \tag{4.35}$$

That improves the

$$\mathcal{B}(B_d^0 \to \mu\mu K^{*0}) < 4.0 \times 10^{-6} \quad (90\%\ C.L.) \tag{4.36}$$

measured in Run I [87]. It is consistent with the predictions of the Standard Model and the measurements of the BaBar and Belle experiments. As the Tevatron continues to gather luminosity, CDF should be able to replace the upper limits given by the 90% and 95% confidence intervals with measurements and confirm the observations made at the B factories.

Part III

Performance of ATLAS modules using the SCTA128 chip

Chapter 5

Detectors for studying rare B decays II: The ATLAS experiment at the LHC

5.1 The Large Hadron Collider

The Large Hadron Collider is the new particle accelerator under construction at CERN. It should be completed by 2005 and will bring protons into head-on collisions at higher energies than ever achieved. The LHC will provide an energy of $7\,TeV$ per beam, which will give rise to a center-of-mass energy of $14\,TeV$. This center-of-mass energy is one magnitude higher than that reached by the Tevatron at Fermilab, and corresponds to the conditions prevailing in the Universe just 10^{-12} seconds after the "Big Bang". The LHC design luminosity is $10^{34} cm^{-2} s^{-1}$. However, in the first few years, while the performance is still being optimized, the machine luminosity will be $\approx 10^{33} cm^{-2} s^{-1}$, so during this period the LHC experiments will be well adapted to exploit the field of B physics. When the design luminosity is reached the focus will shift towards the Higgs sector of the Standard Model. The Higgs boson is responsible for the masses of all known particles and its discovery is the main challenge of the LHC. There are four important experiments planned to be installed at the interaction points of the accelerator: ALICE, ATLAS, CMS and LHCb.

In order to achieve the $10^{34} cm^{-2} s^{-1}$ luminosity the LHC will take advantage of the existing accelerator infrastructure at CERN (Figure 5.1) [109]. Protons will be pre-accelerated and injected from the SPS at an energy of $450\,GeV$. In order to reach the design luminosity the LHC is filled with 2808 proton bunches each containing 1.1×10^{11} protons. The time separation between the bunches is $24.95\,ns$ which corresponds to a 40 MHz collision frequency. After the injection the protons are accelerated up to $7\,TeV$ and remain in the accelerator for periods of ≈ 10 hours, which is called a store. Extremely large magnetic fields are needed in order to bend the $7\,TeV$ proton beams around the $27\,km$ ring of the LHC. Specially designed super-conducting dipoles will provide an $8.33\,T$ magnetic field for both beams. Apart from the 1296 dipoles, a large

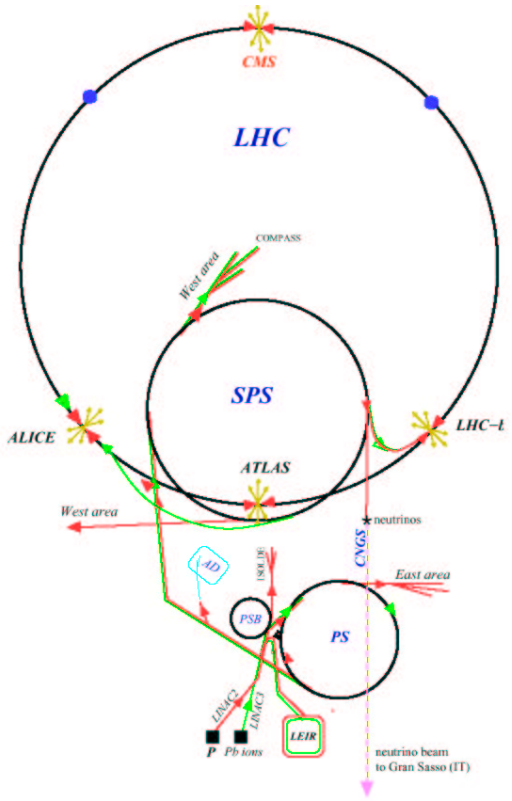

Figure 5.1: Overall view of the LHC accelerator complex.

Energy at collision	$7\,TeV$
Energy at injection	$450\,GeV$
Dipole field at $7\,TeV$	$8.33\,T$
Luminosity	$1 \cdot 10^{34}\,cm^{-2}s^{-1}$
DC beam current	$0.582\,A$
Number of bunches	2808
Number of particles/bunch	$1.15 \cdot 10^{11}$
Bunch spacing	$7.48\,m$
Bunch separation	$24.95\,ns$
Luminosity lifetime	$10\,h$
Total radiated power per beam	$3.8\,kW$
Stored energy prer beam	$366\,MJ$
Filling time per ring	$4.3\,min$

Table 5.1: Design parameters of the LHC

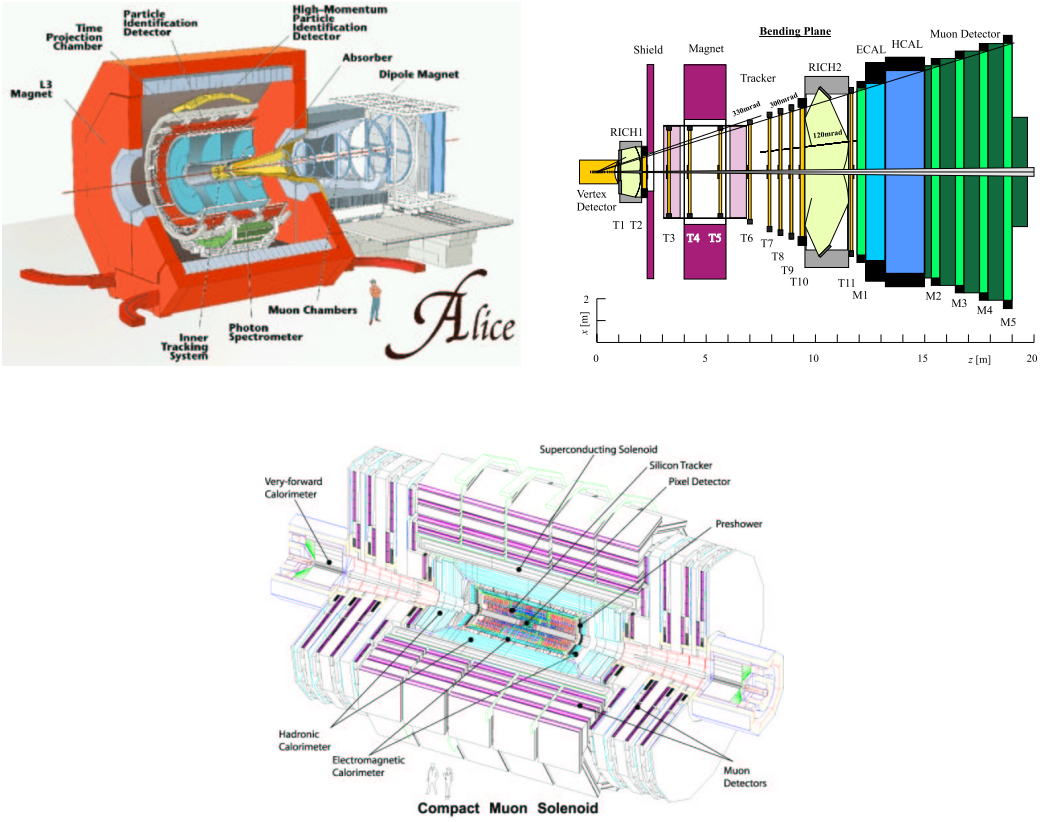

Figure 5.2: Overall view of the ALICE, LHCb and CMS detectors.

number of steering magnets and focusing quadrupoles are needed as well. Some of the design parameters are summarized in Table 5.1.

Besides proton-proton collisions, aimed at exploring physics at the TeV scale, both proton-nucleus and nucleus-nucleus collisions are foreseen as part of the initial experimental program at the LHC. With heavy ions at a centre-of-mass energy of about 5.5 TeV/nucleon, the LHC is the only machine which will reach, and even extend, the energy range probed by cosmic ray nucleus-nucleus collisions. The aim of high-energy heavy-ion physics is the study of strongly interacting matter at extreme energy densities (QCD thermodynamics). Statistical QCD predicts that, at sufficiently high density, there will be a transition from hadronic matter to a plasma of deconfined quarks and gluons – a transition which in the early universe took place in the inverse direction some 10^{-5} s after the Big Bang and which might still play a role today in the core of collapsing neutron stars. In February 2000 the totality of intriguing experimental results obtained at the SPS over several years was folded into a public announcement stating that the formation of a new phase of matter was their best explanation [110]. In mid-June 2003 the researchers at RHIC announced results that show that this new phase of matter is highly non-transparent to fast quarks, which is once more along the lines of what is expected for QGP [111] [112] [113] and [114]. The

heavy-ion detector ALICE (A Large Ion Collider Experiment) is a general-purpose heavy-ion experiment (see Figure 5.2), sensitive to the majority of known observables (including hadrons, electrons, muons and photons) and is the next step in studying high-energy heavy-ion physics [115].

The second of the smaller experiments is LHCb [116] which plans to operate with an average luminosity of $2 \times 10^{32} cm^{-2} s^{-1}$, which should be obtained from the beginning of LHC operation. The LHCb detector is designed to exploit the large number of b-hadrons produced at the LHC. The LHCb is ideally suited to determine all the angles of the two unitarity triangles (i.e. six of the nine unitarity conditions of the CKM matrix) using high-statistics data. The layout of the LHCb detector is shown in Figure 5.2.

ATLAS and CMS are the two big general purpose experiments of the LHC. The ATLAS experiment will be described in section 5.2. CMS is very similar to ATLAS in its physics goals [117]. It consists of a pixel detector, silicon tracker, electromagnetic calorimeter and hadronic calorimeter all placed inside a superconducting solenoid. On the outer side of the solenoid are placed the muon detectors and the very-forward calorimeters around the beam pipe on both sides of the detector (Figure 5.2).

5.2 ATLAS overview

The ATLAS detector is a general purpose pp detector which is designed to exploit the full discovery potential of the LHC. One of the main interests of ATLAS is the origin of mass at the electroweak scale. However, there are many other important goals to reach. These include the searches for heavy W- and Z-like objects, for supersymmetric particles, detailed studies of the top quark, and last, but not least, studies in the B sector, including CP-violation in B-decays.

Already at initial lower luminosities the LHC will be a high-rate beauty and top-quark factory. A particularly rich field will be available in B physics. The main emphasis will be on the precise measurement of the CP-violation in the B_d^0 system and the determination of the angles of the Cabibbo-Kobayashi-Maskawa unitarity triangle. Other important topics include rare B decays and $B\bar{B}$ mixing in the B_s^0 system. In order to study these sectors the detector needs precise secondary vertex determination, the full reconstruction of final states with relatively low-p_T particles, and low-p_T lepton first level trigger thresholds as well as second level track triggering. A typical decay that needs all these features is the one described in the present document, where $\mathrm{B_d^0} \to \mu^+\mu^-\mathrm{K^{*0}}$ is followed by $\mathrm{K^{*0}} \to \mathrm{K}\pi$. Sensitivity to a variety of final state signatures is required, which leads to the following characteristics:

- efficient tracking even at high luminosity for lepton momentum measurements, b-quark tagging, enhanced electron and photon identification, high-precision reconstruction capability of B decay states.

- stand-alone, precise, muon-momentum measurements up to the highest luminosities, and very low-p_T trigger capability at lower luminosity.

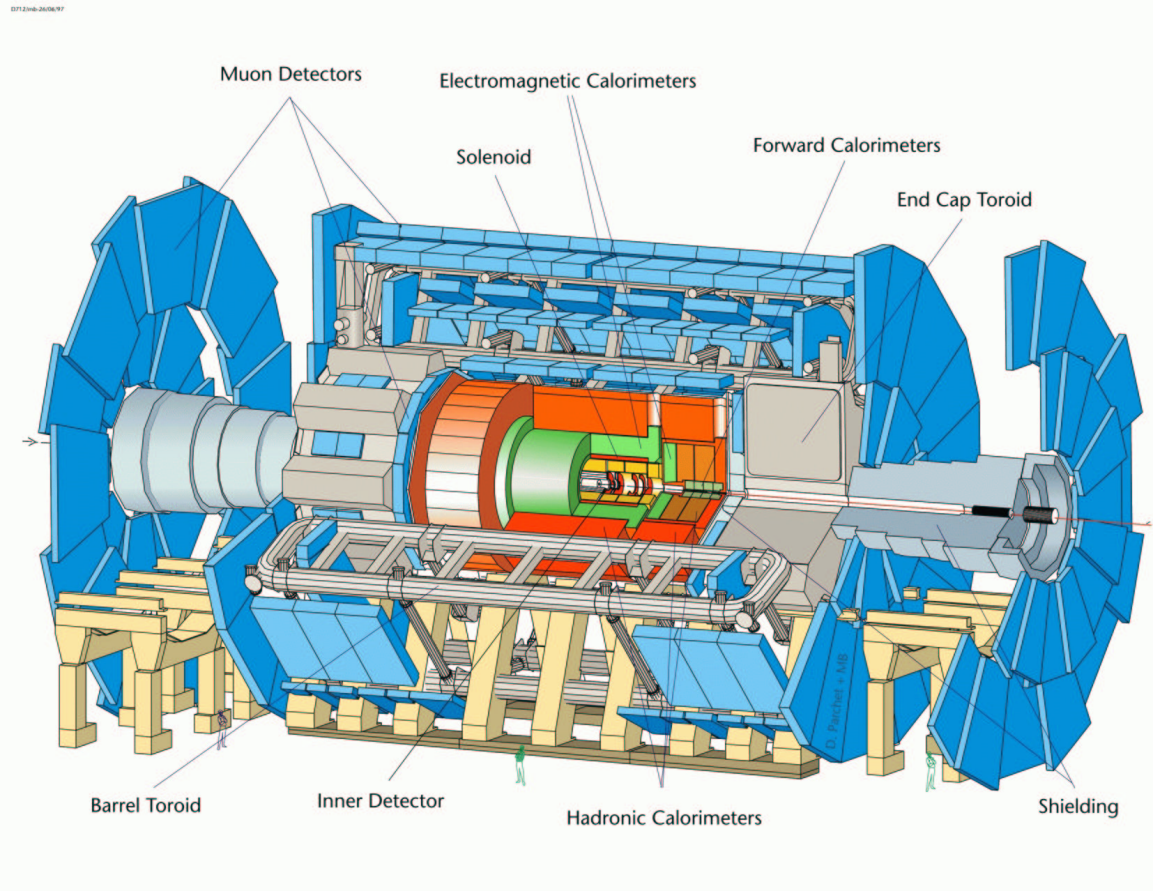

Figure 5.3: Overall view of the ATLAS detector

- good electromagnetic calorimetry for electron and photon identification and measurements, complemented by hermetic jet and missing E_T calorimetry.
- large acceptance in pseudorapidity (η) with almost full azimuthal angle (ϕ) everywhere. The azimuthal angle is measured around the beam axis, whereas pseudorapidity relates to the polar angle Θ which is the angle from the z direction.

It is also very important to achieve large acceptance in η coverage and have the capability of measuring particles at low-p_T thresholds[1].

Figure 5.3 shows the overall view of the ATLAS detector. The magnet configuration is based on an inner superconducting solenoid around the inner detector cavity and large superconducting air-core toroids consisting of independent coils outside the calorimetry. This solution places no constraints on the calorimetry and inner detector thus allowing the best technological solutions. The $2\,Tesla$ solenoid is positioned in front of the barrel electromagnetic calorimeter. Its thickness in radiation length and radial extension has been minimized to avoid degrading the calorimeter performance.

[1] See [118] Table 1.1 for more details.

For this reason, the solenoid coil is integrated into the vacuum vessel of the LAr calorimeter barrel cryostat, thus eliminating the material and space of independent vessel walls. The superconducting air-core toroid consists of a $26\,m$ long barrel part and with an inner bore of $9.4\,m$ and an outer diameter of $19.5\,m$, and two end-caps with lengths of $5.6\,m$ and inner bores of $1.26\,m$, inserted at each end of the barrel. The whole magnet system represents a cold mass of 700 tons and a total weight of 1400 tons.

The inner detector is the central part of the ATLAS detector. It is $6.80\,m$ in length with a radius of $1.15\,m$, fixed by the inner dimension of the cryostat containing the liquid argon EM calorimeter. Pattern recognition, momentum and vertex measurements, and enhanced electron identification are achieved with a combination of discrete high-resolution pixel and strip detectors in the inner part and continuous straw-tube tracking detectors with transition radiation capability in the outer part of the tracking volume. For more details on the inner detector see Section 5.3.

The pseudorapidity range of $|\eta| < 3.2$ is covered by a highly granular Liquid Argon (LAr) electromagnetic sampling calorimeter with excellent performance in terms of energy and position resolution (Figure 5.4). In the endcaps the LAr technology is also used for the hadronic calorimeter, sharing the cryostats with the electromagnetic endcaps as well as with the special LAr forward calorimeters which extend the coverage to $3.2 < |\eta| < 4.9$. The main part of the hadronic calorimetry is provided by a novel scintillator tile calorimeter which is separated into one large barrel and two extended barrel cylinders on each side. The whole calorimetry contributes to a very good jet and missing transverse momentum performance of the ATLAS detector. The LAr calorimetry is contained in a cylinder with an outer radius of $2.25\,m$ and extends to $\pm 6.65\,m$ along the beam axis. The outer radius of the tile calorimeter is $4.25\,m$ and its length is $\pm 6.10\,m$. The total weight of the calorimeter system, including the solenoid flux return iron yoke, which is integrated in the tile calorimeter support structure, is about 4000 tons.

The calorimetry is surrounded by the muon spectrometer (Figure 5.5). The air-core toroid system generates a large field volume and strong bending power with a light and open structure. This reduces multiple scattering effects, and allows an excellent muon momentum resolution using three stations of high-precision tracking chambers. The muon instrumentation is completed with fast trigger chambers. In the barrel region $|\eta| < 1.1$ in the ϕ direction, the layout follows the eight-fold symmetry of the barrel toroid. The drift wires for the high precision measurement run along the ϕ direction, and have a maximum length of $5.7\,m$ in the outermost chambers. Along the η direction, the chambers are segmented into units not larger than $2.6\,m$. In the transition region ($1.1 < |\eta| < 1.4$) the muon tracks are covered by three vertical stations located inside or near the end-faces of the barrel toroid. In the end-cap regions $|\eta| > 1.4$ the first and second stations are located before and behind the end-cap toroids, and the third one close to the end wall of the cavern. The maximum wire-length is $6.3\,m$, and full azimuthal coverage is achieved by staggering of chamber layers. Each of the muon chambers consists of two multilayers of detectors which are mounted to either side of a support structure. The multilayers consist of three or four

individual planes of closely packed detectors. The basic measurement in each muon chamber is a track segment, providing a basis for robust pattern recognition and

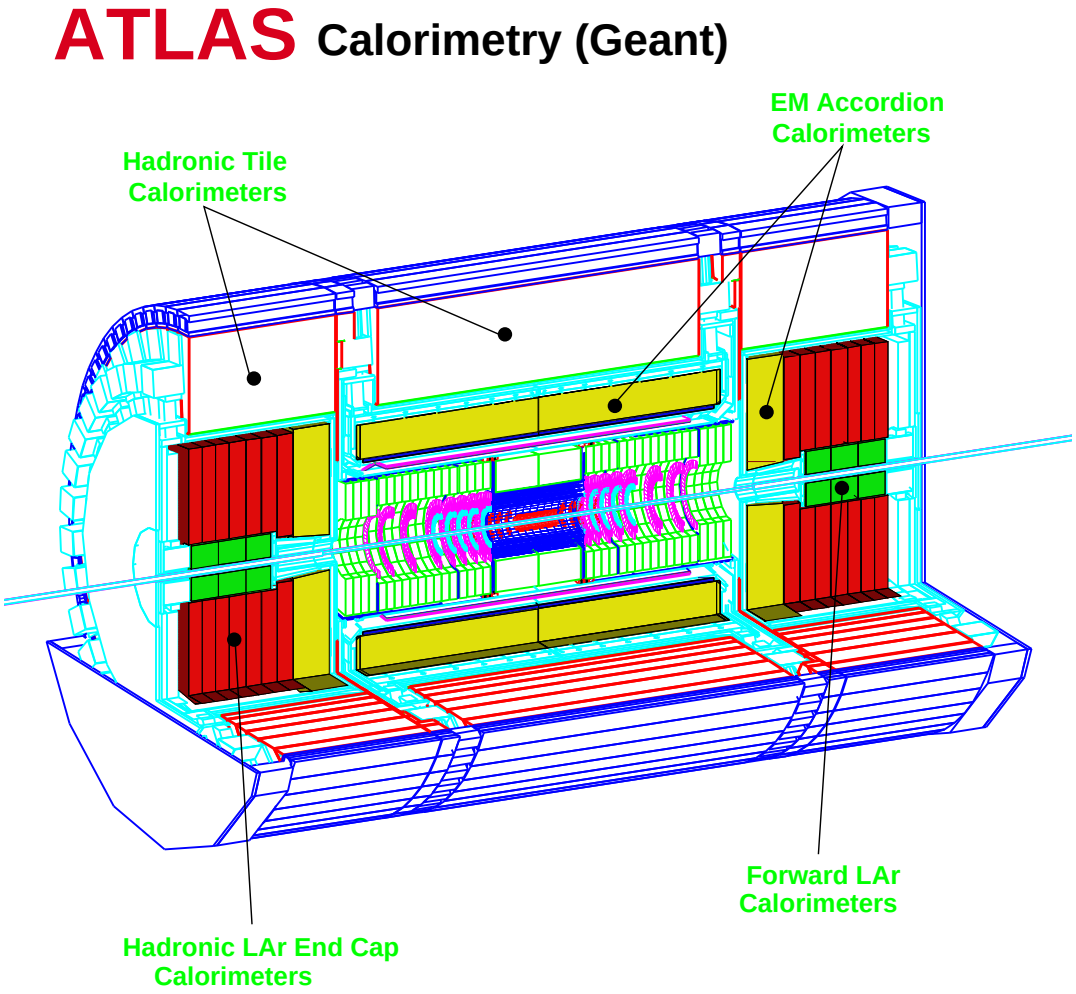

Figure 5.4: Three-dimensional view of the ATLAS calorimetry

momentum determination. The muon spectrometer defines the overall dimensions of the ATLAS detector. The outer chambers of the barrel are at a radius of about $11\,m$. The length of the barrel toroid coils is $\pm 12.5\,m$, and the third layer of the forward muon chambers is located at $\pm 23\,m$ from the interaction point. The overall weight of the ATLAS detector is about 7000 tons.

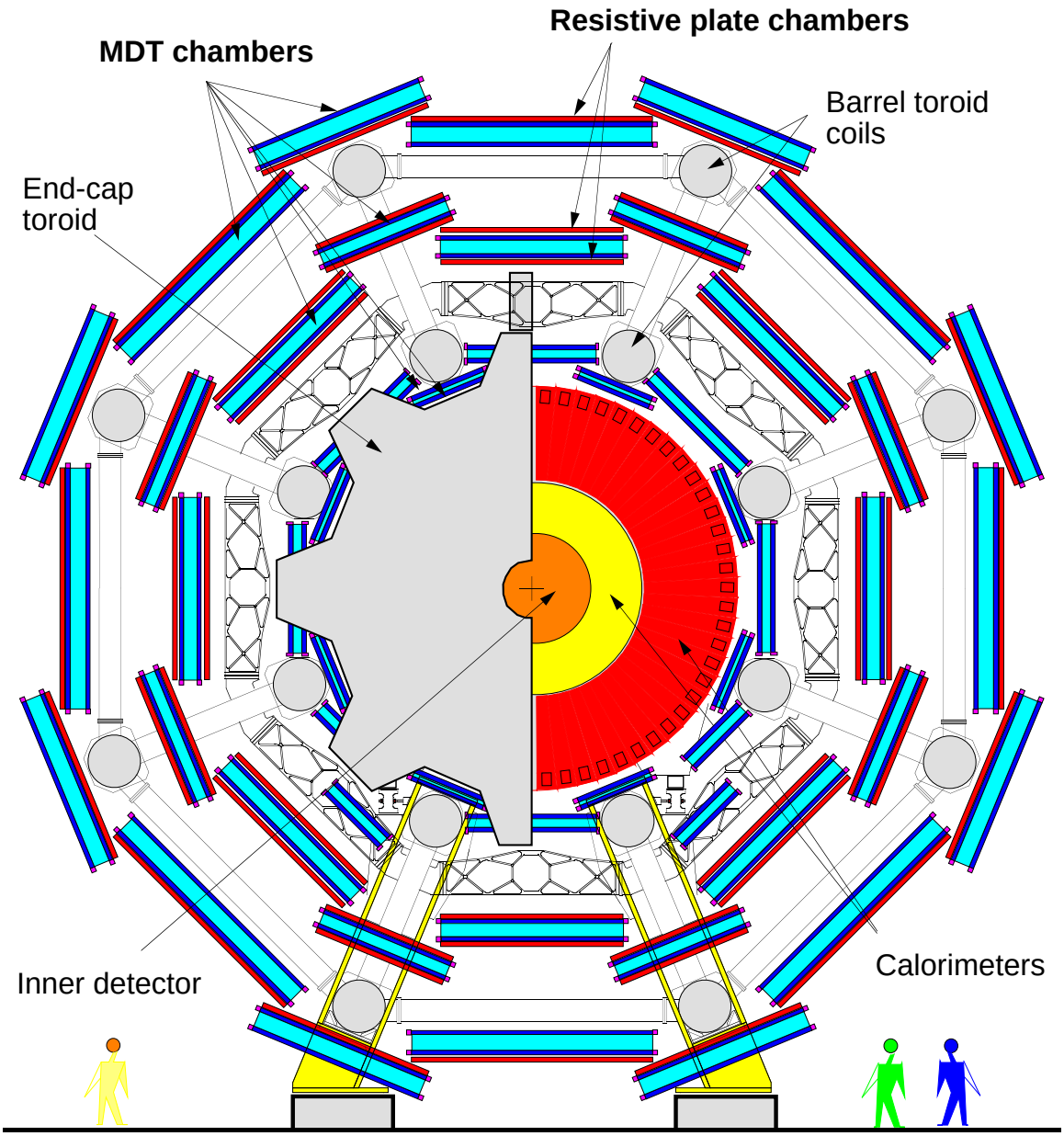

Figure 5.5: Transverse view of the muon spectrometer

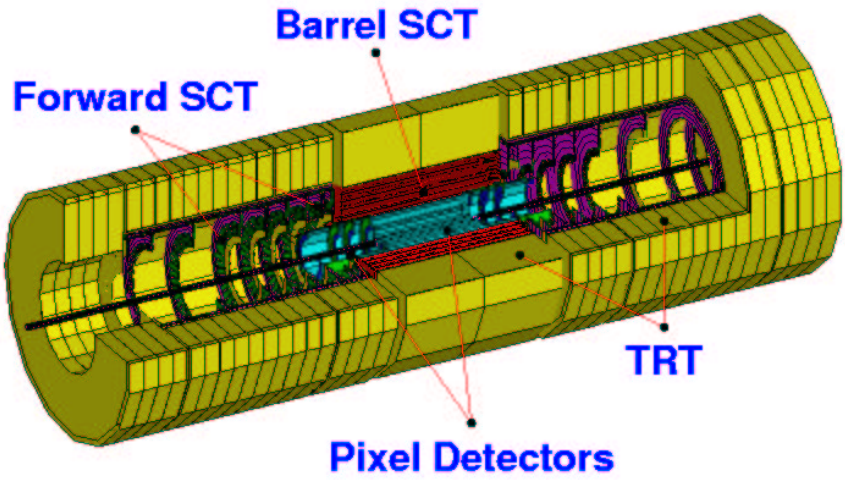

Figure 5.6: The Inner Detector

5.3 The Inner Detector

The inner detector, shown in Figure 5.6, tracks charged particles from the LHC beam-pipe to the electromagnetic calorimeter system. The momentum and vertex resolution targets imply the need for high-precision measurements to be made with fine-granularity detectors given the very large track density expected at the LHC. Highest granularity around the vertex region is achieved using semiconductor pixel detectors. However, the total number of precision layers must be limited because of the material they introduce, and because of their high cost. At least four strip layers and three pixel layers are therefore crossed by each track in this design. A large number of tracking points (typically 36 per track) is given by a straw tube tracker (TRT) which provides the possibility of continuous track-following with much less material per point. The combination of the two techniques gives very robust pattern recognition and high precision in both the ϕ and z coordinates. Mechanically, the Inner Detector consists of three units: a barrel part extending over $\pm 80\,cm$, and two identical end-caps covering the rest of the cylindrical cavity. The precision tracking elements are contained within a radius of $56\,cm$, followed by the continuous tracking, and finally the general support and service area at the outermost radius. In the barrel, the high-precision detector layers are arranged on concentric cylinders around the beam axis in the region with $\eta < 1$, while the end-cap detectors are mounted on disks perpendicular to the beam axis. The pixel layers are segmented in $R\phi$ and z, while the silicon strips use small angle ($40\,mrad$) stereo to measure both coordinates, with one set of strips in each layer measuring ϕ. The barrel TRT straws are parallel to the beam direction. All the end-cap tracking elements are located in planes perpendicular to the beam axis. The strip detectors have one set of strips

running in radial directions, and a set of stereo strips at an angle of $40\,mrad$. The continuous tracking consists of radial straws arranged into wheels.

The layout provides full tracking coverage over $|\eta| < 2.5$, including impact parameter measurements and vertexing for heavy-flavour and τ tagging. The resolution will be typically $\sigma_{R\phi} = 12\,\mu m$ and $\sigma_z = 66 - 77\,\mu m$ for the pixel layers, $\sigma_{R\phi} = 16\,\mu m$ and $\sigma_z = 580\,\mu m$ for the silicon detectors, and $\sigma_{perstraw} = 170\,\mu m$ for the TRT[2]. The secondary vertex measurement performance will be enhanced with an innermost additional layer of pixels, at a radius of about $5.05\,cm$, as close as is practical around the beam pipe. The lifetime of such a detector will be limited by radiation damage, and would need replacement after a few years. A large amount of interesting physics can be done with this detector during the initial lower luminosity running, especially in the B sector. The mechanical design allows for the possibility of replacing the B-layer, which will remain an important tool for the B-tagging.

The pixel detector is designed to provide a very high-granularity, high-precision set of measurements as close to the interaction point as possible. The system provides three of the precision measurements over the full acceptance, and determines the impact parameter resolution and the ability of the Inner Detector to find short-lived particles such as b-quarks and τ-leptons. The two-dimensional segmentation of the sensors gives space points without any of the ambiguities associated with projective geometries, but requires the use of advanced electronic techniques and interconnections for the readout. In addition, the pixel system must be radiation hardened to withstand over $300\,kGy$ of ionising radiation and over $5.10^{14}/cm^2$ neutrons in ten years of operation.

The system offers 80 million detector elements, each $50\,\mu m$ in the $R\phi$ direction and $400\,\mu m$ in z, which are invaluable for the task of pattern recognition in the crowded environment of the LHC. The system consists of three barrels at average radii of $5.05\,cm$, $8.85\,cm$, and $12.25\,cm$, and three disks on each side, between radii of 11 and $20\,cm$, which complete the angular coverage. It is designed to be highly modular, containing 1744 barrel and disk modules [120]. The modules are overlapped on the support structure in order to give a hermetic coverage.

The SCT system is designed to provide four precision measurements per track in the intermediate radial range, contributing to the measurement of momentum, impact parameter and vertex position, as well as providing good pattern recognition by the use of high granularity. It is described in more detail in Section 5.5.

The TRT is based on the use of straw detectors, which can operate at the very high rates needed by virtue of their small diameter and the isolation of the sense wires within individual gas envelopes. Electron identification capability is added by employing a gas mixture based on xenon with the addition of CO_2 and O_2 to detect transition-radiation photons created in a radiator between the straws. This technique is intrinsically radiation hard, and allows a large number of measurements, typically 36, to be made on every track at modest cost. However the detector must cope with a large occupancy and high counting rates at the LHC design luminosity. Each

[2]For more details see [119] Table 1-1.

straw is $4\,mm$ in diameter, giving a fast response and good mechanical properties for a maximum straw length of $144\,cm$. The barrel contains about 50000 straws, each divided in two at the centre in order to reduce the occupancy and read out at each end. The end-caps contain 320000 radial straws, with the readout at the outer radius. The total number of electronic channels is 420000. Each channel provides a drift-time measurement, giving a spatial resolution of $170\,\mu m$ per straw, and two independent thresholds. These allow the detector to discriminate between tracking hits, which pass the lower threshold, and transition-radiation hits, which pass the higher. The barrel section is built of individual modules covering the radial range from 56 to $107\,cm$. The modularity was chosen as a compromise between the ease of construction and maintenance, and the additional structural elements involved. The two end-caps each consist of 18 wheels. The 14 wheels nearest the interaction point cover the radial range from 64 to $103\,cm$, while the last four wheels extend to an inner radius of $48\,cm$ in order to maintain a constant number of crossed straws over the full acceptance. At rates of $12\,MHz$, only about 70% of the straws give correct drift time measurements because of shadowing effects, but the large number of straws per track guarantees a measurement accuracy of better than $50\,\mu m$ averaged over all straws at the LHC design luminosity, including errors from alignment. Hence the TRT contributes to the accuracy of the momentum measurement in the Inner Detector by providing a set of measurements roughly equivalent to a single point of $50\,\mu m$ precision. It aids the pattern recognition by the addition of around 36 hits per track, and allows a simple and fast level-2 track trigger to be implemented. In addition it provides additional discrimination between electrons and hadrons, with a pion rejection varying with η between a factor of 15 and 200 at 90% electron efficiency.

All tracks with $|\eta| < 2.5$ are measured with six precision space-points and about 36 straws, except for a slight degradation across the barrel to end-cap transition region at the largest η. With the B-layer present, seven precision points are obtained. The momentum resolution of the Inner Detector is limited by several factors: the radial space available in the cavity, which limits the lever arm, the strength of the magnetic field, and the intrinsic precision of the detector elements. In addition, above $|\eta| = 1.85$, tracks leave the Inner Detector volume before reaching the maximum radius of the cavity, thereby reducing the field integral available as compared to the lower $|\eta|$ regions. These effects limit the momentum resolution achievable in the end-cap regions, especially for $|\eta| > 2$. This achievable resolution is sufficient to identify the charge sign of particles up to the highest energies expected at LHC.

Extensive simulations have been performed in order to characterize the phyisics performance of the ID [121], [122] and [123]. Since the time of the Physics TDR, only small changes have occurred to the positions and dimensions of the SCT and TRT. However, major changes have been made to the Pixel system, in particular to the innermost layer, the B-layer. The radius of the B-layer has been increased in order to accommodate a larger beam pipe and the whole Pixel detector has been given an independent insertion capability so that it can be inserted later or replaced if damaged by radiation. This latter development has caused a serious increase in the amount of material, with the pixel-barrel radiation-thickness increased by 50%

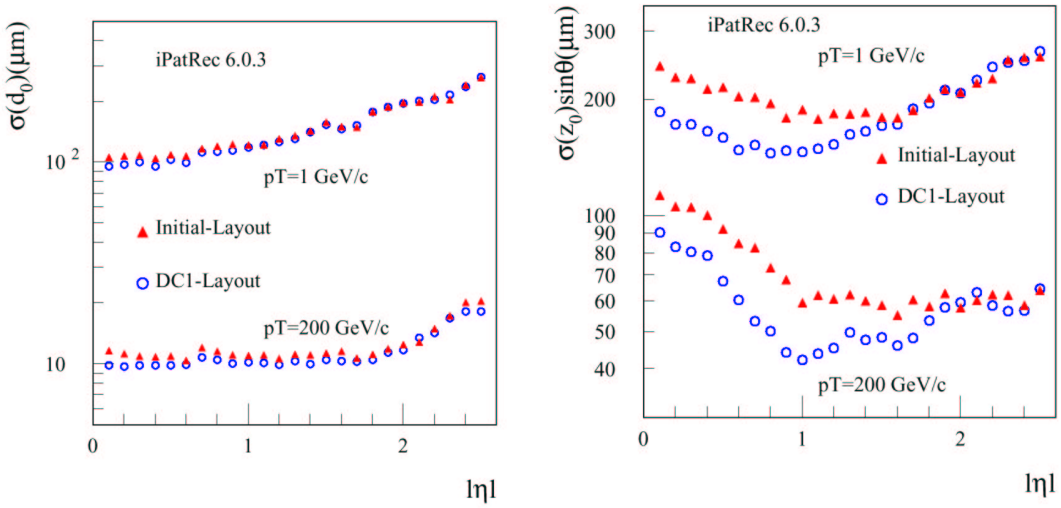

Figure 5.7: Transverse impact parameter resolution (d_0) and longitudinal impact parameter resolution projected transversely to the track direction ($z_0 \times \sin\theta$) as function of $|\eta|$ for muons of $p_T = 1\,GeV$ and $p_T = 200\,GeV$ for both layouts.

and a significant support structure shadowing the complete SCT and TRT end-cap regions. Detailed changes have been made to the pixel granularity with regular bands of larger pixels and non-adjacent bands of ganged channels. The most up-to-date results published use two layouts of the detector: the DC1 layout for which there is a lot of existing data from the DC1 data challenge, and the so called Initial layout where the intermediate pixel layer and part of the end-cap TRT have been removed.

A crucial parameter for the physics performance of the ID is the resolution on the impact parameters of tracks from secondary vertices. The impact parameter resolution can be parametrised[3,4] in Rϕ as

$$\sigma(d_0) = 110 \oplus \frac{94}{p_T}\ \mu m \tag{5.1}$$

with the dedicated B-physics layer of pixels present at $5.05\,cm$ radius. A precise measurement of the transverse impact parameter of a track, d_0, is necessary for primary vertex association and the reconstruction of short-lived secondary vertices. These are essential for heavy flavor tagging and life-time measurements. The resolution of the transverse impact parameter, expressed as a function of $|\eta|$ for the DC1 and Initial layouts, at $p_T = 1$ and $200\,GeV/c$, is given for in Figure 5.7 (left). At high momentum, the resolution is almost constant up to $|\eta| \sim 1.8$, but then degrades rapidly in the end-cap region. The degradation is due to a reduction in the mea-

[3]For the DC1 layout.

[4]The trajectory of a particle moving in a solenoidal magnetic field B with no multiple scattering and negligible bremsstrahlung radiation, can be described by a set of 5 helix parameters: d_0 – the signed transverse impact parameter, ϕ_0 (azimuth) – the ϕ coordinate of the track in the xy plane at the point of closest approach to the origin, z_0 – the longitudinal impact parameter is the value of z of the point on the track that determines d_0, θ – the polar angle that gives the inverse slope of the track in the (r, z) plane, Q/pT – where Q is the charge of the particle.

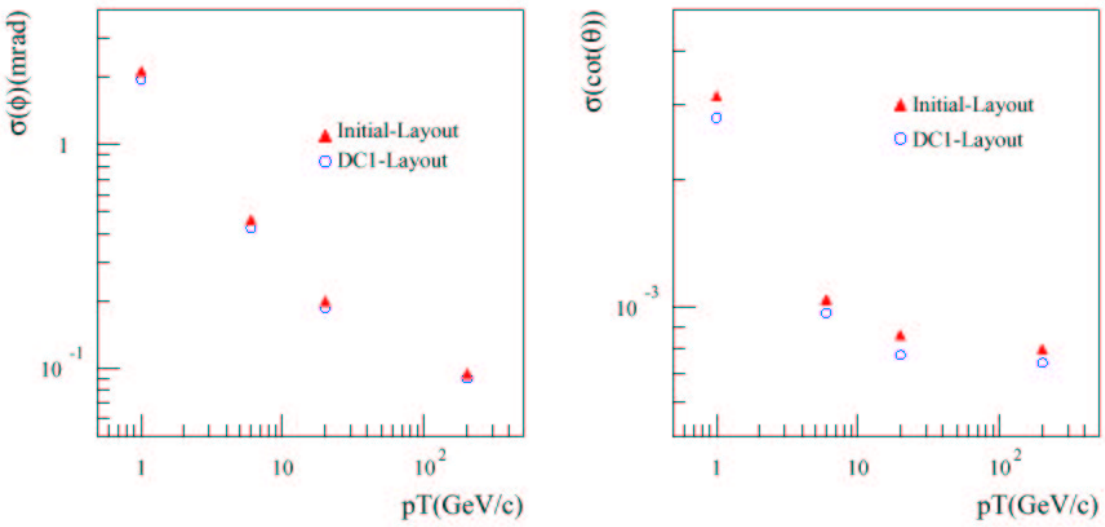

Figure 5.8: Angular resolution in ϕ and $\cot\theta$ of charged tracks as function of p_T for $|\eta| < 0.25$ for both layouts.

sured radial length for tracks longitudinally exiting the tracker which produces an increase in the relative distance to extrapolate back to the beam-line, and thus an increased extrapolation error. At low momentum the resolution is much worse due to the dominant multiple scattering contribution from material up to and including the first measurement. There is also a continuous rise with $|\eta|$, since the material thickness of the beam-pipe and B-layer increase with $\sin\theta$.

The projection of z_0 onto the plane perpendicular to the track direction is also an important measurement for vertexing and B-tagging (Figure 5.7 (right)). At high momentum the smaller clusters cause the resolution as a function of $|\eta|$ to be worst at $|\eta| = 0$, with an improvement by a factor ~ 2 achieved by saturation at $|\eta| \sim 1$. Beyond this value, there is a slow worsening of the resolution for similar reasons to the transverse impact parameter. At low momentum, in the barrel region, one again sees the improvement of resolution with $|\eta|$ due to increasing cluster size, but here the gain is offset by the corresponding increase in multiple scattering. Beyond $|\eta| \sim 1$, the multiple scattering is completely dominant.

The angular resolutions obtained for the DC1 and Initial layouts are shown for central tracks as a function of p_T in Figure 5.8. The effect of the reduction in the B-layer longitudinal granularity is apparent in the $\cot\theta$ resolution. The p_T dependence of the $1/p_T$ resolution integrated over all $|\eta|$ is shown in Figure 5.9. It can be parametrized by $\sigma(1/p_T) = 0.55 \oplus 22/p_T\sqrt{\sin\theta}$ for DC1.

Obviously, these results, based on single muon tracks, represent an idealization of what can be expected in normal LHC operation, independent of pattern recognition problems associated with multi-track events. The reconstruction efficiency for muons is a measure of the optimum single particle efficiency. Pions and electrons

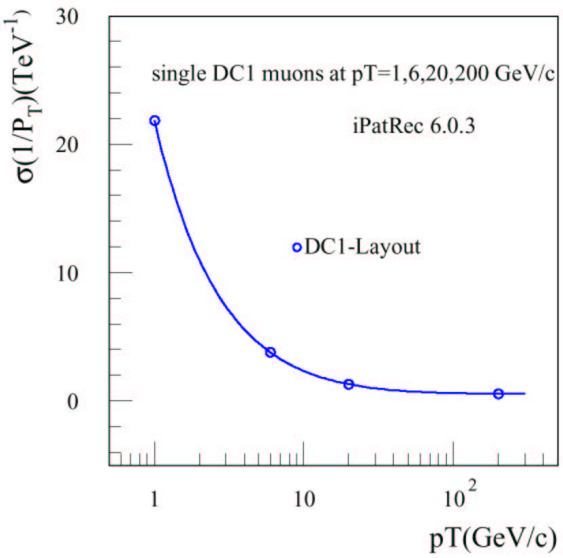

Figure 5.9: Inverse transverse momentum resolution of charged tracks as a function of p_T in $|\eta| < 2.5$ for DC1 layout. The resolution plot for the Initial layout is identical.

have their efficiency reduced by hadronic interactions and bremsstrahlung, respectively. Muons have an overall efficiency $\sim$ 99.5% with losses due to the simulated detector inefficiency and a slight lack of hermeticity in the end-cap region. Pion efficiencies are about 5 to 10% lower than muon efficiencies due to interactions. Three interaction categories can be distinguished; early, intermediate and late. Late interactions, which occur towards the outside of the inner detector, have full efficiency but a loss of resolution from the shorter measured length. Early interactions, which occur in the beam-pipe or Pixel detector, cannot be found because there are too few measurements to define the track. The intermediate category have insufficient correct hits to satisfy the quality criteria, but are nevertheless found when the pattern recognition wrongly associates one or more downstream hits from leading secondary particles. The probability of this occurrence, hence the measured efficiency, increases with momentum. Electron efficiencies are lower than for muons due to catastrophic bremsstrahlung energy losses. However, the major effect of bremsstrahlung is to distort the fitted parameters in the bending plane. In particular, the momentum tends to be underestimated. It was also found that the presence of pile-up, even at high luminosity, has little effect on the track finding efficiency. Tracks have also been studied in jets, for example from $H \rightarrow b\bar{b}$ with $m_H = 400\,GeV$. An efficiency of $\sim$90% can be obtained for tracks with $p_T > 1\,GeV$, with cuts which ensure that the fraction of fake tracks anywhere in the acceptance remains below $\sim$0.5%.

Even though since the Physics TDR performance measurements, the impact parameter resolution at low momentum has been degraded by moving the B-layer further out and increasing its thickness, and the initial angle determination has been weakened by moving the pixel end-cap wheels appreciably closer to the vertex, the

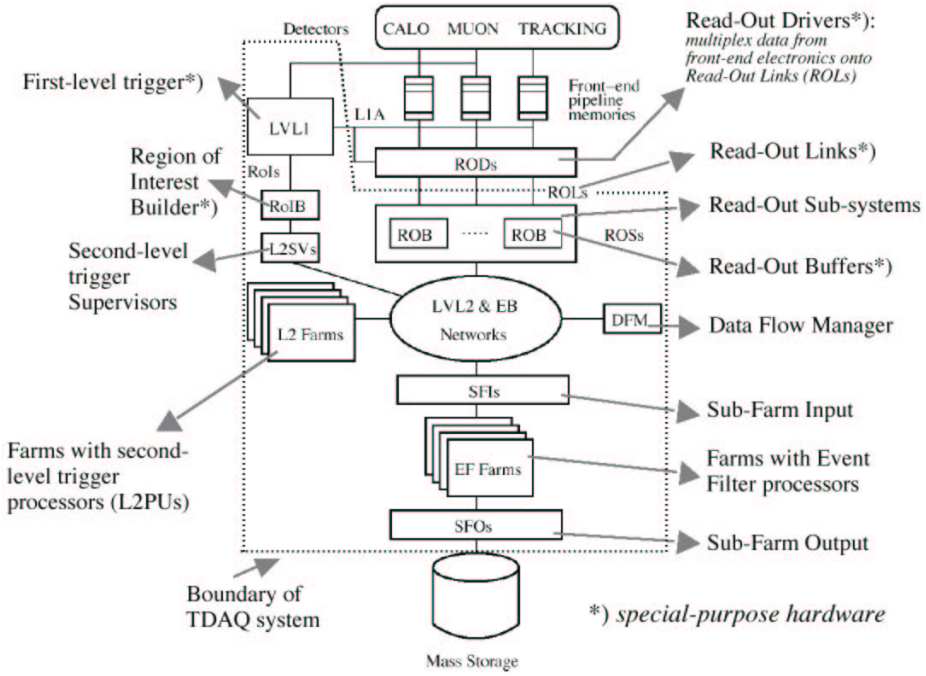

Figure 5.10: Schematic layout of the Trigger and DAQ system of ATLAS.

inner detector remains a crucial element for the B physics, as it allows precise reconstruction of tracks in the high occupancy environment of the LHC. This precision is a necessary requirement in order to reconstruct the secondary vertices and measure precisely such quantities as the lifetimes, which will allow to pick out the physically interesting events from the huge background expected at The LHC.

5.4 Trigger, Data Acquisition and Controls

The Trigger/Data Acquisition (TDAQ) system must be designed and constructed in such a way as to provide ATLAS with highly reliable and efficient data-taking and event-selection capabilities [124], [125], [126]. The ATLAS trigger, data acquisition and controls system consists of four major components (Figure 5.10):

- The Data Flow System is responsible for receiving the detector data, serving a subset of data to the HLT system, and transporting the data for selected events to mass storage.
- The High-Level Trigger (HLT) system is responsible for the post-Level 1 (LVL1) event selection and filtering involving a rate reduction of a factor of several hundred, and for the classification of all accepted events.
- The Online system is responsible for all aspects of experiment and TDAQ operation and control during data-taking, and during testing and calibration runs.

- The Detector Control System (DCS) is responsible for the coherent and safe operation of the ATLAS detector, as well as the interface with external systems and services including the LHC itself.

The Online system is implicitly understood to be connected to all elements in Figure 5.10, and the DCS to all hardware elements which need to be monitored and controlled.

The ATLAS trigger system is composed of three levels. The first level is implemented in custom hardware. It reduces the $40\,MHz$ input rate to about $75\,kHz$. The second and third (Event Filter) levels are referred to collectively as the High-Level Trigger system. They share an overall trigger selection framework, and differ mostly in the amount of event data they access and how they access it as well as in the complexity and speed of the algorithms. While the LVL1 uses only coarse-grained calorimeter and muon information, the second-level trigger (LVL2) can use full-resolution, full-granularity data from all detectors and combine the information from different sub-detectors for the first time. In practice, however, the LVL2 trigger restricts itself to so-called Regions of Interest (RoI), small regions in pseudo-rapidity–azimuth ($\eta - \phi$) space centered on objects identified by LVL1. Data from RoIs make up a small subset of the full event. Pointers to these RoIs are provided by the LVL1 trigger. Data are accessed on demand from the buffers which store the event until the LVL2 decision is made. The LVL2 trigger reduces the $75\,kHz$ rate from LVL1 to about $2\,kHz$. After an event passes LVL2 the full event is built and sent to the Event Filter (EF). Algorithms in the EF can access the full event and will be derived from offline code. The algorithms may be seeded by the results of LVL2. A further reduction to about $200\,Hz$ is achieved by the EF before events are put into mass storage.

5.5 The Silicon Tracker (SCT)

The physics requirements determining the most important detector specifications and layout of the SCT are the following:

- The reconstruction of isolated leptons of p_T >5 GeV with an efficiency of 95% in the range $|\eta| < 2.5$ and with a fake track rate of <1%, imposes the need to reconstruct helices in 3D. This imposes on the combined SCT and pixel system the need for at least six tracking layers able to provide space point information.

- The $(\delta p_T/p_T)$ <0.3 requirement at $p_T = 500\,GeV$ with a beam constraint imposes an $r - \phi$ measurement accuracy of $\sim 20\,\mu m$ at the SCT radius. The requirement to separate multiple vertices within a bunch crossing imposes an accuracy of the z-measurement of $< 1\,mm$ in the SCT. That constraint is made more stringent by requirements of K^0 reconstruction and mass resolution where a z-measurement of $\sim 0.5\,mm$ is required in the SCT.

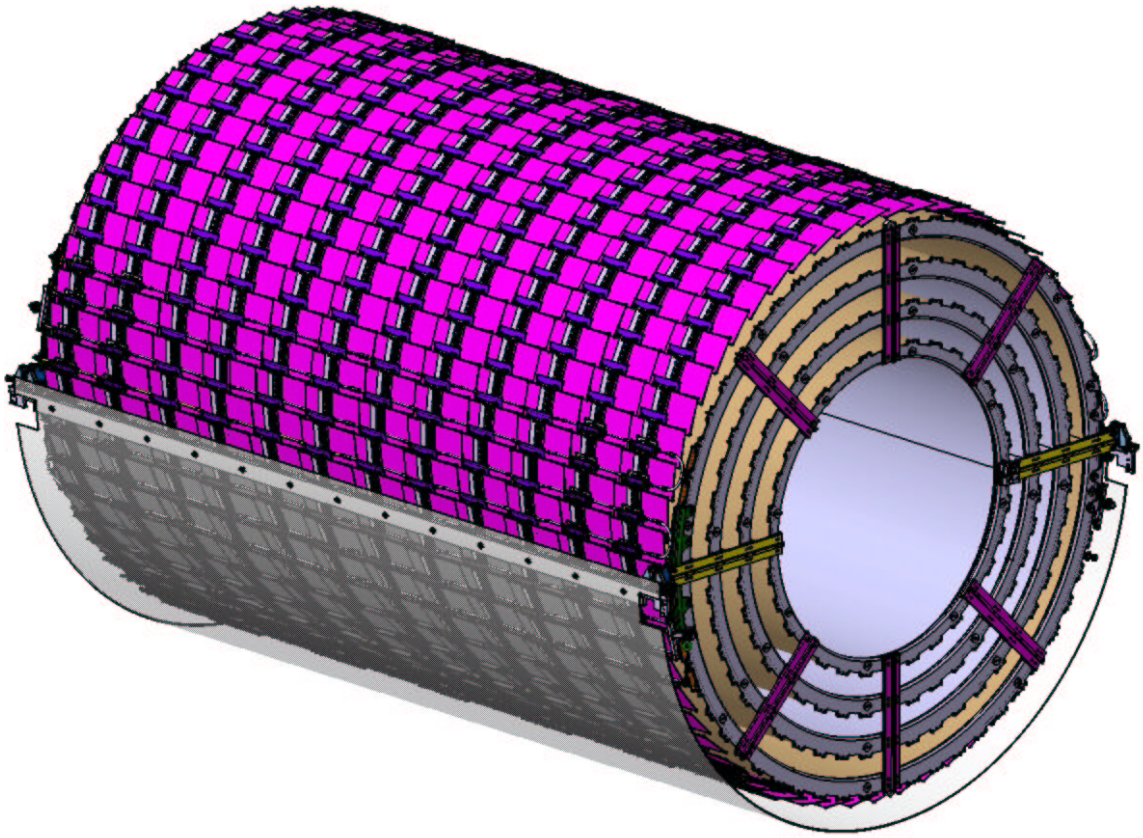

Figure 5.11: The four nested barrels of the SCT.

- The requirement of 2-track resolution of $< 200\,\mu m$ at $R = 30\,cm$, in order to keep track losses in b-jets to <5% also imposes a constraint on the $r-\phi$ readout pitch.

The Semiconductor Tracker is an order of magnitude larger in surface area than any previous generation of silicon microstrip trackers, and in addition must face radiation levels which will alter the fundamental characteristics of the silicon wafers themselves. The SCT consists of four nested barrels (Figure 5.11), and two end-caps, each with nine wheels. The barrel modules are mounted on local supports which allow units of six modules to be tested together before mounting on carbon-fibre cylinders which carry the cooling system; the four complete barrels at radii of 300, 373, 447 and $520\,mm$ are then linked together. There are 2112 identical barrel modules, mounted in 12 per row, and overlapping each other in a tile structure. Individual cylinders are fully covered with 32, 40, 48 and 56 rows. There are 1976 end-cap modules, of three different types, placed on wheels in three rings of 40, 40 and 52 modules (some disks will have two or one ring only).The nine wheels are interconnected by a space-frame. The radial range of each disk is adapted to limit the coverage to $|\eta| \leq 2.5$ by equipping

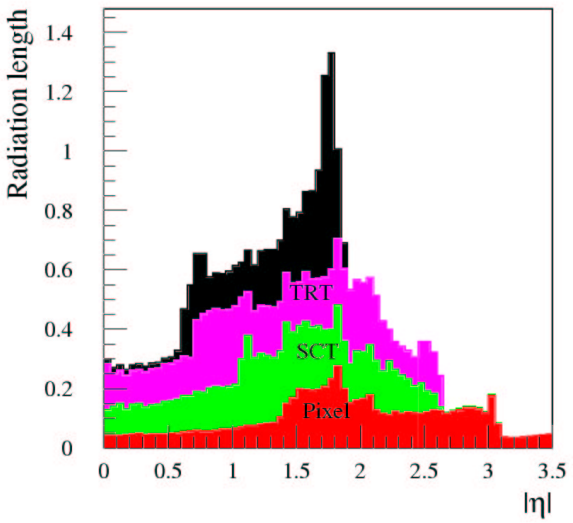

Figure 5.12: Distribution for number of radiation lengths for pixels, SCT, TRT and external services and patch-panels.

each one with the minimum number of rings, and by using 6 cm long modules where appropriate. The system requires a very high dimensional stability, cold operation of the detectors, and the evacuation of the heat generated by the electronics and the detector leakage current.

Every effort has been made to keep the material in the tracking volume to a minimum, by careful design of the active detectors and by the use of low-Z materials (such as aluminium for the power cables, and carbon-fibre reinforced plastic for the support structures (Figure 5.12)).

5.6 The modules

A module is the basic functional sub-unit of the ATLAS SCT. It consists of a set of single sided silicon micro-strip detectors glued back-to-back, an electronics package called the hybrid and an interface to the cooling and mechanical support structure of the tracker. There is a single module design for the barrel region of the SCT, and three designs for the various radial locations in the SCT forward regions. In the barrel region each silicon detector is $6.36 \times 6.40\, cm^2$ with 768 readout strips each with 80 μm pitch. Each module consists of four detectors. On each side of the module, two detectors are wire-bonded together to form 12.8 cm long strips. Two such detector pairs are then glued together back-to-back at a 40 $mrad$ angle, separated by a heat transport plate, and the electronics is mounted above the detectors on a hybrid (Figure 5.13). The readout chain consists of a front-end amplifier and discriminator, followed by a binary pipeline which stores the hits above threshold until the first level trigger decision. The forward modules are very similar in construction but use

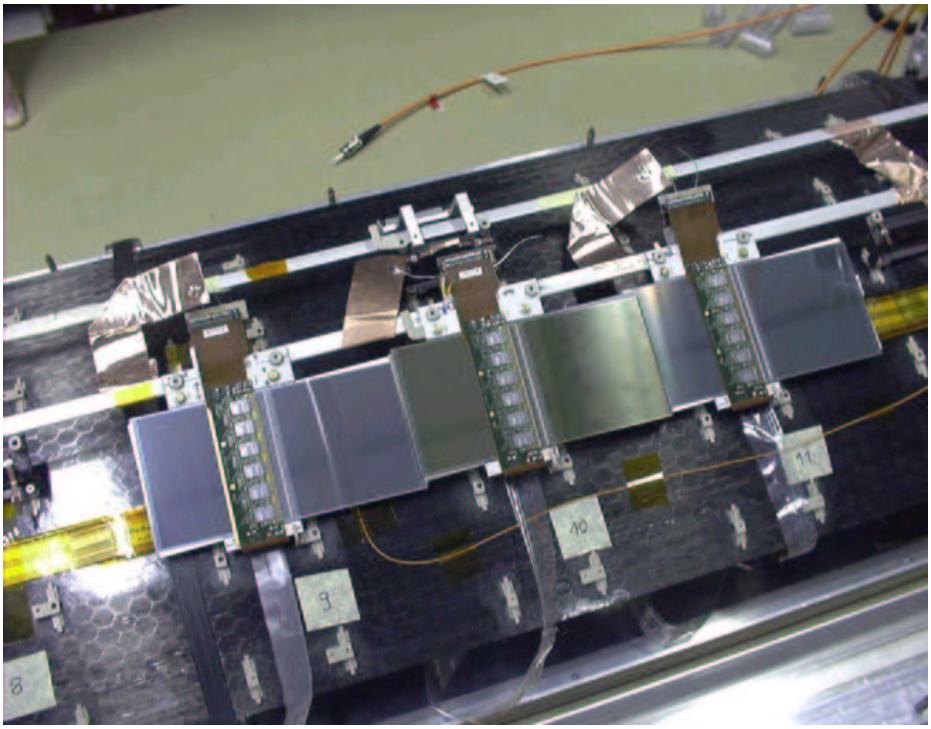

Figure 5.13: 3 SCT barrel modules mounted on a test structure.

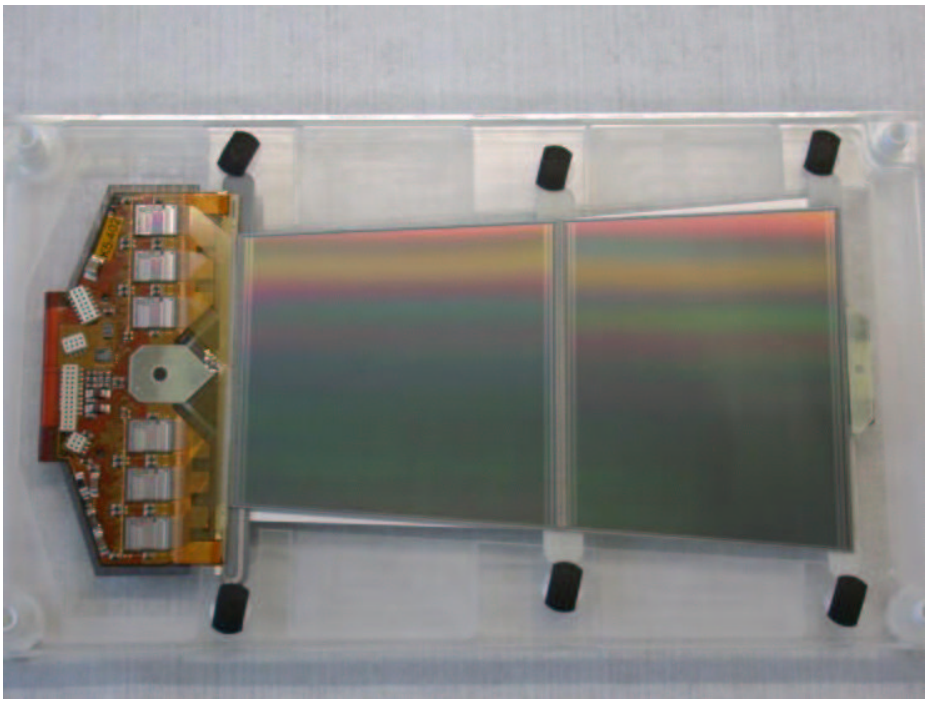

Figure 5.14: SCT forward module.

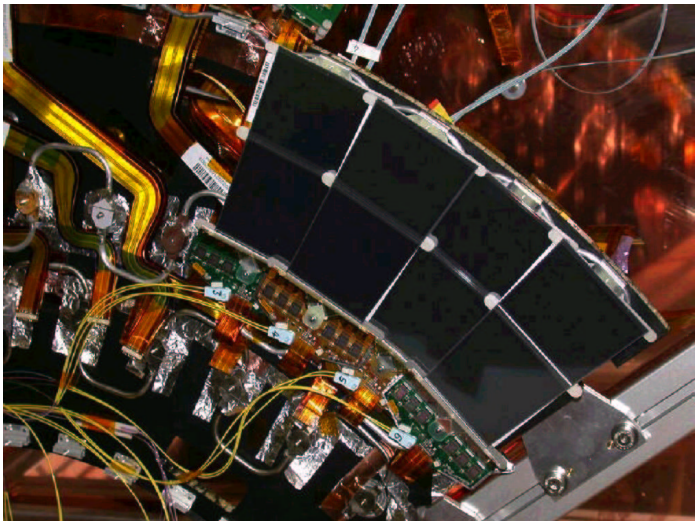

Figure 5.15: Four Outer Modules on the Forward Sector with the wiggly cooling pipes.

tapered strips, with one set aligned radially (Figure 5.14). Forward modules are made with both $\sim$ 12 and 7 cm lengths. For the SCT barrel, the required tracking precision is obtained by modules with an intrinsic point resolution of 23 μm in the $r-\phi$ coordinate per single side measurement.This precision is obtained for the binary readout scheme by using detectors with 80 μm readout pitch. A back-to-back detector pair with a stereo rotation angle of 40 $mrad$ gives a precision of 17 μm in the $r-\phi$ coordinate and 500 μm in the z coordinate from the correlations obtained through fitting. To maintain these resolutions high quality module construction, metrology and position monitoring is required. The mechanical tolerance for positioning wafers within the back-to-back pair must be around 5 μm in lateral strip position, 25 μm in module thickness and 25 μm in z. The forward region measures the longitudinal momentum and the track dip angle. The requirements are very similar to the barrel after allowing for interchange of r and z.

The cooling of silicon detector modules is a very important aspect of the design of the SCT as the heat dissipated within the tracker must be removed in order to maintain the silicon detectors at around -7^{o}C. The total heat load of the modules of the SCT and pixels together with the power loss in the cables within the tracker volume implies a cooling system that should be able to cope with in excess of 100 kW of heat to be removed from a low ambient temperature environment[5]. The baseline design described in [127] planned to use Binary-Ice as coolant. In 1997, the LHCC suggested that evaporative cooling systems should be studied as an alternative, and after thorough measurements the SCT proposed a cooling based on the two-phase flow of C_3F_8 in the review of May 1999. For the forward region in the baseline design the coolant is circulating in Aluminum pipes which follow the 'wiggly' pipe layout in order to reduce forces on the disc from thermal contractions and pipe manufacturing

[5]See [127] page 497.

tolerances (see the pipes on the left side of Figure 5.15). The heat from the hybrids and the sensors is conducted to the coolant via two aluminum cooling blocks for outer and middle modules, and via a single cooling block for the inner modules [128]. There are three separate cooling circuits per quadrant, corresponding to the inner, middle and outer module rings, where the inlets and outlets are manifolded at the patch panel.

5.6.1 Front-end electronics for modules for Si trackers

In many previous tracking detectors, electrons could be drifted over large distances in gaseous detectors, and signals could be transmitted along silicon strip detectors, thus placing the electronics outside of the active tracking volume. The high rates at LHC make this impossible over the acceptance of the ATLAS system. Instead, the tracking detectors must be designed with their electronics in close proximity to the active elements. Therefore the LHC operating conditions present a big challenge to the front-end electronics of Si trackers for experiments designed for high luminosity physics. Requirements on the front-end electronics of Si strip detectors are very demanding. The readout has to be close to the Si sensor and therefore needs to be radiation hard up to doses of $10\,Mrad$ and up to fluences of $3 \cdot 10^{14}$ charged particles/cm^2 and $2 \cdot 10^{14}$ neutrons/cm^2.

Due to the high occupancy expected at full luminosity operation the pulse shaping time has to be short. To avoid pileup of events in single channels double pulse resolution has to be of the order of $50\,ns$. It is convenient to have a peaking time of the output pulse equivalent to the bunch crossing frequency of $40\,MHz$.

The noise performance is dictated by the most probable signal from a minimum ionising particle (MIP) crossing a $300\,\mu m$ thick Si sensor, which is 22500 charges. To obtain a good efficiency for track reconstruction and maintain at the same time a low noise occupancy a signal over noise ratio better than 15:1 is required. This is equivalent to a noise smaller than 1500 e^- Equivalent Noise Charge (ENC).

The size of irreducible noise contributions, shot noise from leakage current in the irradiated Si sensor and base current in an irradiated bipolar junction transistor and preamplifier series noise, are determined by the chosen sensor element size. The sensor element size cannot be too small in order to limit the number of channels, and also cannot exceed a certain size to keep the detector capacitance low. As a compromise for these requirements ATLAS has chosen to have detector geometries with strip length from $6\,cm$ to $12.8\,cm$. The strip pitch is given by the required spatial resolution in the range of $\sigma = 5 - 25\,\mu m$.

Several architectures have been developed for LHC experiments. The two different concepts presented here are the following:

- Full analogue read-out with transmission of all data via analogue optical links to the external read-out processors for digitalisation with flash ADCs. This is the concept used so far in most collider experiments for Si trackers and vertex detectors. It allows individual treatment of data in each channel with optimized

and adaptable software and thereby the most detailed control and monitoring of the whole system. Analogue readout is to a large extent immune to external electromagnetic pickup since common mode noise can be fully eliminated with software. The price to pay is the heavier load on data transmission from the detector as one needs both higher bit rate and better quality for the links. Modules equipped with SCTA128 chips were used to study this architecture.

- Another possibility is the binary scheme for the readout of silicon strip detectors. The binary architecture allows a more compact design and has the advantage of a much reduced data transfer rate with more chips using a single optical link. This architecture is, however, not immune at all to common mode noise and so is very sensitive to external electromagnetic interference. This is the choice of the ATLAS baseline using ABCD chips.

5.6.2 The digital solution (ABCD)

In the beginning two technological options were considered for the binary architecture:

- The ABCD design is a single chip implementation of the binary readout architecture for silicon strip detectors in the ATLAS SCT. It is fabricated using the DMILL technology, which being BiCMOS one, offers a possibility to implement the complete architecture in one chip.

- A design employing two separate chips: CAFE-M a front-end chip realized in the MAXIM bipolar process and ABC, a binary pipeline chip realized in the Honeywell bulk CMOS process.

After thorough testing of both the ABCD and the CAFE-M ABC combination [129] [130] the former was choosen as the option to develop.

The ABCD chip has all the blocks of the binary readout architecture; the front-end circuitry employing a bipolar transistor in the input stage, discriminators, a binary pipeline, a derandomizing buffer, data compression logic and the readout control logic. There were different measurements carried out in order to evaluate the performance of the chip. Electrical prototype modules were built where the chips were placed on a ceramic hybrid and connected to detector strips of various length. A more detailed description of the ABCD design and these measurements is the theme of Section 6.2.

5.6.3 The analogue solution (SCTA)

The analogue solution is represented by the SCTA chip which comprises the following building blocks: 128 channels with front-end amplifiers, analogue memory (ADB) with the capacity to store 128 analogue samples, control logic providing a derandomizing function (up to 8 events), a command decoder and a fast analogue multiplexer to output serial data. In addition to the basic functional blocks, internal calibration circuitry containing an 8-bit DAC to control the calibration level has been implemented to improve the testability of the chip. Four 5-bit DACs for the bias of the analogue

part of the chip have been implemented in order to compensate for the drifts after irradiation and optimize chip performance for various parameters.

An extensive set of measurements was performed in order to evaluate the performance of the chip. The characterization of the front-end part was not only important for the SCTA, but also for the ABCD as well. The two chips share basically the same front-end, but in the case of the ABCD the binary architecture prevents a study of the subtler effects. First, the basic parameters of the chip have been evaluated in a single chip setup using internal calibration circuitry. Next, the chips were mounted on hybrids and connected to silicon detectors. The resulting modules were tested in the laboratory using internal calibration circuitry and radioactive sources. As the final step, the modules were transferred to the SPS X5 West area for beam tests. The analogue modules were also used as a mean of testing a linear optical link for analogue data transmission for LHC experiments. How these measurements were performed and what results did they give rise to is described in great detail in Section 6.3.

5.7 Physics Potential of the ATLAS Detector

The rate of B-hadron production at the LHC is enormous thanks to the large hadronic cross-section for b-quark production and the high luminosity of the machine (even at so-called low luminosity L $=10^{33}\,cm^{-2}s^{-1}$). About one collision in every hundred will produce a b-quark pair, which results in a considerably better signal-to-noise ratio than at lower-energy hadron machines such as the Tevatron. In ATLAS, an inclusive-muon trigger with a p_T threshold of $6\,GeV$ will make an initial selection of B-events. Using this inclusive selection, about 25% of the muon-trigger events will contain b-quarks. In the first year of operation, some 2.3×10^{10} b-quark pair events will be selected for more detailed analysis in the LVL2 trigger and event filter, that are focused on the selection of specific classes of final states. This event rate will be higher than in any accelerator presently operating.

Although the main focus of the ATLAS physics programme is the search for and study of physics beyond the Standard Model, through the production and decay of new types of particles, an important range of B-physics studies is planned. In fact, an important aim of the B-physics work is to test the Standard Model through precision measurements of B-hadron decays that together will over-constrain the CKM matrix, possibly giving indirect evidence for new physics. This programme of work will include the following: precise measurements of CP violation in B-meson decays, which in the Standard Model is due to a single phase in the CKM matrix; precise measurements of the periods of flavour oscillations in B_s^0 as well as B_d^0 mesons, and of relative decay rates such measurements constrain the elements of the CKM matrix; searches for and measurements of very rare decays which are strongly suppressed in the Standard Model and where significant enhancements could provide indirect evidence for new physics. Many of the ATLAS measurements will be more precise than those from experiments at lower-energy machines, thanks to the greater available statistics.

At the LHC, the general-purpose experiments ATLAS and CMS will face stiff

competition from LHCb, which is a dedicated B-physics experiment. However, even though a dedicated experiment can be better optimised for certain event types, ATLAS will be competitive in several channels. ATLAS will thus play an important role in maximizing the combined precision of B-physics measurements from the LHC. It is worth noting that the B-production cross-section is not well understood at the phenomenological level, and that predictions are uncertain to a factor of two or more.

5.7.1 $\mathrm{B} \to \mu\mu(X)$

Certain rare decays, for which the decay products themselves provide a distinctive signature that can be used in the LVL1 trigger, can be studied very effectively in ATLAS making use of the high rate of B-hadron production. These so-called self-triggering modes include decays of the type $\mathrm{B}_{d,s} \to \mu\mu(X)$. As described in Chapter 2 such decays involve flavour-changing neutral currents (FCNC) and are strongly suppressed in the Standard Model, with predicted branching ratios typically in the range $10^{-5} - 10^{-10}$. New physics might result in significant enhancements compared to the Standard Model predictions.

For the purely muonic decays, ATLAS will be sensitive to branching ratios of order 10^{-9} and should be able to measure the branching ratio for $\mathrm{B}_s \to \mu\mu$ assuming the Standard Model prediction. Large-statistics samples will be collected for decays of the type $\mathrm{b} \to (s,d)ll$ that give final states such as $\mathrm{B}^0_d \to K^{*0}\mu\mu$, $\mathrm{B}^0_d \to \rho^0\mu\mu$ and $\mathrm{B}^0_s \to \phi^0\mu\mu$. This will allow precise measurements to be made of the decay dynamics, as well as of the branching ratios, giving significant constraints on new physics.

These rare decay modes are forbidden at the tree level in the Standard Model, so the decays involve loop diagrams. In non-standard models of electroweak interactions, FCNC processes can be allowed at the tree level and thus, the branching ratios of these rare decays would not be so suppressed. In addition, in the presence of new physics, additional particles may be present in the loops again enhancing the decay probability. Due to the very low Standard Model predictions for the branching fractions for purely muonic decays, a significant enhancement in measured branching fractions would clearly demonstrate the effects of new physics. The measurement of the lepton forward backward asymmetry in semimuonic B decays is another promising tool to probe the new physics beyond the Standard Model. In the context of Standard Model, the principal interest lies in the measurement of the branching fractions of the $\mathrm{B} \to \mu\mu(X)$ channels. The measurement of the branching fractions of the decays $\mathrm{B}^0_d \to K^{*0}\mu\mu$ and $\mathrm{B}^0_d \to \rho^0\mu\mu$ allows the CKM matrix-element ratio $|V_{td}|/|V_{ts}|$ to be determined. The square of this ratio is useful also for the estimation of the ratio of the mass differences $\Delta m_s/\Delta m_d$ in the $B^0_d - \bar{B}^0_d$ and $B^0_s - \bar{B}^0_s$ systems, complementary to direct measurements of the oscillation periods.

$\mathrm{B}^0_d \to K^{*0}\mu\mu$, $\mathrm{B}^0_d \to \rho^0\mu\mu$ and $\mathrm{B}^0_s \to \phi^0\mu\mu$ decays

The ATLAS collaboration has performed studies for the rare-decay channels described above with the following branching ratios assumed $\mathcal{B}(\mathrm{B}^0_d \to K^{*0}\mu\mu) = 1 \times 10^{-6}$,

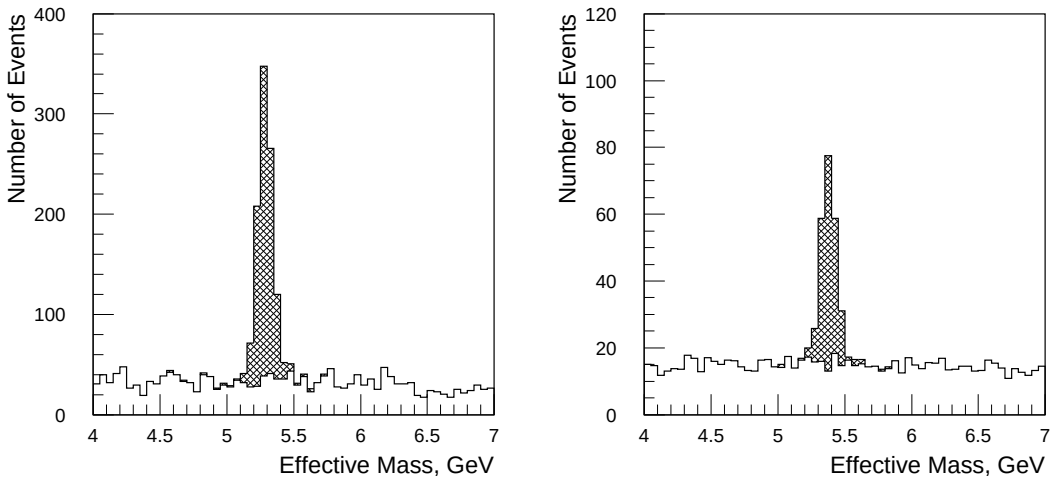

Figure 5.16: Reconstructed signal (cross-hatched) and background for $B_d^0 \to K^{*0}\mu\mu$ (left) and $B_s^0 \to \phi^0\mu\mu$ (right) decays with 30 fb^{-1}.

$\mathcal{B}(B_d^0 \to \rho^0\mu\mu) = 1.5 \times 10^{-6}$, and $\mathcal{B}(B_s^0 \to \phi^0\mu\mu) = 1 \times 10^{-7}$. Events were simulated fully and then reconstructed in the Inner Detector. For each channel 1500 signal events were analyzed with the following experimental cuts: both muons were required to have $p_T(\mu) > 6\,GeV$ and $|\eta(\mu)| < 2.5$, and both hadrons were required to have $p_T(h) > 1\,GeV$ and $|\eta(h)| < 2.5$. The muon reconstruction efficiency was assumed to be 85% for the LVL1 trigger muon, and 95% for the other muon. The reconstruction efficiency for hadrons was found to be 90% averaged over the full pseudorapidity region for $p_T > 1$ GeV. It was found that the individual-muon p_T distributions remain essentially unaffected by the choice of form factors. An important conclusion from this study was that, although the q^2-dependence of form factors affects q^2-dependence of the events, it does not influence the efficiency of triggering and reconstructing the signal events, or the rejection of the background [131].

The mass resolutions obtained by the Gaussian fit with the full reconstruction were: $\sigma(K^{*0}) = 30\,MeV$, $\sigma(B_d^0 \to K^{*0}\mu\mu) = 50\,MeV$, $\sigma(B_d^0 \to \rho^0\mu\mu) = 55\,MeV$, $\sigma(\phi) = 3\,MeV$, and $\sigma(B_s^0 \to \phi^0\mu\mu) = 52\,MeV$. In the case of the resonance, requiring the mass to be in the interval $[0.60, 0.94]\,MeV$ corresponded to 82% efficiency. In order to exclude the reflection of K^{*0} to ρ^0, hadron pairs forming an invariant mass within two standard deviations around the nominal K^{*0} mass using the K/π mass assignments were excluded. For the remaining pairs, both hadrons were assumed to be pions and the effective mass of the pair was required to be within the ρ^0 mass window. The possible reflections from $B_s^0 \to \phi^0\mu\mu$ to $B_d^0 \to \rho^0\mu\mu$ and $B_d^0 \to K^{*0}\mu\mu$ were found to be negligible.

For background studies, the following reactions were simulated by PYTHIA: B_d^0-meson decays $B_d^0 \to J/\psi K_S^0$, $B_d^0 \to \rho^0\mu\mu$ and $B_d^0 \to \omega^0\mu\mu$, B_s^0-meson decays $B_s^0 \to K^{*0}\mu\mu$ and $B_s^0 \to \phi^0\mu\mu$, semimuonic decays of one of the b-quarks, and semimuonic

decays of both b-quarks. It was found that the last reaction gave the main contribution to the background. Therefore, 13000 events of this type were simulated and analyzed similarly to the signal events. The mass distributions for the $B_d^0 \to K^{*0}\mu\mu$ and $B_s^0 \to \phi^0\mu\mu$ signals are shown, together with those for the backgrounds, in Figure 5.16. The application of all cuts leaves about 9% of the simulated signal events. The expected numbers of signal and background events after three years of LHC running at low luminosity are presented in the following table:

Channel	Branching ratio	Signal	Background
$B_d^0 \to K^{*0}\mu\mu$	1.5×10^{-6}	2000	290
$B_d^0 \to \rho^0\mu\mu$	10^{-7}	220	950
$B_s^0 \to \phi^0\mu\mu$	10^{-6}	410	140

From the ratio of the branching fractions for the two decay modes $B_d^0 \to K^{*0}\mu\mu$ and $B_d^0 \to \rho^0\mu\mu$, the ratio $|V_{td}|/|V_{ts}|$ can be determined, since the decay rates are proportional to the respective CKM matrix elements:

$$\frac{N(B_d^0 \to \rho^0\mu\mu)}{N(B_d^0 \to K^{*0}\mu\mu)} = \kappa_d \frac{|V_{td}|^2}{|V_{ts}|^2} \tag{5.2}$$

where κ_d is the ratio of form factors squared. The ratio $|V_{td}|/|V_{ts}|$ can be measured with a statistical accuracy of 14% for 30 fb^{-1} of low-luminosity data; the theoretical systematic uncertainty is about 7% [132]. Note that the reflection from $B_d^0 \to K^{*0}\mu\mu$ to $B_d^0 \to \rho^0\mu\mu$ is sizeable due to the large difference in the branching ratios assumed for the two channels. After assigning the wrong mass hypotheses to the K^{*0} decay products, the decay $B_d^0 \to K^{*0}\mu\mu$, reconstructed as $B_d^0 \to \rho^0\mu\mu$, gives a mass peak below, but close to, the B_d^0 mass. In contrast, the combinatorial background is approximately flat. Taking into account that the branching ratio for $B_d^0 \to K^{*0}\mu\mu$ can be measured with high accuracy, it is assumed that the $B_d^0 \to \rho^0\mu\mu$ signal can be extracted from an overall fit.

The general trend of the behaviour of forward backward (FB) charge asymmetry A_{FB} for Standard Model, shown on Figure 5.17, is that the asymmetry is positive at low q^2, has a zero at $\hat{s} = q^2/M_B^2 \approx 0.14$, and then becomes negative, irrespective of the details of the form-factor behaviour (except for the resonant region). The maximum of $A_{FB}(\hat{s})$ occurs at $\hat{s} = 0.05$. For the MSSM, the shape of A_{FB} is sensitive to the value of C_7, or equivalently to the value of $R_7 = C_7/C_7^{SM}$. For $R_7 > 0$ the shape is similar to that in the Standard Model, but for $R_7 < 0$ the asymmetry is negative at low q^2.

In the simulation, the resonant region $0.33 < \hat{s} < 0.55$ was excluded from the analysis. To estimate the experimental resolution of A_{FB} measurements in $B_d^0 \to K^{*0}\mu\mu$ decays, the total numbers of signal and background events after three years of low-luminosity running were used. If negative values of A_{FB} are experimentally observed in the first $\hat{s}$-region, this will demonstrate a clear signal of non-standard physics. The measurements in the second and third $\hat{s}$-regions, which practically do not depend on

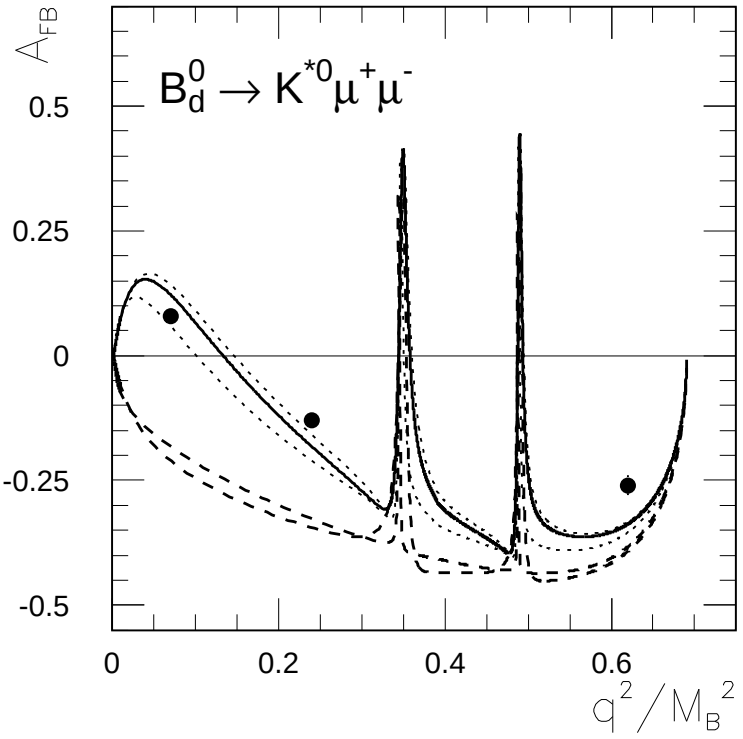

Figure 5.17: Sensitivity of A_{FB} to the Wilson coefficient C_7. The three points are the simulation results. The solid line shows the Standard Model prediction, the dotted lines show the range predicted by the MSSM for $R_7 = C_7/C_7^{SM} > 0$ and the dashed lines show the range predicted by the MSSM for $R_7 < 0$.

the models, will show possible systematic uncertainties in the experimental data. The expected measurement accuracy is sufficient to separate the Standard Model and the MSSM in the case R_7 <0 using measurements in the first $\hat{s}$-region.

$B_d^0 \to \mu\mu$ and $B_s \to \mu\mu$ decays

Purely muonic B-decays are predicted to have very low branching fractions within the Standard Model ($10^{-9} - 10^{-10}$), whereas they may have significantly higher ones in non-standard models. Simulationswere made with PYTHIA event generator. After applying all the cuts, the numbers of events expected for $30\,fb^{-1}$ at low luminosity is sufficient to observe the $B_s \to \mu\mu$ channel, assuming the branching fraction predicted by the Standard Model. The significance of the signal, however, is only $2.8\,\sigma$. The feasibility to reconstruct the purely muonic $B_{d,s} \to \mu\mu$ decays at high luminosity was also estimated. This estimation was based on the assumption that the pixel B layer will be operational at high luminosity, and that no degradation of the impact-parameter and p_T resolutions will occur. For each channel, 1000 signal events with

corresponding pile-up were fully simulated and reconstructed in the Inner Detector. The background was studied at the particle level using the parametrisation for p_T and impact parameter resolutions from ATLFAST. A sample of 10 000 background events with pile-up was used for this study. The numbers of events for both channels and the corresponding backgrounds expected for 100 fb^{-1} are given in the following table:

Channel	Signal	Background
$B_d^0 \to \mu\mu$	14	660
$B_s \to \mu\mu$	92	660

Combining the low- and high-luminosity samples, a $4.3\,\sigma$ significance can be obtained for the $B_s \to \mu\mu$ channel. The 95% CL upper limit for the branching fraction for $B_d^0 \to \mu\mu$ obtained with the combined sample would be 3×10^{-10}. It should be noted, however, that the B mass resolution of $69\,MeV$ is not good enough to separate B_s and B_d on an event-by-event basis, but their relative fractions would have to be fitted from the joint mass distribution. The study of rare muonic B decays at high luminosity will significantly improve the results which can be obtained at low luminosity, especially if data collection is continued for several years.

In conclusion, ATLAS will be able to study rare semi-muonic and muonic B-decays. It will be possible to measure branching ratios of the decay channels $B_d^0 \to K^{*0}\mu\mu$, $B_s^0 \to \phi^0\mu\mu$ and $B_d^0 \to \rho^0\mu\mu$. From the ratio of branching fractions for the two latter channels, it will be possible to determine the ratio $|V_{td}|/|V_{ts}|$ with a 14% statistical accuracy within the Standard Model. Measurements of the forward backward charge asymmetry in the decay $B_d^0 \to K^{*0}\mu\mu$ will also be feasible and may reveal new physics effects, for example in some parameter-space regions of the MSSM. Combining three years of low-luminosity and one year of high-luminosity data taking, the $B_s \to \mu\mu$ decay would be observed and a stringent upper limit for the $B_d^0 \to \mu\mu$ decay would be set, assuming Standard Model branching ratios. Given that these decays are highly suppressed in the Standard Model, there are hopes that any non-standard physics effects would significantly enhance the branching ratios, in which case the signals would be easier to detect.

Chapter 6

Construction and evaluation of ATLAS modules equipped with the SCTA128 chip

6.1 Introduction

The present chapter first introduces the baseline binary chip used for ATLAS modules. Several measurements aiming at checking the relevant design parameters and the radiation-hardness of the modules equipped with ABCD chips will be described. Next, the back-up solution based on an analogue readout chip (SCTA128) will be presented. Measurements of the parameters at chip, hybrid and module level will be described, as well as tests performed in the SPS X5 west beam test area. One of the disadvantages of the ABCD resides in the difficulty of the evaluation of a digital design, as most of the effects, like common mode noise, are masked by the digital output. The ABCD and SCTA128 share basically the same front-end design which makes of the SCTA128 an excellent solution to study the behaviour of the front-end of both chips.

6.2 The digital solution (ABCD)

6.2.1 Evolution of the design of the ABCD chip

The first modules equipped with the ABCD chips from the first batch were built in 1998-1999. These modules were showing much higher noise than expected: 900 electrons on the hybrid, and 1600 electrons when the chips were connected to 6 cm detector strips. In the modules using chips from the second batch there was also observed a large noise increase, observed only when all chips were mounted to the biased detectors. The excess noise was unavoidable on modules with more than a few tenths of channels connected to 12 cm strips at nominal operating conditions. Different combinations in hybrid ground plane geometry and different grounding schemes used to connect the detector bias to the analogue ground of the chip were tested but without gaining any substantial improvement. Another unexpected problem was

that of the large spread of discriminator thresholds. For the binary architecture one of the most critical issues is the uniformity of parameters of the front-end circuit and matching of the discriminator threshold.

In order to correct these problems a new design (ABCD2T/NT) with protection against noise pick-up and the selection of new components from the technology has been done. Both new technology choice and design change were made to reduce the threshold spread observed on ABCD2 chips. The new ABCD2NT version keeps a high gain ($140\,mV/fC$) in signal amplification, but large size analogue components are used to improve the matching properties. Also new high value resistors were used (extrinsic base resistor), instead of low implant resistors. The ABCD2T version is using a more drastic option to reduce offset mismatch: there is a 4 bit linear DAC (trim DAC) included in each channel to correct for individual mismatch of the threshold in the range of $150\,mV$. The 128 trim DACs are loaded with a new instruction set developed for this version of the chip. The ABCD2T design offers, however, better robustness with respect to radiation effects and therefore was chosen as the preferred option for the SCT.

The ABCD2T version has met all basic requirements of the ATLAS SCT, however, detailed evaluation of the ABCD2T chips, including extensive radiation testing, pointed to some possible improvements. These improvements, which concern mainly improvement of the radiation resistance and reduction of the design sensitivity to variation of the process parameters, have been implemented in the ABCD3T version [134]. One of the problems was that the internal calibration circuitry showed non-linearity for low input charges. It was not a critical issue, however, a good absolute precision is required for setting the working threshold in the discriminators which impact the efficiency and noise occupancy. The threshold setting will be based on calibration using internal calibration circuit, so the precision of this circuit around the nominal threshold setting, i.e. $1\,fC$, is a key issue. The source of the non-linearity has been identified and corrected for. Another problem was that the trim DAC response curves appeared to be non-linear and exhibited large spread from channel-to-channel. A non-linear response of the trim DAC is not a serious problem as the trimming procedure is based on measurement of the trim DAC characteristics and using these results in a look-up table. However, trim DACs in some channels become so non-linear that those channels fell outside the trimming range. Since for good chips it is required for all the channels to be within the specification, that effect, if not corrected, would impact significantly the yield in the production. The source of the problem has been identified in the design and an easy correction has been found. Radiation tests also showed that the spread of the discriminator offset increased significantly after irradiation and exceeded the range of the trim DACs. In order to not compromise the precision of threshold correction for non-irradiated chips and to guarantee that for fully irradiated chips all the channels can be corrected, a set of ranges has been implemented in the ABCD3T design. In the ABCD2T chips excessive leakage current was observed after irradiation. The source of the leakage has been traced down and corrected as well for ABCD3T.

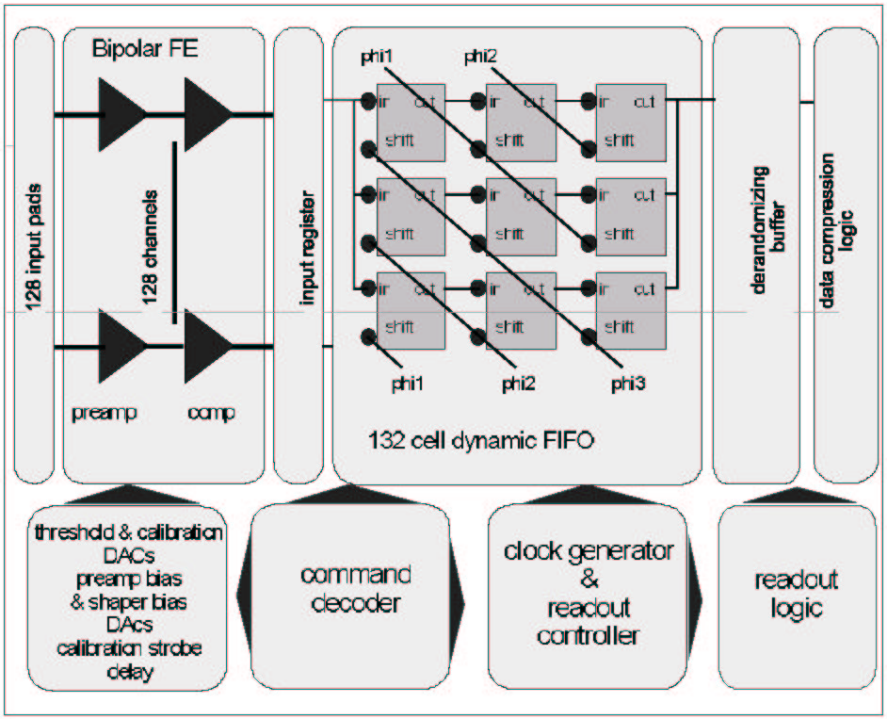

Figure 6.1: ABCD block diagram.

6.2.2 The ABCD chip

The main advantage of the binary readout system is a significant reduction of data to be read out as only addresses of channels which have recorded hits above the threshold are transmitted off the detector. A particularly important aspect for the binary readout architecture is the immunity of the overall system, and so of each component of the system, to the external and internal interference usually referred to as common mode noise, which unlike the analogue version, can not be corrected for. If one takes into account the irreducible noise sources present in the front-end system, i.e. the parallel and series noise of the preamplifier and the shot noise of the detector leakage current, an achievable signal-to-noise ratio is about 15 at the beginning of the experiment and about 10 after irradiation of silicon strip detectors and front-end electronics up to the doses expected after 10 years of LHC operation. With these signal-to-noise ratios there is a very little room for setting the discrimination threshold in such a way that the detector is fully efficient and the noise occupancy is well below the real data rate. Thus, any degradation of the signal-to-noise ratio will lead to either a drastic reduction of efficiency or an increase of noise occupancy.

The ABCD chip contains in a single chip all blocks of the binary readout architecture; the front-end circuit, discriminator, binary pipeline, derandomizing buffer, data compression logic, and the readout control logic, as required for the ATLAS SCT.

The preamplifier-shaper circuit provides signals with a peaking time of $25\,ns$. This

peaking time is sufficiently short to keep the discriminator time walk in the range of $15\,ns$ and the double pulse resolution below $50\,ns$. The preamplifier-shaper circuit is followed by a discriminator with a common threshold for all l28 channels which is controlled by an internal 8-bit DAC. In the ABCD2T design, in addition to the threshold control common for all channels, individual threshold correction per channel using a 4-bit DAC (trim DAC) has been implemented. The trim DACs are used only for correction of the threshold offsets and after the correction they are kept at fixed settings. The threshold scans which are used for extracting the basic analogue parameters of the front-end circuit are performed employing only the main 8-bit DAC that is common for all the channels on the chip. The binary data from the discriminator output are latched in the input register either in the edge sensing mode or in the level sensing mode with a time resolution of $25\,ns$, and clocked into a 132-cell pipeline. The true edge sensing mode puts a more rigorous constraint on the timing performance compared to the level sensing, but it minimizes the rate of data to be transmitted from the detector. Upon receiving a trigger signal the data are transferred from the pipeline to the second level buffer, which is a dual-port static RAM array 128-bit wide and 24-word deep. For each Level 1 trigger signal three columns from the pipeline are stored in the derandomizing buffer, so that the buffer is effectively eight events deep. The data is then compressed in the data compression logic according to one of four possible criteria and read out via a token ring allowing the read-out of six chips on one optical fibre. In addition to the basic functional blocks mentioned above, the ABCD2T chip has a calibration circuit for the internal generation of calibration pulses. The internal calibration circuit is foreseen to be used at various steps of chip testing and module testing as well as for threshold calibration in the experiment. A first purpose of this circuit is providing testability of the chip. It allows to take measurements of analogue parameters; gain, noise, offset, time walk and trim DAC characteristics for every channel during wafer screening without supplying a precise analogue signal to the chips. In order to extract basic analogue parameters of the front-end the discriminator threshold scan is performed for different levels of calibration pulses, corresponding to 1, 2, 3, $4\,fC$ etc of the input charge. From this data one can extract the gain and noise of the front-end circuit and effective offset of the discriminator for each channel according to procedures described in [135]. All these measurements are then repeated for complete modules equipped with 12 ABCD chips each.

6.2.3 Electrical module prototypes

The performance of the digital circuitry of the ABCD2T chips was evaluated using a general purpose IC tester. The logic functionality was verified against Verilog simulations and speed margins were evaluated for various blocks in the chip. The DAC characteristics were measured separately by probing DC voltages at the dedicated pads, which normally are not connected to the external circuitry on the hybrid.

Basic performance of the ABCD2T chips has been evaluated using the prototype SCT modules built of six chips and two daisy chained silicon strip detectors designed

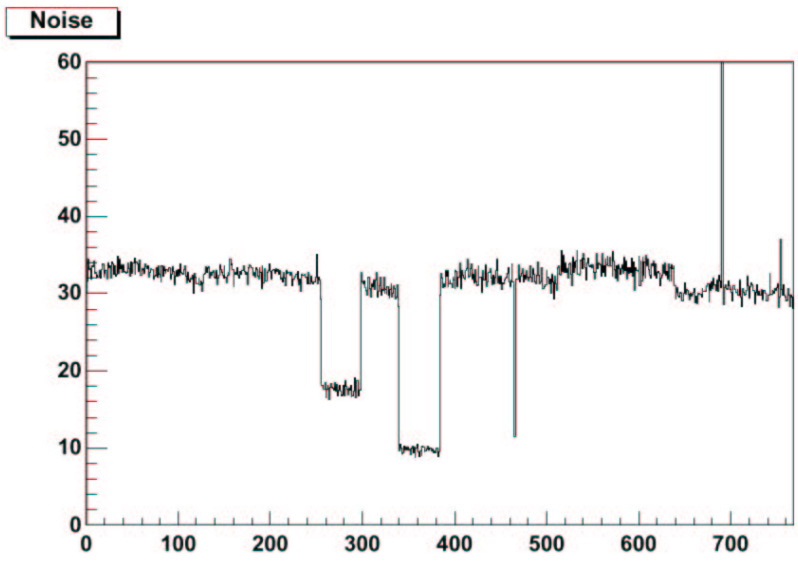

Figure 6.2: Noise in mV versus channel number distribution along a module (6 ABCDNT chips). Channels 256-288 are bonded to 6 cm detector strips. Channels 341-383 are not bonded to the detector. All other channels are bonded to 12 cm detector strips.

according to the SCT specifications [136] [137] [138] [139]. The chips were assembled on a ceramic hybrid and connected to the detectors in so-called centre-tap configuration, i.e. in the centre where the strips from the two detectors are joined together to form effectively 12.8 cm long strips. All basic parameters of the front-end circuit, gain, noise and offset were extracted from threshold scans for given input signals delivered form the internal calibration circuitry. The timing performance was evaluated from the delay scan of the calibration strobe signal. In all these measurements the data was transferred through the pipeline and readout buffer and read out at nominal clock frequency of 40 MHz.

Tests were done with the second batch of the ABCD chip (ABCD2), connected to 6 cm or 12 cm long strip detectors. The performance of modules depended on the signal gain in ABCD2 chips and on the grounding scheme. The design of the chip has been improved according to these observations.

Electrical module prototypes with ABCD2T (low gain, trim DAC version) and ABCD2NT (high gain, no trim DAC) with 12 cm strip detectors were found operating without excess noise in the full range of possible biasing of amplifiers. Figure 6.2 shows the noise measured on a module with 6 chips and strip detector. Chip number 3 (channel range 256 to 383) is mounted with 1/3 channels connected to 12 cm strips, 1/3 to 6 cm strips, and 1/3 are not connected to the detector. All other chips are connected to 12 cm strips. The noise amounts to 1400 (resp. 770, 430) electrons with 12 cm strips (resp. 6 cm and no detector bonded). The gain is as expected in the range of 140 mV/fC. The spread of thresholds was measured to be 7.8 mV rms,

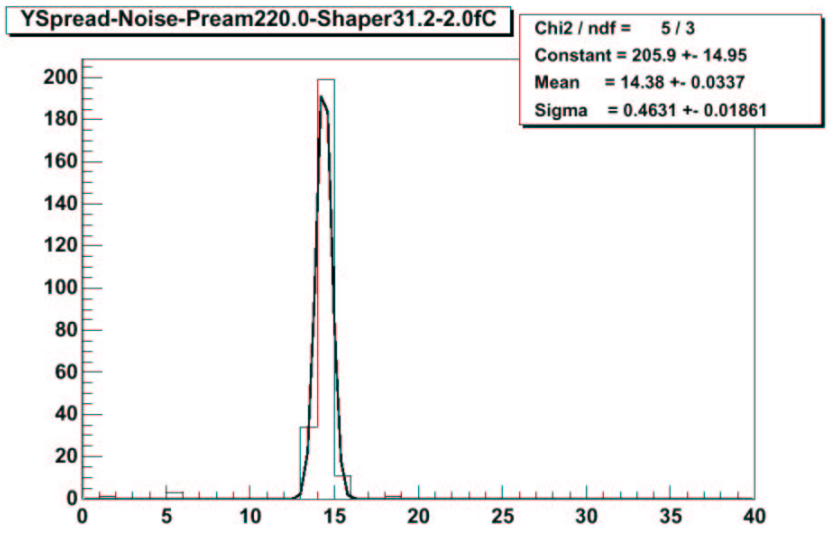

Figure 6.3: Noise distribution in mV along one module (6 ABCD2T chips).

which translates to 5.5% rms spread at 1 fC threshold.

Figure 6.3 shows the noise distribution measured on a module with 6 chips and strip detector (Figure 6.4). All chips are connected to 12 cm strips. The noise amounts to 1375 electrons with the 12 cm strips. The gain is in the range of 65 mV/fC. The spread of the thresholds is 3.3 mV rms, which translates to 5.1% rms spread at 1 fC threshold. This value is obtained after the individual trimming of thresholds for each channel. Before trimming the spread is 11.6 mV rms (18.3% at 1 fC threshold).

6.2.4 Effects of radiation on the ABCD

The DMILL technology is qualified as a radiation resistant one, however, the radiation levels expected for the SCT detector in the ATLAS experiment exceed the upper limits of those specified for the DMILL process, i.e. 10 $Mrad$ of the ionising dose and $1 \times 10^{14}\, n/cm^2$ 1 MeV eq. neutron fluence. In addition, if one takes into account very advanced requirements regarding the noise, speed and power consumption of the ABCD chip, it becomes obvious that radiation effects in the basic devices, although limited, can not be ignored [140].

The performance of the front-end circuit is affected by the major radiation effect in bipolar transistors, i.e. degradation of the current gain factor β. As a result the parallel noise in the front-end increases. Fortunately, the increase of the parallel noise has a small effect on the total noise when the chips are connected to long strips and the noise is dominated by the series noise. Another effect, which was not expected from the beginning but has been observed systematically in all radiation tests for all versions, is an increase of the offset spread in the discriminator. The source of this effect has been identified as worsening of resistor matching. The offset spread

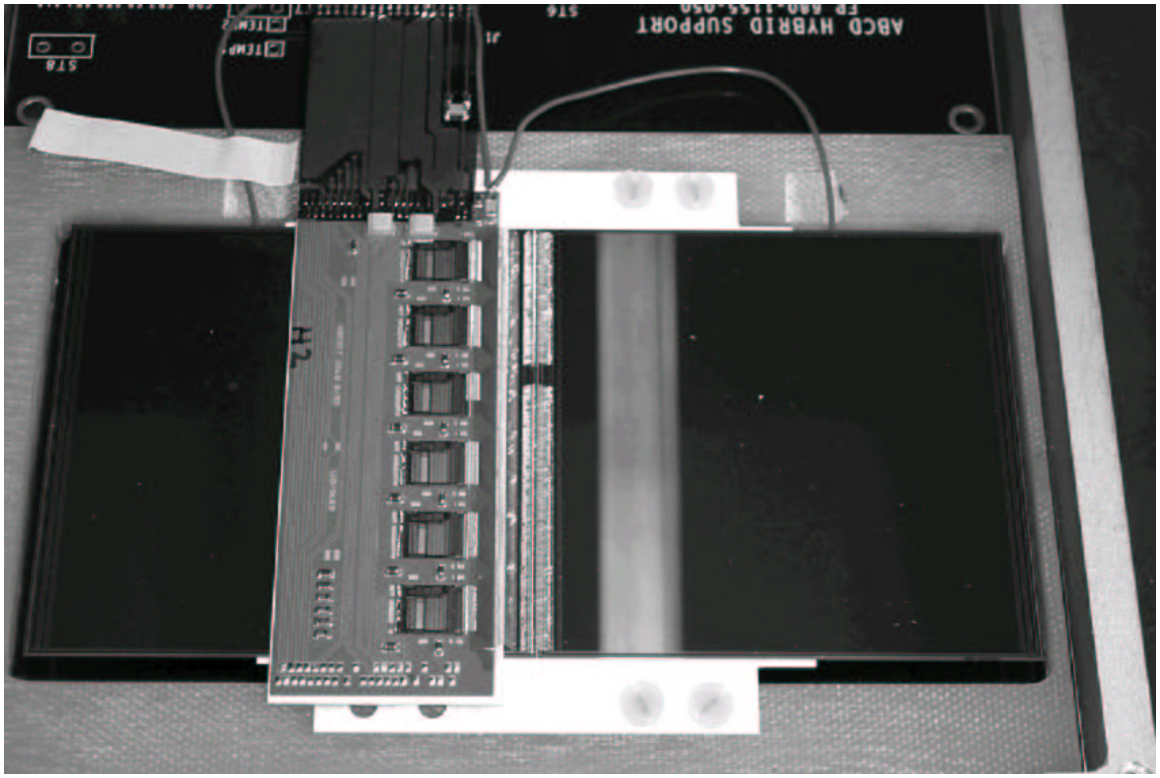

Figure 6.4: Picture of one module prototype with 6 ABCD2T chips for the SCT detector barrel.

increases by a factor 3-4 after proton irradiation and by a factor about 2 after neutron irradiation. After irradiation the trim DACs work correctly and for the majority of channels the offset can be corrected,

Since the ABCD chips will be exposed in the experiment mainly to high energy charged particles and neutrons, single event effects (SEE) are equally important as the total dose effects. Cross sections of SEE for two types of memory cells used in the ABCD design have been measured. For the pipeline in which dynamic memory cells are used the SEE rate has been measured as $5 \times 10^{-7}/bit/s$ [141]. For the static registers the SEE rate has been measured as $1 \times 10^{-7}/bit/s$. None of these numbers seems to create problem for operation of the SCT in the particle fluxes as presently estimated.

6.3 The analogue solution (SCTA128)

SCTA128, a 128-channel analogue front-end chip was developed as a backup for the readout of silicon strip detectors employed in the inner tracking detectors of the LHC experiment. The chip is produced in the radiation hard DMILL technology. The architecture of the chip and its performance on the test bench will be discussed. The chip is used to read out prototype analogue modules compatible in size, functionality

and performance with the ATLAS SCT baseline modules. Several full size detector modules equipped with SCTA128 chips has been built and tested successfully in the lab with radiactive sources as well as in the test beam. The chip has been used for other purposes as well:

- Readout of silicon strip detectors in the NA60 experiment
- Fast readout chip for diamond detectors
- Production quality assurance testing of silicon strip detectors for the ATLAS SCT
- Readout of silicon pad detectors for HPD applications
- Readout of silicon detectors in LHCb

6.3.1 The SCTA128 chip

The chips used for the readout of analogue modules have gone through iterations the basic structure being the same. These iterations were mainly aimed at improving radiation hardness and fault tolerance. Initially the readout chip has been designed in two versions: SCTA128LC optimized for low detector capacitance from $2\,pF$ to $5\,pF$ and SCTA128HC optimized for a higher detector capacitance from $15\,pF$ to $20\,pF$ [142]. The only difference between the two versions was in the front-end blocks the gain of the LC version being $100\,mV/fC$, and that of the HC version $50\,mV/fC$. Only SCTA128HC chips were used for analogue module construction. In the next submission changes were incorporated to adapt a single chip for a wider range of detector capacitance. Although the SCTA128HC chip has been used successfully over two years to build detector modules, it had its limitations. The development of the DMILL technology and the experience gained in testing both analogue and binary modules led to a better understanding and in April 2000 a new version of the analogue chip SCTA128VG [143] was submitted to the TEMIC foundry. In the new design special emphasis was placed on the reduction of possible variations of the circuit parameters with the operating conditions (temperature and power supply) and the variation of process parameters from run to run. Several changes in the structure of the biasing and grounding of the front-end stage both on schematic and at the layout level have been applied to improve the stability of the chip working in a detector system with millions of channels. In the following, whenever SCTA is written the characteristic will apply to both SCTA128HC and SCTA128VG chips.

Figure 6.5 shows the block diagram of the SCTA128VG designed for readout of silicon and diamond detectors with capacitance from $2\,pF$ to $20\,pF$. The chip consists of five basic blocks: front-end amplifiers, analogue pipeline, control logic including the derandomizing FIFO, command decoder and output multiplexer. It contains four 5-bit DACs for the bias of the analogue part of the chip and one 8-bit DAC for the calibration circuit. The front-end circuit is designed in such a way that it can be used with either polarity of the input signal. However, the full readout chain (NMOS switches in the analogue pipeline, output multiplexer) is optimized for p-side strips.

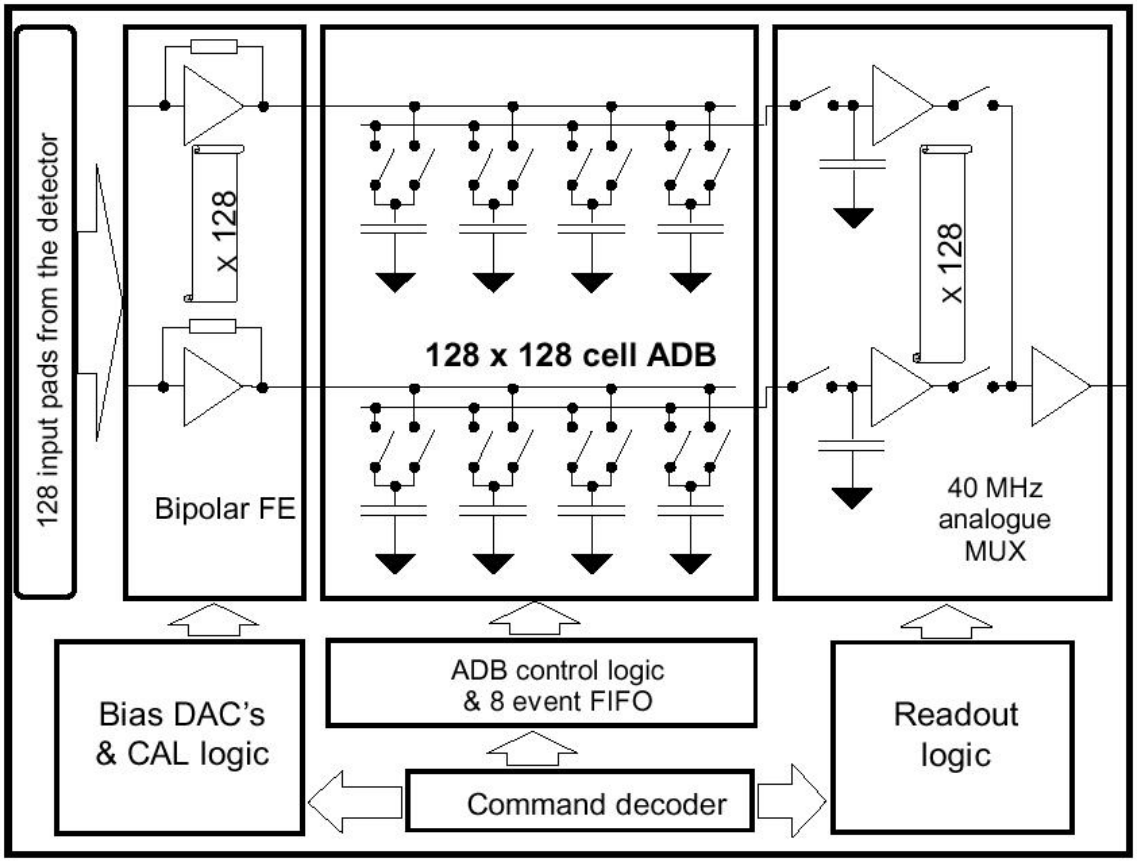

Figure 6.5: Block diagram of the SCTA128VG chips

The front-end circuit is a fast transimpedance amplifier followed by an integrator, providing a semi-gaussian shaping with a peaking time of $20 - 25\,ns$, and an output buffer. The peak values are sampled at $40\,MHz$ rate and stored in the 128-cell deep analogue pipeline. Upon arrival of the trigger the analogue data from the corresponding time slot in the ADB are sampled in the S&H buffer and sent out through the analogue multiplexer. The gain of the FE amplifier is of about $50\,mV/fC$. The designed peaking time for nominal parameters (resistors, capacitors) is roughly $20\,ns$.

There are four 5-bit DACs implemented in the chip. The current in the input transistor can be set using the preamp DAC. The actual bias current providing a maximal signal-to-noise ratio for a given detector capacitance depends on the value of the current gain factor β as well as on the detector leakage current and the detector bias resistance. Therefore for each detector the optimum bias of the input transistor should be found experimentally. The follower DAC (which is not present in the HC LC version) provides a reference current which is used to control bias currents in the two gain stages of the front-end amplifier. The setting of the follower current is not very critical, however, a setting different from the nominal one may be used in order to compensate changes in the circuit due to possible variation of the process parameters.

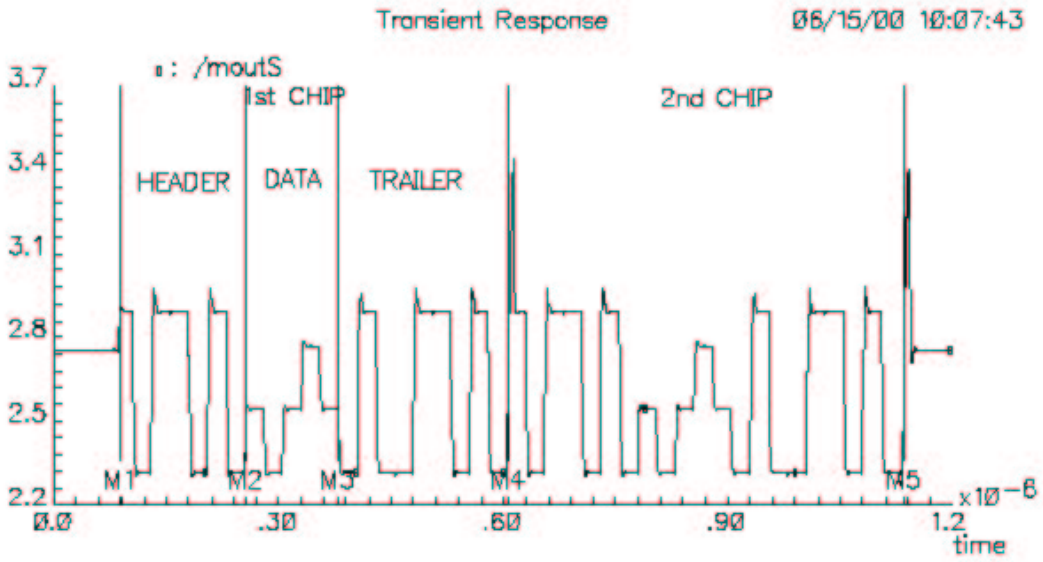

Figure 6.6: Simulation results of 2 chips sending data sequentially (only 5 analogue channels simulated instead of 128).

The shaper DAC provides a reference current which is used to control bias current in the output buffer of the front-end amplifier (in front of the ADB). The reference voltage VREF is used in the front-end circuit as well as in the readout amplifiers so that it provides good tracking of the DC levels in output buffer of the front-end and in the readout amplifier. The bias current in the ADB readout amplifier is controlled by another 5-bit DAC (ADB readout DAC).

Two SCTA128 chips can be read out via one fibre line. The readout sequence is initiated by an L1 trigger transmitted through the command lines. Once the trigger signal arrives, the pointed physical address of the 128-channel memory column with the sampled analogue values is stored in a derandomizing FIFO. The segment written in the pipeline corresponding to the trigger is protected and will not be overwritten before the event has been read-out or the pipeline has been reset. Up to 8 events can be stored in the derandomizing FIFO. In case of overflow the control logic issues the overflow bit, which is bundled with the physical data, and the chip needs to be reset. Since part of the ADB is spent on the derandomizer buffer the overall delay of the ADB is 118 clock cycles. For the next event to be read out the pipeline sends the data to the multiplexer which produces a serial data stream. The second front-end chip on the same fibre waits for the first chip to finish data transmission by pausing the appropriate number of clock cycles before sending the data.

An analogue signal package from one chip consists of a seven bit header (1011010) followed by 128 analogue samples with physical data from the detector, a one bit

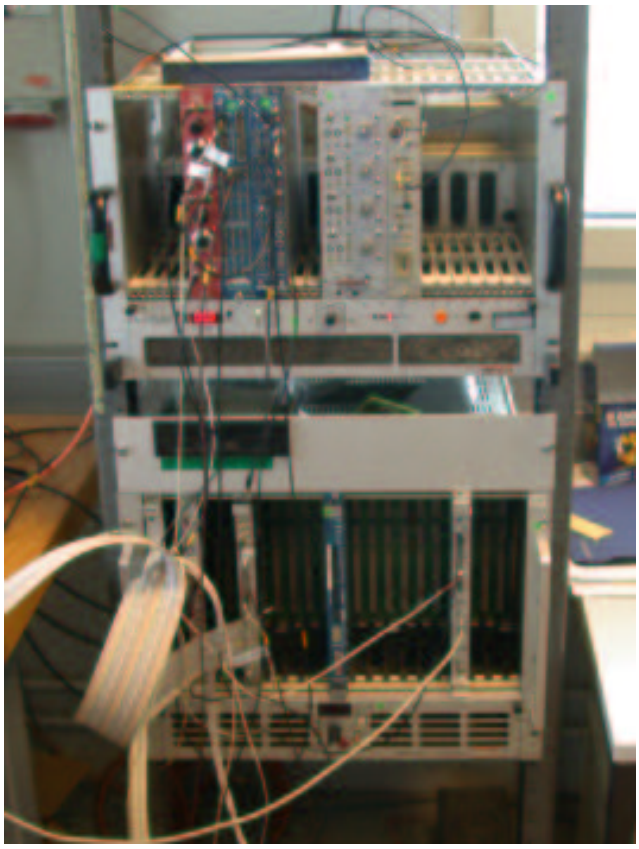

Figure 6.7: The setup used for the SCTA-DAQ

buffer overflow flag, a four bit BCO counter and a four bit T1 counter (Figure 6.6). The above format of the data is independent of mode of readout (single or two chip readout). The total time for readout on one fibre for two chips is thus $2 \times (7 + 128 + 1 + 4 + 4) \times 25\,ns = 7.2\,\mu s$.

The four-bit BCO counter and L1 counter returned by the chip can be used for unique association of each trigger with the physical data from the detector. The maximum clock rate of the multiplexer and the readout circuit is the same as the sampling rate of the data, i.e. $40\,MHz$. The chips can be read out with a lower rate ($40\,MHz$ divided by 2, 4, or 8) which is programmable. All the communication with the chip (i.e. sending the level 1 triggers, sending the software reset, loading the DACs, issuing the internal calibration pulses) is executed via a fast $40\,MHz$ serial interface by sending a bit pattern synchronous to the main clock.

6.3.2 Laboratory setup

The laboratory setup used in order to measure the characteristics is shown on Figure 6.7. The acquisition program was first written under Windows. Later, when National Instruments provided Linux drivers for its apparatus the DAQ program was

ported under Linux [144]. The analysis has always been performed under Linux. The DAQ program can drive the chip either in calibration mode, that is generating internal calibration pulses or in real DAQ mode, where the acquisition is triggered by an extrenal device, in our case a photomultiplier.

The setup consists of the following VME modules:

- SEQSI, which is used to generate the clock and control signals for the chip. It also generates the clock and the start signal for the ADC, and the stop signal for the TDC
- SIROCO is a flash ADC used to integrate the signal from the chip
- TDC is used to measure the correlation between the time of arrival of the trigger and the clock phase of the chip
- CORBO is a VME interrupt generator that will generate a VME interrupt whenever it receives a trigger
- Prescaler: it is optional and is used to divide the SEQSI clock in order to adjust to an SCTA multiplexer frequency smaller than $40\,MHz$

The system works as follows: the data acquisition program can issue software triggers and service external triggers. The software triggers are generated sending a pulse through one of the SEQSI output lines, and injecting that pulse into the TRIGGER input of the SEQSI. A handshake signal is used to avoid multiple triggers while the readout sequence is executed.

For the external triggers the SEQSI cooperates with the CORBO. The trigger produced by the photomultiplier is logically ANDed with the CORBO BUSY line. If the CORBO is not BUSY and the trigger is present, the output is sent back to the IN input of the CORBO to generate the interrupt.

The external trigger will also produce the START pulse for the TDC and, on reception of the trigger, the SEQSI will send the STOP to the TDC. It will also generate the clock and the START signal for the ADC. The delays between the different signals can be set in the SCTA DAQ.

The SCTA multiplexer can be run at frequencies which are smaller than $40\,MHz$. In that case the SIROCO will need a clock with the same frequency in order to correctly make the sampling. This is accomplished by the use of a prescaler. In order to synchronize the clock with the multiplexer clock a reset signal is sent to the scaler every time that the chips are reset.

6.3.3 Single chip tests

The basic parameters of the chip have been evaluated using internal calibration circuitry. The internal calibration circuitry provides a well-defined voltage step at the input of the calibration capacitors connected to every channel. Since the characteristic of the calibration DAC can be measured, the inaccuracy of the electronic calibration is related only to the deviation of calibration capacitors from the nominal

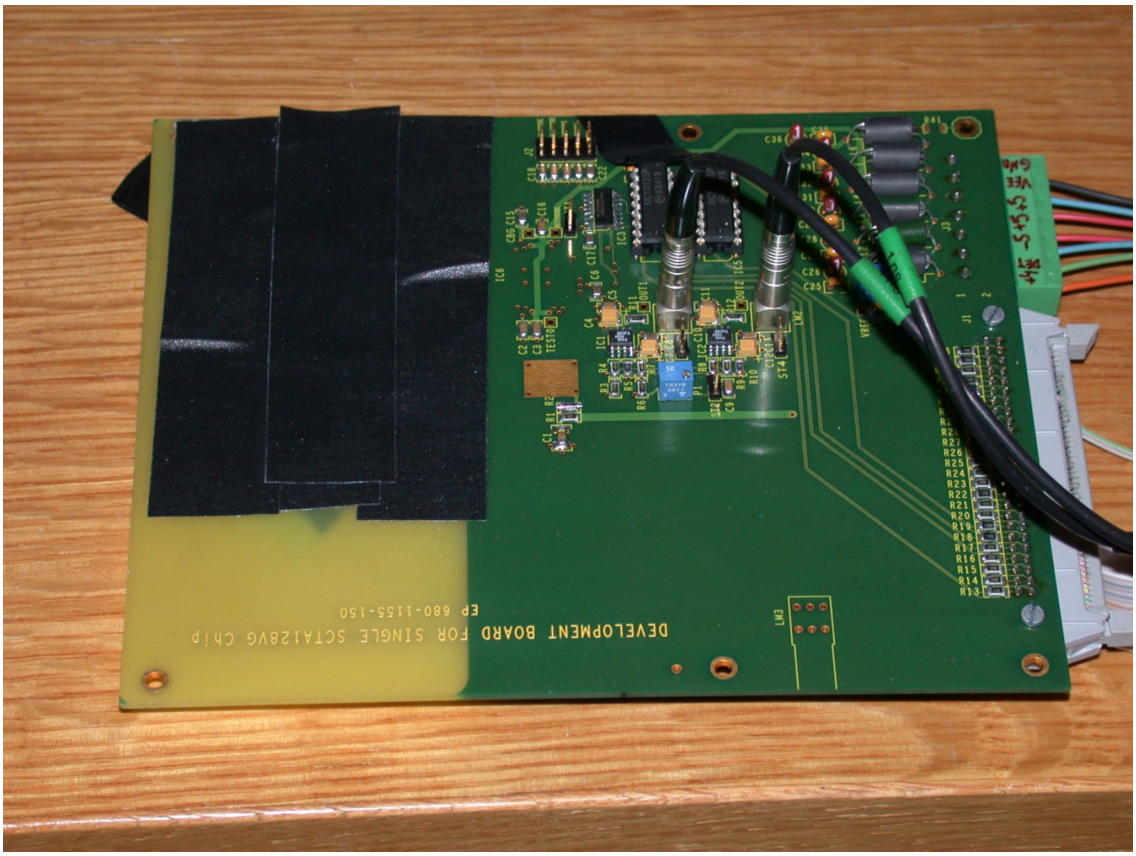

Figure 6.8: Single chip tests (the chip is in a protected space underneath the PCB).

value and the mismatch of the resistors used for the scaling of the calibration voltage. For comparison with the results obtained with the electronic calibration, the absolute calibration of the chip in the set-up with a silicon pad detector and β source is also presented. All the data taken either in the laboratory or in beam tests is corrected for common mode fluctuations and pedestal-subtracted. The calibration factors are extracted from a fit to the header. Instabilities arising during data taking result in the update of the pedestals and noise.

For tracking applications there is no particularly demanding requirement with respect to the linearity. Nevertheless, the SCTA chip has been designed to provide a linear response up to $12\,fC$ of the input charge. Figure 6.9 shows the linearity measured for one channel. The average gain is $25\,mV/fC$ for SCTA128HC and $40\,mV/fC$ for SCTA128VG while a typical spread of gain in 128 channels of one chip is $0.9\,mV/fC$ rms, i.e. 3% (Figure 6.10). Although the uniformity of the gain is not a very critical issue for the analogue architecture the obtained figure allows use of the chip without off-line correction.

The noise performance of the SCTA chip can be optimized according to the detector capacitance by choosing a proper value of the current in the input transistor. An

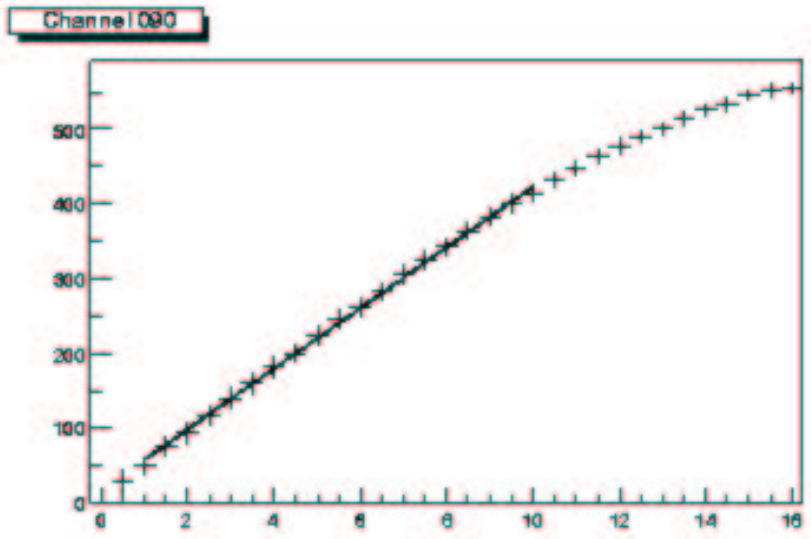

Figure 6.9: Gain linearity for a single channel

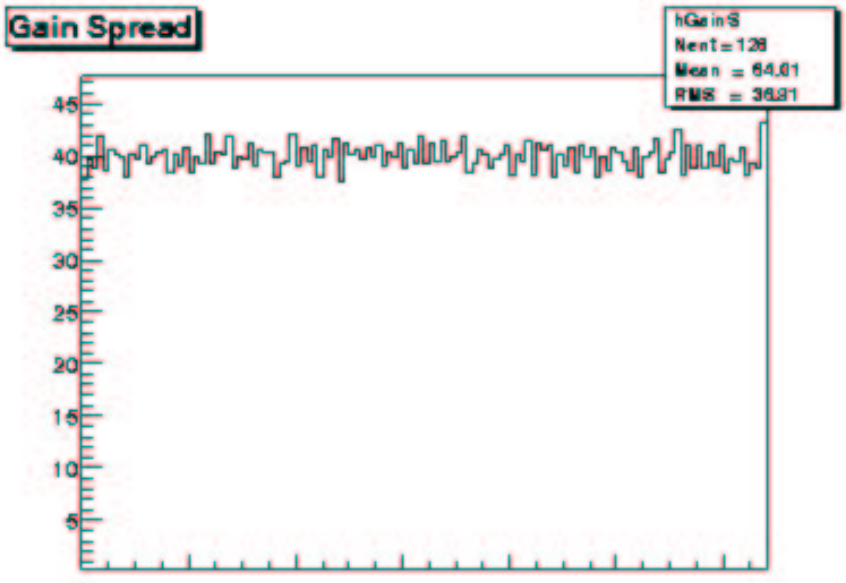

Figure 6.10: Gain across the 128 channels of a single chip

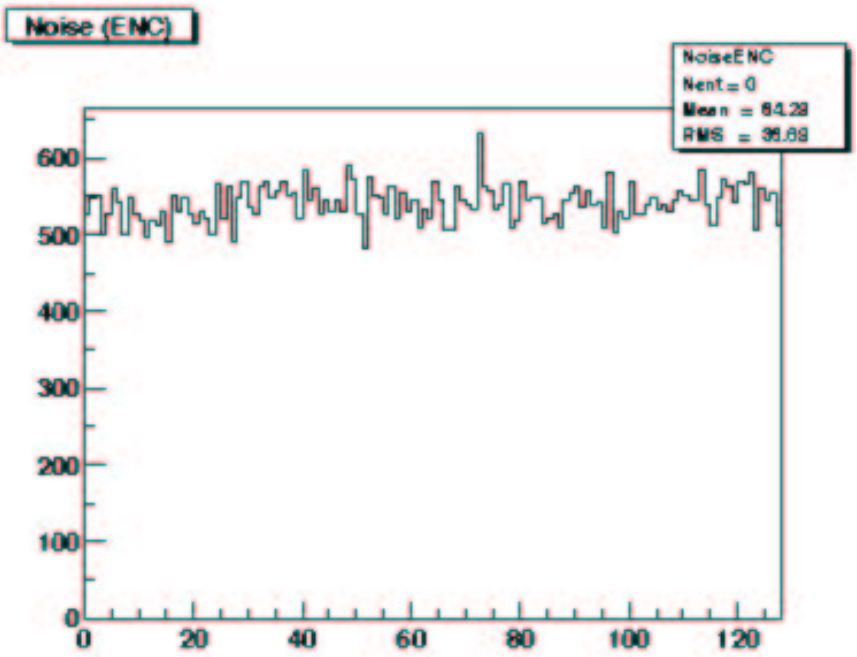

Figure 6.11: Noise across the 128 channels of a single chip

example of the noise distribution is shown on Figure 6.11. The $500 - 550\,e^-$ noise is typical of a single chip not connected to sensor strips.

Since the SCTA chip performs very simple voltage sampling where only analogue value is stored/retrieved from the pipeline, the pedestal spread between ADB cells contributes as additional noise source. By varying the delay between the reset of the read/write pointer in the ADB and the trigger sent to the chip one can obtain the pedestal map in the ADB. Figure 6.12 shows the ADB pedestal map for one chip (128 cells $\times$ 128 channels). From the presented plot one can extract the cell-to-cell pedestal variation as well as the variation of the DC offset spread between the channels.

The distribution of the ADB pedestal spreads for all the channels in one particular chip is shown in Figure 6.13. The $1.1\,mV$ mean value of the distribution is equivalent to $150\,e^-$ ENC of extra, non-correlated contribution to the noise generated by the front-end. For a low value of the input current and a low detector capacitance the additional contribution is about 4%. For higher detector capacitances and respectively higher currents in the input transistor, as required for optimization of noise, this contribution becomes negligible.

The measurment has been done using $40\,MHz$ readout clock for the output multiplexer, which is synchronous with the ADB sampling clock. Using slower multiplexer clock increases the activity of the digital signal asynchronous to the sampling clock which couple through the chip substrate to the inputs of the front-end and increases the pedestal spread. The typical value of RMS pedestal spread in analogue memory for lower readout frequency is in the range of $1.2\,mV$.

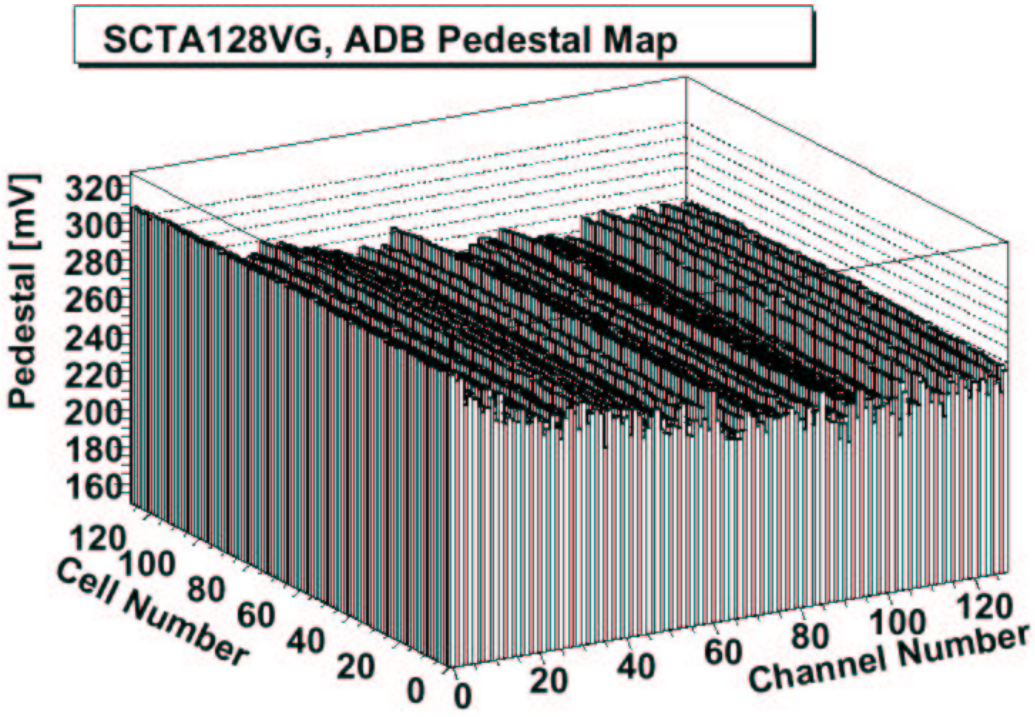

Figure 6.12: ADB pedestal map in one SCTA chip

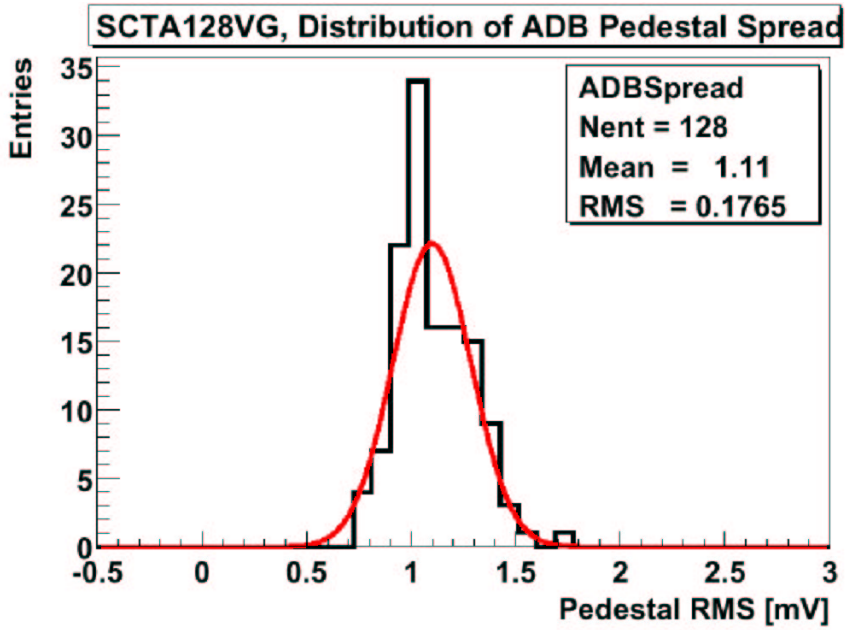

Figure 6.13: ADB pedestal spread distribution for all channels in a chip

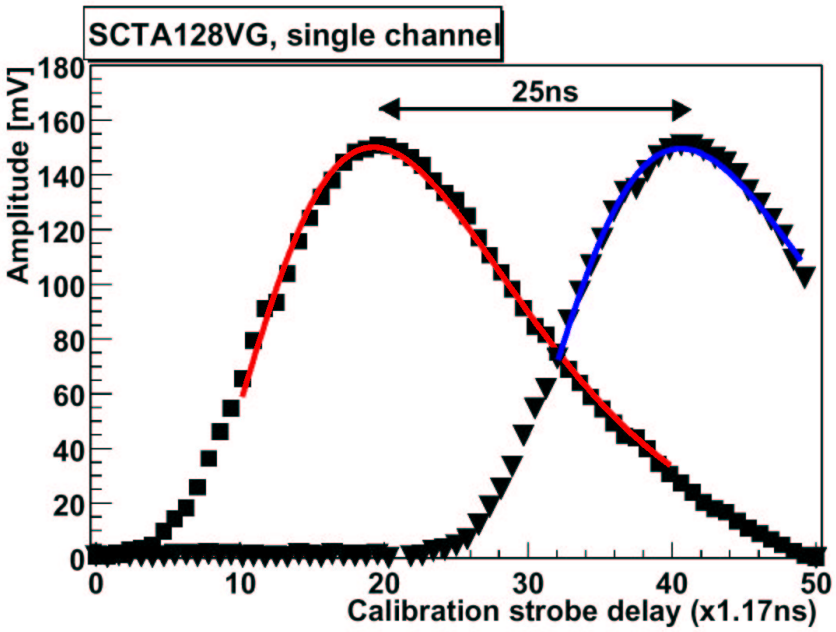

Figure 6.14: Pulse shapes at the output of the multiplexer obtained from the delay scan for two consecutive trigger delays.

The pulse shape at the output of the front-end amplifier has also been studied by scanning the delay of the calibration signal with respect to the 40 MHz-sampling clock for the analogue pipeline. In order to normalize the results to the absolute time scale the measurement has been repeated for two consecutive values of the trigger delay. Figure 6.14 shows the example of the measurement done for one typical channel of the SCTA128VG chip. The injected charge was 3.5 fC. The obtained 18 ns peaking time is in the expected range given by the technology process variation. The RMS spread of the peaking times for all the channels in an SCTA128VG chip was measured to be in the range of 0.6%.

The gain of the output buffer of the analogue multiplexer is in the range of 0.8[V/V]. The gain of the front-end amplifier is about 50 mV/fC. Therefore the final gain of the whole read-out chain is roughly 40 mV/fC. All figures in this section showing the gain and linearity refer to the full processing chain (front-end amplifier, ADB and output multiplexer).

Given the extreme radiation levels expected in the trackers of experiments at the LHC radiation hardness is a very important issue of any front-end chip. The SCTA128HC version of the chip was produced when the DMILL process was not yet completely stabilized. In particular, some resistors in the chip exhibited a high sensitivity to radiation, resulting in increases of up to 50% after the total dose. This effect created problems for the DC bias conditions of the circuit so that the noise performance could not be tested up to the ultimate radiation levels. Although in the SCTA128VG these problems were corrected radiation effects in the devices can not

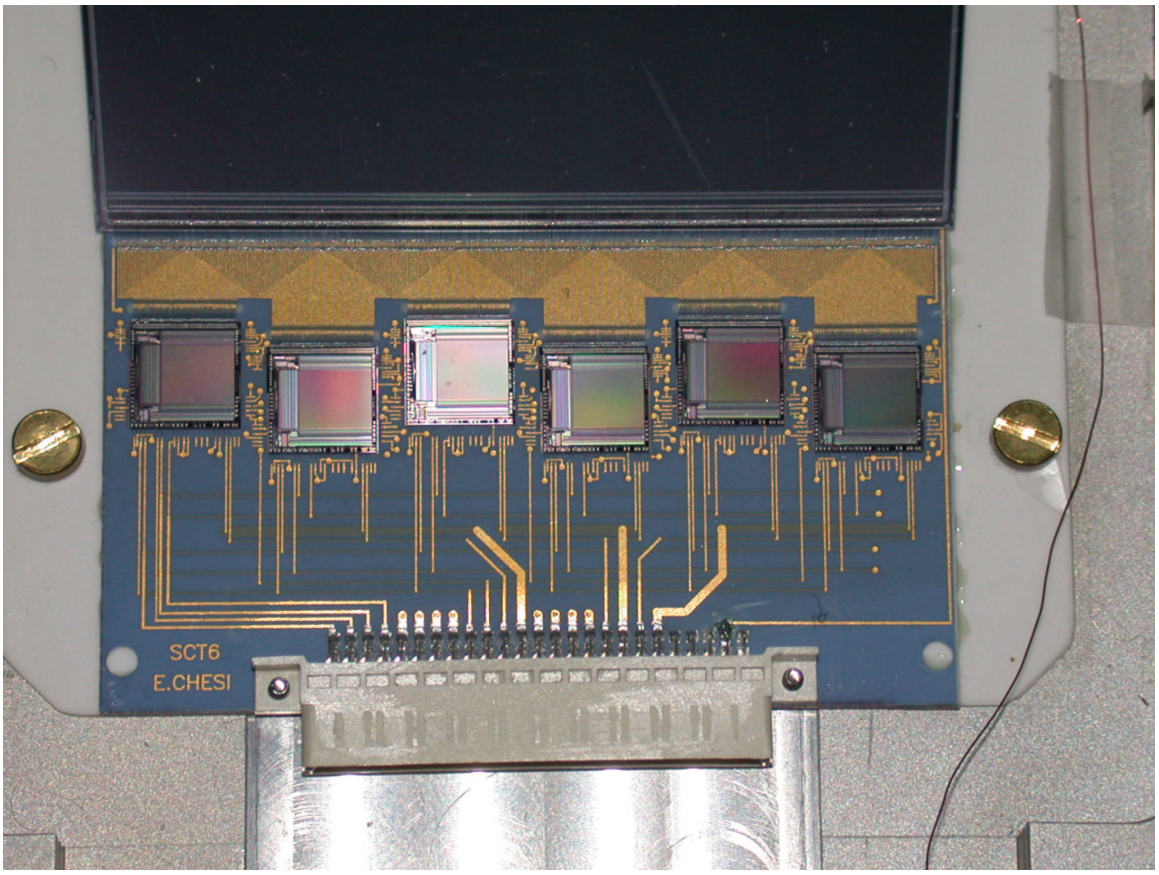

Figure 6.15: A hybrid equipped with 6 SCTA128HC chips

be ignored. The critical issue is the noise in the front-end amplifier. A second order effect is the possible degradation of matching which can affect the uniformity of the channels in terms of gain, speed and ADB performance. X-ray irradiations have been performed at CERN with different dose rates to study these effects. The increase of parallel noise due to the BJT β degradation is as expected and can be neglected in the case of a chip working in a module connected to a detector when the serial noise due to the capacitive load is dominant. As expected there was a small decrease of gain (7%) and analogue power consumption (8%). The peaking time and the uniformity of the ADB pedestals were unaffected by X-ray irradiation. For more information on irradiation tests of the SCTA chip see [145] and[146].

6.3.4 Module construction

The microstrip silicon sensors for the ATLAS experiment are single sided 285 μm thick detectors with highly p-doped implant strips in a high resistivity n-type substrate. The implanted strips are AC-coupled to the Al-readout strips via a silicon-dioxide/silicon-nitride layer. The coupling capacitance is of the order of $20\,pF/cm$.

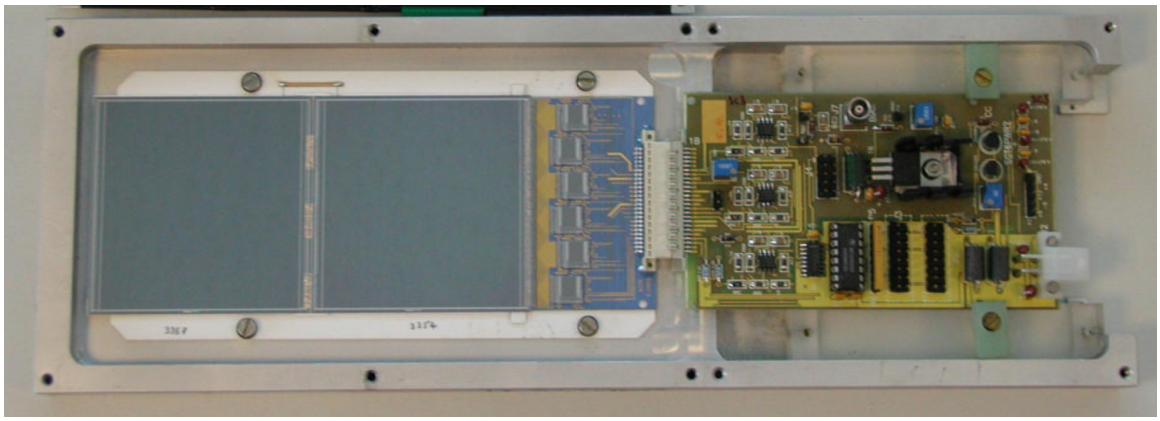

Figure 6.16: Module equipped with SCTA128HC chips and AC-coupled ATLAS barrel detectors.

The strips are biased from a common bias line through polysilicon resistors. The pitch of the detector is $80\,\mu m$.

A module consiting of 6 SCTA128HC chips and two $6 \times 6\,cm$ silicon strip detectors was built (Figure 6.16). The 6 chips were placed on a ceramic hybrid with integrated fan-in needed to match the strip pitch of $80\,\mu m$ and the pitch of the input pads on the chip, which is $60\,\mu m$. The hybrid was glued onto a ceramic board (Al_2O_3) using non-conducting glue. Then spacers were placed on the ceramic in order to compensate for the $720\,\mu m$ thickness of the hybrid in order to connect the guard ring of the detector directly to the ground line at the edge of the hybrid. The two CSEM ATLAS barrel detectors were placed in end tapped configuration in order to avoid pick up between the hybrid and the detectors. Their backplanes were connected together.

The ceramic "ladder" provided a good flat surface to be supported for the bonding jig. The strips of the detector closest to the hybrid were all bonded to the integrated pitch adaptor. As there are 6 chips on a hybrid which are to be read out in pairs it was decided to bond one chip per pair to one sensor, and the other to both sensors. That means one chip's channels are connected to $6\,cm$ strips and the other chip's channels are connected to $12\,cm$ strips. This configuration enables us to study the effect of strip capacitance on the front-end of the chips. Bondings between the two detectors were done accordingly: 128 bonded channels were followed by 128 unbonded ones.

The ceramic piece with the hybrid and the sensors was then mounted in a specially designed metal box. This box was meant to hold the module in the beam telescope as well as to provide mechanical protection and light-tightness. The grounding scheme of the box was extensively studied in order to avoid any pick-up problems. The box accomodated the ceramic with the hybrid and the sensors as well as the support card that was servicing the hybrid.

It was also interesting to compare the performance of the AC-coupled detectors with the DC-coupled ones. The ATLAS baseline has chosen the AC-coupled detectors for the barrel and forward modules of the SCT. However, if the performance of DC-coupled detectors could be proven to be corresponding to the requirements, it could

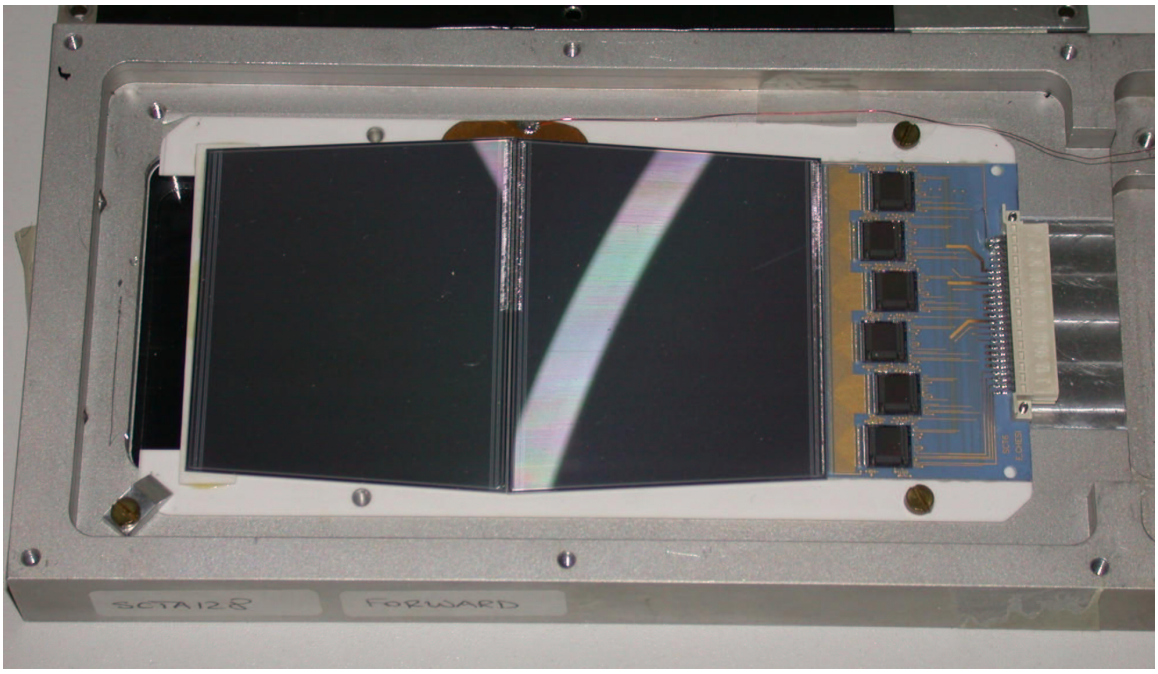

Figure 6.17: Module equipped with SCTA128HC chips and DC-coupled ATLAS forward detectors.

result in important cost savings for the collaboration. The DC-coupled modules used were wedge 32 type forward p-on-n sensors. The first three chips were bonded to 6 cm strips, while the last three were bonded to 12 cm strips. Concerning the mechanical assembly, few changes were needed. The same hybrid and same ceramic "ladder" were reused as for the "barrel" module. In order to see the effects of different strip capacitance, two such forward detectors were connected together on their outer side, the inner side of one of them being connected to the hybrid (Figure 6.17). The first three chips of the hybrid were bonded to only one of the detectors, while the other three were bonded to both of them. Other, than this geometrical difference, the "barrel" and "forward" modules are identical.

Finally, as the new SCTA128VG chips were produced, a module equipped with barrel AC-coupled detectors was produced in order to evaluate their performance. It was assembled in exactly the same way as the first "barrel" AC-coupled module.

6.3.5 Si strip detector module at the test bench

The modules were tested at different stages of the construction in order to notice any irregular behaviour. Hence, tests were performed after placing each pair of chips on the hybrid. After all 6 chips have been placed on the hybrid, extensive tests were carried out in order to characterize the chips. For example, Figure 6.18 shows The main characteristics of the leftmost two chips after they were glued to the hybrid. Neither the gain nor the noise performance has been degraded. It shows that the

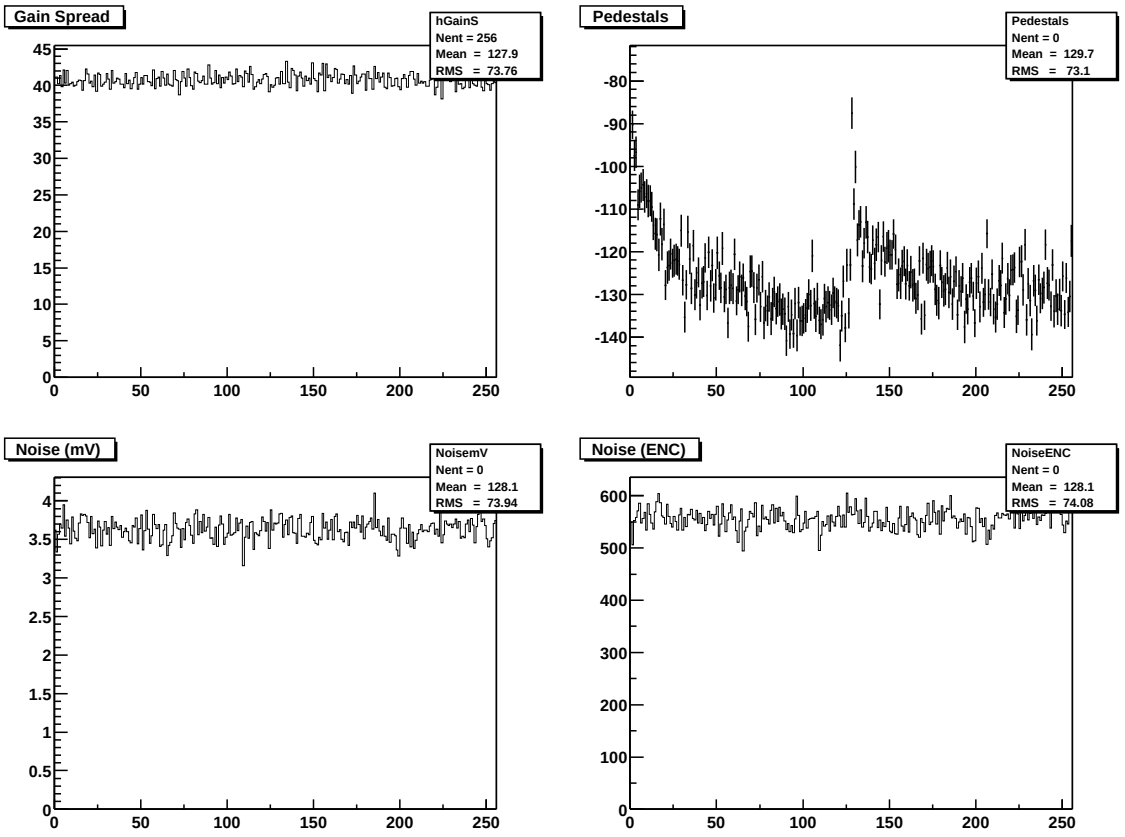

Figure 6.18: Characteristics of the two leftmost chips on the hybrid

mechanical operations (glueing, bonding) have not damaged the chip. It also shows that there is no additional pickup between the chips, hence proving the robustness of the hybrid design concerning the grounding scheme.

The next step in testing was performed when the detector was connected to the chips. Checks were performed in order to see whether the gain stayed the same and whether the noise increased as expected from the strip length. Figure 6.19 shows an example gain distribution of the leftmost two chips which are now connected to a detector. It can be quickly deduced from the plots which chip is connected to $6\,cm$ silicon strips and which one to $12\,cm$. For the first 128 channels the noise increased to $1700\,e^-$ as expected from a capacitance generated by $12\,cm$ strips. The noise is only $1100\,e^-$ for the channels which are connected to half that capacitance (i.e. $6\,cm$ strips). One can also observe that the process of bonding resulted in some channels being shorted (no gain) and some channels picking up noise. When constructing the first prototypes these types of problems are normal. However, in production, solutions must be found to reduce the number of deficient channels to one per chip.

The noise performance of the SCTA chip was optimized according to the detector capacitance by adjustment of the current in the input transistor. Figure 6.20 shows

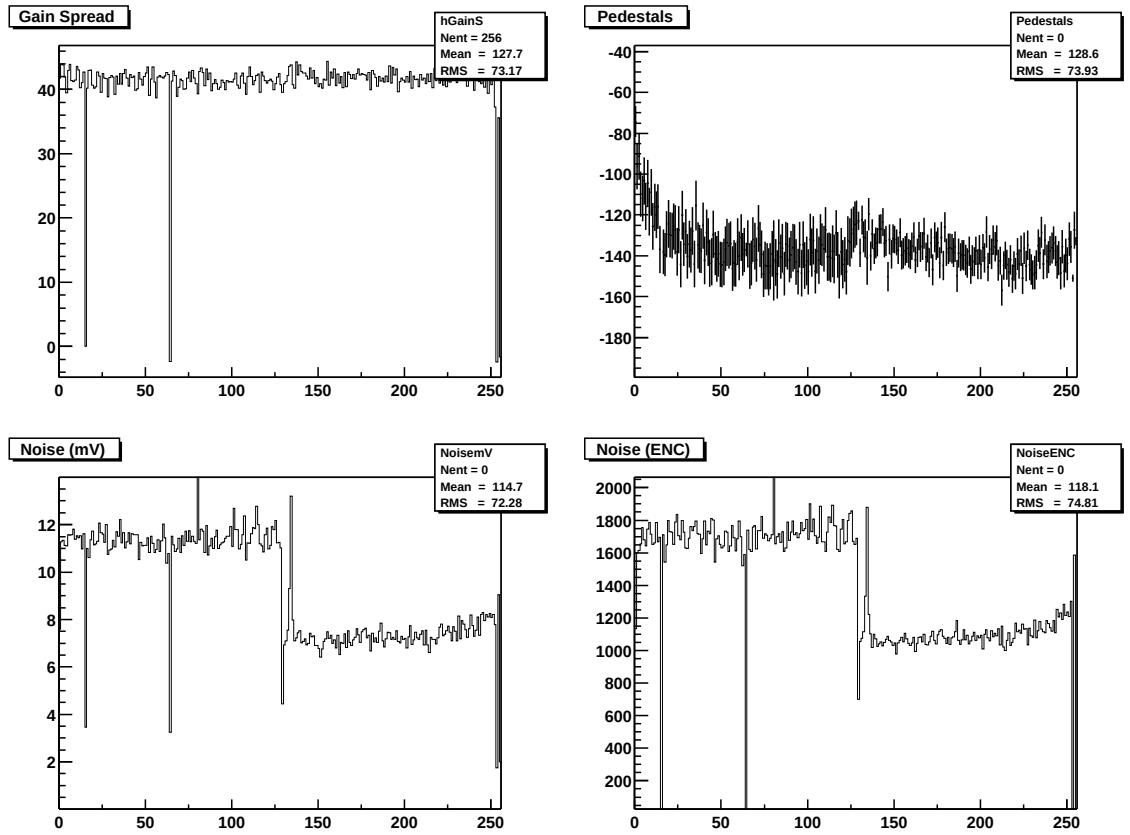

Figure 6.19: Characteristics of the leftmost two chips of the module

the results of noise measurements of one module with SCTA128VG chips connected to 6.4 and 12.8 cm long silicon strip detectors. The measurement has been done for various bias conditions of the input transistor. The noise performance of the chips connected to 12.8 cm strips could be improved by increasing the bias current of the output transistor. However, the reduction of ENC is relatively smaller for high current since the noise of the base spread resistance and the noise of the strip resistance become limiting factors.

Another important test was to see the chip behaviour not only with internal calibration circuitry, but with real particles as well. It was also important to prove the linearity of the electronics, i.e. that on the absolute scale the system's response is linear. In order to do that γ-ray sources were placed on top of the sensor. The chips were read out continuously in the 8-sample mode. The data acquisition program was searching for pipeline cells with signals exceeding the noise by $5\,\sigma$. These events were recorded for further analysis. A fit was made to the samples using the known waveform of the shaper output. The peak values from these fits were histogrammed for various radioactive sources such as Americium, Terbium and Cobalt. These tests demonstrated the linearity of the chip (Figure 6.21).

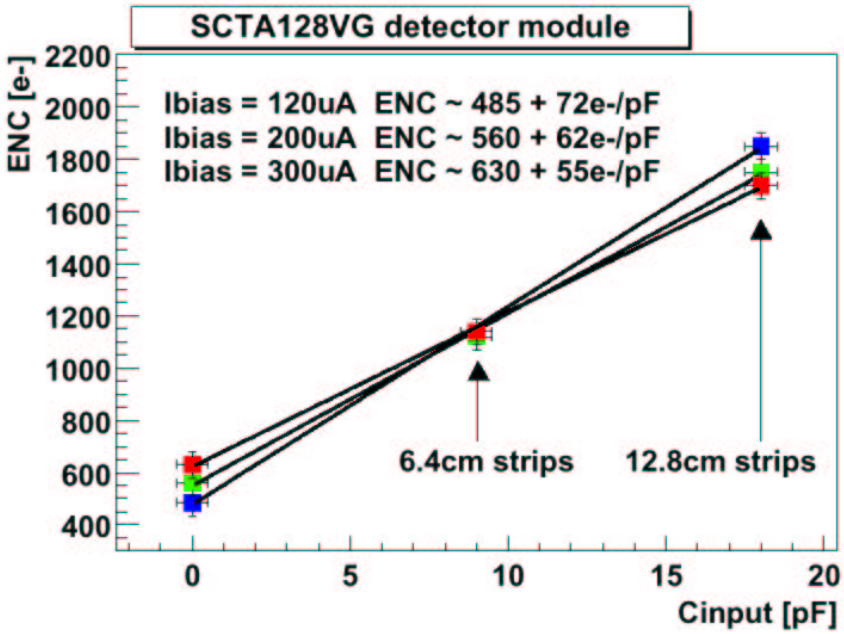

Figure 6.20: ENC for SCTA128VG chips connected to various length silicon strip detectors

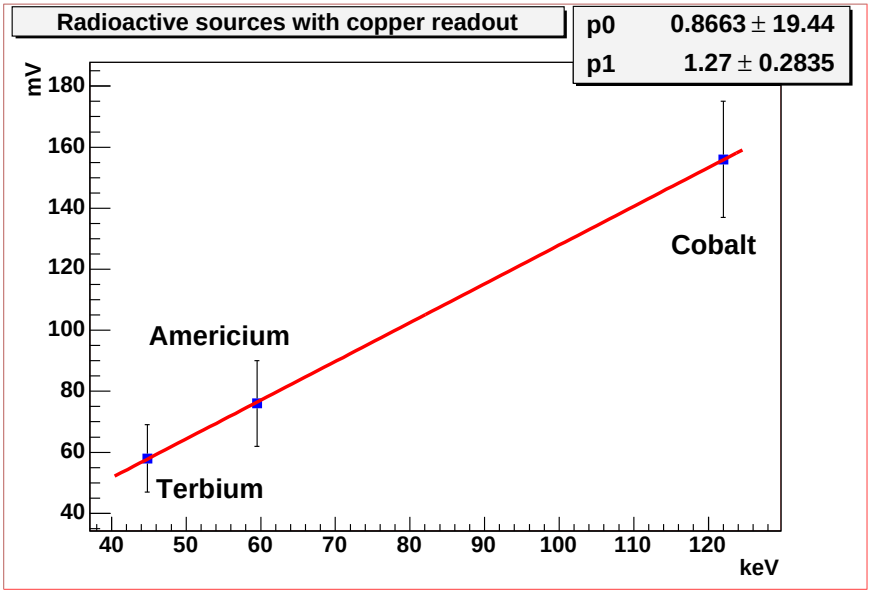

Figure 6.21: Linearity of the chip based on radioactive source tests.

6.3.6 Beam test setup

Then the module was moved to the SPS X5 west area for a beam test, where its performance in 'real' conditions was studied. The box containing the module had an axis for mounting in the beam telescope around which it was possible to turn it as well as dowel pins to ensure precise positioning. There was also a metal plate which was fixed in the beam telescope and had holes for the dowel pins at positions which were placing the module at 0, 15, 30, 45, 50 degrees compared to the plane perpendicular to the beam. The box had also two additional axes in order to be able to shift the whole box to the left or to the right compared to the z axis and illuminate the two other pairs of chips.

The beam telescope of RD42 was used [147]. The beam telescope had 8 silicon detector planes, each with a size of (length $\times$ width $\times$ thickness) = ($12.8\,mm \times 12.8\,mm \times 300\,\mu m$). The strips of a plane were oriented either vertically (V) or horizontally (H). The 8 planes were grouped in two modules where 2 vertical planes were sandwiched between two horizontal planes (HVVH). The SCTA128 module was placed in between to have good quality tracking. The silicon detectors were single sided p-on-n strip detectors with a pitch of $50\,\mu$m. The beam telescope provided the track position with a resolution of $2\,\mu m$ in both coordinates perpendicular to the tracks.

The system was triggered using a fast plastic scintillator placed in the beam in front of the telescope. A total of 256 strips per plane were read out using low noise VA2 (CMOS) electronics. The data acquisition system, based on VME bus with ELTEC E-16 processor running OS/9 had a typical acquisition rate of 100 to 300 trigger events per spill. The data was recorded on EXABYTE magnetic tapes during spill breaks.

6.3.7 Beam test results

For the analysis of beam test data first a set of events is processed in order to obtain the pedestals, the electronic noise and the calibration factors for the readout flash ADC card. Then a search for clusters is performed, selecting strips having signals higher than 4 times their noise. Any neighbouring strips with a signal over noise figure exceeding the value of 3 are added into the cluster definition. The signal over noise distributions for the cluster signals for $12.8\,cm$ strips are shown in Fig 6.22. The most probable value of the signal-to-noise ratio is 19. These values are largely sufficient to provide a high particle detection efficiency while keeping the noise occupancy well below ATLAS requirements.

For the given strip pitch of $80\,\mu m$ and perpendicular tracks most of the events result in single strip hits. For those events the spatial resolution is expected to be that of a binary system, i.e. pitch/$\sqrt{12}$. For double strip hits one gets a significant improvement of the spatial resolution by weighting the reconstructed position with signal amplitudes for the neighbouring strips. In our test we had around 85% of single strip hit events and 15% of double strip hits. The spatial resolutions are $21.4\,\mu m$ and

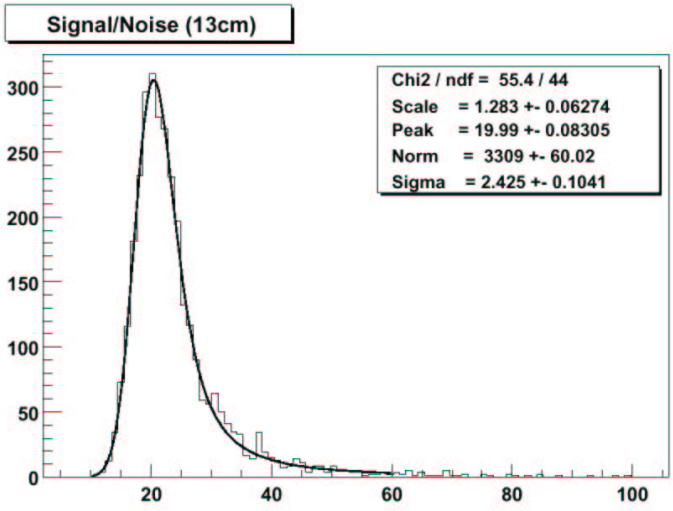

Figure 6.22: Signal over noise for 12.8 cm strips

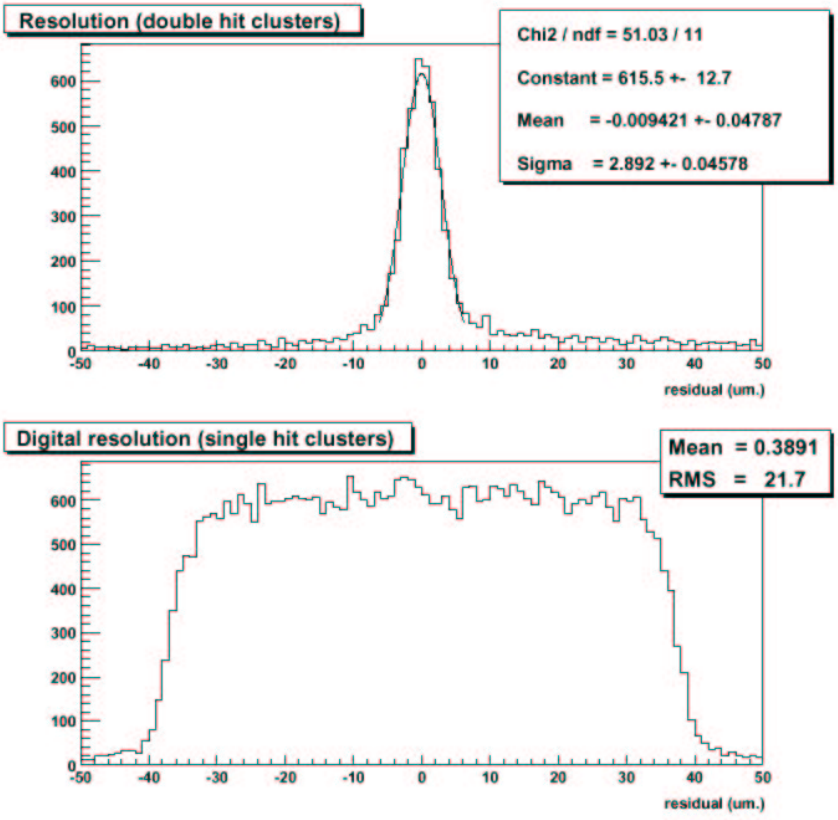

Figure 6.23: Resolution of double-hit and single-hit clusters.

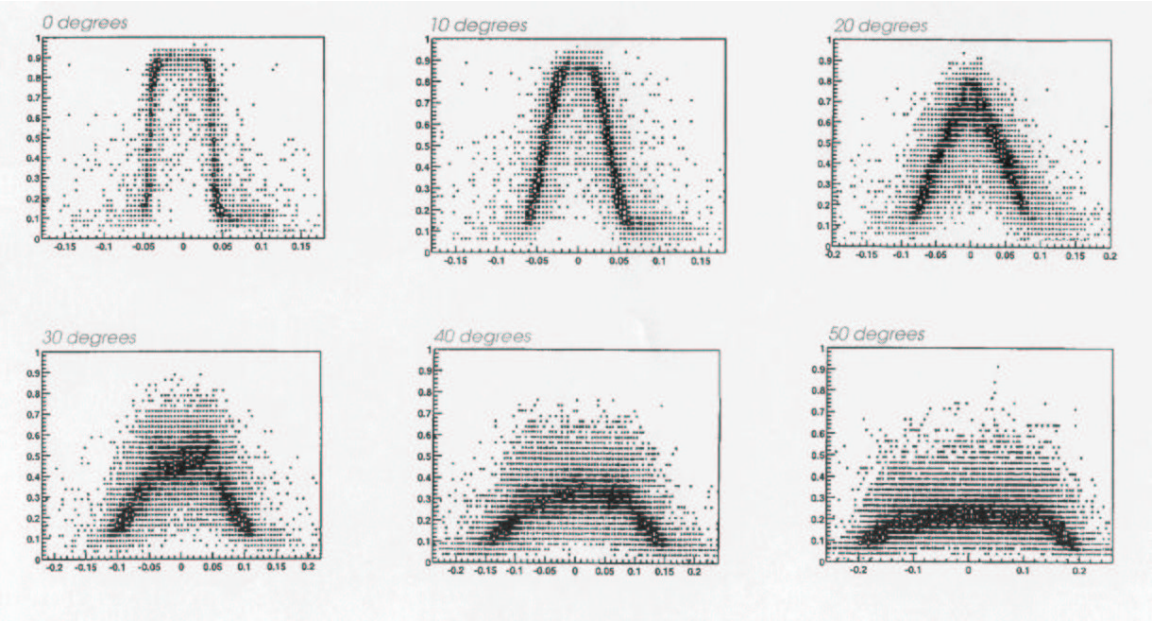

Figure 6.24: Charge sharing among adjacent strips

$3.0\,\mu m$ respectively (Figure 6.23) [148] [149]. Given the relatively small fraction of double strip hits in our test the overall spatial resolution is dominated by the single strip hits. In the experiment, however, the fraction of double strip hits is expected to be much higher due to inclined tracks and effects of the magnetic field which results in additional smearing of the charge collected in the detector.

Figure 6.24 shows the response of the module to inclined tracks, as we rotate it around the axis parallelto the vertically running strips. Charge sharing is increasing with increasing angle as expected.

Another important parameter describing the overall performance of the detector module is the noise occupancy for a given tracking efficiency. The plot showing the noise occupancy versus tracking efficiency for tested modules is presented in Figure 6.25. For the efficiency calculation only events with one well-reconstructed track were considered.

The "barrel" module equipped with the SCTA128VG chips was tested in the beam as well. Figure 6.26 shows a signal over noise distribution of data taken with $100\,GeV$ pion beam. The chips were operated under normal conditions with the input transistor current set to $200\,\mu A$.

6.3.8 Test of a linear optical link

A four-channel linear optical link has been developed to enable analogue data transmission in LHC experiments for the analogue front-end chip SCTA128 [150] [151] [152]. Signals from a prototype module have been transmitted at $40\,MHz$ using the

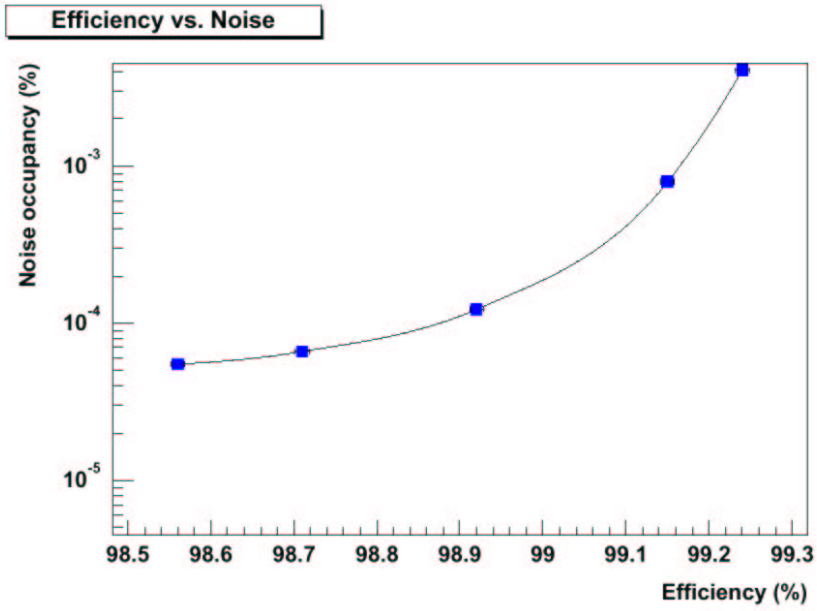

Figure 6.25: Noise occupancy versus efficiency for 12.8 cm silicon strip detector module equipped with SCTA128HC chips.

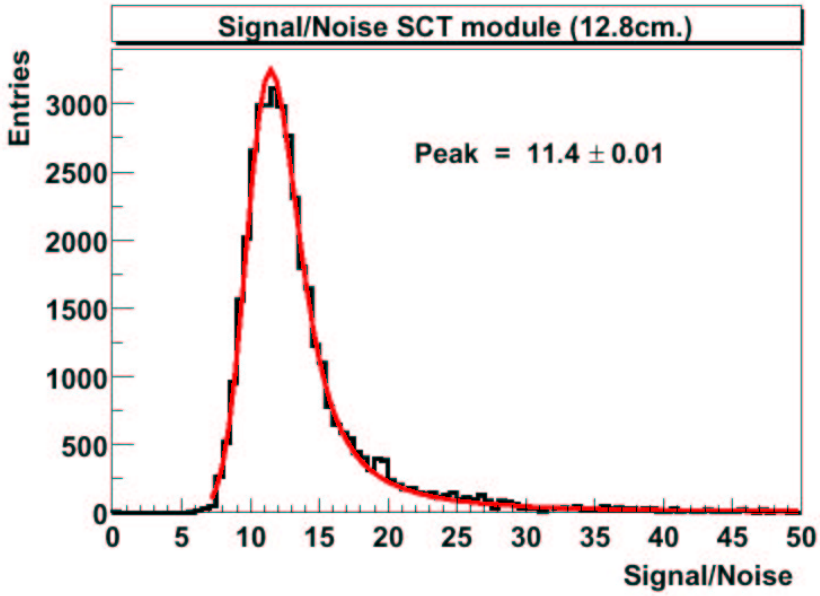

Figure 6.26: Signal over noise from data taken with 100 GeV pion beam for a chip connected to 12.8 cm detector strips.

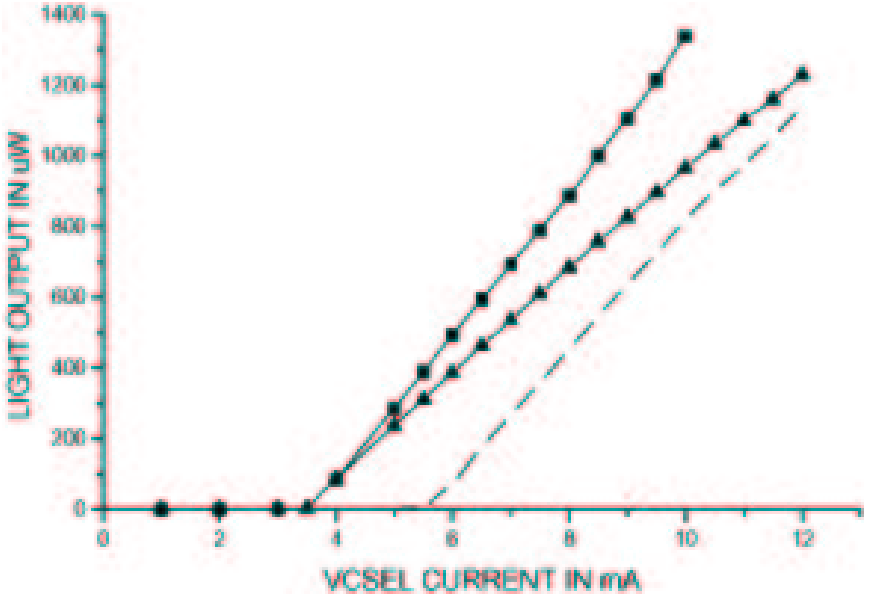

Figure 6.27: VCSEL light output versus current

Mitel 4D469 VCSEL and matching PIN diode at a wavelength of $850\,nm$.

The use of Vertical Cavity Surface Emitting Lasers (VCSELs) for low-cost radiation hard links for the transmission of digital information in the LHC experiments is now well established. The transmission of analogue information, however, presents greater problems. VCSELs are characterised by low-threshold currents, typically less than $6\,mA$, high optical power output, $1\,mW$ of optical coupled power being easily available, high slope efficiencies, typically $250\,mW/A$ and high bandwidth, typically $2\,GHz$, limited by the packaging. Studies have shown VCSELs to be radiation hard. Unfortunately, VCSELs display discontinuous non-linearity in their current versus light output characteristic, due to mode shifts of the light output produced by the Fabry-Perot resonance defined by its distributed Bragg reflector mirrors. Previous studies have shown that acceptable linear performance can be achieved by selecting the modulated range of the VCSEL. Recently developed devices by MITEL show a wide linear range without the need of careful selection.

The linear transfer characteristic was measured by varying the direct current in the VCSEL and measuring the light output. This is shown for three VCSELs in Figure 6.27. The "knee" is observed to be between 3 and $6\,mA$. Slope efficiencies were better than $250\,mW/A$. The non-linearity has been measured to never exceed 1% over the linear range (Figure 6.28).

If the dynamic range is assumed to be 10 MIPs, corresponding to a 1 V output from the receiver, then the additional noise of the optical link is equivalent to 170 RMS electrons to be added in quadrature to the total system noise. The output signal of the optical link, consisting of a header followed by the baseline, is shown at $40\,MHz$ on Figure 6.29.

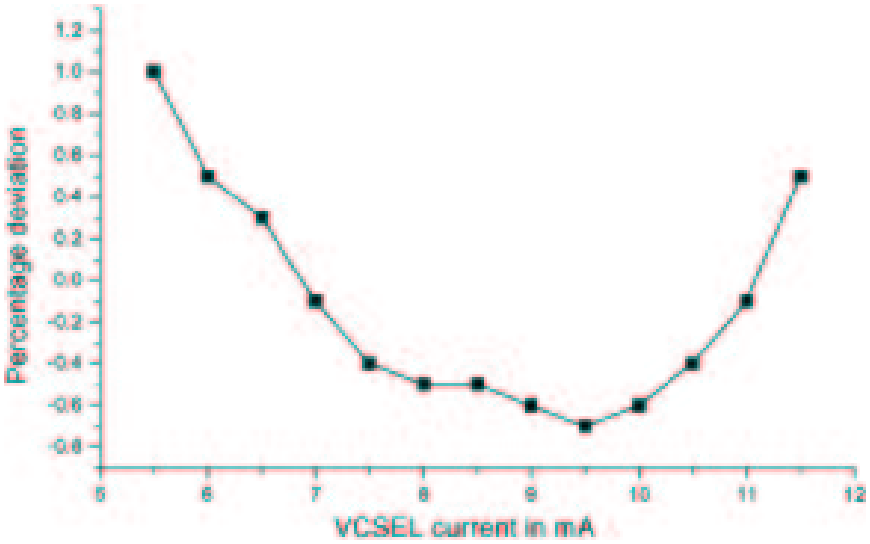

Figure 6.28: Residuals of least-squares fit

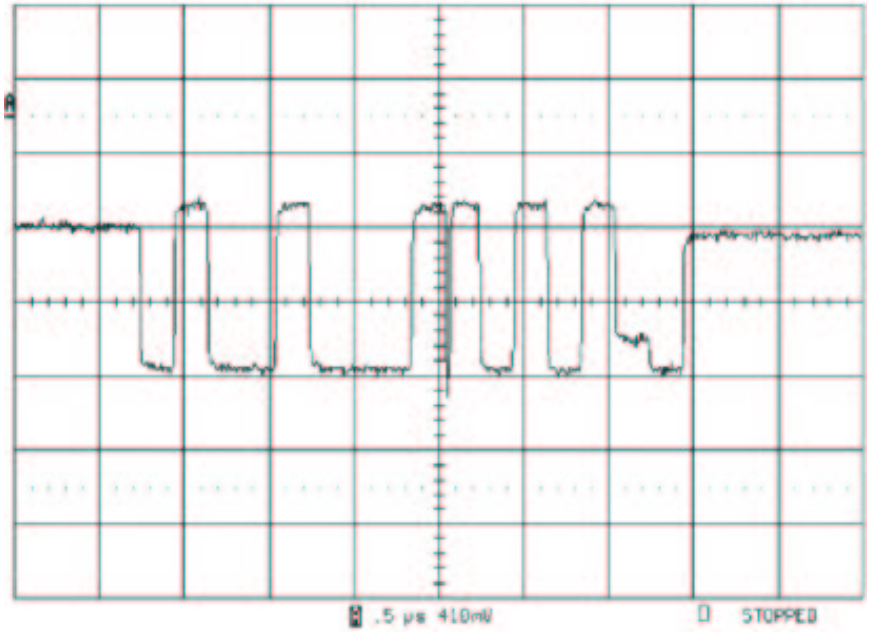

Figure 6.29: Header of an SCTA chip with optical readout.

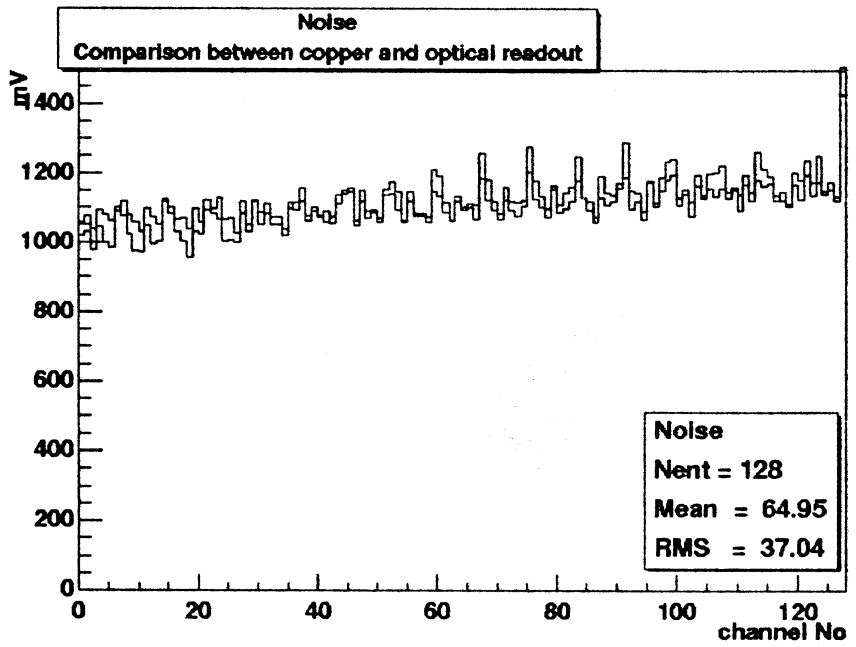

Figure 6.30: Noise for copper and optical readout.

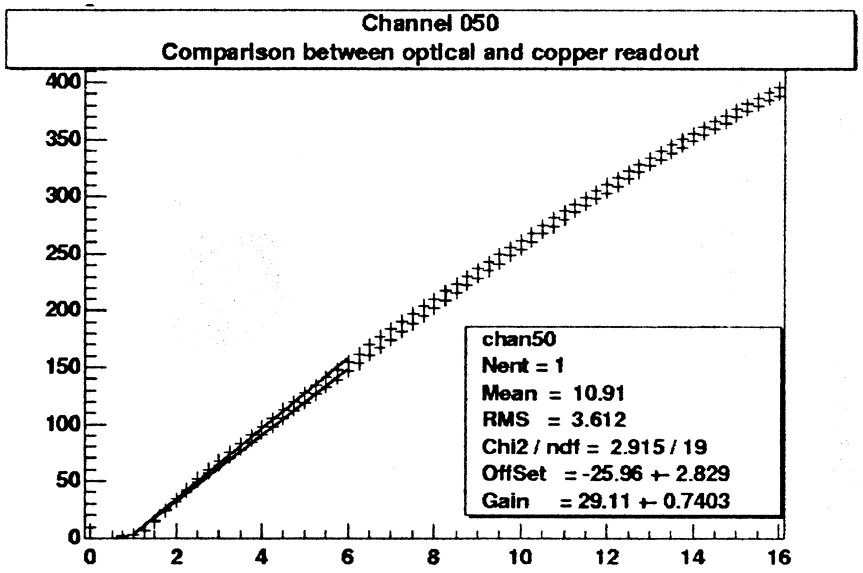

Figure 6.31: Calibration linearity for copper and optical readout.

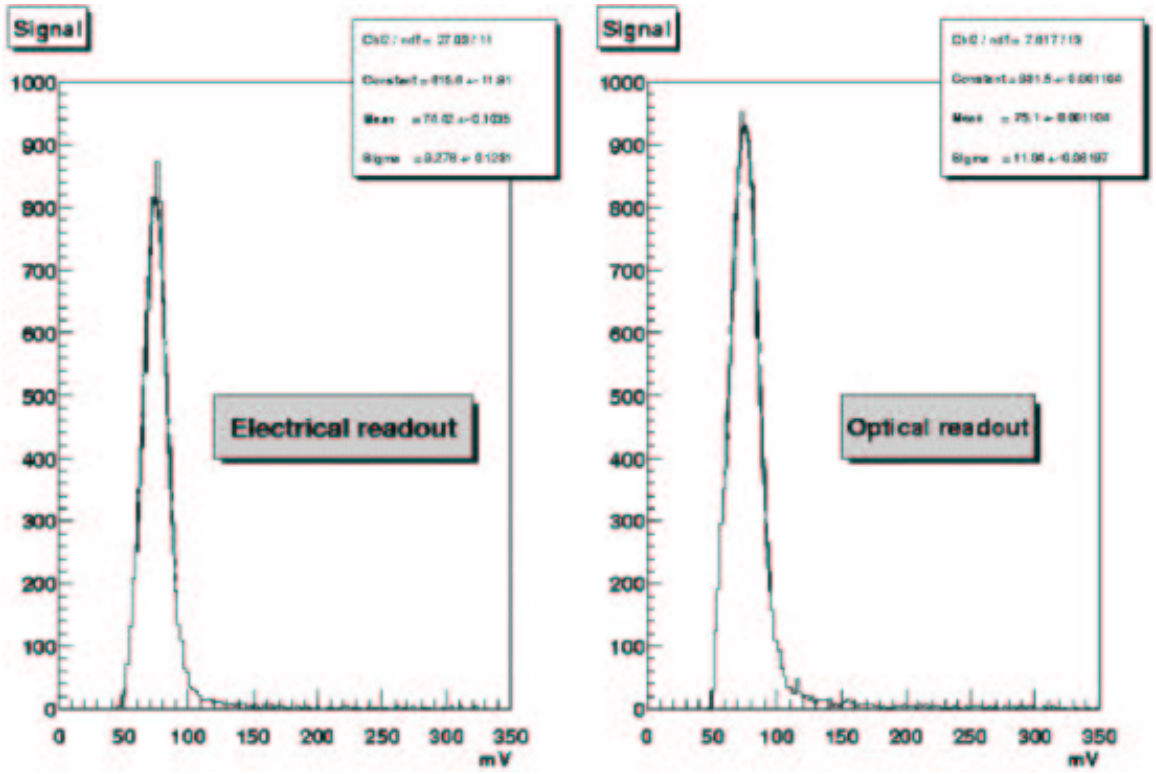

Figure 6.32: ^{241}Am spectra for both copper and optical readout

Figure 6.30 shows the noise for 128 channels for copper and optical readout performed on the "barrel" module equipped with SCTA128HC chips. The important conclusion is that the optical readout adds a negligible amount of noise to that of the front-end and the 6 cm detector strips. Figure 6.31 shows the gain linearity for a single channel both for copper and for optical readout.

The same module was bench tested with an ^{241}Am source as well. The resulting spectra are shown in Figure 6.32 for both copper and optical readout. The optical readout causes no observable shift or distortion in the spectrum.

It was also important to prove the linearity with radioactive sources, i.e. that on the absolute scale the system's response is still linear for optical readout. Tests like those described in section 6.3.5 were carried out again with Americium, Cobalt and Terbium sources, and showed that there was no degradation in linearity (Figure 6.33).

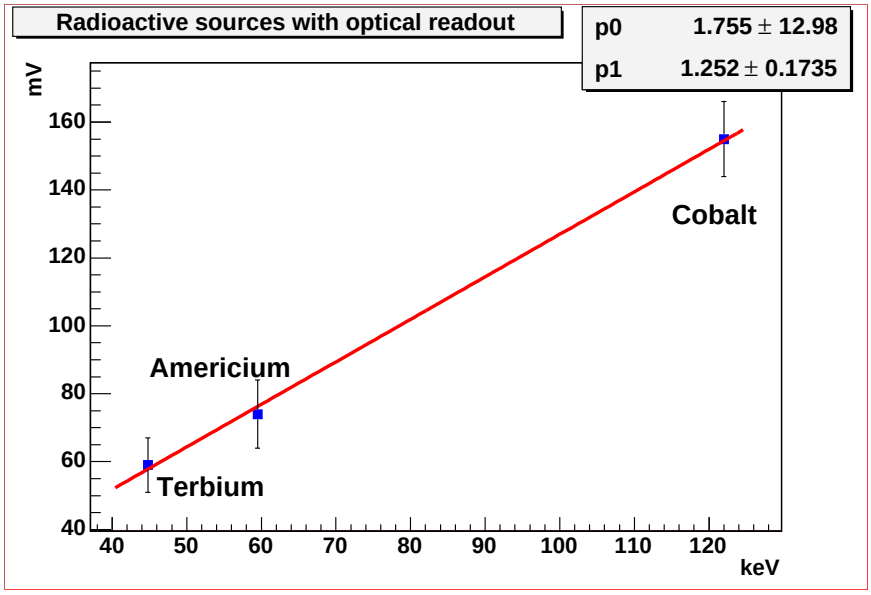

Figure 6.33: Chip response linearity with radioactive sources and optical readout

6.3.9 Conclusions

The ABCD3T chip is the final version of the binary readout for the ATLAS Semiconductor Tracker. It incorporates fixes of minor imperfections identified in the previous prototypes. The ABCD2T and ABCD3T chips have been used extensively for building complete SCT modules used then in the beam tests and the multi-module system test. Results obtained with the ABCD2T version of the ABCD readout chips show a gain uniformity of less than 3%, noise levels of 1400 (respectively 770, 430) electrons with 12 cm length (respectively 6 cm and no detector bonded) silicon strip detectors. The channel-to-channel uniformity of threshold was 18.3% at 1 fC before trimming and 5.1% at 1 fC after, proving that the trimming functionality works as expected. About 100 ABCD2T and ABCD3T chips have been irradiated in various tests up to the total doses as expected in the ATLAS SCT. All these tests showed consistent results and the single event effect rates of $1-5\times10^{-5}/bit/s$ measured for the different registers are adequate for correct operation of the SCT.

The SCTA chip is an implementation of a full analogue architecture satisfying the requirements of LHC experiments. The analogue performance of the SCTA chip is adequate for the readout of LHC type silicon strip detector modules. Excellent uniformity of the analogue parameters on chip level has been shown. The gain linearity was measured to be excellent up to 12 fC of the input charge and the spread of gain in 128 channels of a single chip was around 3%. The variation between the peaking times of the pulse shape at the output of the front-end amplifier for the different channels of a single chip were found to be below 1%. The results of the X-ray irradiation have shown radiation hardness of the SCTA chip up to the ionizing doses required by the LHC experiments.

ATLAS-type modules have been constructed with both AC-coupled and DC-coupled sensors to test the performance of the SCTA chips. The noise which increased due to the capacitance of the silicon detector strips was found to be $1700\,e^-$ and $1100\,e^-$ for $12.8\,cm$ and $6.4\,cm$ detector strips, respectively. Tests with radioactive sources confirmed the linearity seen using internal calibration.

The modules were also evaluated in beam tests at the SPS accelerator complex. The spatial resolution for single hit clusters was found to be $21\,\mu m$ as expected from the digital resolution of silicon detectors with an $80\,\mu m$ pitch. The resolution of double hit clusters was found to be $3\,\mu m$. The noise occupancy remained below 10^{-4} even for tracking efficiencies reaching 99%.

Due to their analogue architecture, the modules equipped with the SCTA chips were also used to study the performance of a linear optical link developed for analogue data transmission of LHC experiments. It was shown that the link does not add noticeable noise and does not affect the linearity of the system, thus satisfying the criteria of transmitting the signals without distortions.

The studies performed on the SCTA chip have also contributed significantly to the understanding of the ABCD front-end. These studies resulted in modifications which helped to achieve acceptable yields for the digital design. Furthermore, the SCTA chips have been used extensively for the irradiation studies of the silicon detectors for the SCT.

The presented results show that SCT modules meet the performance required for providing precise tracking in the ATLAS experiment. The low occupancy coupled with the high tracking efficiency ensures that the SCT together with the Pixel detector provides enough precision points for excellent secondary vertex reconstruction and impact parameter resolution. The single hit cluster resolution was found to be $21\,\mu m$, and it is even an order of magnitude better for double hit clusters, which should be numerous given the magnetic field present in the tracking volume. These qualities make the SCT a formidable link in the study of B physics, including the search for decays such as $\mathrm{B}_d^0 \to \mu\mu K^{*0}$, studied within the framework of CDF in Chapter 4.

Appendix A

Number of signal events for the $\mathrm{B}_d^0 \to J/\psi K^{*0}$ decay

This Appendix shows the number of signal events for the $\mathrm{B}_d^0 \to J/\psi K^{*0}$ decay as a function of the L_{xy}, $\Delta\Phi$ and $Isolation$ cuts. Each plot shows a scan of L_{xy} and $\Delta\Phi$ cuts corresponding to a given $Isolation$ cut. Figures A.1 through A.7 correspond to different $Isolation$ cuts from 0.5 to 0.8 in steps of 0.05. On these figures the first column represents the number of signal events for the $\mathrm{B}_d^0 \to J/\psi K^{*0}$ decay when there is no L_{xy} cut applied, while the other nine columns represent cuts from $0.015\,cm$ up to $0.135\,cm$ in steps of $0.015\,cm$; the uppermost row represents the number of signal events for the $\mathrm{B}_d^0 \to J/\psi K^{*0}$ decay when there is no $\Delta\Phi$ cut applied, while the other nine rows represent upper cuts on $\Delta\Phi$ from $0.072\,rad$ down to $0.008\,rad$ in steps of $0.008\,rad$.

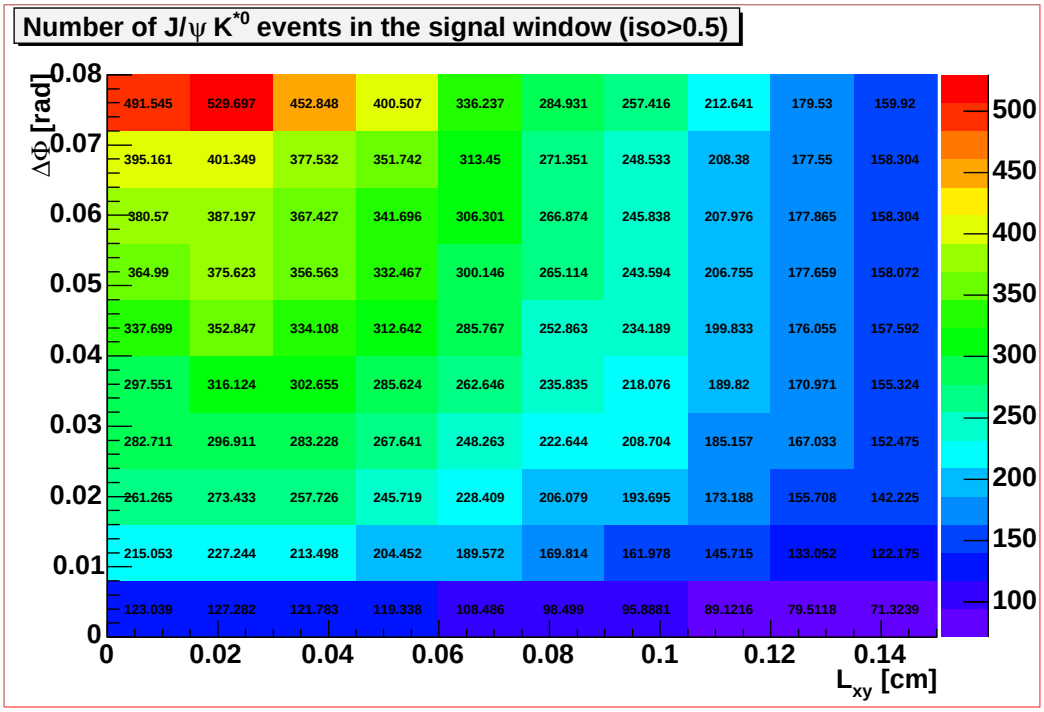

Figure A.1: Number of $B^0_d \to J/\psi K^{*0}$ events for $Iso > 0.5$.

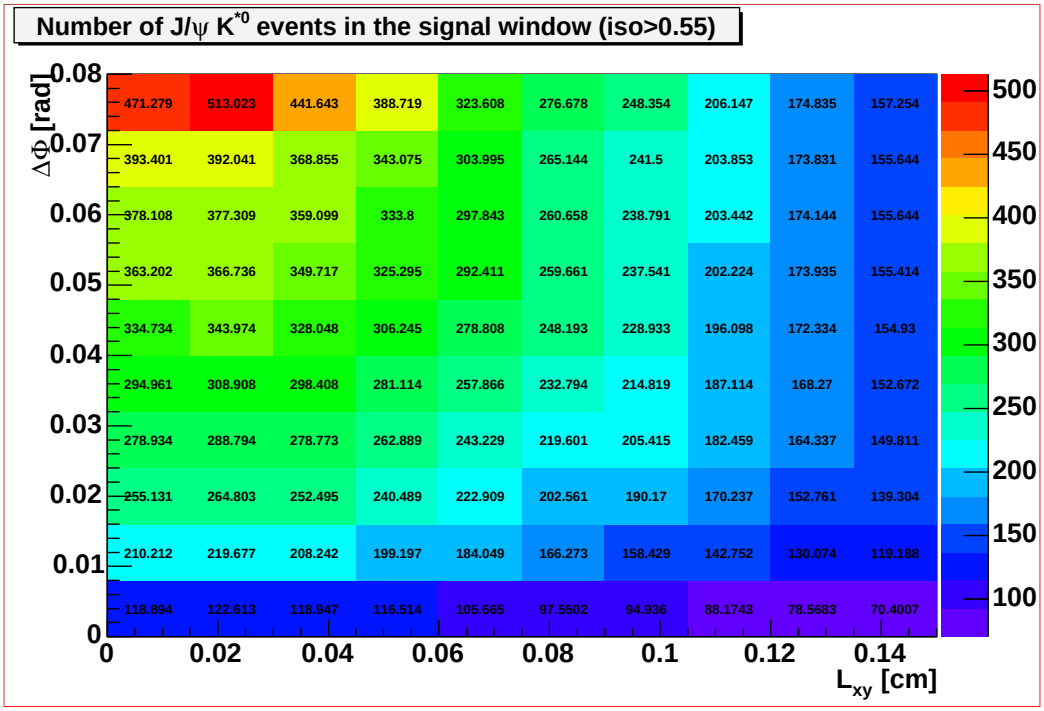

Figure A.2: Number of $B^0_d \to J/\psi K^{*0}$ events for $Iso > 0.55$.

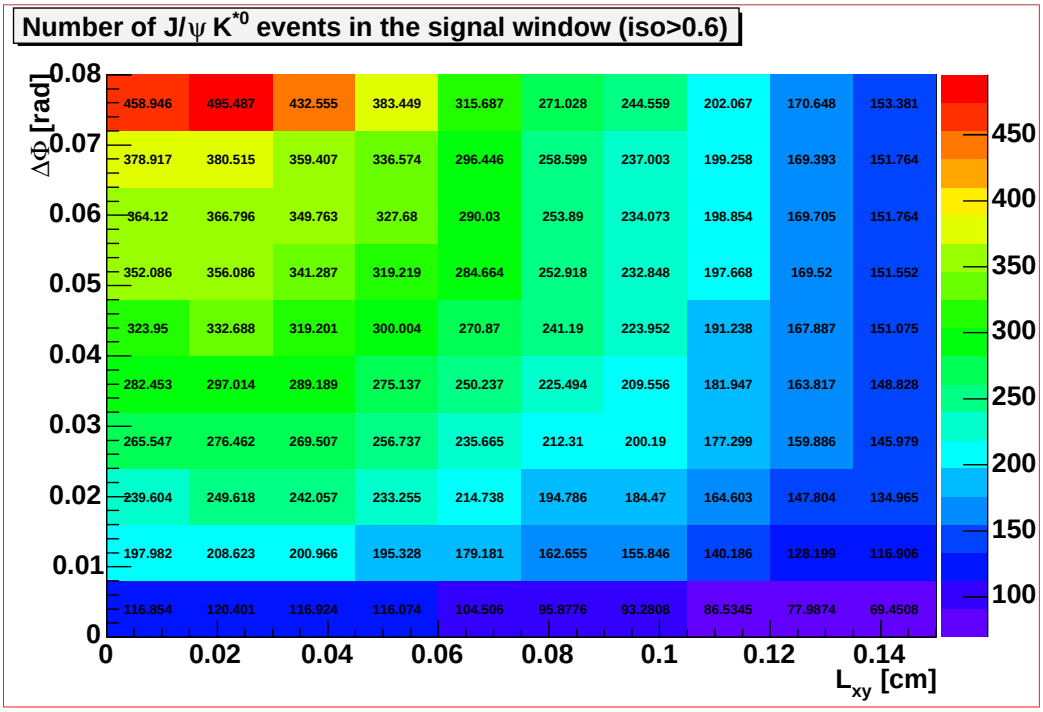

Figure A.3: Number of $B_d^0 \to J/\psi K^{*0}$ events for $Iso > 0.6$.

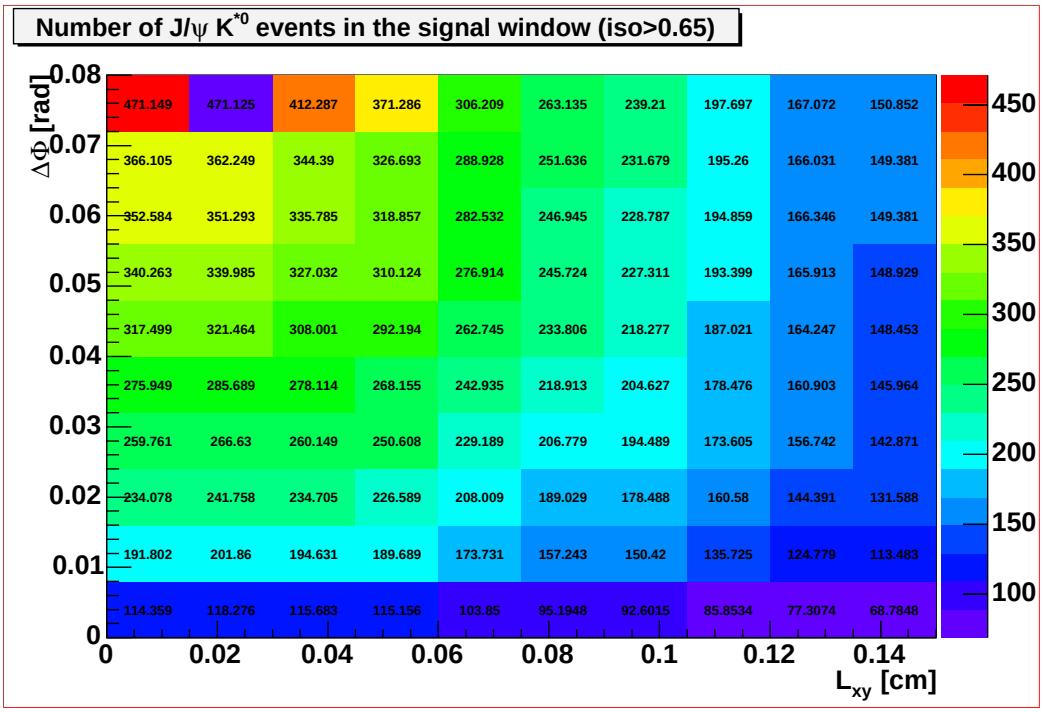

Figure A.4: Number of $B_d^0 \to J/\psi K^{*0}$ events for $Iso > 0.65$.

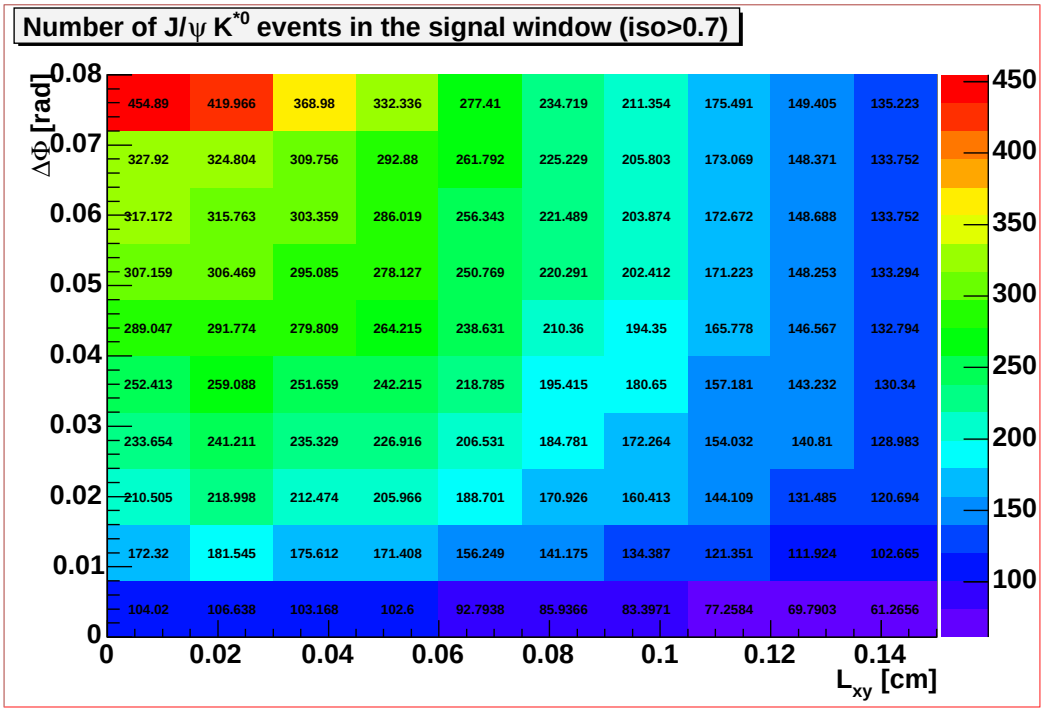

Figure A.5: Number of $B^0_d \to J/\psi K^{*0}$ events for $Iso > 0.7$.

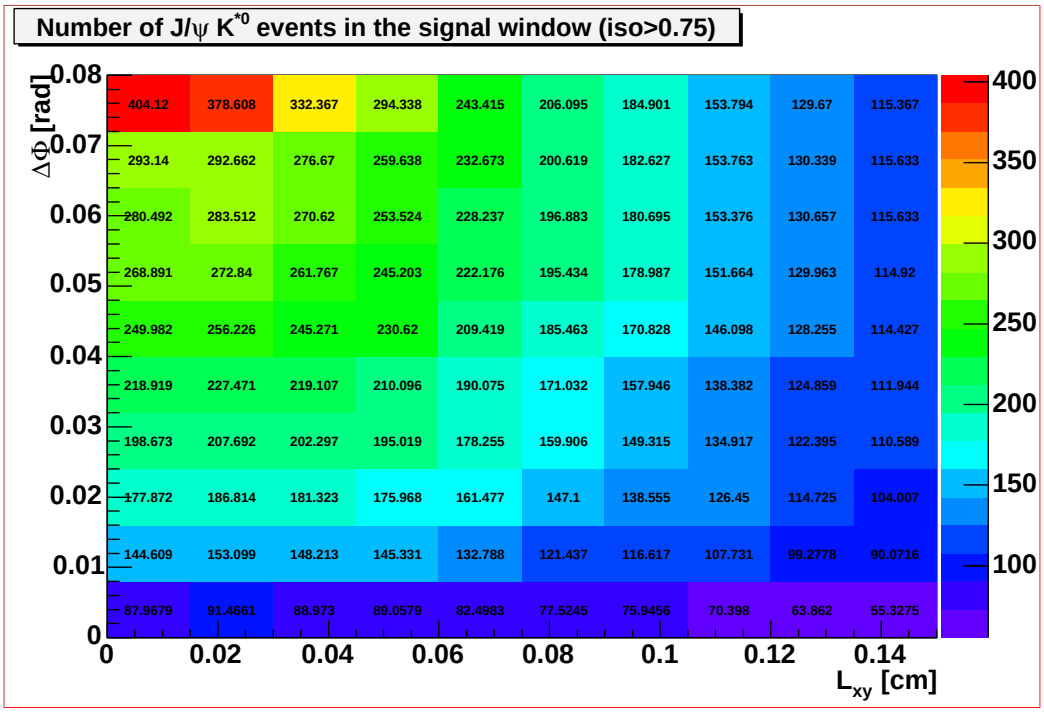

Figure A.6: Number of $B^0_d \to J/\psi K^{*0}$ events for $Iso > 0.75$.

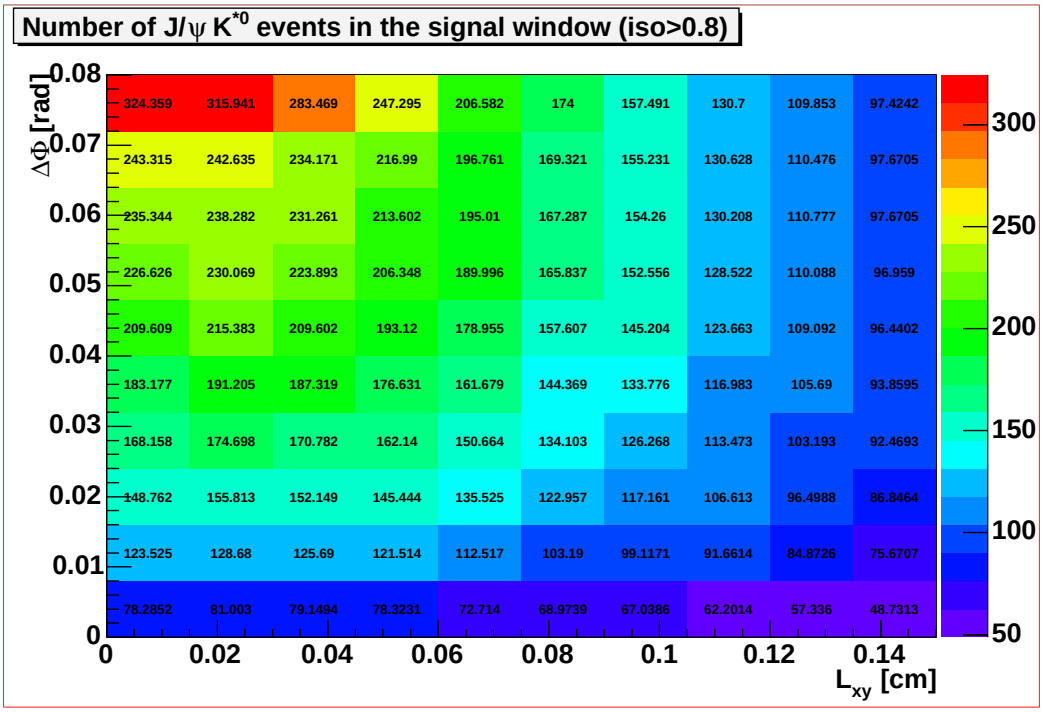

Figure A.7: Number of $B_d^0 \to J/\psi K^{*0}$ events for $Iso > 0.8$.

Appendix B

Signal optimization plots for $S^2/(S+B)$

This Appendix shows figures of merit

$$fom2 = \frac{S^2}{(S+B)} \tag{B.1}$$

for the $B_d^0 \to \mu\mu K^{*0}$ decay as a function of the L_{xy}, $\Delta\Phi$ and $Isolation$ cuts. Each plot shows a scan of L_{xy} and $\Delta\Phi$ cuts corresponding to a given $Isolation$ cut. Figures B.1 through B.7 correspond to different $Isolation$ cuts from 0.5 to 0.8 in steps of 0.05. On these figures the first column represents the figure of merit when there is no L_{xy} cut applied, while the other nine columns represent cuts from $0.015\,cm$ up to $0.135\,cm$ in steps of $0.015\,cm$; the uppermost row represents the figure of merit when there is no $\Delta\Phi$ cut applied, while the other nine rows represent upper cuts on $\Delta\Phi$ from $0.072\,rad$ down to $0.008\,rad$ in steps of $0.008\,rad$.

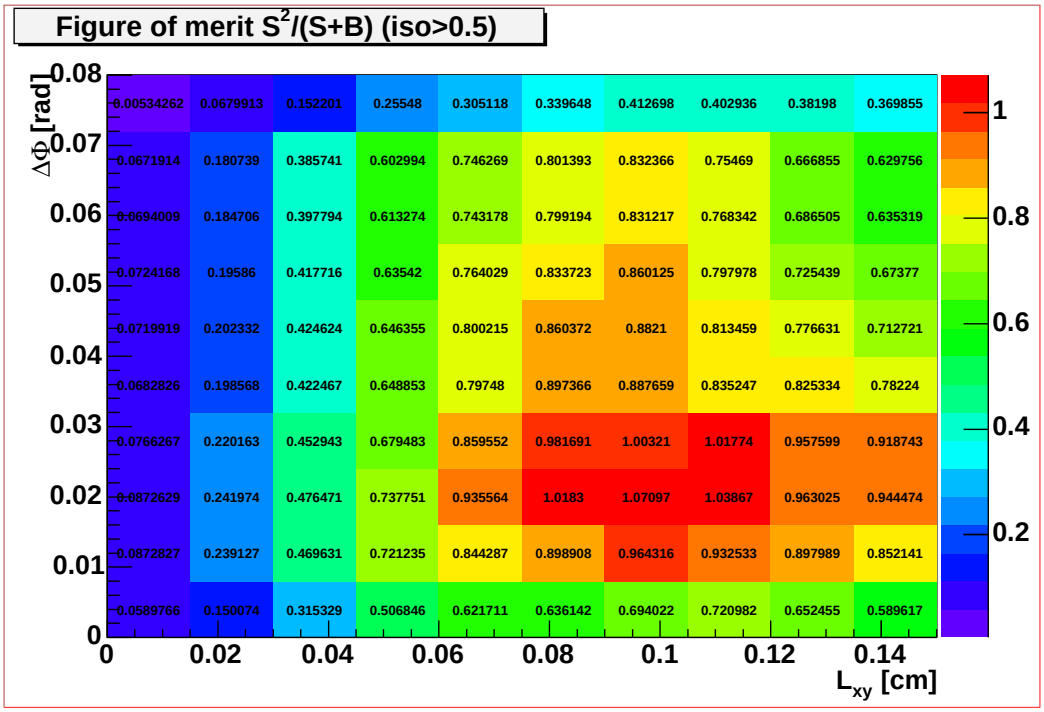

Figure B.1: Figure of merit $S^2/(S+B)$ for $Iso > 0.5$.

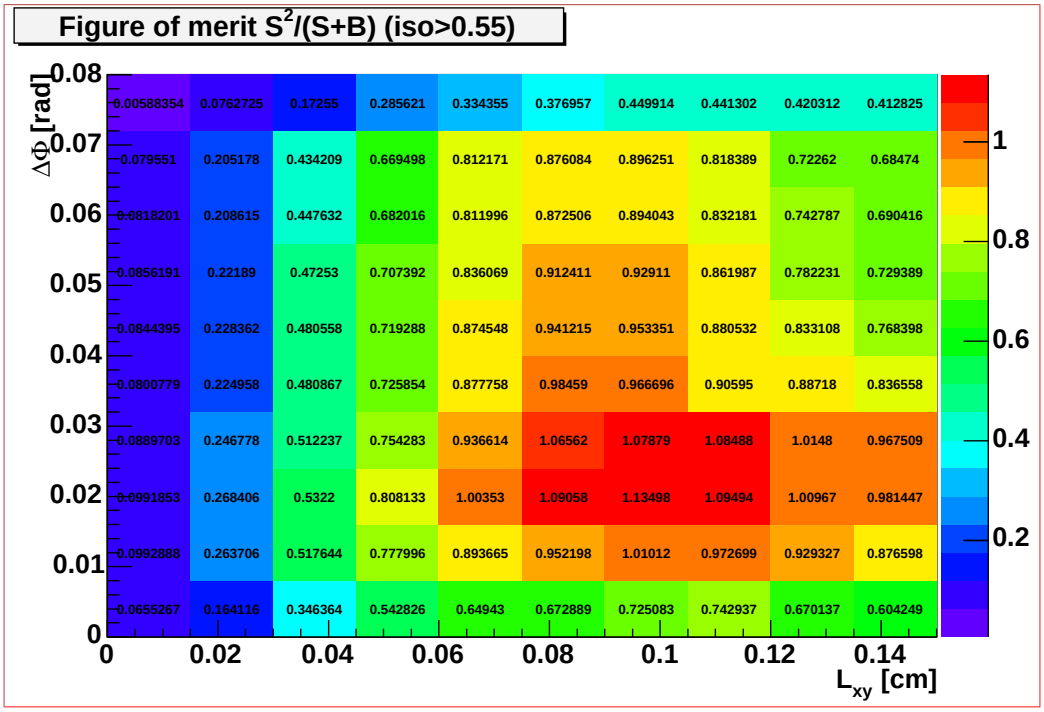

Figure B.2: Figure of merit $S^2/(S+B)$ for $Iso > 0.55$.

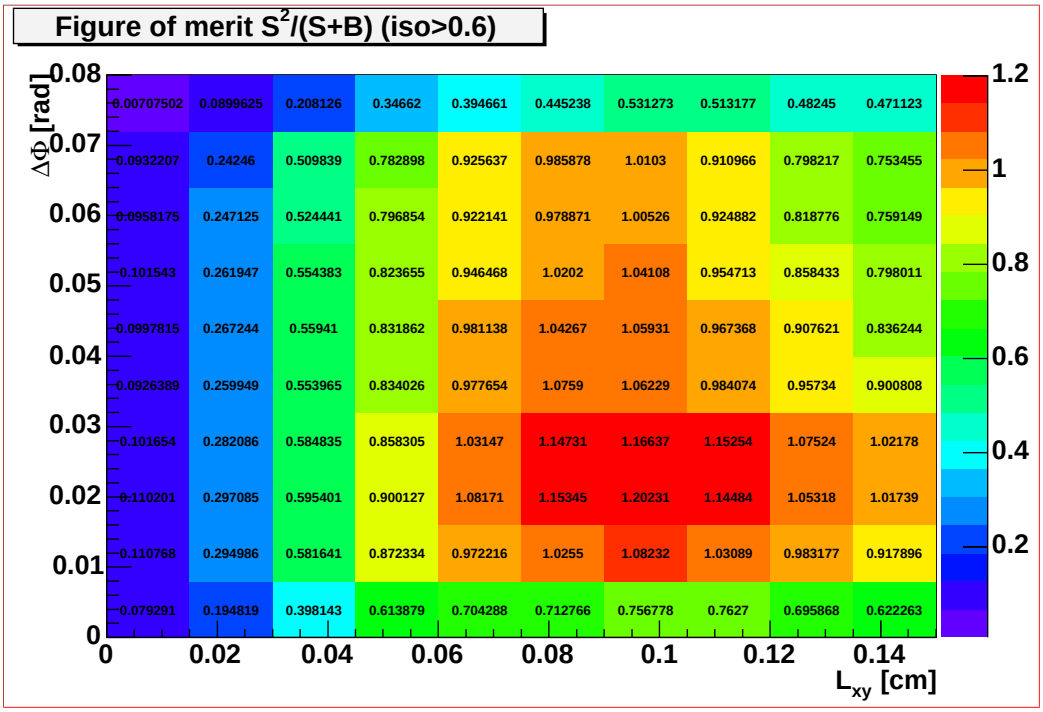

Figure B.3: Figure of merit $S^2/(S+B)$ for $Iso > 0.6$.

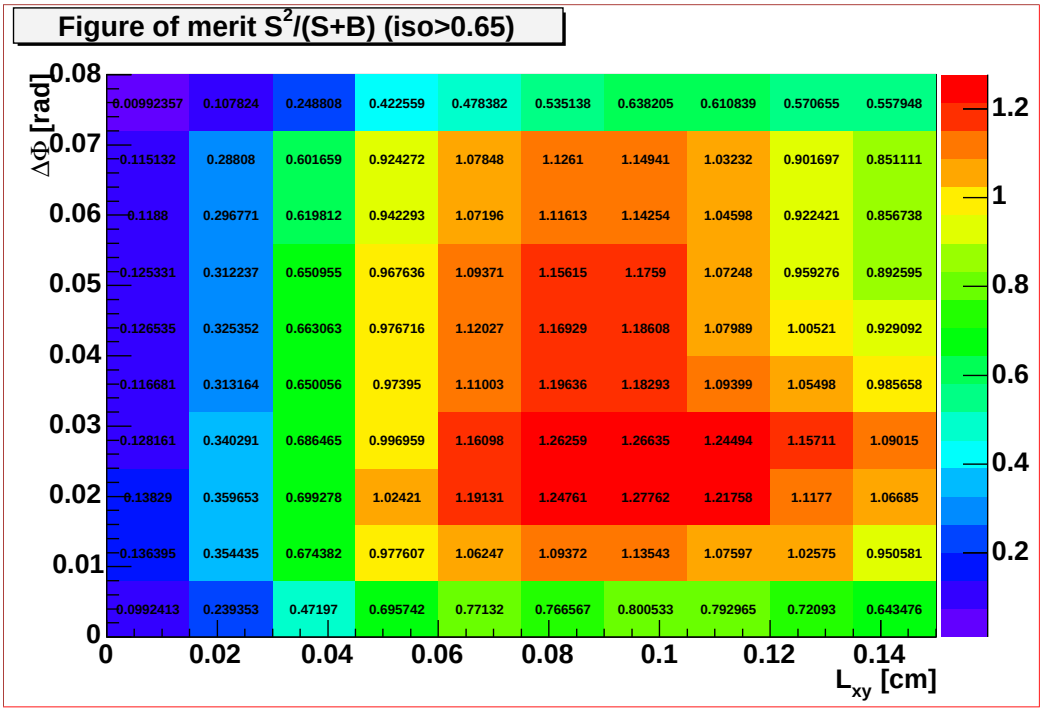

Figure B.4: Figure of merit $S^2/(S+B)$ for $Iso > 0.65$.

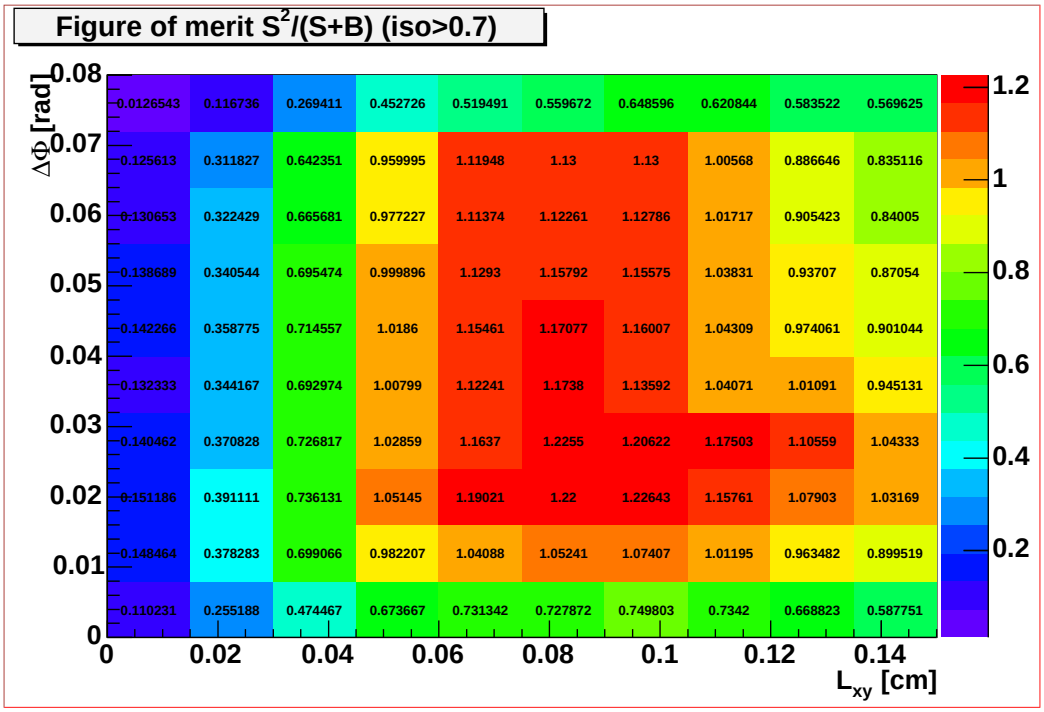

Figure B.5: Figure of merit $S^2/(S+B)$ for $Iso > 0.7$.

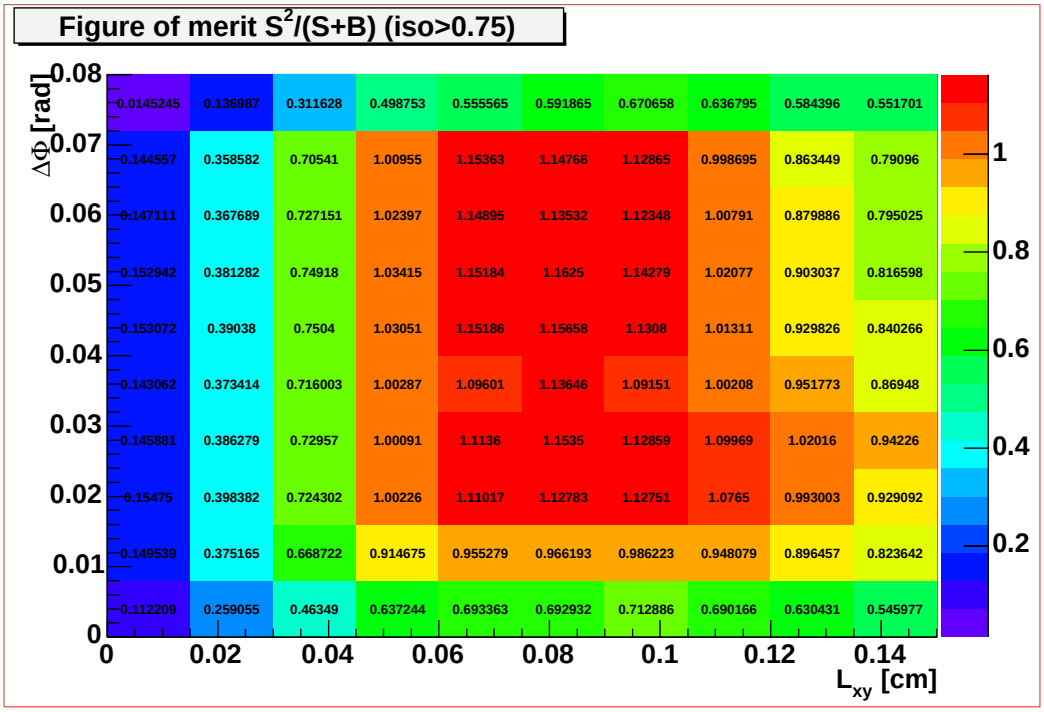

Figure B.6: Figure of merit $S^2/(S+B)$ for $Iso > 0.75$.

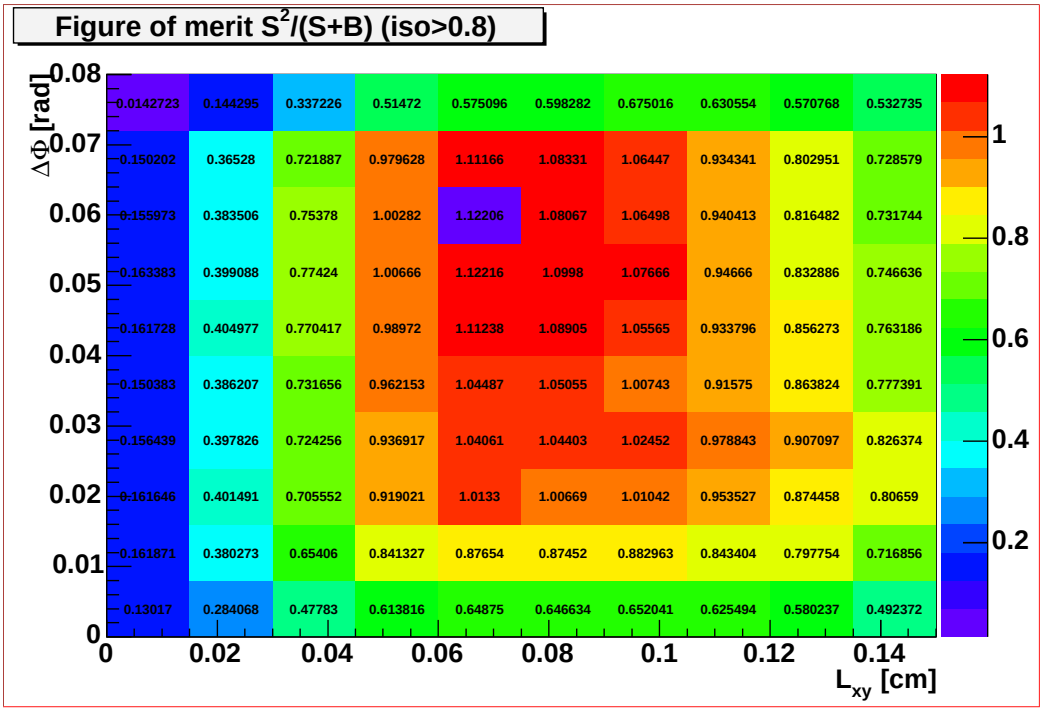

Figure B.7: Figure of merit $S^2/(S+B)$ for $Iso > 0.8$.

Appendix C

Signal optimization plots for $S^2/(a/2+\sqrt{B})^2$

This Appendix shows figures of merit

$$fom3 = \frac{S^2}{(\frac{a}{2}+\sqrt{B})^2} \tag{C.1}$$

for the $B_d^0 \to \mu\mu K^{*0}$ decay as a function of the L_{xy}, $\Delta\Phi$ and $Isolation$ cuts. The value of a has been chosen to search for a one σ discovery. Each plot shows a scan of L_{xy} and $\Delta\Phi$ cuts corresponding to a given $Isolation$ cut. Figures C.1 through C.7 correspond to different $Isolation$ cuts from 0.5 to 0.8 in steps of 0.05. On these figures the first column represents the figure of merit when there is no L_{xy} cut applied, while the other nine columns represent cuts from $0.015\,cm$ up to $0.135\,cm$ in steps of $0.015\,cm$; the uppermost row represents the figure of merit when there is no $\Delta\Phi$ cut applied, while the other nine rows represent upper cuts on $\Delta\Phi$ from $0.072\,rad$ down to $0.008\,rad$ in steps of $0.008\,rad$. For the present data $a = 1$ was chosen (see Section 4.5.4).

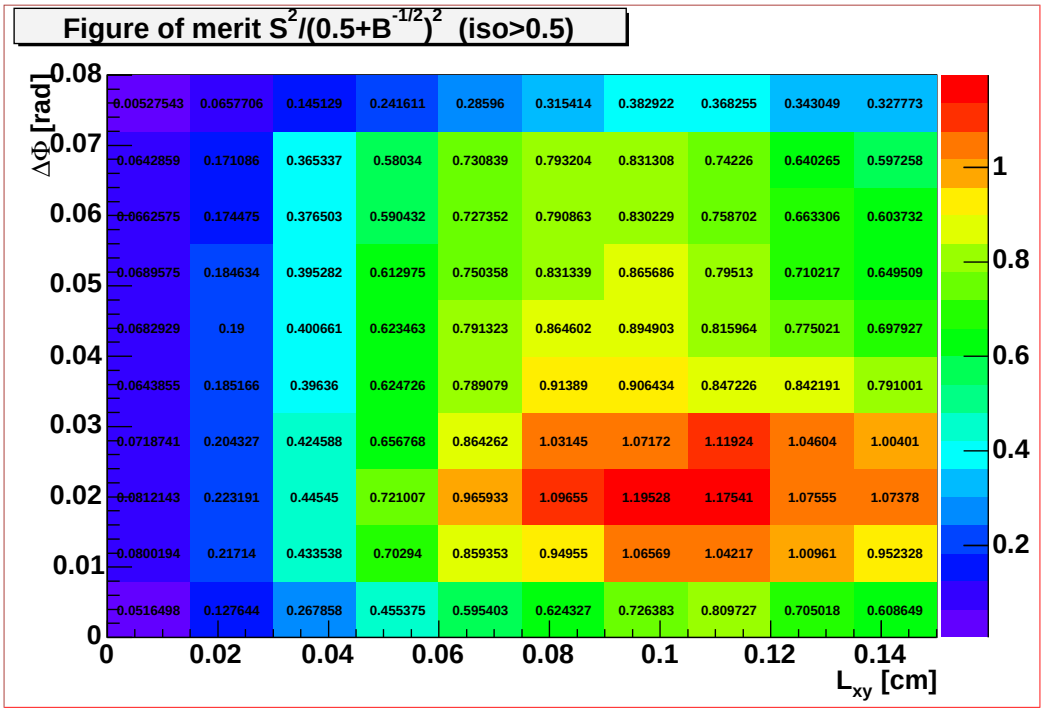

Figure C.1: Figure of merit $S^2/(a/2+B)^2$ for $Iso > 0.5$.

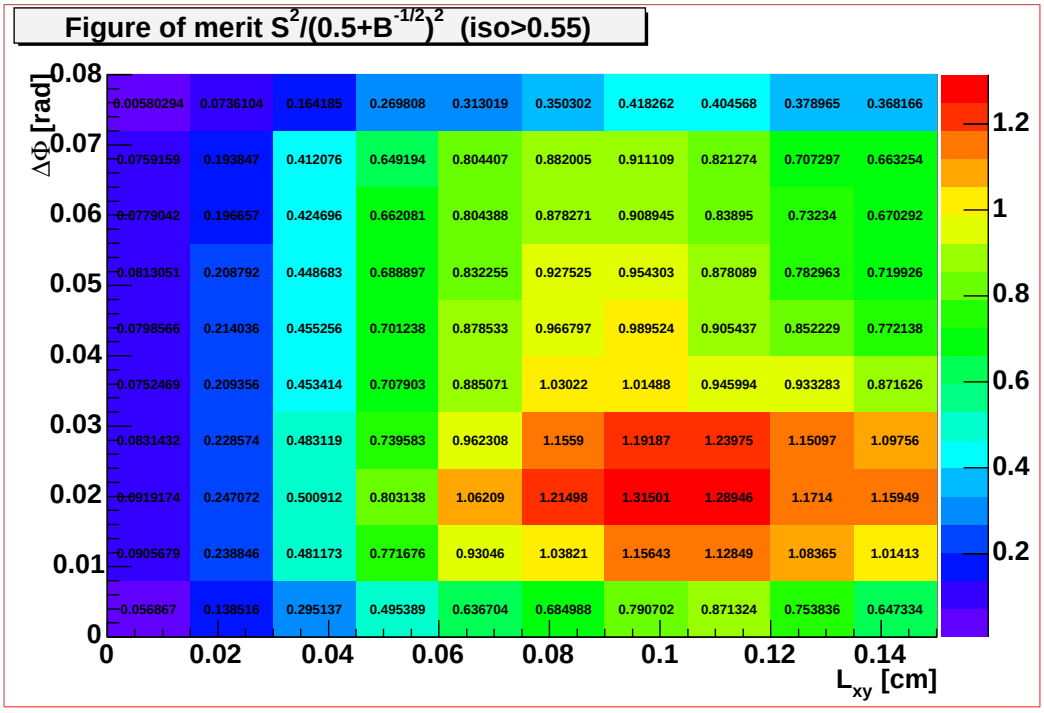

Figure C.2: Figure of merit $S^2/(a/2+B)^2$ for $Iso > 0.55$.

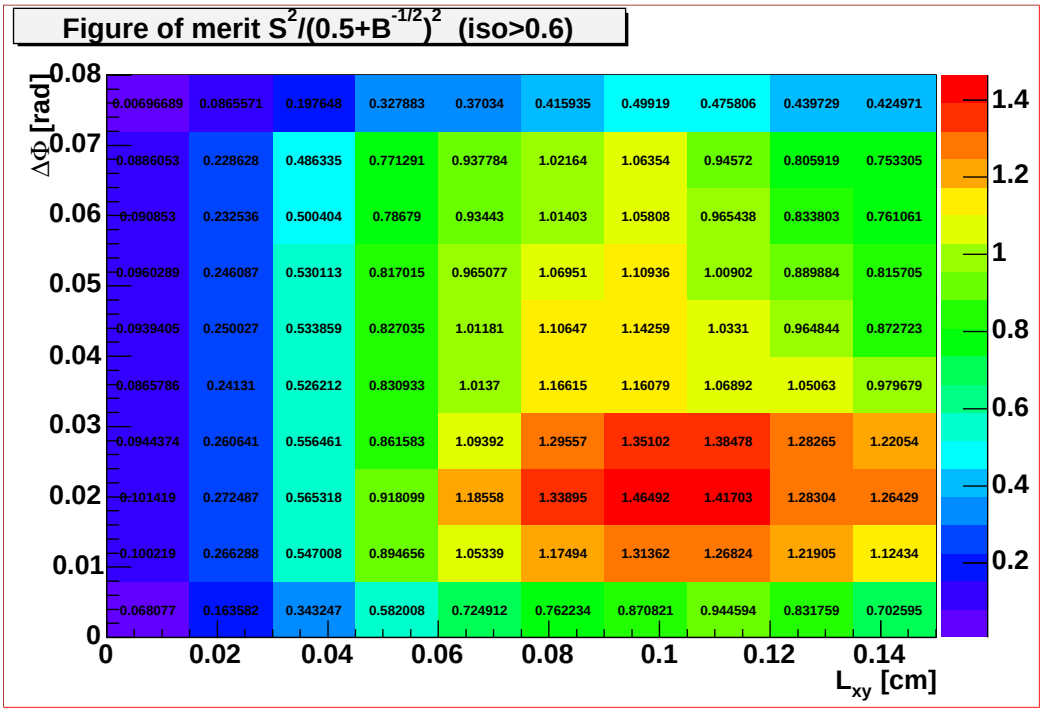

Figure C.3: Figure of merit $S^2/(a/2+B)^2$ for $Iso > 0.6$.

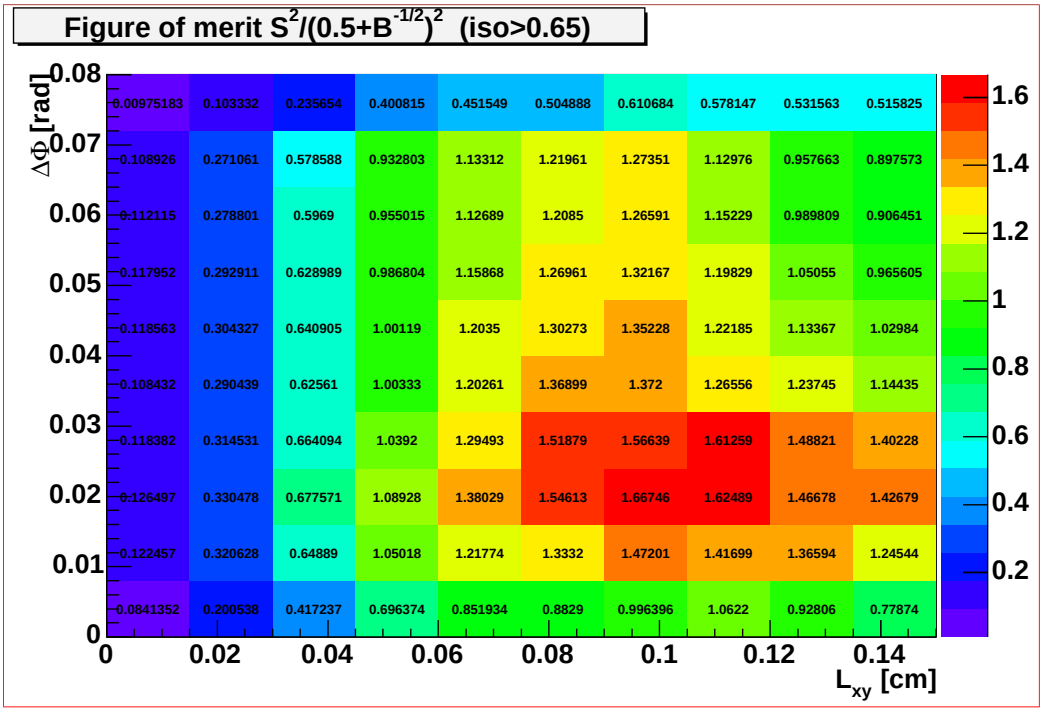

Figure C.4: Figure of merit $S^2/(a/2+B)^2$ for $Iso > 0.65$.

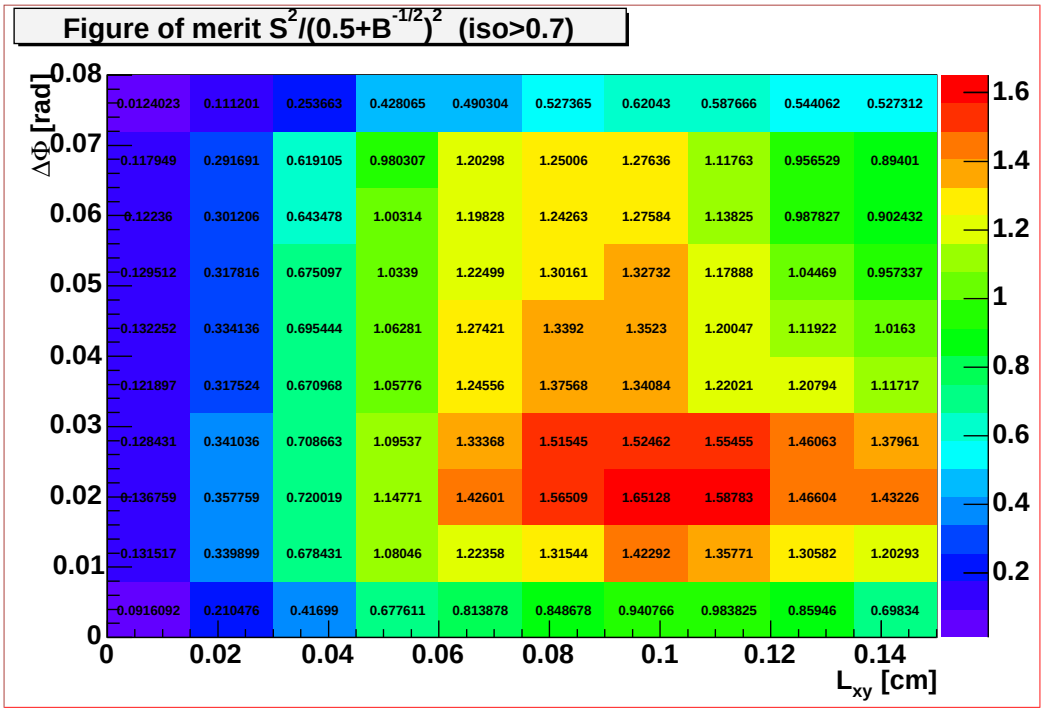

Figure C.5: Figure of merit $S^2/(a/2+B)^2$ for $Iso > 0.7$.

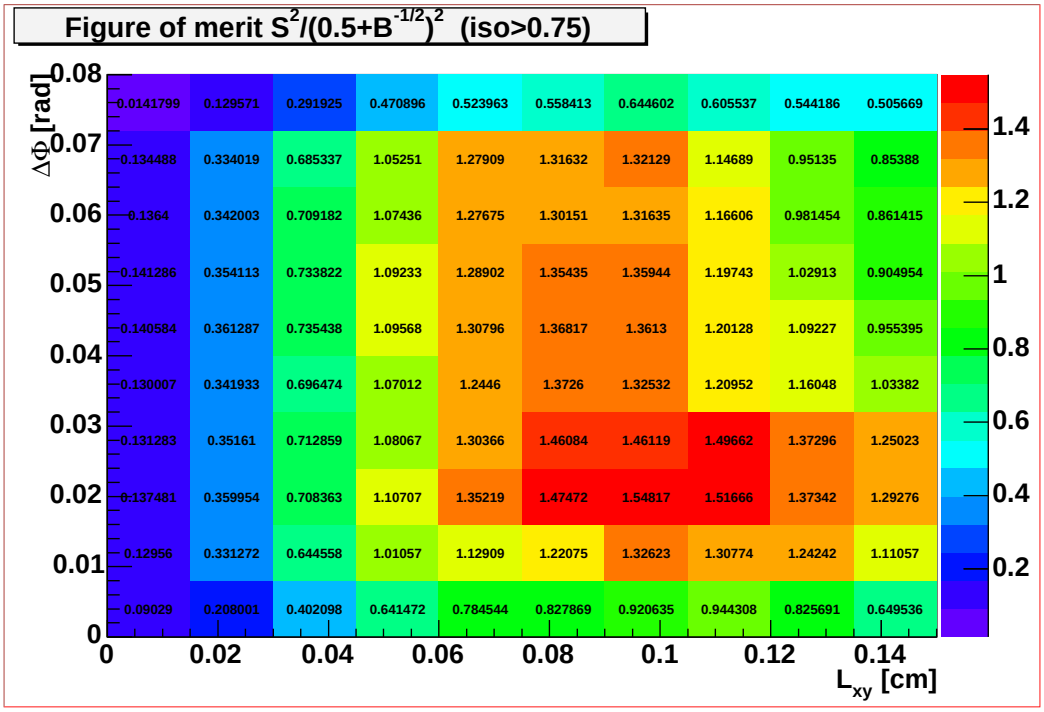

Figure C.6: Figure of merit $S^2/(a/2+B)^2$ for $Iso > 0.75$.

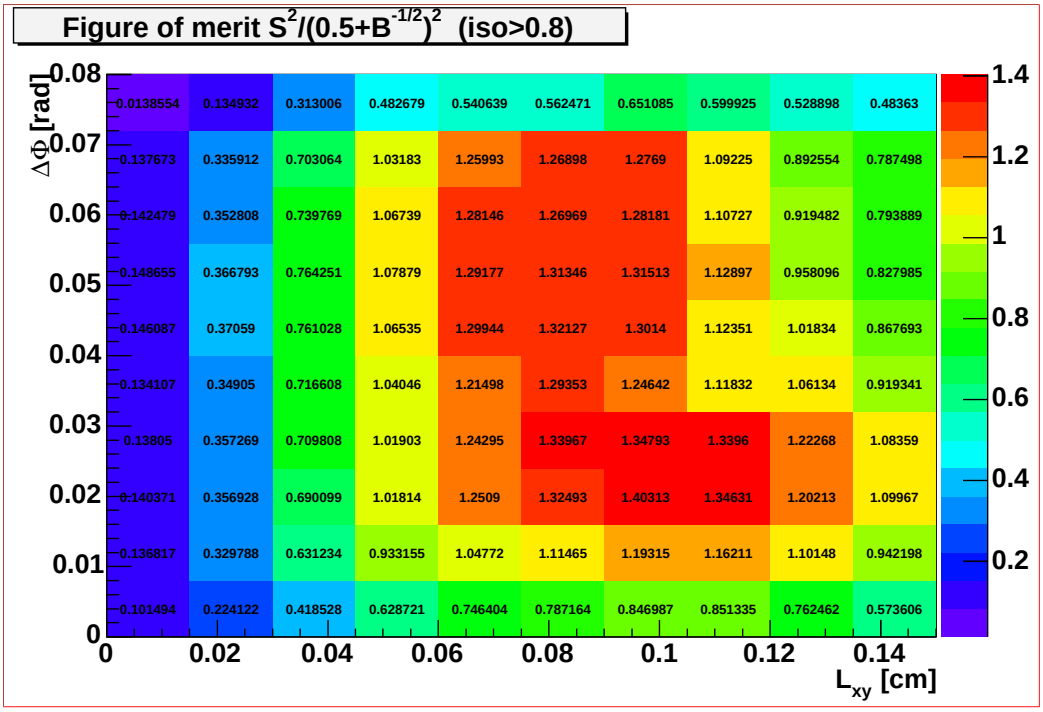

Figure C.7: Figure of merit $S^2/(a/2+B)^2$ for $Iso > 0.8$.

Appendix D

Estimated background for the $\mathrm{B}_d^0 \to \mu\mu K^{*0}$ decay

This Appendix shows the number estimated background events for the $\mathrm{B}_d^0 \to \mu\mu K^{*0}$ decay as a function of the L_{xy}, $\Delta\Phi$ and $Isolation$ cuts. Each plot shows a scan of L_{xy} and $\Delta\Phi$ cuts corresponding to a given $Isolation$ cut. Figures D.1 through D.7 correspond to different $Isolation$ cuts from 0.5 to 0.8 in steps of 0.05. On these figures the first column represents the number of estimated background events for the $\mathrm{B}_d^0 \to \mu\mu K^{*0}$ decay when there is no L_{xy} cut applied, while the other nine columns represent cuts from $0.015\,cm$ up to $0.135\,cm$ in steps of $0.015\,cm$; the uppermost row represents the number of estimated background events for the $\mathrm{B}_d^0 \to \mu\mu K^{*0}$ decay when there is no $\Delta\Phi$ cut applied, while the other nine rows represent upper cuts on $\Delta\Phi$ from $0.072\,rad$ down to $0.008\,rad$ in steps of $0.008\,rad$.

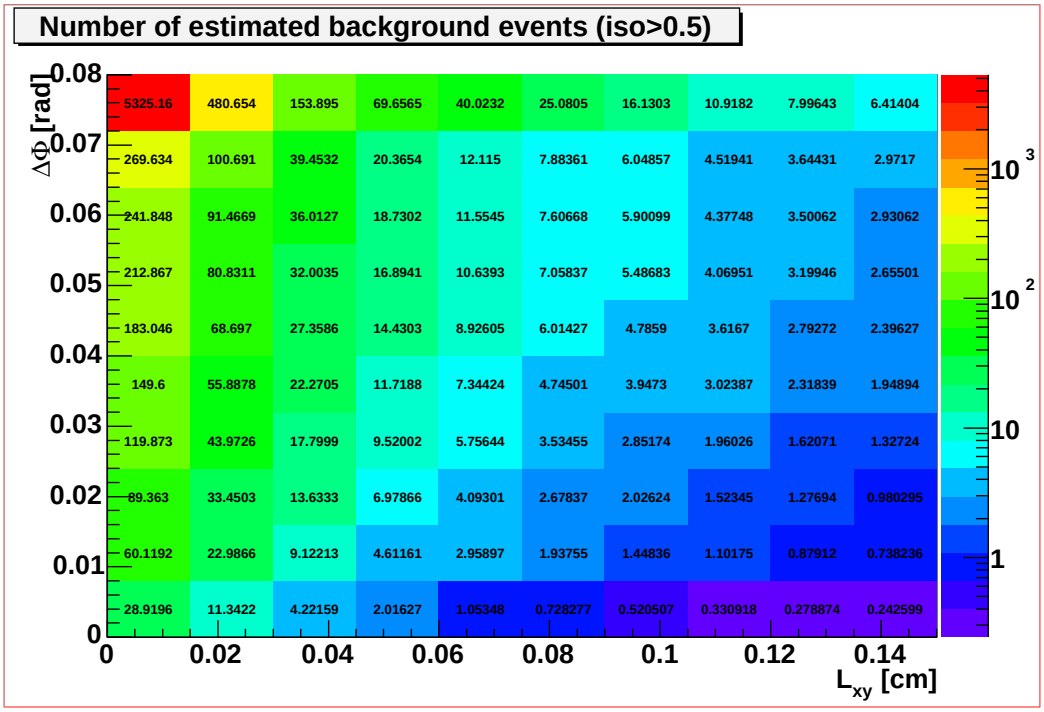

Figure D.1: Estimated background for the $B^0_d \to \mu\mu K^{*0}$ decay for $Iso > 0.5$.

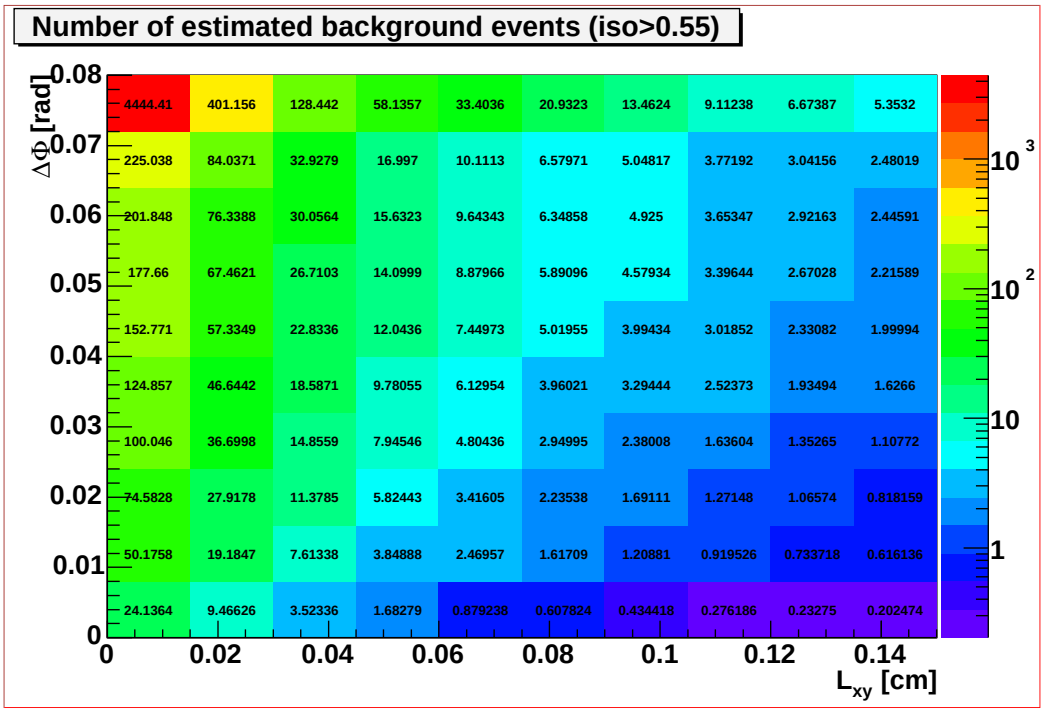

Figure D.2: Estimated background for the $B^0_d \to \mu\mu K^{*0}$ decay for $Iso > 0.55$.

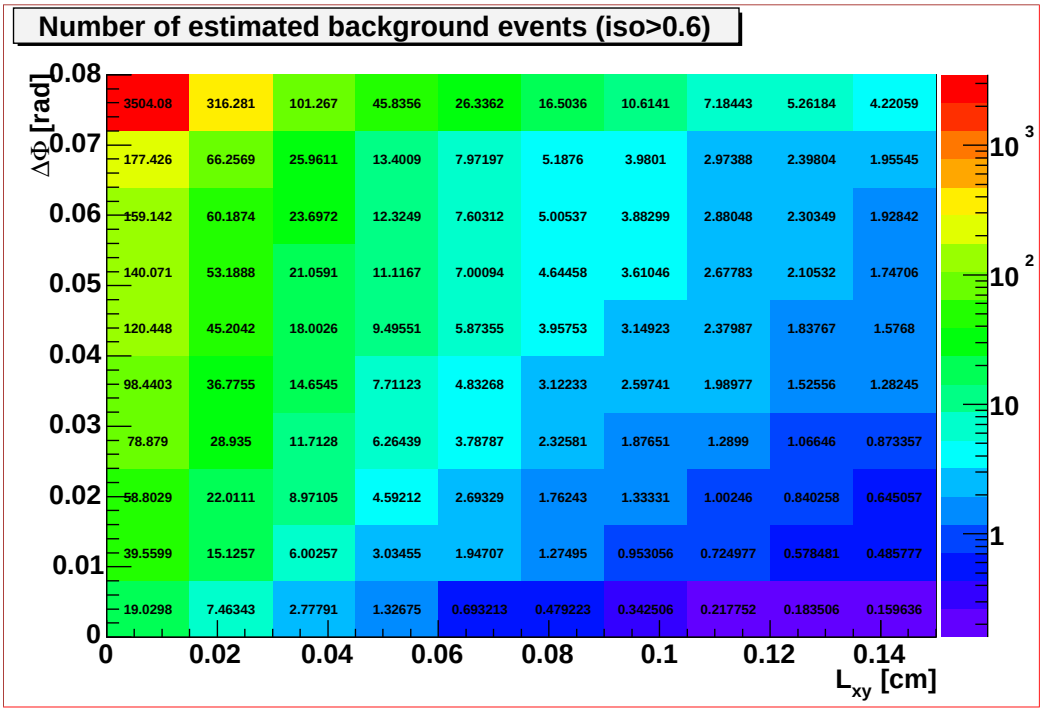

Figure D.3: Estimated background for the $B_d^0 \to \mu\mu K^{*0}$ decay for $Iso > 0.6$.

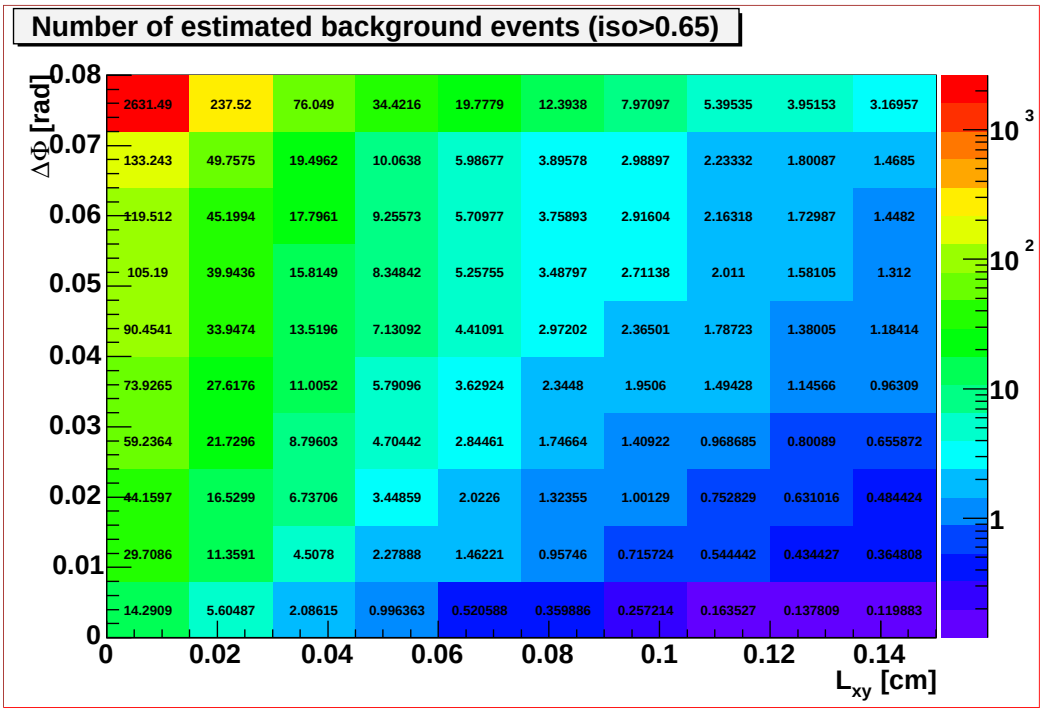

Figure D.4: Estimated background for the $B_d^0 \to \mu\mu K^{*0}$ decay for $Iso > 0.65$.

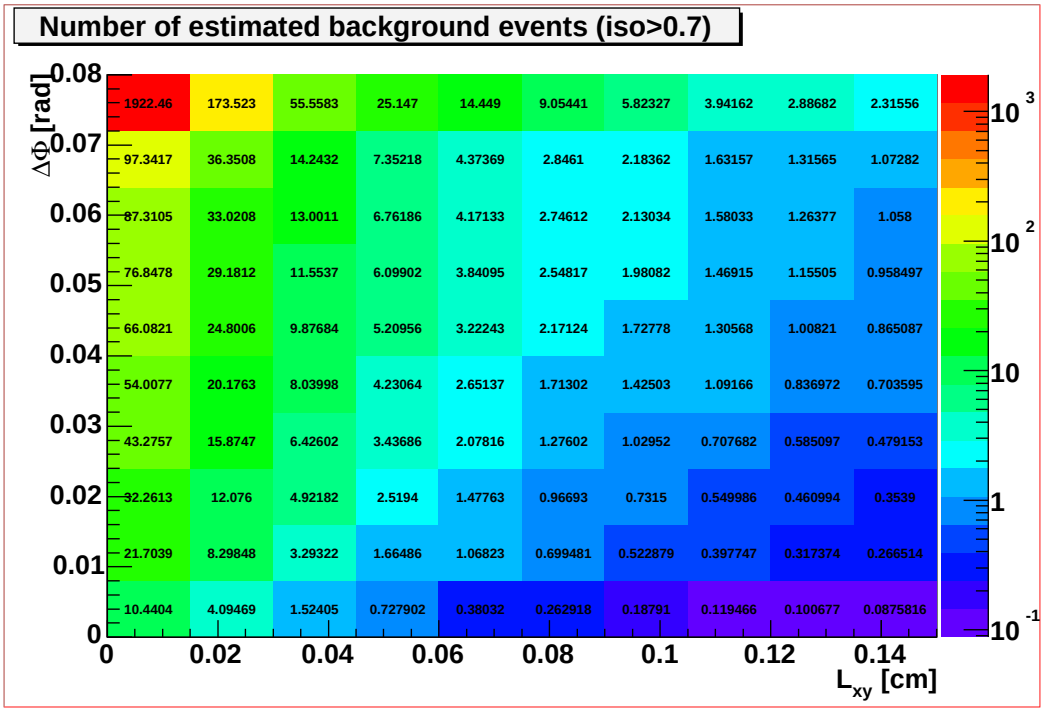

Figure D.5: Estimated background for the $B^0_d \to \mu\mu K^{*0}$ decay for $Iso > 0.7$.

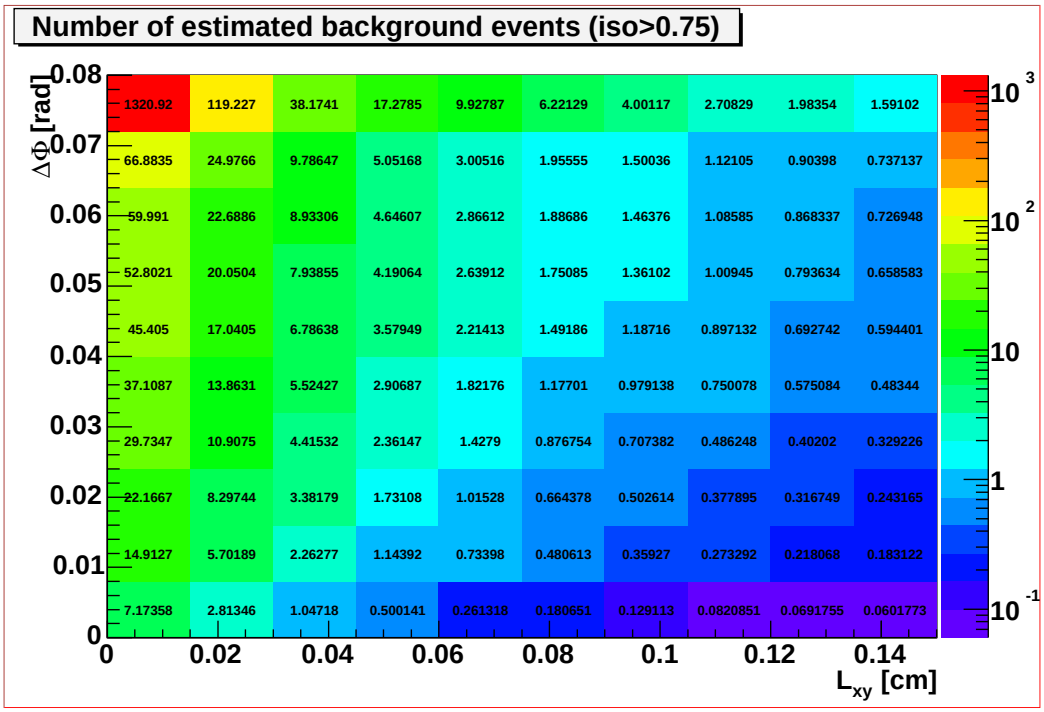

Figure D.6: Estimated background for the $B^0_d \to \mu\mu K^{*0}$ decay for $Iso > 0.75$.

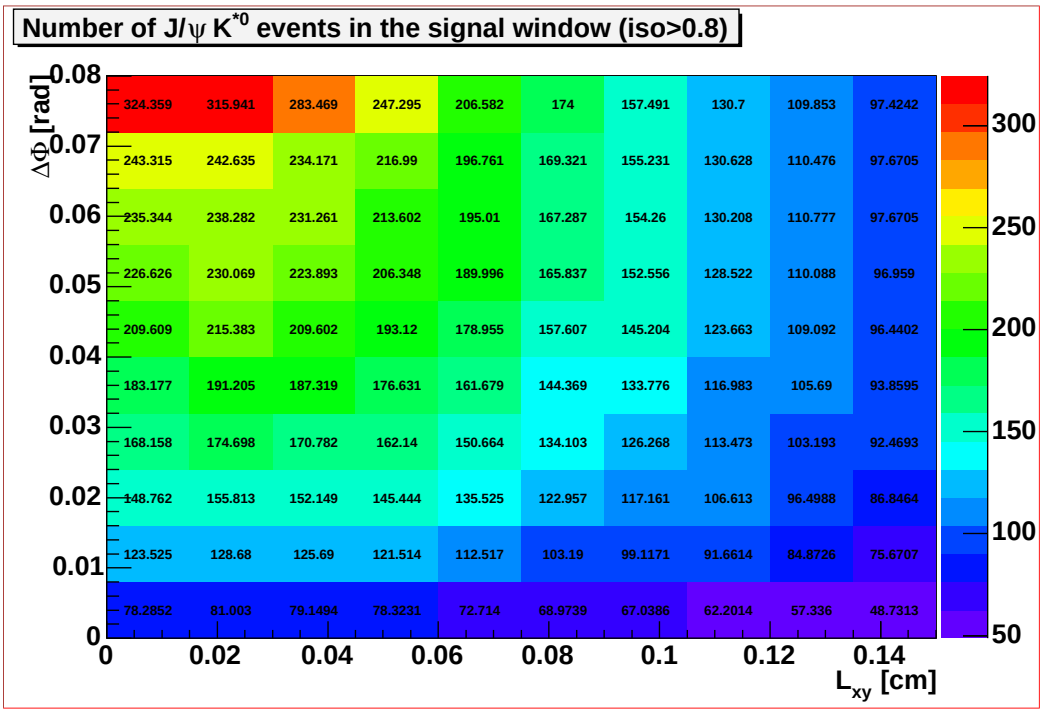

Figure D.7: Estimated background for the $B_d^0 \to \mu\mu K^{*0}$ decay for $Iso > 0.8$.

Appendix E

Number of estimated signal events for the $\mathrm{B}_d^0 \to \mu\mu K^{*0}$ decay

This Appendix shows the number estimated signal events for the $\mathrm{B}_d^0 \to \mu\mu K^{*0}$ decay as a function of the L_{xy}, $\Delta\Phi$ and $Isolation$ cuts. Each plot shows a scan of L_{xy} and $\Delta\Phi$ cuts corresponding to a given $Isolation$ cut. Figures E.1 through E.7 correspond to different $Isolation$ cuts from 0.5 to 0.8 in steps of 0.05. On these figures the first column represents the number of estimated signal events for the $\mathrm{B}_d^0 \to \mu\mu K^{*0}$ decay when there is no L_{xy} cut applied, while the other nine columns represent cuts from $0.015\,cm$ up to $0.135\,cm$ in steps of $0.015\,cm$; the uppermost row represents the number of estimated signal events for the $\mathrm{B}_d^0 \to \mu\mu K^{*0}$ decay when there is no $\Delta\Phi$ cut applied, while the other nine rows represent upper cuts on $\Delta\Phi$ from $0.072\,rad$ down to $0.008\,rad$ in steps of $0.008\,rad$.

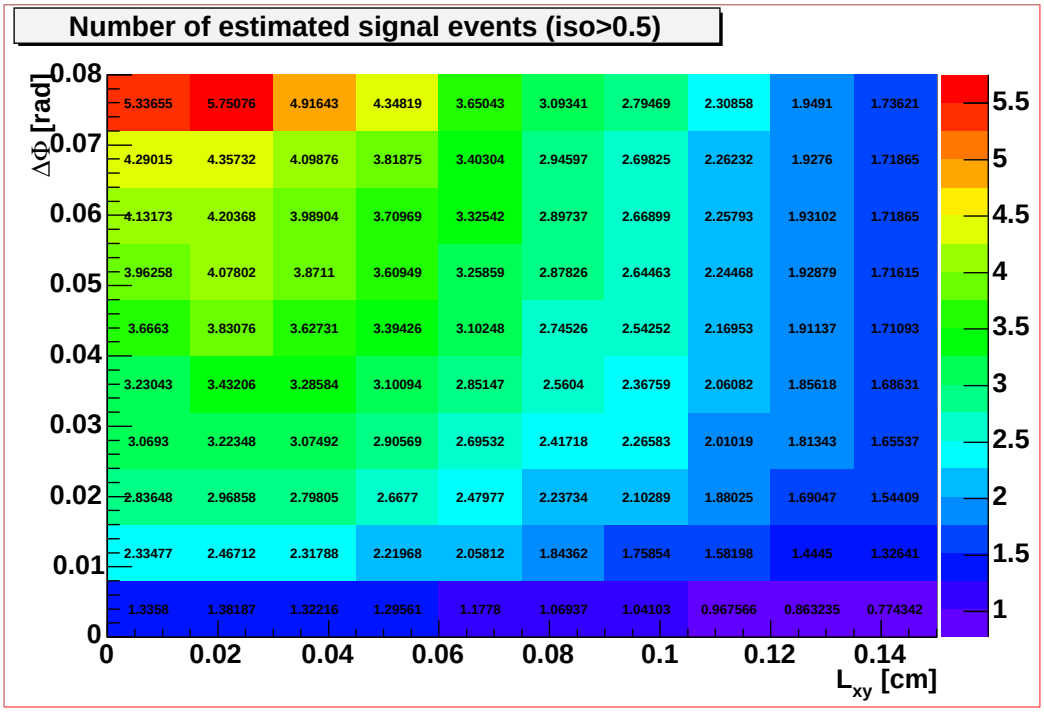

Figure E.1: Number of estimated $B^0_d \to \mu\mu K^{*0}$ events for $Iso > 0.5$.

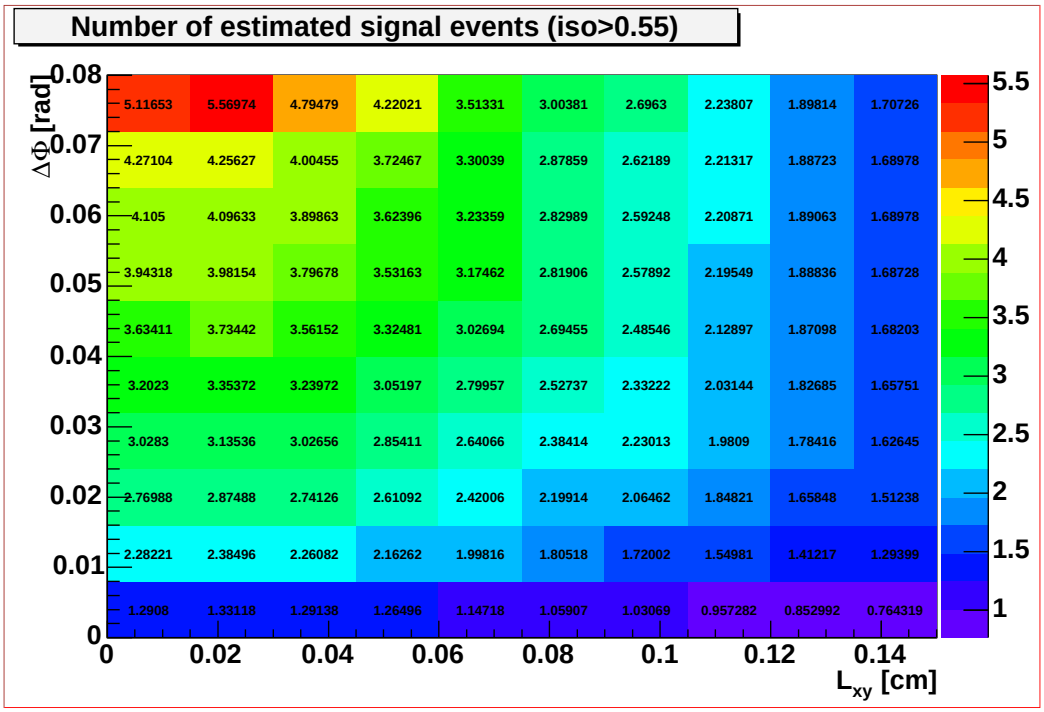

Figure E.2: Number of estimated $B^0_d \to \mu\mu K^{*0}$ events for $Iso > 0.55$.

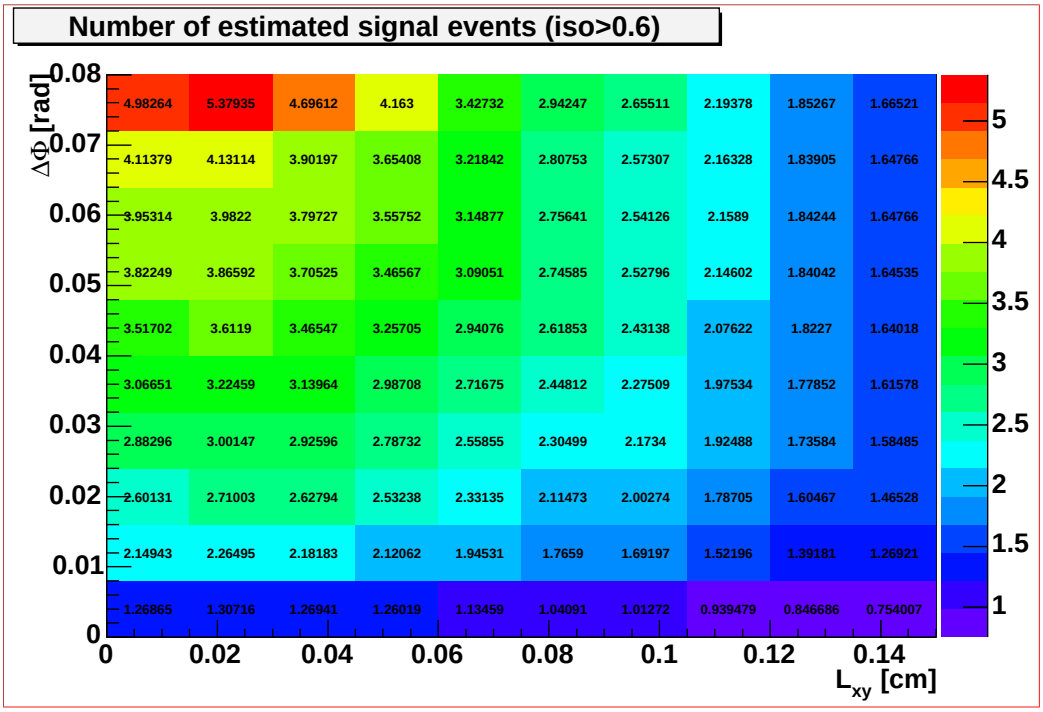

Figure E.3: Number of estimated $B_d^0 \to \mu\mu K^{*0}$ events for $Iso > 0.6$.

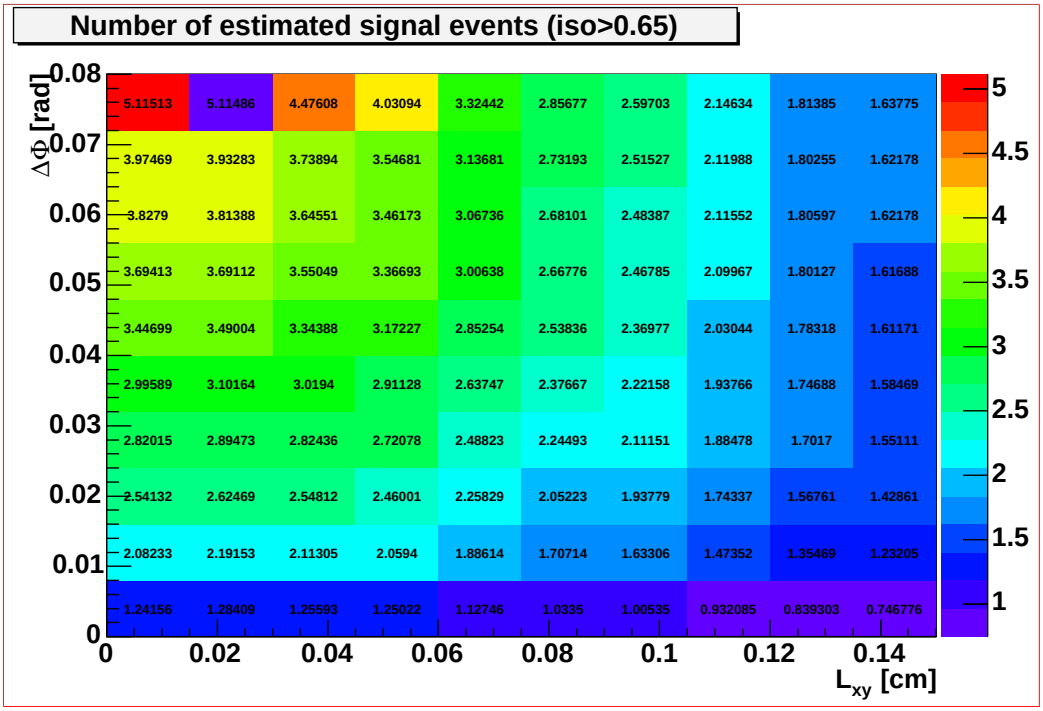

Figure E.4: Number of estimated $B_d^0 \to \mu\mu K^{*0}$ events for $Iso > 0.65$.

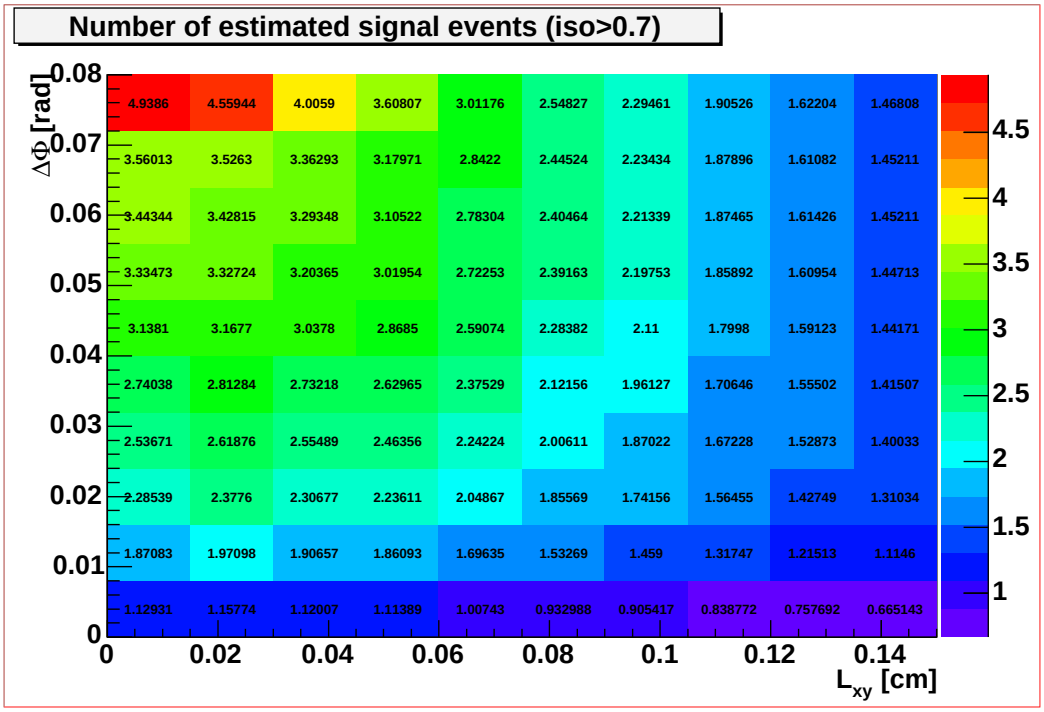

Figure E.5: Number of estimated $B^0_d \to \mu\mu K^{*0}$ events for $Iso > 0.7$.

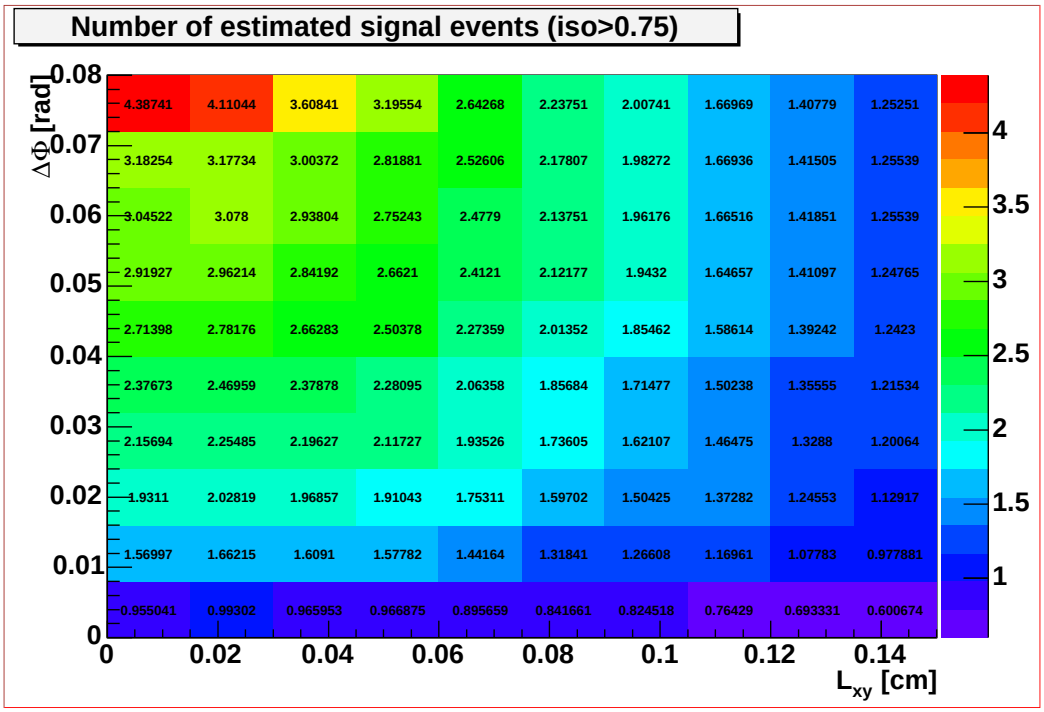

Figure E.6: Number of estimated $B^0_d \to \mu\mu K^{*0}$ events for $Iso > 0.75$.

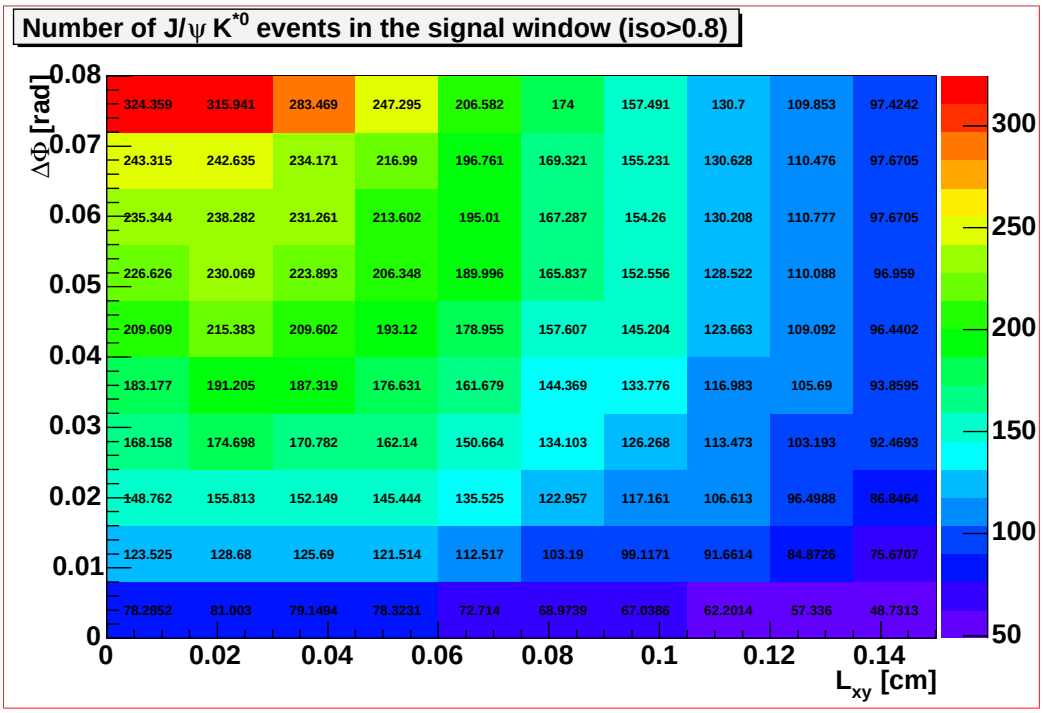

Figure E.7: Number of estimated $B_d^0 \to \mu\mu K^{*0}$ events for $Iso > 0.8$.

Bibliography

[1] F. Halzen and A. Martin, *Quarks & Leptons*, John Wiley & Sons, New York, 1984

[2] David Griffiths, *Introduction to Elementary Particles*, Harper & Row Publishers, New York, 1987

[3] Particle Data Group, *The Review of Particle Physics, Particle Listings 2003*

`http://pdg.lbl.gov`

[4] Andrzej J. Buras, Robert Fleischer, *Quark mixing, CP violation and rare decays after the top quark discovery*, hep-ph/9704376

`http://arxiv.org/abs/hep-ph/9704376`

[5] A. Ali, G. Hiller, *A theoretical reappraisal of branching ratios and CP asymmetries in the decays* $B \to (X_d, X_s)\ell^+\ell^-$ *and determination of the CKM parameters*, *Euro. Phys. Jour.* C**8**, 619 (1999)

`http://www.springerlink.com/app/home/content.asp?wasp`
`=fl9grlrwrrce6d62eaak&referrer=contribution&format`
`=2&page=1&pagecount=11`

[6] C. S. Kim, T. Morozumi, A. I. Sanda, $B \to X_q l^+ l^-(q = d, s)$ *and determination of* $|V_{td}/V_{ts}|$, *Phys. Rev.* D**56**, 7240 (1997)

`http://prola.aps.org/pdf/PRD/v56/i11/p7240_1`

[7] T. Affolder*et al.*, *A Measurement of* $\sin 2\beta$ *from* $B \to J/\psi K^0_S$ *with the CDF Detector*, *Phys. Rev.* D**61**, 072005 (2000)

`http://prola.aps.org/abstract/PRD/v61/i7/e072005`

[8] B. Aubert*et al.* (BaBar collaboration), *Measurement of the CP Asymmetry Amplitude* $\sin 2\beta$ *with* B^0 *Mesons*, *Phys. Rev. Lett.* 89, 201802 (2002)

`http://ojps.aip.org/getpdf/servlet/GetPDFServlet?filetype=`
`pdf&id=PRLTAO000089000020201802000001&idtype=cvips`

[9] K. Abe *et al.* (Belle Collaboration), *Improved measurement of mixing-induced CP violation in the neutral B meson system*, *Phys. Rev.* D**66**, 071102 (2002)

http://ojps.aip.org/getpdf/servlet/GetPDFServlet?filetype=pdf&id=PRVDAQ000066000007071102000001&idtype=cvips

[10] Tom Browder, *Results on the CKM angle ϕ_1 (β)*, presented at the XXI International Symposium on Lepton and Photon interactions at High Energies, Fermilab, 2003

http://conferences.fnal.gov/lp2003/program/S5/browder_s05_ungarbled.pdf

[11] A. B. Carter and A. I. Sanda, *Phys. Rev.* D**23**, 1567 (1981); I. I. Bigi and A. I. Sanda, *Nucl. Phys.* B**193**, 85 (1981)

[12] A. Höcker, H. Lacker, S. Laplace and F. Le Diberder, *A new approach to a global fit of the CKM matrix*, *Eur. Phys. J.* C**21**, 225-259 (2001)

http://www.edpsciences.org/articles/epjc/pdf/2001/12/epjc0729.pdf

[13] Klaus Schubert, *CKM Matrix Element Magnitudes*, presented at the XXI International Symposium on Lepton and Photon interactions at High Energies, Fermilab, 2003

http://conferences.fnal.gov/lp2003/program/S6/schubert_s06.pdf

[14] Home page of the CKM fitter group

http://ckmfitter.in2p3.fr/

[15] Belle collaboration, *Measurement of Time-Dependent CP-Violating Asymmetries in $B^0 \to \phi K_S, K^+K^-K^0_S$ and $\eta' K^0_S$ Decays*, *Phys. Rev. Lett.* 91, 261602 (2003)

http://ojps.aip.org/getpdf/servlet/GetPDFServlet?filetype=pdf&id=PRLTAO000091000026261602000001&idtype=cvips

[16] Hassan Jawahery, *CKM Unitarity Angles α and γ*, presented at the XXI International Symposium on Lepton and Photon interactions at High Energies, Fermilab, 2003

http://conferences.fnal.gov/lp2003/program/S5/jawahery_s05.pdf

[17] C. Bobeth, A. J. Buras, F. Krger, J. Urban, *CD Corrections to $B \to X_{d,s}\nu\bar{\nu}$, $B_{d,s} \to l^+l^-$, $K \to \pi\nu\bar{\nu}$ and $K_L \to \mu^+\mu^-$ in the MSSM*, *Nucl. Phys.* B**630**, 87-131 (2002)

http://documents.cern.ch/cgi-bin/
setlink?base=preprint&categ=hep-ph&id=0204225

[18] A. Ali, E. Lunghi, C. Greub, G. Hiller, *Improved Model-Independent Analysis of Semileptonic and Radiative Rare B Decays*, *Phys. Rev.* D**66**,034002 (2002)

http://ojps.aip.org/getabs/servlet/GetabsServlet?prog=
normal&id=PRVDAQ000066000003034002000001&idtype=cvips&gifs=no

[19] A. Ali, P. Ball, L. T. Handoko, G. Hiller, *Comparative study of the decays* $B \to (K, K^*)l^+l^-$ *in the standard model and supersymmetric theories*, *Phys. Rev.* D**61**, 074024 (2000)

http://prola.aps.org/pdf/PRD/v61/i7/e074024

[20] D. Melikhov, N. V. Nikitin, S. Simula, *Rare exclusive semileptonic* $b \to s$ *transitions in the standard model*, *Phys. Rev.* D**57**, 6814-6828 (1998)

http://prola.aps.org/abstract/PRD/v57/i11/p6814_1

[21] C. Q. Geng, C. P. Kao, *Lepton Polarization Asymmetry in* $B \to K^{(*)}l^+l^-$, *Phys. Rev.* D**54**, 5636-5641 (1996)

http://prola.aps.org/abstract/PRD/v54/i9/p5636_1

[22] P. Colangelo, F. De Fazio, P. Santorelli, and E. Scrimieri, *QCD sum rule analysis of the decays* $B \to Kl^+l^-$ *and* $B \to K^*l^+l^-$, *Phys. Rev.* D**53**, 3672-3686 (1996)

http://prola.aps.org/abstract/PRD/v53/i7/p3672_1

[23] CDF Collaboration, *Search for the Flavor-Changing Neutral Current Decays* $B^+ \to \mu^+\mu^- K^+$ *and* $B^0 \to \mu^+\mu^- K^{*0}$, *Phys. Rev. Lett.* 83, 3378-3383 (1999)

http://prola.aps.org/abstract/PRL/v83/i17/p3378_1

[24] CLEO Collaboration, *Improved Upper Limits on the FCNC Decays* $B \to K\ell^+\ell^-$ *and* $B \to K^*(892)\ell^+\ell^-$, *Phys. Rev. Lett.* 87, 181803 (2001)

http://ojps.aip.org/getabs/servlet/GetabsServlet?prog=
normal&id=PRLTAO000087000018181803000001&idtype=cvips&gifs=yes

[25] B. Aubert *et al.* (BABAR Collaboration), *Search for the Rare Decays* $B \to Kl^+l^-$ *and* $B \to K^*l^+l^-$, *Phys. Rev. Lett.* 88, 241801 (2002)

http://ojps.aip.org/getabs/servlet/GetabsServlet?prog=
normal&id=PRLTAO000088000024241801000001&idtype=cvips&gifs=yes

[26] K. Abe *et al.* (Belle Collaboration). *Observation of the Decay* $B \to Kl^+l^-$, *Phys. Rev. Lett.* 88, 021801 (2002)

http://ojps.aip.org/getabs/servlet/GetabsServlet?prog=normal&id=PRLTAO000088000002021801000001&idtype=cvips&gifs=yes

[27] Jeffrey D. Richman (BABAR Collaboration), *Evidence for the flavor changing neutral current decays* $B \to K\ell^+\ell^-$ *and* $B \to K^*\ell^+\ell^-$, ICHEP 2002, Amsterdam, July 27, 2002

https://oraweb.slac.stanford.edu:8080/pls/slacquery/BABAR_DOCUMENTS.DetailedIndex?P_BP_ID=3278

[28] B. Brau, *Selected topics on rare B decays*, presented at the 5th International Conference on Hyperons, Charm and Beauty Hadrons, Vancouver, June 25-29, 2002

http://beach2002.physics.ubc.ca/talks/Ben_Brau.pdf

[29] K. Abe *et al.* (Belle Collaboration), *Study of the Electroweak Penguin Decay* $B \to K^{(*)}\ell^+\ell^-$, BELLE-CONF-0241

http://belle.kek.jp/conferences/ICHEP2002/Papers-pdf/belle-conf-0241.pdf

[30] *Radiative and electroweak rare B decays*, presented by Mikihiko Nakao in Lepton-Photon 2003 on behalf of Belle, BaBar, CLEO, CDF and D0

http://conferences.fnal.gov/lp2003/program/S7/nakao_s07.pdf

[31] K. Abe *et al.* (Belle Collaboration), *Observation of* $B- > K^*l^+l^-$, *Phys. Rev. Lett.* 91, 261601 (2003)

http://ojps.aip.org/getpdf/servlet/GetPDFServlet?filetype=pdf&id=PRLTAO000091000026261601000001&idtype=cvips

[32] A. Ishikawa *et al.* (Belle Collaboration), *Observation of* $B \to K^*\ell^+\ell^-$, hep-ex/0308044

http://arxiv.org/abs/hep-ex/0308044

[33] B. Aubert *et al.* (BABAR Collaboration), *Evidence for the Rare Decay* $B \to K^*l^+l^-$ *and Measurement of* $B \to Kl^+l^-$, PUB-03/021

https://oraweb.slac.stanford.edu:8080/pls/slacquery/bbrdownload/babar-pub-03021.ps?P_FRAME=DEST&P_DOC_ID=6935

[34] C. Greub, A. Ioannissian, D. Wyler, *Effects of new physics in the rare decays* $B \to Kl^+l^-$ *and* $B \to K^*l^+l^-$, *Phys. Lett.* B**346**, 149 (1995)

`http://preprints.cern.ch/cgi-bin/setlink?base=preprint&categ=hep-ph&id=9408382`

[35] J. L. Hewett, J. D. Wells, *Searching for supersymmetry in rare B decays*, *Phys. Rev.* D**55**, 5549(1997)

`http://preprints.cern.ch/cgi-bin/setlink?base=preprint&categ=hep-ph&id=9610323`

[36] T. M. Aliev, A. Ozpineci, M. Savci, *Exclusive* $B \to K^*l^+l^-$ *decay with polarized* K^* *and new physics effects*, *Phys. Lett.* B**511**, 49-58 (2001)

`http://documents.cern.ch/cgi-bin/setlink?base=preprint&categ=hep-ph&id=0103261`

[37] T. M. Aliev, M. K. Cakmak, A. Ozpineci, M. Savci, *New physics effects to the lepton polarizations in the* $B \to Kl^+l^-$ *decay*, *Phys. Rev.* D**64**, 055007 (2001) (10 pages)

`http://documents.cern.ch/cgi-bin/setlink?base=preprint&categ=hep-ph&id=0103039`

[38] T. M. Aliev, M. K. Cakmak, M. Savci, *General analysis of lepton polarizations in rare* $B \to K^*l^+l^-$ *decay beyond the standard model*, *Nucl. Phys.* B**607**, 305-325 (2001)

`http://documents.cern.ch/cgi-bin/setlink?base=preprint&categ=hep-ph&id=0009133`

[39] T. M. Aliev, A. Ozpineci, M. Savci, *Fourth generation effects in rare exclusive* $B \to K^*l^+l^-$ *decay*, *Nucl. Phys.* B**585**, 275-289 (2000)

`http://documents.cern.ch/cgi-bin/setlink?base=preprint&categ=hep-ph&id=0002061`

[40] T. M. Aliev, D. A. Demir, M. Savci, *Probing the sources of CP violation via* $B \to K^*l^+l^-$ *decay*, *Phys. Rev.* D**62**, 074016 (2000)

`http://ojps.aip.org/getabs/servlet/GetabsServlet?prog=normal&id=PRVDAQ000062000007074016000001&idtype=cvips&gifs=no`

[41] T. M. Aliev, C. S. Kim, Y. G. Kim, *A Systematic Analysis of the Exclusive* $B \to K^*l^+l^-$ *Decay*, *Phys. Rev.* D**62**, 014026 (2000)

http://ojps.aip.org/getabs/servlet/GetabsServlet?prog=
normal&id=PRVDAQ000062000001014026000001&idtype=cvips&gifs=no

[42] *Study of the Flavor-Changing Neutral Current Decay $B \to K^{(*)}l^+l^-$ with Belle*, Thesis of Akimasa Ishikawa, Nagoya University, March 2002

http://belle.kek.jp/belle/theses/doctor/
ishikawa02/main.ps.gz

[43] *Search for the Decays $B_d^0 \to \mu^+\mu^-$, $B_s^0 \to \mu^+\mu^-$ and $B_s^0 \to \mu^+\mu^-\phi$ in $p\bar{p}$ Collisions at $\sqrt{s} = 1.8\,TeV$*, Thesis of Thomas Speer, University of Geneva, 2000

[44] Giulia Manca, *A Measurement Of The Ratio $R = \frac{\sigma_{W^\pm} \cdot Br(W^\pm \to e^\pm \nu)}{\sigma_{Z^0} \cdot Br(Z^0 \to e^+e^-)}$ in $p\bar{p}$ collisions at 1.96 TeV*, CDF internal note CDF/THESIS/ELECTROWEAK/CDFR/6521

http://www-cdf.fnal.gov/thesis/cdf6521_ratiothesis.ps.gz

[45] *A Measurement of the Z Boson Production Cross-section Multiplied by the Muon Branching Fraction*, Thesis of Gavin Hesketh, 2003

http://www-d0.fnal.gov/results/publications_talks/
thesis/hesketh/thesis.ps

[46] *Electron Identification and its Application to the Measurment of the Top Quark Production Cross Section*, Thesis of Florian Beaudette, 2003

http://www-d0.fnal.gov/results/publications_talks/
thesis/beaudette/thesis.ps

[47] F. Abe *et al.* (CDF Collaboration), *Observation of top quark production in anti-p p collisions*, *Phys. Rev. Lett.* 74, 2626-2631 (1995)

http://prola.aps.org/abstract/PRL/v74/i14/p2626_1

S. Abachi *et al.* (D0 Collaboration), Observation of the top quark, *Phys. Rev. Lett.* 74, 2632-2637 (1995)

http://prola.aps.org/abstract/PRL/v74/i14/p2632_1

[48] M. Church, *Substantial Upgrades to Tevatron Luminosity*, hep-ex/0105041

http://documents.cern.ch/cgi-bin/
setlink?base=preprint&categ=hep-ex&id=0105041

[49] Steve Holmes, *Performance Goals for the Accelerator Complex*, P5 Meeting at Fermilab, March 26, 2003, unpublished

http://www.fnal.gov/directorate/program.planning/P5_Holmes.pdf

[50] *Run II Plan V2.0 (Part-1)*, Presentation of P. Bhat in the Director's Review of Run II Luminosity Plan, January 20-22, 2004, unpublished

http://www-bdnew.fnal.gov/doereview04/Temple/
Presentations/03_bhat_Temple04.ppt

[51] *The Run II Luminosity Upgrade*, sent to DOE June 15, 2003, unpublished

http://www-bd.fnal.gov/doereview03/docs/Overview7.1.pdf

[52] *Recycler Status and Commissioning Plan/Electron Cooling*, Presentation of S. Nagaitsev in the Director's Review of Run II Luminosity Plan, January 20-22, 2004, unpublished

http://www-bdnew.fnal.gov/doereview04/Temple/
Presentations/05_Nagaitsev_Temple04.ppt

[53] *Run II Handbook*

http://www-bd.fnal.gov/lug/runII_handbook/RunII_index.html

[54] http://www.fnal.gov//pub/inquiring/physics/
accelerators/chainaccel.html

[55] http://www.fnal.gov/pub/now/tevlum.html

[56] http://www-cdfonline.fnal.gov/opshelp/stores/

[57] *Commissioning of the Run IIa CDF Slicon Detector*, Presented by A. Sill in the 8th International Conference on Instrumentation for Colliding Beam Physics

http://www-cdf.fnal.gov/internal/silicon/talks/Instr2002.pdf

[58] *Status of CDF Tracking*, Presented by S. Nahn at ICHEP 2002

http://www-cdf.fnal.gov/internal/silicon/talks/trackIChep.ppt

[59] The CDF II Collaboration, *The CDF II Detector Technical Design Report*, FERMILAB-Pub-96/390-E

http://www-cdf.fnal.gov/internal/upgrades/tdr/tdr.html

[60] *The CDF II Silicon Tracker*, Presented by I. Volobouev at DPF 2002

http://dpf2002.velopers.net/talks_pdf/280talk.pdf

[61] C. Issever (CDF Collaboration, *The CDF Run IIa Silicon Detector and its Upgrade RunIIb*, FERMILAB-CONF-03/401-E. Published Proceedings 12th International Workshop on Vertex Detection, Lake District, Cumbria, UK, September 14-19, 2003

`http://www-cdf.fnal.gov/physics/conferences/cdf6782_vertex2003_v3.ps`

[62] R. Rossin (CDF Collaboration), *The CDF Silicon Vertex Detector for Run II*, FERMILAB-CONF-03/397-E. Published Proceedings 8th International Conference on Advanced Technology and Particle Physics (ICATPP 2003): Astroparticle, Particle, Space Physics, Detectors and Medical Physics Applications, Como, Italy, October 6-10, 2003

`http://www-cdf.fnal.gov/physics/conferences/cdf6735_Como2003proceedings_2.pdf`

[63] C. Hill (CDF Collaboration), *Operational Experience and Performance of the CDFII Silicon Detector*, FERMILAB-CONF-03/412-E. Published Proceedings 6th International Conference on Large Scale Applications and Radiation Hardness of Semiconductor Detectors, Florence, Italy, September 29-October 1

`http://www-cdf.fnal.gov/physics/conferences/cdf6764_run2a_si_op_rd03.ps`

[64] *Commissioning, operation and first physics results of the CDF Run2a Silicon and status of its future upgrade for Run2b*, Presented by G. Bolla on EPS-HEP July 2003

`http://www-cdf.fnal.gov/internal/silicon/talks/EPSHEP-GB.pdf`

[65] COT Group, A. Mukherjee, R. Wagner, *CDF Central Outer Tracker*, CDF internal note CDF/DOC/TRACKING/CDFR/6227, unpublished

`http://www-cdf.fnal.gov/cdfnotes/cdf6227_CDF_COT.ps`

[66] K Burkett (CDF Collaboration), *Design and Construction of the CDF Central Outer Tracker*, FERMILAB-Conf-2000-128-E

`http://www-cdf.fnal.gov/physics/conferences/cdf5321_cot_pisa_v1.ps`

[67] *The Central Outer Tracker for Run II at CDF*, presented by D. Ambrose in the 9^{th} Pisa Meeting May 25-31, 2003

`http://penn01.fnal.gov/~cot/tlk/elba-2003-talk.ps`

[68] C. Chen *et al.*, *Measurement of the Track Reconstruction Efficiency in the COT Using a MC Track Embedding Technique*, CDF internal note CDF/PHYS/BOTTOM/CDFR/6394, unpublished

`http://www-cdf.fnal.gov/cdfnotes/cdf6394_cot_eff_v3.ps`

[69] L. J. Balka *et al.*, *The CDF central electromagnetic calorimeter*, *Nucl. Instrum. & Meth.* A**267**, 272-279 (1988)

`http://www.Sciencedirect.com/science?_ob=IssueURL&_tockey`
`=%23TOC%235314%231988%23997329997%23352577%23FLP%23Volume_267,`
`_Issues_2-3,_Pages_237-563_(1_May_1988)&_auth=y&view=c&_acct=`
`C000050221&_version=1&_urlVersion=0&_userid=10&md5=`
`ac62fa29f2fc2e74f20be978fa1cc9b4`

[70] Y Fukui *et al.*, *CDF end plug electromagnetic calorimeter using conductive plastic proportional tubes*, *Nucl. Instrum. & Meth.* A**267**, 280-300 (1988)

`http://www.Sciencedirect.com/science?_ob=IssueURL&_tockey=`
`%23TOC%235314%231988%23997329997%23352577%23FLP%23Volume_267,`
`_Issues_2-3,_Pages_237-563_(1_May_1988)&_auth=y&view=c&_acct=`
`C000050221&_version=1&_urlVersion=0&_userid=10&md5=`
`ac62fa29f2fc2e74f20be978fa1cc9b4`

[71] G. Ascoli *et al.*, *The CDF Central Muon Detector*, *Nucl. Instrum. & Meth.* A**268**, 33-40 (1988)

[72] The CDF Collaboration, *The 1992 CDF Muon System Upgrade*, CDF internal note CDF/PUB/MUON/PUBLIC/2858

[73] G. Brandenburg, T. Liss, P. Schlabach *et al.*, *The CDF Run 1 Muon System Upgrade*, CDF internal note CDF/DOC/MUON/PUBLIC/6362

`http://www-cdf.fnal.gov/cdfnotes/cdf6362_Run1_muon_upgrade.ps`

[74] *Performance of the CDF Cherenkov Luminosity Counters*, Presented by Song Ming Wang at DPF 2002

`http://dpf2002.velopers.net/talks_pdf/62talk.pdf`

[75] D. Acosta *et al.*, *The performance of the CDF Luminosity Monitor*, Submitted to *Nucl. Instrum. & Meth.*, May 2002

`http://www-cdf.fnal.gov/internal/people/links/`
`JacoboKonigsberg/instr02.ps`

[76] D. Acosta *et al.*, *The CDF Cherenkov Luminosity Monitor*, CDF internal note CDF/PUB/CDF/PUBLIC/5559, published in Nucl. Instr. & Meth. A**461**, 540-544 (2001)

`http://www-cdf.fnal.gov/cdfnotes/cdf5559_CLC_NIM.ps.gz`

[77] E.J. Thomson *et al.* (CDF Collaboration), *Online track processor for the CDF upgrade*, *IEEE Trans. Nucl. Sci.* 49, 1063 (2002)

`http://ieeexplore.ieee.org/xpl/tocresult.jsp?isNumber=22285&page=2`

[78] Yuri Gotra, James Kraus, Ting Miao, *Run II Level 1 Low p_T Muon Trigger Efficiency Measurement*, CDF internal note CDF/PHYS/TRIGGER/PUBLIC/6162, unpublished

`http://www-cdf.fnal.gov/cdfnotes/cdf6162_L1_trigger_eff_v1.ps`

[79] M. Casarsa *et al.*, *SVT absolute efficiency from simulation*, Reco Tag Meeting of February 21, 2003

`http://www-cdf.fnal.gov/internal/physics/bottom/reco-tag/TALKS/030221/casarsa.ps.gz`

[80] I. Vila (CDF Collaboration), *Performance and First Physics Results of the SVT Trigger at CDF II*, FERMILAB-CONF-03/219-E, Published Proceedings 2nd Workshop on the CKM Unitarity Triangle, Durham, England, April 5-9, 2003

`http://www-cdf.fnal.gov/physics/conferences/cdf6564_SVT_Durham.ps`

[81] J. Thom (CDF Collaboration), *Rare Charm and B Decays at CDF*, FERMILAB-CONF-03/387-E, Published Proceedings International Europhysics Conference on High-Energy Physics (HEP 2003), Aachen, Germany, July 17-23, 2003

`http://www-cdf.fnal.gov/physics/conferences/cdf6752_rare_D_B_EPS2003.ps`

[82] B. Ashmanskas *et al.* (CDF Collaboration), *The CDF Silicon Vertex Trigger*, FERMILAB-CONF-03/168-E, Published Proceedings 9th Pisa Meeting on Advanced Detectors: Frontier Detectors for Frontier Physics, La Biodola, Isola d'Elba, Italy, May 25-31, 2003

`http://www-cdf.fnal.gov/physics/conferences/cdf6502_elba_svt.ps`

[83] M. Bishai (CDF Collaboration), *Beauty and Charm Physics at CDF Run II*, FERMILAB-CONF-03/310-E, Published Proceedings 4th International Symposium on LHC Physics and Detectors (LHC 2003), Batavia, IL, May 1-3, 2003

http://www-cdf.fnal.gov/physics/conferences/
cdf6657_lhc2003_proc_rev2.ps

[84] K. Anikeev *et al.*, *EVB and Level3 for Aces*, CDF internal note CDF/DOC/LEVEL-3/PUBLIC/5793, unpublished

http://www-cdf.fnal.gov/cdfnotes/cdf5793_Level3_EVB_for_Aces.ps.gz

[85] K. Anikeev *et al.*, *Event Builder and Level 3 Manual for Experts*, CDF internal note CDF/DOC/ONLINE/PUBLIC/6138, unpublished

http://www-cdf.fnal.gov/cdfnotes/cdf6138_Evb_Level3_MANUAL.ps

[86] R. G. C. Oldeman (CDF Collaboration), *Performance of CDF for B Physics*, FERMILAB-CONF-03/156-E, Published Proceedings 2nd Workshop on the CKM Unitarity Triangle, Durham, England, April 5-9, 2003

http://www-cdf.fnal.gov/physics/conferences/
cdf6469_Bperformance.ps

[87] Wolfram Erdmann, Thomas Speer, *Search for the rare decays* $B^+ \to \mu\mu K^+$ *and* $B_d^0 \to \mu\mu K^{*0}$, CDF internal note CDF/ANAL/BOTTOM/CDFR/4517

http://www-cdf.fnal.gov/cdfnotes/cdf4517_rare_B_search.ps.gz

[88] Allan Clark, Xin Wu, Andras Zsenei, *Run II Dimuon Trigger for Rare B Decays*, CDF internal note CDF/DOC/BOTTOM/CDFR/5635, unpublished

http://www-cdf.fnal.gov/cdfnotes/
cdf5635_run2_rareb_dimu_trig.ps.gz

[89] *Rare B Triggers Status and Plans*, Presented by András Zsenei at the Trigger and Dataset Working Group August 6, 2002

http://www-cdf.fnal.gov/internal/upgrades/daq_trig/
twg/files02/020806_zsenei.pdf

[90] *Rare B trigger status and optimization*, Presented by András Zsenei at the Trigger and Dataset Working Group November 7, 2002

http://www-cdf.fnal.gov/internal/physics/bottom/
jpsi/Nov7_02/Andras_nov7.pdf

[91] K. Bloom and W.-M. Yao, *"Outside-In" Silicon Tracking at CDF*, CDF internal note CDF/DOC/TRACKING/CDFR/5991, unpublished

http://www-cdf.fnal.gov/cdfnotes/cdf5991_OI_Tracking.ps.gz

[92] M. Feindt, S. Menzemer, K. Rinnert, *TrackingKal - A Tracking and Alignment Software Package for the CDFII Silicon Detector*, CDF internal note CDF/THESIS/TRACKING/PUBLIC/5968

`http://www-cdf.fnal.gov/thesis/cdf5968_silicon_tracking.ps.gz`

[93] Paolo Gatti, *Performance of the new tracking system at CDF II*, CDF internal note CDF/THESIS/TRACKING/PUBLIC/5561

`http://www-cdf.fnal.gov/thesis/cdf5561_tracking_performance.ps.gz`

[94] K. Kelley, B. Mattingly, P. Sphicas, *A Study of the Isolation of B Mesons*, CDF internal note CDF/ANAL/BOTTOM/CDFR/2765, unpublished

`http://www-cdf.fnal.gov/cdfnotes/cdf2765_b_meson_isolation.ps.gz`

[95] G. Bauer J. Friedman K. Kelley T. Shah P. Sphicas, *A Study of the Isolation of B-Mesons Part II*, CDF internal note CDF/ANAL/BOTTOM/CDFR/3684, unpublished

`http://www-cdf.fnal.gov/cdfnotes/cdf3684_b_isolation_part_ii.ps.gz`

[96] G. Punzi, *Sensitivity of searches for new signals and its optimization*, physics/0308063

`http://doc.cern.ch//archive/electronic/physics/0308/0308063.pdf`

[97] D.Glenzinski, M.Herndon, T.Kamon, V.Krutelyov, C.-J.Lin, J.Thom, A.Yagil, *A Search for $B_s \to \mu^+\mu^-$ Decays Using RunII Data*, CDF internal note CDF/DOC/BOTTOM/CDFR/6397

`http://www-cdf.fnal.gov/cdfnotes/cdf6397_BsMuMu_170pb.ps`

[98] Search for FCNC decay $B_s \to \mu\mu$, presentation of D. Glezinski at the RECO-TAG meeting of July 24, 2003

`http://www-cdf.fnal.gov/internal/physics/bottom/`
`bmtg_minutes/Jul_24_2003/BGroup_BsMuMu_030724.pdf`

[99] K.Anikeev, G.Bauer, I.Furic, S.Gromoll, A.Korn, I.Kravchenko, Ch.Paus, A. Rakitin, J.Tseng, *Calibration of Energy Loss and Magnetic Field using J/psi Events in Run II*, CDF internal note CDF/DOC/BOTTOM/CDFR/5958, unpublished

`http://www-cdf.fnal.gov/cdfnotes/cdf5958_eloss-bfield-calib.ps.gz`

[100] Feldman, G J; Cousins, R D, *A Unified Approach to the Classical Statistical Analysis of Small Signals*, *Phys. Rev.* D**57**, 3873-3889 (1998)

http://prola.aps.org/abstract/PRD/v57/i7/p3873_1

[101] Bob Cousins, private communication

[102] G. Feldman, *Multiple Measurements and Parameters in the Unified Approach*, Workshop on Confidence Limits, Fermilab, March 28, 2000

http://conferences.fnal.gov/cl2k/copies/feldman2.pdf

[103] Wolfgang A. Rolke and Angel M. Lopez, *Confidence intervals and upper bounds for small signals in the presence of background noise*, *Nucl. Instrum. & Meth.* A**458**, 745 (2001)

[104] J. Conrad, O. Botner, A. Hallgren, and C. Perez de los Heros, *Including systematic uncertainties in confidence interval construction for Poisson statistics*, *Phys. Rev.* D**67**, 012002 (2003)

http://ojps.aip.org/getpdf/servlet/GetPDFServlet?filetype=pdf&id=PRVDAQ000067000001012002000001&idtype=cvips

[105] Gary C. Hill, *Comment on "Including systematic uncertainties in confidence interval construction for Poisson statistics"*, *Phys. Rev.* D**67**, 118101 (2003),

http://ojps.aip.org/getpdf/servlet/GetPDFServlet?filetype=pdf&id=PRVDAQ000067000011118101000001&idtype=cvips

[106] N. Reid, D.A.S. Fraser, *Likelihood inference in the presence of nuisance parameters*, physics/0312079

http://xxx.lanl.gov/abs/physics/0312079

[107] http://www.physics.ucla.edu/~cousins/stats/expandedtables_68_90_95.ps

[108] *The ATLAS Inner Tracker and the detection of light supersymmetric Higgs bosons*, Thesis of Marcel Vos, University of Twente, 2003

http://atlas.web.cern.ch/Atlas/documentation/thesis/vos/vosthesis.pdf

[109] The Large Hadron Collider Home Page

http://lhc-new-homepage.web.cern.ch/lhc-new-homepage/

[110] http://www.cerncourier.com/main/article/40/3/13

[111] S. S. Adler *et al.* (PHENIX Collaboration), *Absence of Suppression in Particle Production at Large Transverse Momentum in* $\sqrt{s_{NN}} = 200\,GeV$ *d+Au Collisions*, nucl-ex/0306021,

www.arxiv.org/abs/nucl-ex/0306021

[112] B.B.Back *et al.* (PHOBOS Collaboration), *Centrality dependence of charged hadron transverse momentum spectra in d+Au collisions at* $\sqrt{s_{NN}} = 200\,GeV$, nucl-ex/0306025

www.arxiv.org/abs/nucl-ex/0306025

[113] I. Arsene *et al.* (BRAHMS Collaboration), *Transverse Momentum Spectra in Au+Au and d+Au Collisions at* $\sqrt{s_{NN}}$*=200 GeV and the Pseudorapidity Dependence of High* p_T *Suppression*, nucl-ex/0307003

www.arxiv.org/abs/nucl-ex/0307003

[114] J. Adams *et al.* (STAR Collaboration), *Multiplicity fluctuations in Au+Au collisions at* $\sqrt{s_{NN}} = 130\ GeV$, nucl-ex/0307007

www.arxiv.org/abs/nucl-ex/0307007

[115] ALICE Collaboration, *ALICE: technical proposal for a large ion collider experiment at the CERN LHC*, CERN-LHCC-95-71, LHCC-P-3, Geneva, CERN, 1995

http://documents.cern.ch/cgi-bin/setlink?base=generic&categ=public&id=cer-0214817

[116] LHCb Collaboration, *LHCb: Technical Proposal*, CERN-LHCC-98-004, LHCC-P-4, Geneva, CERN, 20 Feb 1998

http://lhcb-tp.web.cern.ch/lhcb-tp/

[117] CMS Collaboration, *Technical proposal*, CERN-LHCC-94-38, LHCC-P-1, Geneva, CERN, 1994

http://documents.cern.ch/cgi-bin/setlink?base=generic&categ=public&id=cer-0212026

[118] ATLAS Collaboration, *ATLAS: technical proposal for a general-purpose pp experiment at the Large Hadron Collider at CERN*, CERN-LHCC-94-43, LHCC-P-2, Geneva, CERN, 1994, ISBN 92-9083-067-0

http://documents.cern.ch/cgi-bin/setlink?base=generic&categ=public&id=cer-0212025

[119] *ATLAS TDR 4*, CERN/LHCC/97-16, ISBN 92-9083-102-2

http://atlas.web.cern.ch/Atlas/GROUPS/INNER_DETECTOR/TDR/tdr.html

[120] Home page of the Pixel detector (ATLAS)

`http://atlas.web.cern.ch/Atlas/GROUPS/INNER_DETECTOR/PIXELS/pixel.html`

[121] ATLAS Collaboration, *ATLAS Detector and Physics Performance: Technical Design Report 1*, CERN-LHCC-99-014, ATLAS-TDR-14, Geneva, CERN, 25 May 1999

`http://documents.cern.ch/cgi-bin/setlink?base=generic&categ=public&id=cer-0317330`

[122] ATLAS Collaboration, *ATLAS Detector and Physics Performance: Technical Design Report 2*, CERN-LHCC-99-015, ATLAS-TDR-15, Geneva, CERN, 25 May 1999

`http://documents.cern.ch/cgi-bin/setlink?base=generic&categ=public&id=cer-0317331`

[123] N. Benekos, R. Clifft, M. Elsing, A. Poppleton, *ATLAS Inner Detector Performance*, ATLAS internal note ATL-COM-INDET-2003-023, unpublished

`http://doc.cern.ch//archive/electronic/cern/others/atlnot/Communication/indet/com-indet-2003-023.pdf`

[124] *ATLAS High Level Trigger, Data Acquisition and Controls*, ATLAS-TDR-016, CERN-LHCC-2003-022

`http://doc.cern.ch//archive/electronic/other/generic/public/cer-002375189.pdf`

[125] J. Vermeulen *et al.*, *The Baseline DataFlow System of the ATLAS Trigger & DAQ*, ATL-DAQ-2003-032

`http://doc.cern.ch//archive/electronic/cern/others/atlnot/Note/daq/daq-2003-032.pdf`

[126] R. Hauser, *The ATLAS Trigger System*, SN-ATLAS-2003-027, ATL-DAQ-2003-047

`http://doc.cern.ch//archive/electronic/cern/preprints/snotes/sn-atlas-2003-027.pdf`

[127] *ATLAS TDR 5*, CERN/LHCC/97-17, ISBN 92-9083-103-0

`http://atlas.web.cern.ch/Atlas/GROUPS/INNER_DETECTOR/TDR/tdr-figs.html#Vol.II`

[128] http://www.hep.man.ac.uk/atlas/module/

[129] D. Campbell *et al.*, *The development of a rad-hard CMOS chip for the binary readout of the ATLAS semiconductor tracker*, 5th Conference on Electronics for LHC Experiments, Snowmass, CO, USA, 20 - 24 Sep 1999, CERN-LHCC-99-033

http://doc.cern.ch/archive/cernrep//1999/99-09/p152.pdf

[130] T. Dubbs *et al.*, *The developement of the CAFE-P/CAFE-M bipolar chips for the ATLAS semiconductor tracker*, 5th Conference on Electronics for LHC Experiments, Snowmass, CO, USA, 20 - 24 Sep 1999, CERN-LHCC-99-033

http://doc.cern.ch/archive/cernrep//1999/99-09/p123.pdf

[131] D. Melikhov *et al.*, *Studying the physics beyond the Standard Model in rare semileptonic B-decay* $\mathrm{B}_d^0 \to K^{*0}\mu\mu$ *- with ATLAS detector*, ATLAS Internal Note PHYS-98-123 (1998)

[132] A. Ali, Gian-F. Giudice, T. Mannel, T. M. Aliev, C. S. Kim and M. Savci, *Towards a model-independent analysis of rare B decays*, *Phys. Lett.* B**441**, 410 (1998), ERN-TH-7346-94, hep-ph-9408213, Geneva, CERN, 2 Aug 1993 Published in: *Z. Phys.* C**67** 417-432 (1995)

[133] *Evaluation of Silicon sensors for the ATLAS Silicon Tracker, and TPC reconstruction in the HARP Experiment*, Thesis of Maria Cristina Morone, Geneva, 2003

[134] *ABCD3T Specification ver. 1.2*

http://chipinfo.web.cern.ch/chipinfo/docs/abcd3t_spec_v1.2.pdf

[135] W. Dabrowski, J. Kaplon, R. Szczygiel, *SCT128B - a prototype chip for binary readout of silicon strip detectors*, *Nucl. Instrum. & Meth.* A**421** 303-315 (1999)

[136] F. Anghinolfi *et al.*, *Performance of the electrical module prototypes for the ATLAS silicon tracker*, 5th Conference on Electronics for LHC Experiments, Snowmass, CO, USA, 20 - 24 Sep 1999, CERN-LHCC-99-033

http://doc.cern.ch/archive/cernrep//1999/99-09/p118.pdf

[137] W. Dabrowski *et al.*, *Design and performance of the ABCD chip for the binary readout of silicon strip detectors in the ATLAS semiconductor tracker*, *IEEE Trans. Nucl. Sci.* 47 (2000) no.6 (pt.1), pp.1843-50 1999 IEEE Nuclear Science Symposium and Medical Imaging Conference, Seattle, WA, USA, 24 - 30 Oct 1999 - IEEE, Piscataway, NJ, 1999. - 382-9 (vol.1)

[138] J. Bernabeu *et al.*, *Results of the 1999 H8 beam tests of ATLAS-SCT prototypes*, *Nucl. Instrum. & Meth.* A**466** (2001) no.2, pp.397-405

http://weblib.cern.ch/cgi-bin/ejournals?publication=Nucl.+Instrum.+Methods+Phys.+Res.,+A&volume=466&year=2001&page=397

[139] W. Dabrowski *et al.*, *The ABCD binary readout chip for silicon strip detectors in the ATLAS silicon tracker*, 4th Workshop on Electronics for LHC Experiments, Rome, Italy, 21 - 25 Sep 1998, CERN-LHCC-98-036 - pp.175-179

[140] W. Dabrowski *et al.*, *Radiation hardness of the ABCD chip for the binary readout of silicon strip detectors in the ATLAS semiconductor tracker*, 5th Conference on Electronics for LHC Experiments, Snowmass, CO, USA, 20 - 24 Sep 1999, CERN-LHCC-99-033

http://doc.cern.ch/archive/cernrep//1999/99-09/p113.pdf

[141] W. Dabrowski *et al.*, *Progress in development of the readout chip for the ATLAS semiconductor tracker*, 6th Workshop on Electronics for LHC Experiments, Cracow, Poland, 11 - 15 Sep 2000, CERN-LHCC-2000-041 - pp.115

http://doc.cern.ch/archive/cernrep/2000/2000-010/p115.pdf

[142] *SCTA128LC & SCTA128HC Chip Specification Version 0.1*

[143] *SCTA128VG Specification version 1.3*

http://chipinfo.web.cern.ch/chipinfo/docs/scta128vg_spec1-3.pdf

[144] *Documentation for the SCTA128VG Linux Data Acquisition software*

http://chipinfo.web.cern.ch/chipinfo/docs/sctadaq.pdf

[145] E. Chesi *et al.*, *Performance of a 128 channel analogue front-end chip for readout of Si strip detector modules for LHC experiments*, *IEEE Trans. Nucl. Sci.* 47 (2000) no.4 (Pt.1), pp.1434-1441, 1999 IEEE Nuclear Science Symposium and Medical Imaging Conference, Seattle, WA, USA, 24 - 30 Oct 1999 - IEEE, Piscataway, NJ, 1999. - pp.94-101

[146] J. Kaplon *et al.*, *Progress in Development of the Analogue Read-out Chip for Silicon Strip Detector Modules for LHC Experiments*, 7th Workshop on Electronics for LHC Experiments, Stockholm, Sweden, 10 - 14 Sep 2001, CERN-LHCC-2001-034

http://doc.cern.ch/archive/cernrep/2001/2001-005/p90.pdf

[147] Dirk Meier, *Diamond Detectors for Particle Detection and Tracking*, PhD thesis submitted at University of Heidelberg, January 1999

http://atlas.web.cern.ch/Atlas/documentation/thesis/meier/thesis.html

[148] J. Lozano Bahilo *et al.*, *Results with Si Strip Detector Modules with Full Analogue Readout for LHC*, 4th International Meeting on Front End Electronics for Tracking Detectors at Future High Luminosity Colliders , 16 - 19 May 2000, Perugia, Italy

[149] J. Kaplon *et al.*, *Analogue read-out chip for Si strip detector modules for LHC experiments*, 6th Workshop on Electronics for LHC Experiments, Cracow, Poland, 11 - 15 Sep 2000, CERN-LHCC-2000-041 - pp.120

`http://doc.cern.ch/archive/cernrep/2000/2000-010/p120.pdf`

[150] J. Lozano-Bahilo, A. Rudge, A. Zsenei, *A linear optical link using radiation hard VCSELs*, *Nucl. Instrum. & Meth.* A**461** (2001) no.1-3, pp.530-6

`http://weblib.cern.ch/cgi-bin/ejournals?publication=Nucl.+Instrum.+Methods+Phys.+Res.,+A&volume=461&year=2001&page=530`

[151] J. Lozano-Bahilo, A. Rudge, A. Zsenei, *A Linear Optical Link using VCSELs*, 4th International Meeting on Front End Electronics for Tracking Detectors at Future High Luminosity Colliders, 16 - 19 May 2000, Perugia, Italy

[152] J. Lozano-Bahilo, A. Rudge, A. Zsenei, *A Linear Optical Link Using Radiation Hard VCSELs*, Frontier Detectors for Frontier Physics, 8^{th} Pisa Meeting on Advanced Detectors, May 21-27, 2000 - La Biodola, Isola d'Elba, Italy